Characterisation of Plastic and Creep Strains From Lattice Orientation Measurements

Thesis

Faculty of Mathematics, Computing & Technology

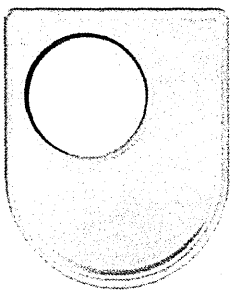

The Open University

Department of Engineering & Innovation

Characterisation of Plastic and Creep Strains from Lattice Orientation Measurements

By

David Njuguna Githinji

December 2013

A THESIS SUMMITTED TO THE DEPARTMENT OF ENGINEERING & INNOVATION OF THE OPEN UNIVERSITY FOR THE DEGREE OF DOCTOR OF PHILOSOPHY

DATE of SUBMISSION : 31 DECEMBER 2013

DATE of AWARD : 21 FEBRUARY 2014

ABSTRACT

Electron backscatter diffraction (EBSD) is a powerful technique for measuring crystallographic orientation in polycrystalline materials. This thesis explores the potential of EBSD for characterising localised inelastic strain from lattice orientation measurements. A systematic study under uniaxial isothermal loading conditions was performed to examine the influence of microstructure and deformation conditions on strain-induced lattice orientation changes (misorientation). The study was conducted on both service-aged and un-aged Type 316H stainless steels through a series of monotonic tests in tension, compression and in constant load creep.

The study demonstrates that the development of misorientation depends on many factors which need consideration before EBSD can be applied for strain assessment. It is shown that the measured evolution of misorientations is a function of microstructure and grain size. A misorientation-based strain assessment method is proposed which is relatively insensitive to microstructure and grain size. In service-aged steel, the measured evolution of misorientations is shown to be independent of the deformation temperature (between 24°C and 550°C) and deformation mode (tension vs. compression) for strain rates down to about $10^{-6}s^{-1}$. Empirical correlations between the accumulated plastic strain and different misorientation metrics are developed for true strains up to 0.23. However, at 550°C the evolution of measured misorientations is shown to be strain rate dependent below $10^{-6}s^{-1}$.

The potential of EBSD to distinguish plastic strain from creep strain is demonstrated. Misorientation development is shown to occur at a faster rate with increasing strain in plastic than in creep deformation. Similarly, the proportion of twin boundaries in service-aged steel is shown to reduce with increasing strain at a faster rate in creep than in plastic deformation. Two novel methods for creep strain estimation are proposed which utilise the disparities in the misorientation development and twin boundary reduction under the two different deformation regimes.

A good correspondence is established between the strain estimates from the proposed methods and those derived from hardness measurements and digital image correlation. The methods are shown to be applicable to real power plant components through successful mapping of plastic and creep strain distributions in weldments after different periods in service.

ACKNOWLEDGEMENTS

I wish to address my deepest gratitude to my supervisors Dr. Shirley M. Northover and Prof. John P. Bouchard for their guidance, support and fruitful discussions over the course of this study. I would also like to thank them for offering me an opportunity to pursue PhD studies. In addition I wish to express my gratitude to The Open University and EDF Energy for the financial support and provision of research materials. I extend my thanks to Dr. Dave Dean and Mr. Mike Spindler from EDF Energy Structural Integrity Group for their advice and discussions which helped to shape the research for the needs of the power generating plants in UK.

I am very grateful to the technical members of staff for their assistance during this project. Particular reference is made to Mr. Pete Ledgard for his assistance in sample machining, Mr. Stan Hiller for his guidance in optical microscopy and mechanical testing, Mr. Gordon Imlach for his assistance in scanning electron microscopy and electron backscatter diffraction, Dr. Colin Gagg for his assistance in creep testing, and Dr. Ian Norman for his training and guidance in nanoindentation measurements. I wish also to thank Mrs Heather Davies for the training she offered on transmission electron microscopy.

Special thanks to all PhD students in the material engineering group for their friendship and support during my stay. I will forever remember our lunchtime discussions and our weekend football tournaments. I salute you Dr. Paddea and Dr. Traore for your great comradeship. To all staff members in the department, thank you for your friendship.

Finally, I wish to sincerely thank my wife Julia, my daughter Gracie and son Jimmie for tolerating my absenteeism and for their continuous support over the years. This thesis is dedicated to them and to my parents.

David Njuguna Githinji

December 2013.

PREFACE

This thesis is submitted for the degree of Doctor of Philosophy of The Open University, United Kingdom. The research described herein was conducted in the Department of Engineering & Innovation, Faculty of Mathematics, Computing and Technology, between November 2010 and December 2013 under the supervision of Dr. Shirley M. Northover and Prof. John P. Bouchard.

This work is original to the best of my knowledge, except where reference is made to the work of others. This work has not been submitted in whole or part for any other degree at any other university. Part of this work has been published in an academic journal and presented in a conference as listed below:

1. Githinji D, Northover S, Bouchard PJ and Rist M, *An EBSD Study of the Deformation of Service-Aged 316 Austenitic Steel*, Metallurgical and Materials Transactions A, 2013. **44**(9): p. 4150-4167.
2. Githinji D, Northover S, Bouchard PJ and Rist M, *An EBSD Based Investigation of Plasticity of an Aged 316 Austenitic Stainless Steel during Room and High Temperature Deformation*, EBSD conference, Teddington, United Kingdom, 2012.

David Njuguna Githinji

December 2013.

TABLE OF CONTENTS

LIST OF FIGURES

LIST OF TABLES

NOMENCLATURE

Corresponding units are given in the text

Symbol	Description
T_m	Absolute melting temperature
Q	Activation energy for plastic flow
ϖ	Angle between indenter's opposite facets
γ	Austenite phase in iron
B	Barrelling coefficient in compression test
k	Boltzmann's constant in creep power law
ϑ_{hkl}	Braggs angle
b	Burgers vector magnitude
ϕ	Constant in Hall-Petch equation
α	Constant in Taylor's equation
Ω	Creep sensitivity factor for EBSD metrics
ε_c	Creep strain
r	Critical radius for dislocation bowing
D_{gb}	Diffusion coefficient along grain boundaries
ρ	Dislocation density
ε	EBSD measurement step-size
ζ	Elastic strain correction factor
λ	Electromagnetic wavelength
φ	Electron backscattering coefficient
η	Electron diffraction order
$\varphi_1, \varphi, \varphi_2$	Euler angles
$\{hkl\}$	Family of planes
Γ	Gamma function
Θ	Grain mean misorientation
ζ	Grain size
H_c	Height coefficient in compression test
φ	Inclination angle between incident beam and defect plane in TEM
d_{hkl}	Interplanar spacing
λ	Inter-precipitate distance
D_v	Lattice diffusion coefficient
a	Lattice parameter
μ	Logarithmic mean in lognormal distribution
δ	Logarithmic standard deviation in lognormal distribution

Θ_d	Mean misorientation threshold for grain's deformation
ε_m	Minimum creep strain rate
θ	Misorientation angle
ρ_m	Mobile dislocation density
v_m	Mobile dislocation velocity
O_v	Ovality coefficient in compression test
σ_i	Overall crystal lattice resistance
v_p	Poisson's ratio
ε_p	Prior plastic strain
P_r	Primary creep stage
w	Projected dislocation length
n	Sample size
S_c	Secondary creep stage
Λ	Scale parameter in gamma distribution
g'	Secondary electron yield
s	Shape parameter in gamma distribution
G	Shear modulus
τ	Shear stress
υ	Solute atom concentration
v	Statistical variance
$\dot{\varepsilon}_s$	Steady state creep rate
m	Strain rate sensitivity exponent
β	Stress exponent in power law creep equation
t	TEM foil thickness
ϑ	TEM foil tilt angle
T_e	Tertiary creep stage
ε_t	Total strain
ε	True strain
σ	True stress
R	Universal gas constant
E	Young's modulus

ABBREVIATIONS

AISI	American Iron and Steel Institute
AMIS	Average Intragrain Misorientation
BF	Bright Field

CCD	Charge-Coupled Device
CSL	Coincident Site Lattice
DGF	Deformed Grain Fraction
DMD	Differential Misorientation Development
DP	Diffraction pattern
DIC	Digital Image Correlation
DSA	Dynamic Strain Aging
EDM	Electric Discharge Machining
ECD	Equivalent Circle Diameter
f.c.c	Face Centred Cubic
FB	Fusion Boundary in weldment
FZ	Fusion Zone
GND	Geometrically Necessary Dislocation
GBS	Grain Boundary Sliding
HAZ	Heat Affected Zone in weldment
HTT	High Temperature Tensile
HTST	High Temperature Strain-rate Tensile
ISRTT	In-Situ Room Temperature Tensile
KAM	Kernel Average Misorientation
LAMF	Low Angle Misorientation Fraction
LAM	Low Angle Misorientation
MLI	Mean Lineal Intercept
MUD	Multiples of Uniform Density
MMA	Manual Metal Arc
OM	Optical Microscopy
OIM	Orientation Imaging Microscopy
RST	Re-solution Heat Treatment
RTT	Room Temperature Tensile
ST	Solution Treatment
STRTT	Solution Treated Room Temperature Tensile
SFE	Stacking Fault Energy
SSD	Statistically Stored Dislocation
SAZ	Strain Affected Zone in weldment
TBF	Twin Boundary Fraction
3D	Three Dimensional

CHAPTER 1

INTRODUCTION

1.1. Background and research aims

The supply of electrical power in the UK comes mainly from gas-, coal- and nuclear-fuelled power stations [1]. Most of the old nuclear power stations are approaching the end of their design lives of 30 to 40 years [2, 3] and are set to be decommissioned within the next few years. Research is on-going to underwrite safe and economic extension of their lifetimes mainly due to: increasing costs of new construction and decreasing capital resources, limited availability of suitable sites for new construction, conservative assessments which underestimate the true design life of a component and availability of better and more reliable life assessment methodologies and technologies [2]. At the same time the need for increased power plant efficiency is high for both economic reasons and also to cut down on CO_2 emission per unit of energy produced in fossil-fired power stations.

The global warming phenomenon is attributed to the increased concentration of greenhouse gases in the earth's atmosphere [4]. CO_2 is a major greenhouse gas in the atmosphere with 33% of UK emission coming from the fossil-fired power stations in 2011 [5]. To increase the thermodynamic efficiency of large scale power generation, steam-turbine plants need to operate at higher steam temperatures and pressures, for example with maximum values of about 600°C and 30MPa giving 40-45% efficiencies in power generation compared to <40% efficiencies obtained at about 550°C and 17MPa [2, 6]. To accommodate these changes in operational conditions, new and improved steels have been developed such as high alloy austenitic steels for boiler components and pipe-work sections [7, 8]. The main degradation mechanism for metallic materials operating at such elevated temperatures is creep; which is a time-dependent inelastic deformation occurring at relatively low stresses as a result of diffusive atomic rearrangement. Under these

conditions therefore, the risk of component creep failure after prolonged operation still remains. For safe operation of safety critical nuclear power plant, it is highly desirable to be able to quantify the state of creep damage in a component as this will allow development and evaluation of life-extension plans.

Creep degradation in gas cooled nuclear power plant components such as superheater tailpipes, which are made from high carbon AISI Type 316 austenitic stainless steel, often occurs at localised regions e.g. around weldments [9]. In most cases such degradation limits the efficiency of the power plants and also the components' lives [3]. Consequently, the need for local strain assessment techniques with high spatial resolution cannot be overemphasized if these components are expected to operate safely within and without their design lives. Assessment of localised strain is important since it provides an indication of where failure is likely to initiate.

Design codes often specify an allowable stress for the required design life of a power plant component [10]. But for life extension, or where unforeseen degradation mechanisms prevail, it is essential to evaluate the evolution of strain over time, either by calculation or measurement, to ensure timely repairs and/or replacements (and thereby avoid catastrophic failures). This is particularly true around welds. In this way, reliable plant operation will be ensured, thereby maximizing financial return on investment while at the same time maintaining a safe operating environment.

The need to measure and characterise localised inelastic deformation in safety critical components promptly, reliably, accurately and at a high spatial resolution was the main motivation behind the current work. Existing creep damage evaluation techniques such as those based on replica metallography, hardness measurement, ultrasonic measurement and quantitative metallography [3, 7, 11-13] either have limited spatial resolution and/or detect creep damage in the tertiary stages of creep. The use of these techniques in assessment of localised deformation is often limited [11]. In the current

work, assessment of strain accumulations is based on electron backscatter diffraction. The method evaluates relative changes in crystal lattice orientation arising from accumulation of lattice defects such as dislocations. This method will therefore allow early detection of creep deformation, quantitative assessment of creep deformation and localised assessment of creep deformation owing to its high spatial resolution. However, this method requires sample extraction and its application for on-site strain assessment is therefore limited to thick-walled components. In the thin-walled components such as superheater tubes, the method will be applied mainly for post mortem studies allowing characterisation of inelastic strain histories of the failed components. Such assessment can be used to establish critical strain at failure which can be used in Ductility Exhaustion model [14] for creep damage assessment. The new method will be of great interest to operators of power generating plants operating at high temperatures as it will complement existing creep damage assessment techniques. The use of multiple techniques in a complimentary manner minimizes the risk of in-service failures which can be hazardous and expensive both in terms of components' repair/replacement costs and the loss of earning owing to unplanned shutdowns, reduced plant availability and lost production. Since the method has the potential of allowing direct characterisation of accumulated strain in components subjected to creep degradation, it can be a useful tool for reliable prediction of a component's remaining life.

The main objective of the current research is therefore to explore the potential of electron backscatter diffraction (EBSD) for characterising localised inelastic strain at high spatial resolution in austenitic stainless steel. Specifically the research aims are:

- To investigate how lattice orientations evolve with the accumulation of plastic and creep strains in Type 316H stainless steels of varied microstructures. The investigation will cover the following:
  - ✓ Uniaxial isothermal mechanical testing in tension, compression and in creep.

- ✓ Material characterisation using both optical and electron microscopy.
- ✓ Standardisation of sample preparation procedures for EBSD measurements.
- ✓ Optimisation of EBSD measurement parameters for strain analysis.
- ✓ Lattice orientation measurements at spatial resolution less or equal to 1μm.

- To develop methodologies derived from the lattice orientation measurements for assessing localised plastic and creep strain in Type 316H stainless steels. The changes in lattice orientations as a function of strain will be evaluated taking into consideration the effects of strain rate, temperature and the microstructural changes. Effort will be geared towards developing a universal method of assessing strain-induced lattice orientation changes that is relatively insensitive to microstructural variations.
- To validate the strain assessment methods through comparative assessment of their strain estimates to strains measured through extensometry, digital image correlation and hardness methods.
- To establish the applicability of the strain assessment methods by estimating plastic and creep strain distributions in ex-service weldments that have been exposed to different service lives in UK Advanced Gas-cooled Reactor (AGR) power plants.

1.2. Thesis layout

This thesis consists of 9 chapters which report on various topics considered in the development of EBSD-based strain assessment methods. Chapter 1 covers the motivation behind the current work and the thesis objectives.

In Chapter 2 a review of the plastic and creep deformation behaviour of Type 316 austenitic stainless steels is given in terms of the basic deformation mechanisms, effects of precipitation on deformation behaviour and effects of prior deformation on creep behaviour. Later in the chapter the effects of welding on microstructure and strain

distribution are examined before reviewing existing creep assessments techniques and their ability to assess localised deformation. In the final section of this chapter a specific review is given on EBSD which is being applied in the current work for localised assessment of both plastic and creep deformation.

Chapter 3 reports on various experimental techniques used in this thesis. The techniques are divided into three main groups: mechanical testing techniques used for introducing controlled deformation in the steels studied, microstructural assessment techniques used for examining the chemical, microstructure and dislocation structure of the deformed steels and strain assessment techniques used for characterising the induced strain in the deformed steels.

Chapter 4 introduces the Type 316H stainless steel samples considered in this thesis in terms of their heat treatment histories, service histories and chemical compositions. The chapter also reports on characterisation of their mechanical properties, grain sizes, precipitation, dislocation densities and dislocation structures.

The influence of microstructure, thermal aging and grain size on the development of strain-induced lattice orientation changes is covered in Chapter 5. The chapter provides the details of the steels used, tests conducted, measurement and data analysis performed during these investigations.

In Chapter 6 the influence of plastic strain on lattice misorientation development under different deformation conditions of temperature, mode (tension vs. compression) and strain rate is reported. The chapter provides details of the mechanical tests conducted, EBSD measurements and the data analysis performed. In the chapter the development of strain-induced misorientation is investigated and methods proposed for plastic strain assessment. In the last section of this chapter an empirical model for predicting local misorientation distribution as a function of deformation conditions is presented and discussed.

The influence of creep strain on misorientation development is covered in Chapter 7. The chapter provides details of the creep tests conducted, EBSD measurements and the data analysis performed. The chapter also explores the differences between plastic- and creep-induced misorientations development and proposes methods for creep strain assessment.

The validation of the proposed strain assessment methods and their applicability to real power plant components is detailed in Chapter 8. The chapter also covers comparative strain assessments based on EBSD, hardness and digital image correlation measurements.

Chapter 9 presents the overall conclusions drawn from this work. Suggestions are also provided about future work which will bring closer the realisation of EBSD as a routine technique for creep monitoring and assessment of austenitic materials in high temperature applications.

CHAPTER 2

LITERATURE REVIEW

2.1. Introduction

Before progressing to a review of the plastic and creep deformation behaviour of Type 316 austenitic stainless steels it is first necessary to define and explain the basic terms used in any study of the mechanical properties of metallic materials.

2.1.1. Basic concepts of metallic material deformation

In general, deformation is the change in physical dimensions of a body when subjected to an external load. Elastic deformation occurs when the original dimensions are recoverable on unloading unlike inelastic deformation where a permanent offset occurs.

The concept of true strain relates deformation to the instantaneous value of the body's dimensions. Two forms of inelastic strain are considered in this work: plastic and creep strain. Plastic strain is a permanent change in dimensions and in metals it often arises from the motion of dislocations under the action of a shear stress acting along a slip plane in the slip direction. Normal and shear stresses are generally defined as forces per unit area acting perpendicular and parallel to a particular plane, respectively. Dislocations are linear defects in the crystalline structure which can have an edge or a screw character depending on whether their Burgers vector is normal or parallel to the dislocation line. A mixed dislocation has both edge and screw character. The Burgers vector of a dislocation is a lattice translation vector that quantifies the difference between the distorted lattice around the dislocation and the perfect lattice [15]. During deformation, dislocation motion is impeded by obstacles in the crystal lattice such as precipitates and other dislocations. This produces the phenomenon of strain hardening, where, as the plastic strain increase, a higher stress is required to produce a given further deformation.

Creep strain is a predominantly elevated temperature ($>0.4T_m$, where T_m is the absolute melting point of a material [16]) deformation in which diffusive atomic rearrangements in the crystal lattice reduce strain hardening and allow continuous deformation at a constant stress (time-dependent yielding).

Assessment of the inelastic strain in metallic materials is important as it helps to ascertain their structural integrity. Failure can occur in such material when they fail to perform their intended functions either due to excessive inelastic deformation or fracture.

2.1.2. Literature review structure

The primary objective of the current study is to investigate the potential of electron backscatter diffraction for characterising inelastic strain in Type 316H stainless steel. The chapter starts by reviewing the composition of and the precipitation occurring in these steels. This is followed by a review on their plastic deformation and the influence of microstructural features such as dislocation, solute atoms, precipitates, and grain boundaries on their strain hardening.

To understand how creep deformation is likely to influence lattice orientation changes in the steel, a review on the main creep deformation mechanisms is undertaken. Later in the chapter, the influence of carbide precipitation and prior plastic deformation on the creep responses is also reviewed since the main material investigated in this thesis is service-aged. Since in many components operating under creep conditions failure originates at a welded joint, a brief review on the effects of welding on microstructural changes and strain accumulation is given. This is followed by a review of the currently available creep assessment techniques and their ability to assess localised deformation. The chapter concludes with a specific review on electron backscatter diffraction which is used in the current work for the assessment of localised strains.

2.2. Type 316 austenitic stainless steels

Type 316 austenitic stainless steels are iron-chromium-nickel alloys that are characterised by a face-centred cubic (*f.c.c*) austenite structure at room temperature. They exhibit good high-temperature strength, corrosion and oxidation resistance [17-19] and so they are widely used in industry e.g. in power generating plants for critical components such as superheater tubing [7, 8]. Typically, these alloys contain, by weight percentage: 0.03-0.1% C, 16-18% Cr, 10-14% Ni, 2-3% Mo, <2% Mn and 0.1-0.16% N [20]. These alloying elements have an influence on both the crystal structure and the properties of the steel. For instance;

Chromium (Cr) addition imparts corrosion and oxidation resistance at high temperature through formation of an adherent self-healing chromium oxide (Cr_2O_3) surface layer. Cr, which has a body-centred cubic (*b.c.c*) structure, forms a substitutional solid-solution in austenite and is known to promote a ferritic structure which is also *b.c.c* [17]. Cr also facilitates the precipitation of secondary phases such as carbides and sigma-phase [21, 22]. The effect of precipitation on the deformation behaviour of Type 316 stainless steel is reviewed later in section 2.2.2.3 and 2.2.3.2.

Nickel (Ni) which has an *f.c.c* structure is the main substitutional element that is added to stabilise the austenite structure at room temperatures [17]. The *f.c.c* austenite structure is responsible for the good ductility and toughness properties of the steel. The compactness of the structure also reduces the diffusion rates and thermal conductivity, and gives relatively high coefficients of thermal expansion [7].

Molybdenum (Mo) which is a ferrite stabilizer improves creep resistance of the steels through substitutional solid-solution hardening (see section 2.2.2.2). Mo also facilitates the precipitation of carbides (e.g. Fe_3Mo_3C) [23] and on long-term aging it promotes the formation of sigma- and Lave-phases [21, 22].

Carbon (C) forms an interstitial solid-solution in austenite and is known to promote the austenite structure. It provides mechanical strength through solid-solution hardening and also through precipitation hardening (see section 2.2.2.3) when minor alloying elements such as niobium (Nb), titanium (Ti) and/or vanadium (V) are present. Carbon also lowers the intergranular corrosion resistance by reducing the chromium content in the matrix through the precipitation of chromium-rich carbides [18]. Type 316 stainless steel grades are denoted by 'L' if they contain low carbon content (<0.03 wt %) and by 'H' when their carbon content is high (0.04-0.1 wt %). The low carbon content minimizes sensitisation [18] but this also lowers the creep resistance. The use of high carbon grade improves creep resistance and to ensure all carbon remains in solid-solution they are often solution heat treated at high temperature e.g. 1040°C for cold rolled Type 316H steel [18]. At this temperature the solubility of carbon in austenite is about 0.5 wt % [24].

Nitrogen (N) is an interstitial solute that promotes the austenite structure and serves to improve mechanical strength through solid-solution hardening and also through precipitation hardening when nitrides and carbonitrides are formed [7].

Manganese (Mn) additions in stainless steel serve as a nickel substitute since Mn stabilises the austenite structures at room temperature. It contributes to strengthing effects by increasing the solubility of nitrogen in the austenite phase [25].

The addition of minor elements such as Ti (0.7 wt % max) and Nb (1 wt % max) which are stronger carbide formers than Cr [26] reduces sensitisation since they are preferentially precipitated instead of Cr, thus minimising its depletion along the grain boundaries regions. They also improve mechanical strength though solid-solution hardening and also through precipitate hardening when intragranular nitrides and carbonitrides are formed [23].

2.2.1. *Precipitation in Type 316 stainless steels*

Type 316 stainless steels contain a number of alloying elements in supersaturated solid-solution in the austenite phase, which tend to precipitate and form second phases such as carbides and intermetallics at elevated temperatures. Precipitation plays an important role in the achievement of good creep properties as explained later in section 2.2.3.2. The precipitation processes are mainly controlled by solute atom diffusion and so their rates depend on the aging temperature and time.

Carbon has a relatively high thermodynamic affinity for chromium and readily forms carbides when it supersaturates in the austenite phase and its diffusion rates and that of Cr are sufficient to allow precipitation [25]. The solubility and diffusion rate of carbon decreases with temperature and supersaturation is reached at temperatures below 900°C. At room temperature the austenite structure (γ) is supersaturated but no precipitation occurs due to limited diffusion rates of both carbon and chromium. As the temperature increases, the carbon diffusion rates also increase but at a higher rate along the grain boundary than in the bulk. Accordingly, carbide precipitation occurs initially along the grain boundary regions (see Fig. 2.1) causing chromium depletion in the solid-solution such that the corrosion and oxidation resistance of the steel is reduced locally (i.e. sensitisation).

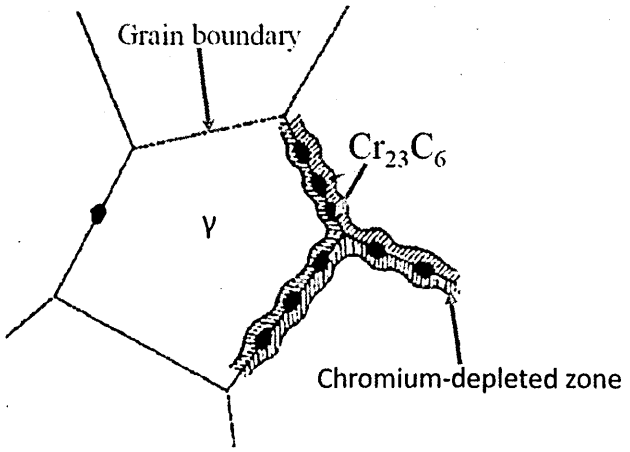

Fig. 2.1. Schematic drawing showing chromium depletion zones along grain boundaries [25].

Alloying elements such as Mo and Ni accelerate carbide precipitation by diminishing carbon's solubility in austenite, while chromium has a reverse effect. This is essentially due to the thermodynamic effects of these elements on C in the austenite phase, where Cr atoms attract C while Mo and Ni repel it out of the solid-solution [23]. The carbon diffusion rate is also increased by the presence of dislocation structures within the grain interior [25].

The general precipitation in an annealed Type 316 stainless steel as a function of aging time can be predicted from the temperature-time precipitation (TTP) diagram shown in Fig. 2.2. At temperatures above 500°C, $M_{23}C_6$ which is mainly $Cr_{23}C_6$, but other elements such as Fe, Ni and Mo can substitute Cr, is rapidly precipitated. It has an *f.c.c* structure with lattice parameter varying between 1.057 and 1.068 nm [17]. As seen in Fig. 2.3, the carbide precipitation which is dependent on the carbon diffusion rate occurs successively at grain boundaries, incoherent twin boundaries, coherent twin boundaries and finally intragranularly [21-23, 25]. The precipitation of $M_{23}C_6$ occurs throughout the aging period (see Fig. 2.2).

As the aging time increases at temperatures about 600°C, M_6C precipitate forms where the general notation M includes elements such as Mo, Ti, Nb, V, and Fe. It has an *f.c.c* structure with lattice parameter varying between 1.095 and 1.128 nm.

At temperatures above 600°C and after prolonged aging times, intermetallics such as Laves phase (e.g. Fe_2Mo, Fe_2Nb and Fe_2Ti) are formed mostly intragranularly [21, 22]. Sigma phases which consist of Fe-Cr/Fe-Cr-Mo intermetallics are also formed under these conditions. They are known to increase the steel's susceptibility to embrittlement [27] and precipitate at triple points, grain boundaries, incoherent twin boundaries, and on intragranular inclusions. At temperatures above 700°C and after long aging times, χ phase precipitates form often on grain boundaries and intragranularly on dislocations [18, 22, 26, 28].

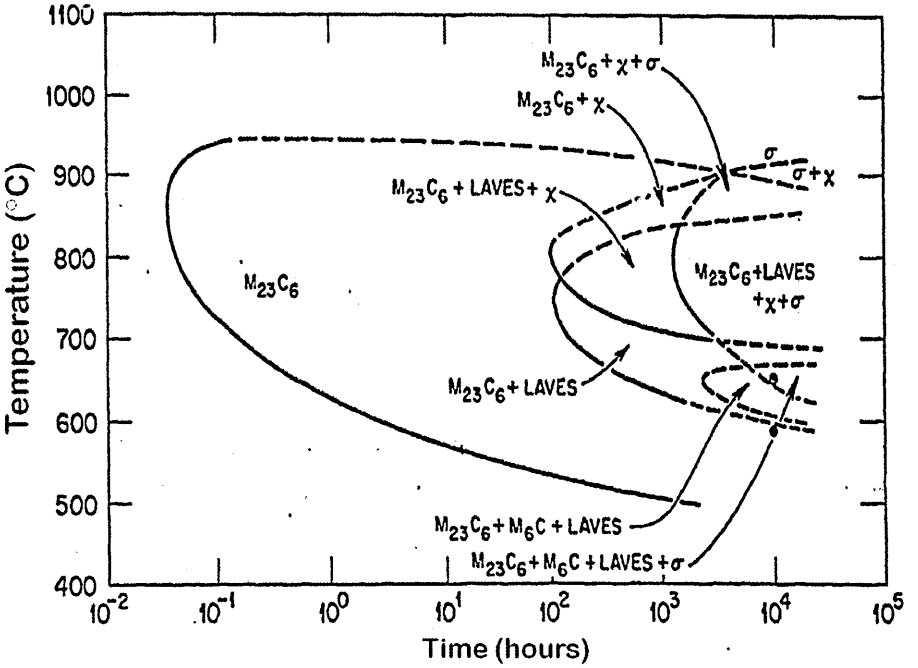

Fig. 2.2. Time-temperature-precipitation diagram of solution annealed Type 316 stainless steel [22].

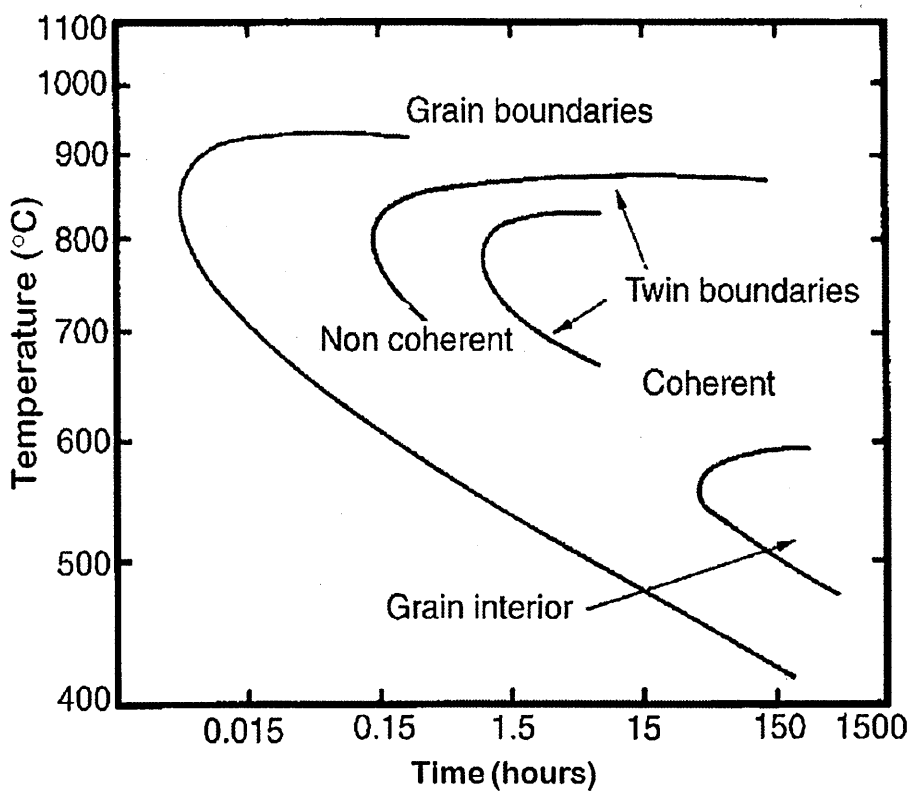

Fig. 2.3. Diagram showing preferred sites for precipitation after aging at different temperatures [25].

In Type 316 stainless steel, solution heat treatment (annealing) serves to re-dissolve chromium carbides into solid-solution. Typically, this is carried out at temperatures between 1050°C-1150°C [24] at which point the solubility of carbon in austenite is at its maximum [29]. The annealing time is often kept short to limit grain growth. A rapid cooling (quench) from the treatment temperature to ambient temperature gives a supersaturated austenite solid-solution. Re-precipitation of carbides is likely between 425°C and 900°C [18, 20] as the carbon is rejected from the solid-solution owing to supersaturation of the austenite and the relatively high carbon diffusion rates at these temperatures. Annealing also lead to the recovery of the dislocation structures [30].

2.2.2. Plastic deformation in Type 316 stainless steels

Type 316 stainless steels have an *f.c.c* crystal structure and therefore 12 possible slip systems, defined by four close-packed {111} planes and three close-packed <110> directions. A slip system refers to a crystallographic plane and a direction on this plane along which dislocation motion occurs. Plastic deformation occurs at ambient temperature by dislocation glide. The gliding motion involves breaking and reconfiguring the atomic bonds (see Fig. 2.4) immediately around the dislocation line when the critical resolved shear stress (τ_s) [15] is attained along the slip plane on the application of stress (σ).

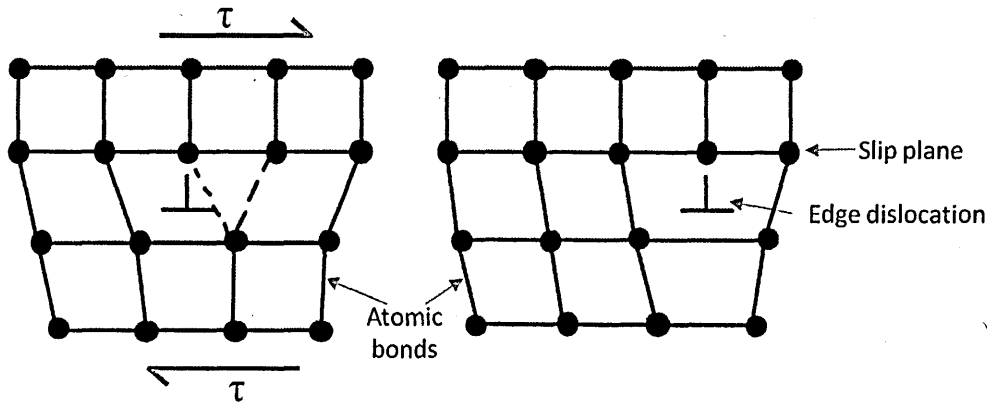

Fig. 2.4. Schematic illustrations of an edge dislocation glide along a slip plane.

The operative slip system in *f.c.c.* structures is the one with the highest Schmid factor (i.e. ratio of resolved shear stress to applied axial stress) [15, 31]. Cross slip can also occur when screw dislocations move to different slip planes and this is common at elevated temperatures and in materials of high stacking fault energy (SFE) [32]. A stacking fault is a planar defect in the lattice where the regular stacking sequence of atomic planes is interrupted. It is characterised by two partial dislocations (extended dislocation) at an equilibrium separation determined by a balance between repulsive forces of the partials and the attractive forces due to surface tension of the stacking fault (i.e. the characteristic SFE of a material). Extended screw dislocation can only cross slip when their partials constrict into a perfect dislocation. This occur readily in metals with a high SFE e.g. aluminium, owing to their narrow stacking fault, and also at high temperature since constriction can be assisted by thermal activation [15]. At low temperatures the movement of edge dislocations is limited mainly to glide but as the temperature increases, such dislocations can change their slip plane through climb (see section 2.2.3.1.2).

Deformation can also occur through twinning in a definite direction and on a specific crystallographic plane (e.g. {111}). Perfect twin boundaries are characterised by a misorientation of 60° about the <111> axis and have 1 in every 3 lattice sites coinciding. They are described as Σ3 coincident site lattice (CSL) boundaries where Σ represents the reciprocal density of coinciding sites [33]. In austenitic steel, deformation through mechanical twinning mainly occurs at low temperatures [17] while annealing following plastic deformation results in the formation of annealing twins [33, 34].

The main strengthening mechanism in Type 316 stainless steels is strain hardening. In the annealed state, the steel has a relatively low yield stress (e.g. 205MPa at 0.2% proof stress) but a high ultimate tensile strength (UTS) of about 500MPa [35], attributed to its high rate of strain hardening. The low SFE of the steel and the corresponding difficulty in the cross-slip of screw dislocations contribute to the high rate of strain hardening [36]. The

rate can be determined from the flow curve's slope ($d\sigma/d\varepsilon$) [31], where σ and ε represents the true stress and true strain, respectively (see Fig. 2.5).

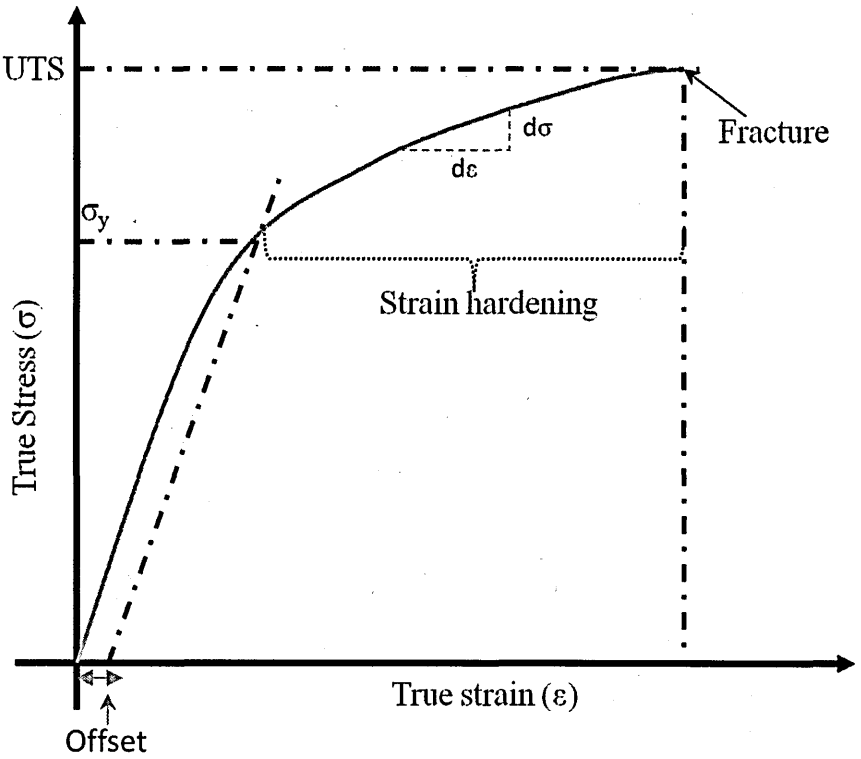

Fig. 2.5. Typical true stress-true strain curve for Type 316 stainless steel (σ_y: offset yield stress).

The important microstructural features that contribute to strain hardening include dislocations, solute atoms, precipitates and grain boundaries.

2.2.2.1. Dislocation strengthening

Dislocation strain hardening/strengthening occurs when dislocation movement is impeded by other dislocations in the microstructure. Accordingly, the hardening increases with increasing strain owing to the increased densities of dislocations arising from emission from grain boundary irregularities such as ledges, from condensation of vacancies and/or from multiplication of dislocation through a Frank-Read mechanism [15]. Essentially it is the elastic interaction between dislocations stress fields that impedes their motions. The pile-up of dislocations on barriers on slip planes produces a back-stress

which opposes the applied stress along the slip planes thus contributing to the strain hardening effect. The interaction of dislocations also results in the formation of jogs in the dislocation lines which restrict the motions of screw dislocations [15]. Since the phenomenon of cross-slip is limited to screw dislocations, restriction of their movement contributes to strain hardening. Generally, the flow stress (σ) increases with strain hardening and is related to the structure by:

$$\sigma = \sigma_i + \alpha G b \rho^{0.5} \qquad \text{Eq. 2.1}$$

where σ_i is the overall crystal lattice resistance to dislocation movement, α is the interaction constant that is a function of obstacle shear strength, G is the shear modulus, ρ is the dislocation density and b is the magnitude of the Burgers vector [37]. This strain hardening is more effective when the annihilation of dislocations is relatively low e.g. at low temperatures.

2.2.2.2. Solid-solution strengthening

Solid-solution involves the addition of elements in the crystalline lattice of the base metal which produces distortion due to size differences between the solute atoms and the base atoms. The local distortion of the parent lattice in the vicinity of the solute atom and the difference in the local value of elastic constant near it, make the solute act as a discrete obstacle to dislocation motion. Interactions thus occur between dislocations and the stress field in the region of the solute atoms. The contribution of the solute atoms to strain hardening can be obtained from Eq. 2.1, by replacing ρ with υ which represents the solute concentration [38]. In this case, α is relatively small but the areal density of the solute in the slip plane is relatively large resulting in an appreciable solution hardening. However, the strain hardening varies as $\upsilon^{2/3}$ [32] when the solute atoms' strain fields overlap and they cease to act like discrete obstacles.

Since α depends mainly on the misfit in the parent lattice, the strain hardening is more prevalent in interstitial solid-solutions, where solute atoms occupy interstitial positions in the parent lattice, than in substitutional solid-solutions where solute atoms occupy lattice sites in the parent lattice [31, 38].

2.2.2.3. The effects of precipitation on strain hardening

In Type 316 stainless steel, precipitation can occur both intragranularly and along the grain boundaries, as mentioned earlier. The strain hardening due to intragranular precipitation can be attributed to the additional stress that is required by a dislocation to cut through a small coherent precipitate [15]. As the precipitates coarsen with aging time, α also increases and so does the strain hardening. However, when particles become non-coherent, strong and impenetrable, the strain hardening is determined by the additional stress required to bow and move dislocation past the precipitates [7]. However, for this to happen the average spacing (j) between precipitates must be twice (or more) the critical curvature radius (r) the dislocation requires to pass between the obstacles. It has been shown that $r = Gb/2\tau_0$, where τ_0 is the shear stress required to bend a dislocation to a radius r [15]. When $j = 2r$ then $\tau_0 = Gb/j$, and so the resistance to dislocation flow decreases with particle coarsening. Usually average inter-particle spacing increases with increasing average particle size [8]. For finely dispersed particles (i.e. $j << r$) the local stress fields are not sufficient to bow out the dislocation between them. The resistance to dislocation movement in this case is proportional to the particle concentration and adds to the solid-solution hardening as mentioned earlier.

As shown schematically in Fig. 2.6 a dislocation loop is left on each particle as a dislocation passes. This occurs as the oppositely signed parts of the dislocation loop annihilate [15]. As the number of loops increases on each particle they exert a back stress on dislocation sources, resulting in strain hardening commonly known as Orowan

strengthening. The build-up of dislocation loops on the particles also creates a dislocation cell-like structure defined by relatively diffuse walls of dense tangles of dislocations [31].

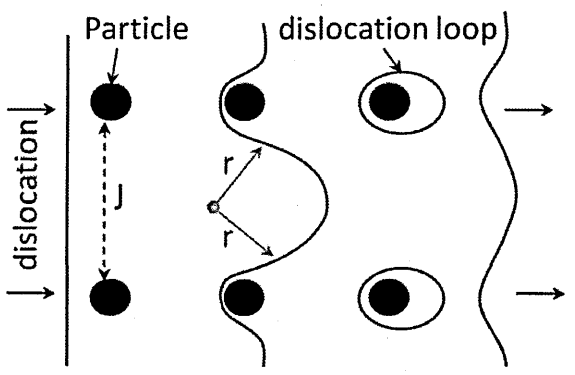

Fig. 2.6. Schematic drawing showing bowing and looping of a dislocation on widely spaced particles [31].

2.2.2.4. Strengthening from grain boundaries

In crystal structures grain boundaries are discontinuities that impede dislocation motion. The abrupt change in orientation at grain boundaries means slip is transmitted indirectly from grain to grain. The stress field created by a pile-up of dislocations at a grain boundary produces shear stresses on the potentially active slip planes of the adjacent grain thus helping to propagate plastic deformation in that grain. Since the stress at the head of a dislocation pile-up increases with grain size [15], strain is transmitted across the boundary more easily in coarse-grained than in fine-grained material. The relationship between the flow stress and the grain size (ζ) at ambient temperature is generally given by the Hall-Petch equation as:

$$\sigma = \sigma_i + \phi\zeta^{-0.5} \qquad \text{Eq. 2.2}$$

where ϕ is a constant whose value depends on the material and the characteristics of the microstructure [31].

In polycrystalline material, two distinct classes of dislocations are generated within the grain during deformation: statistically stored dislocations (SSDs) interact randomly

within grain's interior and have a net Burgers vector of zero while the geometrically necessary dislocations (GNDs) have a net non-zero Burgers vector and serves to accommodate lattice curvatures particularly along the grain boundaries [31, 39]. GNDs help to keep the deforming grain boundaries intact [40]. Near grain boundaries the slip occurs on multiple systems due to the constraints imposed by the grain boundaries. This creates a gradient in ρ between the regions at the grain's core and those in the vicinity of the grain boundaries. The gradient reduces with the grain size resulting in a more uniform deformation in fine than in coarse grains. It has been demonstrated experimentally that ρ is an inverse function of the grain size (χ) [31] and so from Eq. 2.1 the flow stress is also given by:

$$\sigma = \sigma_i + \alpha G b \chi^{-0.5} \qquad \text{Eq. 2.3}$$

Thus, the strain hardening rate will be greater in fine- than in coarse-grained material.

2.2.2.5. The effects of temperature and strain rate on strain hardening

Generally, at constant temperature and strain, flow stress relates to the strain rate as:

$$\sigma = c\dot{\varepsilon}^{\eta} \qquad \text{Eq. 2.4}$$

where η is the strain rate sensitivity, $\dot{\varepsilon}$ is the strain rate and c is a constant [31]. For metals at room temperature, η is <0.1 but increases rapidly at temperatures above $0.5T_m$.

At room temperature, the material's strength is mainly controlled by interactions between dislocation and barriers in the structure and so variations in strain rate have little effect on strain hardening. As the temperature increases, the atomic diffusion rate also increases and dislocations recover through climb and rearrangement (see section 2.2.3.1.2). In this case, variation in the strain rate influences the flow stress since recovery processes are time dependent. At constant strain and strain rate, the flow stress varies with temperature as:

$$\sigma = c_1 e^{Q/RT} \qquad \text{Eq. 2.5}$$

where Q is the activation energy for plastic flow ($Jmol^{-1}$), R is the universal gas constant ($Jmol^{-1}$), C_1 is a constant and T is the testing temperature in Kelvin [31].

2.2.3. Creep deformation in Type 316 stainless steels

Creep is the time dependent inelastic deformation of materials that are exposed to elevated temperatures, often $>0.4T_m$ [16], over long durations at relatively low stresses, mostly below the material's yield stress. At such temperatures, the atomic diffusion rate is appreciable and dislocation mobility is improved. Fig. 2.7 shows a typical creep curve obtained under constant load. The creep response is characterised by four main regimes identified by their different creep rates. These are instantaneous strain, primary creep (decelerating), secondary creep (steady-state) and tertiary creep (accelerating). Generally, the shape of the creep curve is a function of the applied stress and temperature and can exhibit primary dominance at low stresses and temperatures or tertiary dominance at high stresses and temperatures [8]. The changes in the creep rate as a function of time results from microstructural changes within the material such as precipitation, coarsening of precipitates, cavitations, subgrain development and re-crystallisation [41].

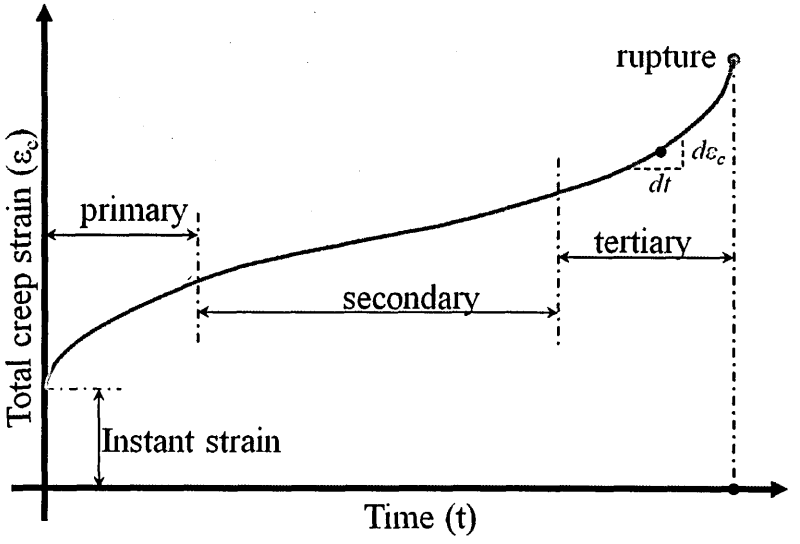

Fig. 2.7. Typical constant load creep curve (schematic).

Primary creep is characterised by a decreasing creep rate owing to increasing strain hardening from the finite number of mobile dislocations introduced on loading. The density of mobile dislocations increases with applied stress [16, 42] and so does the primary creep rate. The increased atomic diffusion rates at elevated temperature facilitate dislocation climb (see section 2.2.3.1.2). This leads to the formation of 3D dislocation network in the low SFE materials such as Type 316 stainless steels [43] which do not cross slip easily. The increased mobility also increases the chances of dislocation annihilation when interaction occurs between oppositely signed dislocations.

Secondary creep is typified by a creep rate that is almost constant. At this stage equilibrium exists between strain-hardening and recovery processes producing a steady-state creep rate. In many instances a steady-state rate is not realised, particularly for alloys, and so the minimum creep rate is normally quoted. The minimum creep rate is an important design parameter since it occupies a large proportion of material's service-life.

For creep behaviour investigated under constant load conditions, tertiary creep follows the secondary creep. It is characterised by an increasing creep rate and is common in creep tests performed at high stresses and temperatures. The occurrence of metallurgical changes such as the formation of cavities, coarsening of precipitates and re-crystallisation during this stage serves to accelerate the creep rate either by reducing the effective cross-sectional area of specimen or by reducing the resistance to dislocation motion [44]. The evolution of cavities predisposes the material to failure, as they coalesce, forming cracks which may lead subsequently to rupture.

2.2.3.1. Creep deformation mechanisms

The creep deformation mechanisms are mainly stress and temperature dependent. The dominant mechanism at given conditions of stress and temperature can be predicted from the creep deformation mechanism map of Type 316 stainless steel, shown in Fig. 2.8.

On this map, the applied stress (σ) is normalised by the material's shear modulus (G) and the testing temperature (T) by the absolute melting temperature (T_m) of the material. The maps are constructed from constitutive equations defining each mechanism at different combinations of stress and temperature. Superimposed on the maps are contours of constant strain rate calculated as an average value from the constitutive equations of all mechanisms contributing to creep at each point in the map.

Generally, when a number of mechanisms are operating independently of each other it is the fastest one that will prevail. The main creep deformation mechanisms in Type 316 stainless steel are dislocation glide, dislocation creep, diffusion creep and grain boundary sliding.

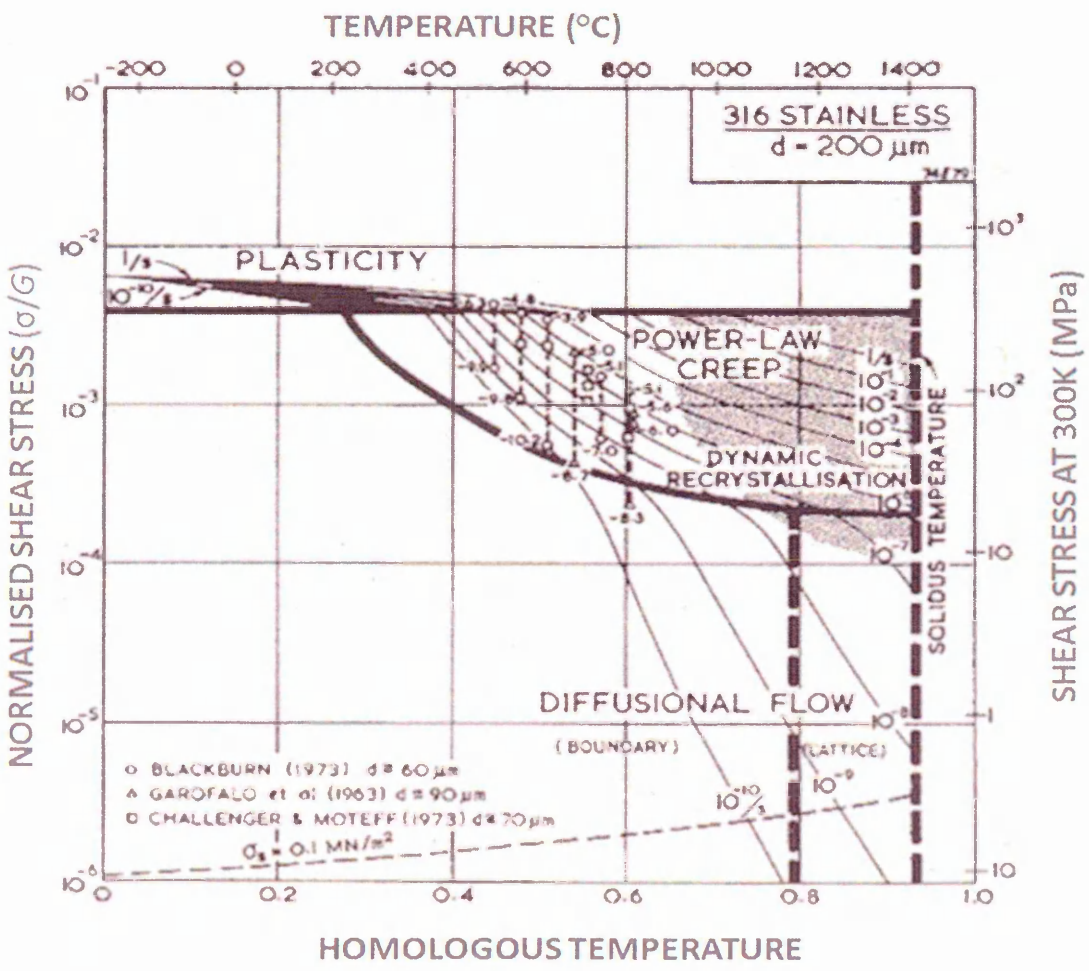

Fig. 2.8. Deformation mechanism map for Type 316 stainless steel with an average grain size of 200μm [16].

2.2.3.1.1. Dislocation glide

This is a creep deformation mechanism that involves the movement of dislocations along the slip planes and overcoming barriers through thermal activation. The internal resistance to dislocation flow is reduced by thermally activating them to surmount short-range stress fields generated, for example, by coherent precipitates or solute atoms. This mechanism occurs at high stress ($\sigma/G > 10^{-2}$) and its creep rate ($\dot{\varepsilon_d}$) is related to the density (ρ_m) and velocity (v_m) of mobile dislocations through the Orowan equation [16]:

$$\dot{\varepsilon_d} = \rho_m b v_m \quad and \quad \rho_m = \left(\frac{\sigma}{Gb}\right)^2 \qquad \text{Eq. 2.6}$$

At constant applied stress and relatively low temperatures ($<0.5T_m$), the creep rate depends on v_m which is determined by the impediment of dislocation motion by obstacles such as solute atoms.

2.2.3.1.2. Dislocation creep

Dislocation creep or power law creep occurs at relatively high temperature and stresses (see Fig. 2.8). It involves the dislocation glide along the slip planes and climb over obstacles (see Fig. 2.9).

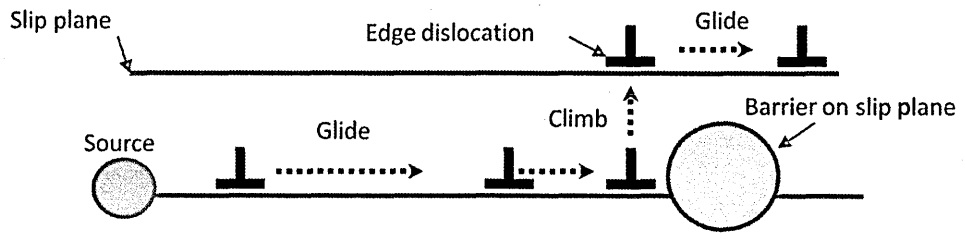

Fig. 2.9. Schematic illustration of a dislocation glide and climb process [8].

The climb is a thermally activated process as it involves diffusion of vacancies or interstitials to or away from a dislocation, allowing it to change its slip plane, thus bypassing obstacles. The improved mobility of dislocations through climb and cross-slip processes allows them to annihilate by mutual interactions or to accumulate to form a low

angle boundary (a low-energy configuration). A low angle boundary is essentially an array of dislocations which separate regions of a crystal differing in orientation by <5°[15]. Through these recovery processes the tangles and networks of interlocked dislocations are gradually released and rearranged thus reducing their density. However, at steady-state the recovery rate is balanced by the strain hardening rate and so the density of dislocations remains almost constant [8]. For this mechanism the rate controlling process is the atomic diffusion for the climbing step while the glide step is responsible for all the strain. The minimum creep rate for this mechanism at temperatures $>0.5T_m$ and relatively high stresses is described by a power law as:

$$\dot{\varepsilon}_s = \frac{AD_vGb}{kT}\left(\frac{\sigma}{G}\right)^{ɲ} \qquad \text{Eq. 2.7}$$

where ɲ is the stress exponent ~4-7 for pure metals, A is a material constant, k is the Boltzmann's constant and D_v is lattice diffusion coefficient [16]. At low stresses and high temperature, climb through lattice diffusion is dominant while at higher stresses or lower temperatures climb through dislocation core diffusion (pipe diffusion) becomes dominant, and $\dot{\varepsilon}_s$ varies as $(\sigma^{ɲ+2})$ instead of $(\sigma^{ɲ})$ [44]. In pipe diffusion, point defects in the crystal lattice such as vacancies migrate along the imperfect cores of linear crystalline defects such as dislocations.

At $\sigma/G > 10^{-3}$ the power-law breaks down as the stress exponent increases rapidly with stress. A transition from a climb-controlled power law creep to a glide-controlled creep whose $\dot{\varepsilon}_s$ varies exponentially with the stress, has been cited as a plausible reason for the break-down [8, 44]. It should be noted dislocation creep maybe accompanied by dynamic re-crystallization especially at temperatures $>0.6T_m$ (see Fig. 2.8) leading to a reduction in dislocation densities in heavily deformed regions through formation of new strain free grains [16].

2.2.3.1.3. Diffusion creep

Diffusion creep occurs at high temperatures and relatively low stresses (see Fig. 2.8) and involves the movement of atoms/vacancies not dislocations. Nabarro-Herring creep occurs when vacancies diffuse from regions of higher concentrations (e.g. grain boundaries under tension) to regions of lower concentrations (e.g. grain boundaries under compression) through the grain while the atoms flows in counter direction as shown schematically in Fig. 2.10. In the case of a pure crystal, the steady-state rate, which is grain size (ζ) dependent, is given by [44]:

$$\dot{\varepsilon}_s = \frac{14\sigma b^3 D_v}{kT\zeta^2} \qquad \text{Eq. 2.8}$$

Diffusion can also occur along the grain boundaries when the temperatures are around $0.4T_m$, as in the case of the Coble creep represented by:

$$\dot{\varepsilon}_s = \frac{50\sigma b^4 D_{gb}}{kT\zeta^3} \qquad \text{Eq. 2.9}$$

where D_{gb} is the grain-boundary diffusion coefficient [44]. The secondary creep rate in this case, varies linearly with stress and the activation energy for creep is that for grain boundary self-diffusion. The bond energies between the moving atom and its neighbours determine the magnitude of the activation energy for diffusion. Along the grain boundaries and the cores of lattice dislocations, atomic arrangements are less regular, resulting in fewer atomic bonds and thus lower activation energies than that for lattice diffusion. However, since the volume of relatively disordered regions is small compared to the total volume of the polycrystalline material, their contribution to the overall diffusion rate is negligible at high temperature when the lattice diffusion is rapid.

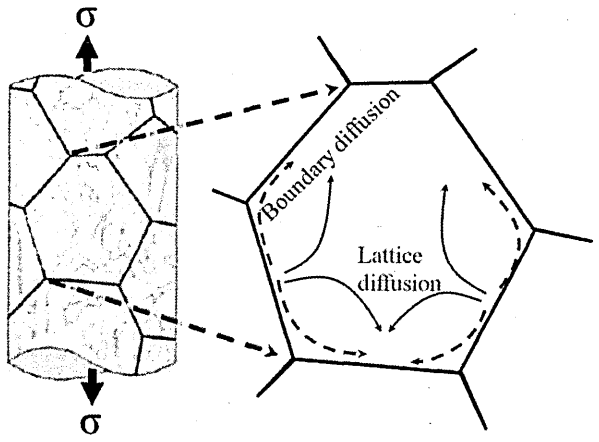

Fig. 2.10. Schematic representation of vacancy movement through the lattice (Nabarro-creep) and along the grain boundaries (Coble creep) under diffusion creep [16].

2.2.3.1.4. Grain boundary sliding (GBS)

GBS becomes an active creep deformation mechanism at high temperature and/or at reduced creep rates [44]. Above the equicohesive temperature [31] the regions near the grain boundaries are weaker than the grain's interior and thus deform plastically through shear in the direction of boundary. This leads to stress concentration at the grain corners, which may initiate wedge cracking, commonly found in austenitic stainless steels. GBS may also cause stress concentration at hard particles on the grain boundary and tensile stresses on grain boundary ledges, which may be sufficient to nucleate cavities through mechanisms such as vacancy condensation and direct decohesion [45]. A reduction in strain rate may allow the stress at concentration sites to relax through creep. This can lead to an increase in GBS.

The tendency for GBS reduces with increasing grain size owing to reduced grain boundary area. A gradient in creep deformation may therefore exist when GBS is dominant in microstructures with varying grain sizes as in the case of weldments. This may lead to localised creep deformation in the fine-grained zone of a weld heat-affected zone.

In conclusion, the predominant creep deformation mechanism depends mainly on stress and temperature. From the deformation mechanism map it is possible to predict the

prevalent creep mechanism in a component, although only in very general terms since the conditions of stress and temperature are rarely constant. For instance, the predicted creep mechanism in an AGR boiler component made from Type 316 stainless and operating at 550°C and 17MPa internal steam pressure, is diffusion creep. However, the application of these maps on welded components is limited as the maps are derived from the behaviour of solution annealed 316 stainless steel and welds have inherent plastic deformation.

2.2.3.2. Effects of precipitation on creep behaviour

Introduction of a fine dispersion of precipitates or insoluble particles in the matrix improves creep resistance by providing effective barriers to dislocation glide and climb but, as mentioned earlier, this effect is largely dependent on particle sizes. Coarsening of precipitates can have a detrimental effect on the creep resistance since it influences the ease with which the dislocations move. For pure metals or solid-solutions, the stress exponent in the power-law creep, ranges between 4 and 7 but with precipitates present in the matrix, it varies widely [16]. A stress exponent of about 10-14 has been reported in Type 316 steel deformed at 600°C using 150-260MPa. It was postulated that this was as a result of high density of intragranular carbides [46].

Dense precipitation of $M_{23}C_6$ carbides on dislocations during the steady-state creep of Type 316 steel deformed at 593-650°C using 241-234MPa has been suggested to suppress the recovery processes and thus the formation of subgrain structures. At temperatures above 700°C and stresses below 151MPa, the formation of these structures has been attributed to an increase in the mobility of dislocations owing to a reduction in precipitate density [42].

The effects of intergranular precipitation on GBS has been demonstrated in Type 347H stainless steel creep tested at 700°C using an initial stress of 137MPa [47]. GBS was found to increase with decrease in the density of intergranular $M_{23}C_6$ carbides. The pinning

of grain boundaries by high density of intergranular precipitates may limit the generation of vacancies and thus retard diffusional creep [8].

2.2.3.3. Effects of prior-deformation on creep behaviour

Investigation of prior deformation effects on creep behaviour is critical since most components used in power generating plants enters service in a prestrained condition e.g. welded components. From most studies conducted on Type 316 stainless steels, prestraining generally reduces the creep loading strain but has a variable effect on the creep rupture strains and minimum creep rates. For instance, steels prestrained in tension at room temperature followed by creep testing at 575°C using 450MPa, an increase in the prestrain levels reduced the creep rupture strains and the minimum creep rates [48]. A similar reduction in creep rate was reported for steels prestrained at 650°C followed by creep testing at 650°C, using an initial stress of 140MPa [49]. However, for Type 316 steel prestrained in compression at room temperature followed by creep testing at 550°C using an initial stress of 300MPa, an increase in the prestrain levels resulted in an increase in the minimum creep rate and a reduction of the creep rupture strains [50].

Generally, prior deformation increases the number density of dislocations which serve to limit the movement of dislocations in the subsequent creep loading. At elevated temperatures, the precipitation of carbide serves to pin the dislocations introduced during the prestraining, further limiting their movement. Under dislocation creep, limitation of dislocation movement reduces the accumulated creep strain. Prestraining therefore reduces the density of mobile dislocations in the structure and following the Orowan equation (Eq. 2.6) a corresponding decrease in creep rate occurs. In cases where prestraining increases the creep rate, it has been postulated that most of the dislocations introduced during the prestraining stage remains mobile in the subsequent creep testing [50, 51].

2.2.4. *Type 316 stainless steel weldments*

Welding is an important joining method particularly in the fabrication of complex components. This process is characterised by a thermal cycle consisting of intense heating followed by rapid cooling which leads to the formation of three metallurgical zones: the fusion zone (FZ) zone, the heated-affected zone (HAZ), and the base-metal (BM) zone (see Fig. 2.11). During welding the applied intense heat melts the metal forming a molten pool which on solidification forms the FZ whereas the HAZ is a region which experiences peak temperatures ranging from the melting point near the fusion boundary (FB) to ambient temperature in the BM [52].

In Type 316 stainless steels which are single-phase alloys, some of the metallurgical changes expected in the HAZ include variations in grain sizes and carbide precipitates as a function of the distance from the FB. Close to the FB the HAZ will be free of precipitates (solid-solution zone) owing to the high solubility of carbon and the rapid cooling which suppresses carbide precipitation. Precipitation of carbides is likely in the regions of HAZ experiencing peak temperatures in the range 425-900°C (see section 2.2). As illustrated in Fig. 2.11, the HAZ experiences a wide variation of peak temperatures which may influence the grain sizes distribution in this zone. High temperatures near the FB may result in some grain growth while regions experiencing lesser heat may undergo re-crystallization, resulting in a finer grained structure than the base metal [52]. Owing to these microstructural inhomogeneities, a gradient in mechanical properties is often evident across the weldment.

The thermal gradient arising from welding can also create a chemical gradient in the weldment as the rate of lattice diffusion in a metallic material is temperature dependent [8]. There may, therefore, be a gradient in the concentration of alloying elements over the distance between the FB and the BM.

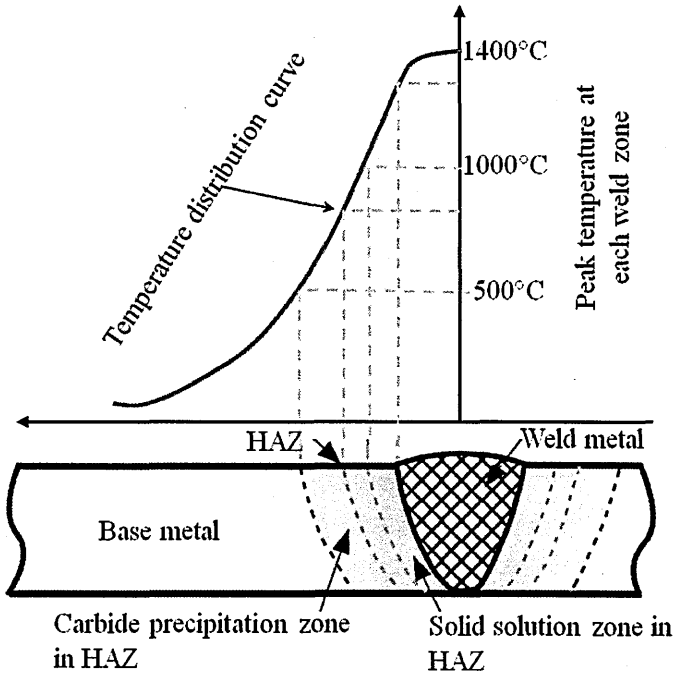

Fig. 2.11. Schematic diagram showing metallurgical zones in Type 316 stainless steel weldment [53].

The welding thermal cycle induces thermal stresses owing to the differences in the thermal expansion arising from the rapidly changing temperature [52, 54]. In Type 316 stainless steels, these stresses are promoted due to their relatively high coefficient of thermal expansion and relatively poor thermal conductivity [18, 55]. Plastic deformation occurs in the weld when the thermal stresses exceed the material's yield stress and its accumulation during the thermal process contributes to residual stress in the final weldments [54]. Post-weld heat treatment can reduce or eliminate these residual stresses by allowing them to relax primarily by plastic deformation and secondarily by creep [18]. Precipitation of chromium carbides in the weld at service temperatures >425°C can also be promoted by the presence of dislocations (see section 2.2.1).

2.3. Strain assessment techniques

Many power plant components operate under conditions conducive for creep deformation [3]. Monitoring of creep deformation and damage is therefore essential in

guaranteeing their structural integrity. A number of techniques have been developed and are often used in a complementary manner to enhance the reliability and accuracy of creep deformation assessment. The available techniques can be classified into three main groups:

2.3.1. Metallurgical-based techniques

A good example in this group is replica metallography [12] which characterises creep cavities on the component's surface in terms of number, size and distribution as a function of the component service life. The inability to detect subsurface defects is their main drawback even though creep damage in welds usually manifest on the surface except in some cases e.g. Type IV cracking [56]. In-service carburization and oxidation of the upper few microns of the steel limits the general applicability of this method.

2.3.2. Macroscopic measurement-based techniques

This group consists of techniques which assess creep damage through macroscopic measurement of scalar quantities such as the creep rate, creep strain and hardness. Samples are extracted from a component in service and mechanically tested in the laboratory to estimate the component's remaining life from the measured mechanical properties [57]. This assessment is limited in terms of statistical representation owing to constraints on the number of extractable samples.

In other techniques, strain gauges or inscribed marks on a component's surface are used to measure dimensional changes arising from accumulation of creep [13]. However, this mode of assessment is not applicable to the detection of localised creep deformation since it gives values averaged over the measurement distance. A promising technique in this group which can be used for monitoring localised creep deformation is digital image correlation (DIC) [58, 59] which tracks the displacement of random speckles on a component's surface from a series of digital images captured over time as the deformation progresses. An algorithm is used to calculate local strain through a hierarchical matching

process of the speckles and calculation of the displacements from their original positions. The main limitation of this method in the assessment of localised creep deformation lies in the pixel resolution of the camera used, variations in sample illumination and presence of surface contamination.

Hardness measurement is one of the methods that is routinely used in the assessment of strain in austenitic stainless steels. Even though it is not an intrinsic material property, hardness exhibits a good correspondence with the number density of dislocations in a material [60]. Hardness is determined at a macro-, micro- or at the nano-scale depending on the maximum load applied and penetration depth of the indenter [61]. Macro-hardness measurement (which uses load $\geqslant$2N) has been used to characterise plastic strain in Type 316 stainless steel, where hardness increased monotonically with increasing strain [62, 63]. Hardness has also been used to characterise creep deformation in Type 304 stainless steel. An increase in hardness in the early stages of creep was postulated to arise from the strain hardening while softening in the final stages of creep was attributed to recovery processes, carbide coarsening and creep damage accumulations [41]. However, the reliability of this technique is limited by its poor reproducibility and a large scatter in the data owing to factors such as local microstructural variations and indenter measurement errors [11]. The large scatter in the measurements also limits its application in the assessment of localised strain [64]. As a result of the aforementioned limitations, macro-hardness is often used as a screening tool for identifying creep softened regions that needs further investigation with other techniques.

Improved hardness measurements can be obtained by indenting at the nano-scale (nanoindentation) with a very precise tip while collecting real-time load-displacement (into the surface) data. This data together with the known geometry of the indentation tip is used to calculate a material's hardness as explained later in section 3.2.5. This method therefore

avoids the error arising from the optical measurement of indentation, in macro-hardness measurement.

2.3.3. Techniques based on the measurement of physical properties

Techniques in this group evaluate creep deformation from the changes in the physical properties of a material such as magnetic properties, electrical conductivity, electrical resistivity, acoustic emission, and ultrasonic properties [11, 65, 66]. Since their measurements are averaged out over a relatively large volume, their use in the assessment of localised creep deformation is limited. Most of these techniques are also in their developmental stages and are therefore not routinely used in industry.

However, one technique in this group that is very promising in terms of assessing localised deformation at high spatial resolution is electron backscatter diffraction (EBSD). It assesses the crystal lattice rotations arising from strain accumulation and although it is still at the developmental stages it has attracted a lot of interest based on the growing number of recent publications in which it has been applied to the study of metals and alloys. Assessment of localised strain is important since it provides an indication of where failure is likely to originate.

Design codes often specify an allowable stress for the required design life of a power plant component [10]. But for life extension, or where unforeseen degradation mechanisms prevail, it is essential to evaluate the evolution of strain over time, either by calculation or measurement, to ensure timely repairs and/or replacements (and thereby avoid catastrophic failures). This is particularly true around welds. The main objective of the current research is to explore the potential of EBSD for characterising localised inelastic strain at high spatial resolution in Type 316 stainless steels. This technique which will be used mainly for off-site strain assessment will be reviewed in detail in the following section.

2.4. Electron Backscatter Diffraction (EBSD)

2.4.1. Introduction

In the preceding sections deformation in metallic materials has been described in terms of imperfections in the crystal lattice in the form of dislocations. Therefore, by assessing the relative changes in crystal lattices it is possible to estimate the degree of deformation accumulated in a given material. EBSD is an established technique for analysing near-surface crystallographic orientations and its potential in characterising creep and plastic deformation is investigated in the current work. The working principles of the technique and its applicability in strain measurements will be reviewed in this section.

2.4.2. Historical background

In the current work, the diffraction of electrons from crystalline material is employed for inelastic deformation studies. Diffraction is the apparent bending of waves when incident at a specific angle to an opening of a particular dimension. The use of electron backscatter diffraction patterns for obtaining crystallographic information from material inside a scanning electron microscope (SEM) were first described by [67]. Further development proceeded with the introduction of on-line computer-assisted indexing of the EBSD patterns and in 1986 the first commercial system became available. However, it was not until the early '90s when automated detection of the diffraction band in the EBSD pattern was made possible. This was achieved through the application of a Hough transform [68, 69] and enabled the first fully automated EBSD system to be introduced [70, 71] leading to the invention of orientation imaging microscopy (OIM). The technique has now matured and is considered a standard tool for crystalline material characterisation with the number of publications based on it rising almost exponentially [72] over the years.

2.4.3. *Working principles of EBSD technique*

The principles of EBSD technique have been extensively discussed in the literature in several reviews [72-76] and books [77-80]. This section will therefore give an overview of the technique in terms of the basic principles and how it can be applied in the assessment of deformation.

The EBSD technique is a modification of the standard usage of SEM. Its working principles can be described generally in terms of electron-material interactions and the generation, acquisition, recording, detection and indexing of arising diffraction patterns (DP). The whole process is automated and controlled from a central computer as illustrated schematically in Fig. 2.12. The measurement is managed through data acquisition software which controls both the SEM operation and the data acquisition procedures. The interrogation and analysis of the acquired diffraction data is performed using data processing software. This may be done later, away from the SEM.

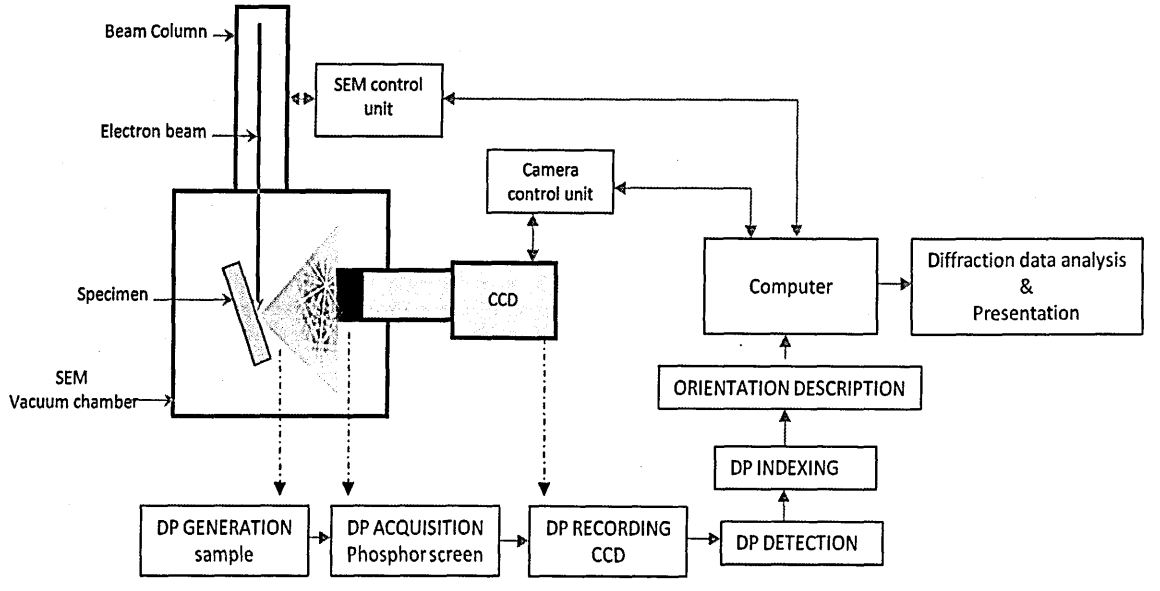

Fig. 2.12. Schematic representation of an EBSD system [81].

2.4.3.1. Electron-material interactions

The interaction of a high energy electron beam with atoms at a specimen surface produces a variety of secondary particles such as secondary electrons (SEs), backscattered electrons (BSEs), auger electrons and also characteristic X-rays, which may be utilised for material characterisation as illustrated in Fig. 2.13 [82, 83].

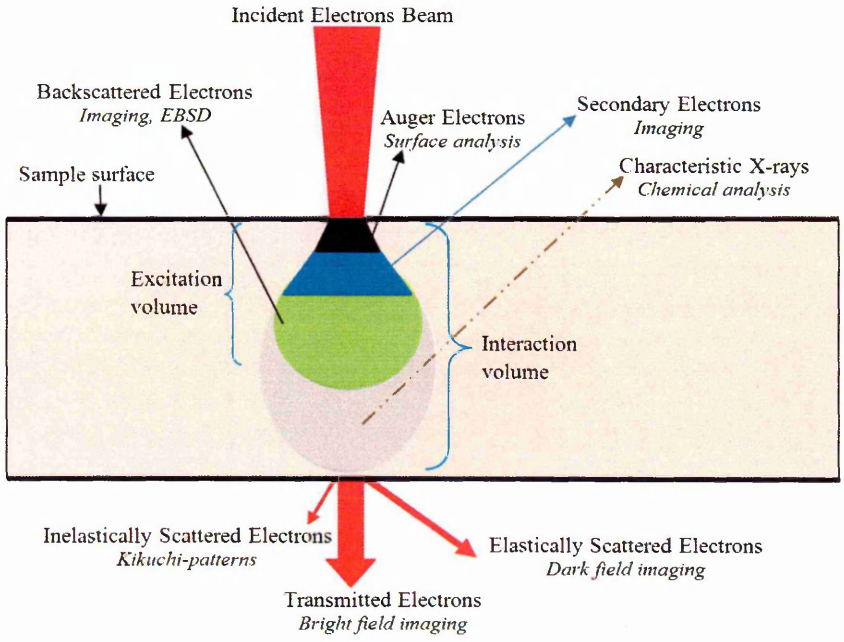

Fig. 2.13. Schematic drawing of electron-substrate interactions [82].

The BSEs results from single or multiple elastic scattering of incident electrons which subsequently escape from the specimen with energies which approach those of the incident electrons [80]. The proportion of incident electrons backscattered (backscattering coefficient - η) depends on the atomic number and the specimen tilt angle with respect to the incident electron beam (see Fig. 2.14). The dependence of the η on the atomic number allows for composition contrast mapping while the elastic scattering of the BSEs provides crystal orientation information. Due to the high energies of the BSEs their sampling volume is relatively large which reduces their spatial resolution. By comparison, SEs are low energy electrons (<50eV) [83] produced through interaction between incident electrons and weakly bound conduction electrons of the specimen's atoms and only those

close to the surface escape. The proportion of SE emitted to the number of incident electrons (SE yield - ɡ) has a weak dependence on the atomic number but is strongly influenced by the relative orientation of the specimen surface thus making it highly suited for topographical imaging.

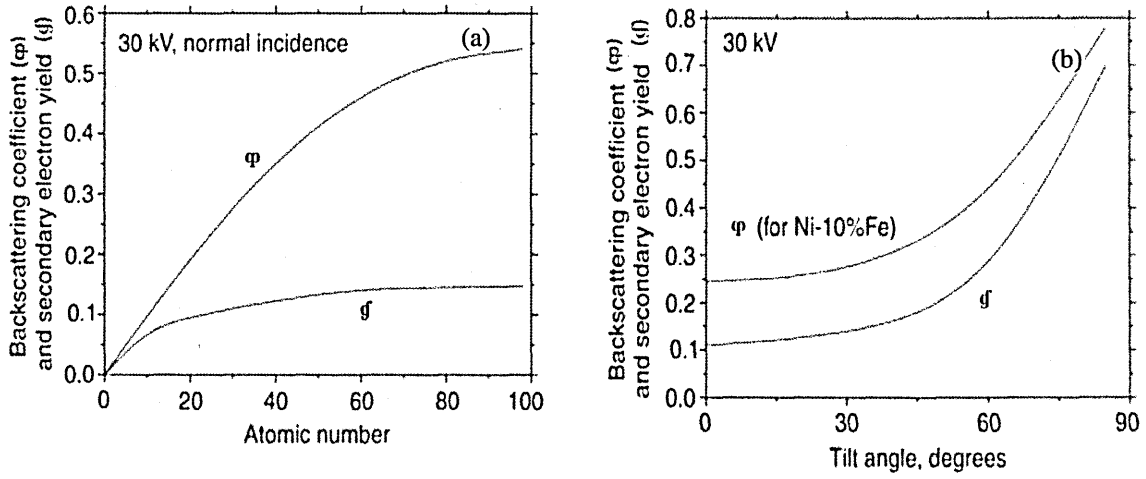

Fig. 2.14. Variation of backscattering coefficient and secondary electron yield with (a) atomic number, and (b) specimen tilt angle with respect to the incident beam [83].

The size of the interaction volume (see Fig. 2.13) between the incident electrons and the specimen is dependent on the distance the electrons can travel within the material which is a function of atomic weight, incident beam energy, material density and atomic number [83]. The importance of the interaction volume size will be discussed later in section 2.4.4.3.

2.4.3.2. Diffraction pattern generation

Electrons in a focused beam interacting with the atoms of a specimen are scattered both elastically and inelastically giving rise to a diffuse beam in the interaction volume with a wide range of trajectories. A proportion of these scattered electrons are incident upon various crystallographic planes within a crystalline sample, at angles satisfying Bragg's criterion and so they are coherently diffracted and backscattered out of the specimen if close to the surface. Bragg's law is of the form:

$$\eta\lambda = 2d_{hkl} \sin \vartheta_{hkl} \qquad \text{Eq. 2.10}$$

where λ is the wavelength of the incident electron beam which is a function of the accelerating voltage, d_{hkl} is the interplanar spacing, η is the diffraction order and ϑ_{hkl} is the Bragg's angle [82]. In order to maximise the proportion of BSEs, the specimen is usually tilted by 70° from the horizontal (see Fig. 2.14b).

The omni-directional electron scattering within the interaction volume ensures that the diffraction occurs from all lattice planes in a crystal, yielding a cone of diffracted electron about the normal to each set of the crystallographic planes as illustrated in Fig. 2.15. At high accelerating voltage, the Bragg's angle is very small [82] and so the opening angles of the diffraction cones approaches 180°. The projection of the cone edges on a flat surface thus appears as a pair of two parallel lines (Kikuchi band) corresponding to crystallographic planes (*hkl*) and (*-h-k-l*). The geometric projection of the diffracting plane is represented by the plane through the centre of the cones and serves as the reference line in the determination of interplanar angles.

The set of bands observed depends on the orientation of the crystalline region under the beam and defines the EBSD pattern. The bands have a distinct width which is a function of the SEM geometry and the accelerating voltage (V). An increase in V causes a decrease in λ and hence a decrease in the band's width. The intersection of the projected bands corresponds to a zone axis and the angles between them matches the interplanar angles. The band's angular width is twice the Bragg angle and varies inversely with the interplanar spacing.

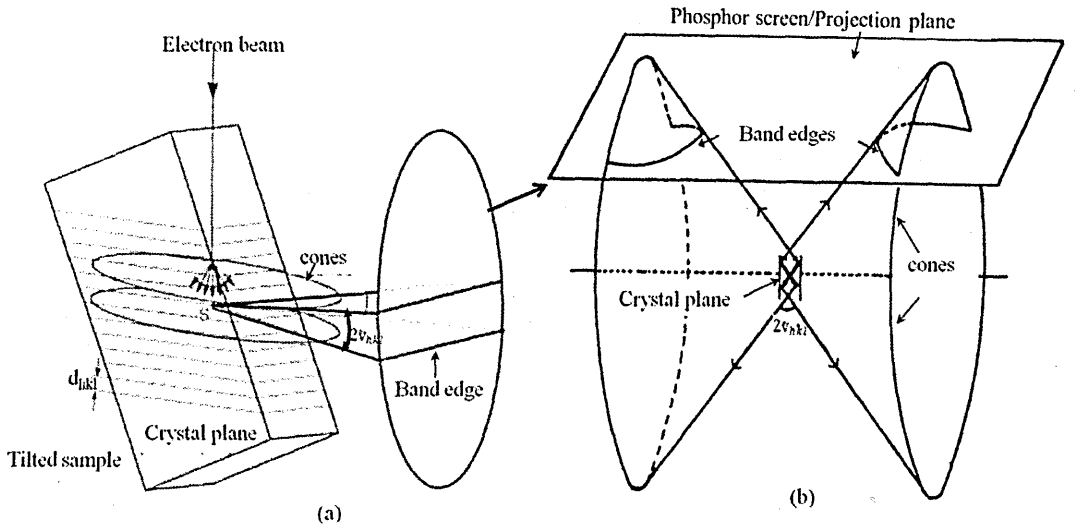

Fig. 2.15. Schematic diagrams showing (a) diffraction band formation on a projection plane, and (b) diffraction cone formation [73, 78].

2.4.3.3. Diffraction pattern acquisition and recording

The diffraction patterns are acquired on a phosphor screen which is integrated to a charge-coupled device (CCD) camera. The screen is normally parallel to the incident electron beam and has a reflective aluminium coating which serves as an energy filter by absorbing low energy electrons. The coating also conducts electrons away from the screen, thus reducing charging effects [84, 85]. The sensitivity of the CCD camera is improved through pixel binning which effectively increases the pixel area. This decreases the pattern acquisition time by reducing the exposure times of the camera. As explained later in section 2.4.4.3.2, pixel binning also reduces the angular resolution of the camera.

2.4.3.4. Diffraction pattern detection

To allow the determination of crystallographic orientation the digitised diffraction patterns must be detected by the acquisition software. The detection is based on a Hough transformation which converts each pixel in the image space into a sinusoidal curve in Hough space. All the pixels describing a particular diffraction line have their sinusoidal curves intersecting at a single point in Hough space [68]. The problem of detecting bands

is thus reduced to finding peaks of maximum intensity in the Hough space. Increasing the Hough transform resolution increases the accuracy of locating a point in Hough space. This improves the accuracy of diffraction line detection and thus of orientation measurement. However, the pattern acquisition time is increased as more time is required for transforming each point in the image space.

2.4.3.5. Pattern averaging and background correction

The detected bands have inherently low signal to noise ratio due to scintillation of the phosphor screen by low energy BSEs. It is estimated that only 5% of the backscattered electrons contribute to the diffraction pattern while the rest are inelastically scattered and contribute to background noise [86]. The ratio is improved by using a stationary beam (SEM spot mode) which enables generation of an averaged pattern with reduced noise from multiple images/frames acquired at a point. Application of background correction procedures also serve to improve the ratio by subtracting a smoothed background image from the acquired averaged pattern [78]. The smoothed image is obtained from the diffraction pattern image through the application of an averaging convolution mask which eliminates the diffraction bands while retaining the overall image gradient. By increasing the pixel area on the CCD camera through binning, the point-to-point noise is further reduced which also serves to improve the signal to noise ratio.

2.4.3.6. Band relative intensities

The relative intensities of the detected EBSD bands are calculated using a kinematical electron diffraction model which assumes elastic scattering of electrons. In this model the amplitude of the diffracted electron beam from the plane of a unit cell is considered to be proportional to the structure factor and the amplitude of the incident electron beam. A structure factor of zero implies zero intensity for the diffracted beam from a given plane. The structure factor varies between the planes and so their diffraction

bands have different intensities. Generally, in an *f.c.c* structure only those planes with all odd or all even Miller indices diffract [82]. Since different grains have different planes in reflective positions they tend to produce different overall intensities and thus have different contrasts in the image quality maps as explained later in section 2.4.5.1.1a.

2.4.3.7. Diffraction pattern indexing

Once the diffraction bands have been detected their corresponding diffracting planes are identified from the measured values of band intensity, band width and interplanar angles (represented by the angles between the bands). To identify the plane the measured values are compared with the theoretical values calculated for all diffracting planes in a crystal. A correspondence between the values allows the diffraction pattern to be indexed. The pattern indexing is therefore only possible when the crystal structure of the material is known.

Typically, in highly symmetric crystal structures the indexing routine considers 5 to 10 of the most intense diffraction bands and the first 3 to 4 families of $\{h\ k\ l\}$ planes e.g. {111}, {200}, {220} and {311} in *f.c.c* structure owing to their high structure factors. The tolerance allowed between the measured and the theoretical interplanar angle, typically about 5°, increases the possibility of getting more than one possible solution for any set of bands considered. In such cases the indexing routine uses a voting scheme [69, 87] to identify the most probable solution of the pattern which the system uses for generating simulated bands. The reliability of indexing is assessed through a pattern misfit parameter described as the mean angular deviation (MAD). This parameter measures the angular deviation between the simulated bands and the detected bands with a low value indicating a good match and thus high reliability of the band indexing. Where indexing is not possible owing to poor pattern quality, a zero solution is returned. Once the indexing of diffraction bands is completed the crystallographic orientation of the crystal lattice is expressed either

in Euler angle, in axis-angle notation or in a rotation matrix as explained later in section 2.4.4.4.

2.4.3.8. Quality of diffraction pattern

To achieve accurate indexing of DPs their quality has to be good enough to allow detection by the Hough transform routines. The quality is judged from the diffuseness of the pattern, attributable to factors such as a high density of dislocations in the crystal lattice, lattice strains, surface contamination, a defocused electron beam, and/or superposition of two or more patterns at grain boundaries. As mentioned in section 2.2.2.4, plastic deformation introduces both GNDs and SSDs in the crystal lattice. A high density of SSDs or GNDs in the diffraction volume causes local perturbations of the diffracting lattice planes (see Fig. 2.16) leading to incoherent scattering which degrades the DP quality [88]. If an array of GNDs (see Fig. 2.16b) forms a subgrain boundary in the diffraction volume, this will also degrade the DP quality through a superposition of the DPs from the different subgrains.

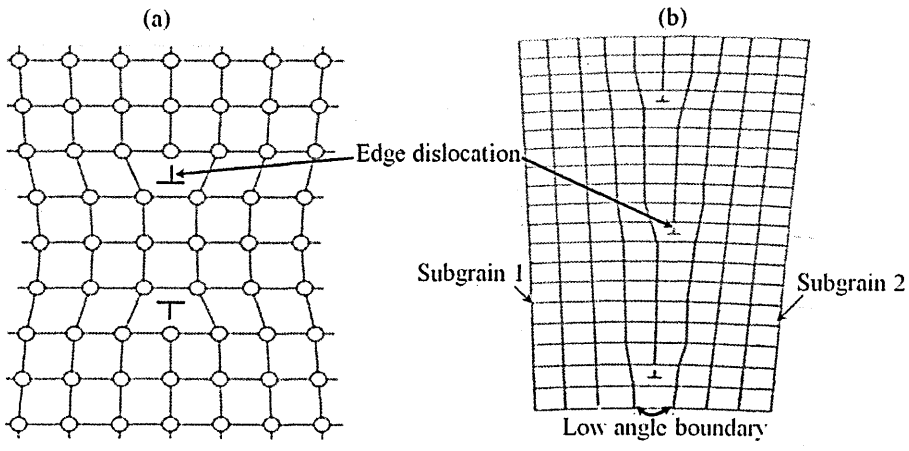

Fig. 2.16. Schematic illustration of (a) local disturbances in the crystal lattice, and (b) subgrain boundary formation [15].

In solid-solutions (see section 2.2.2.2) the local distortion of the lattice due to interstitial or substitutional atoms may lead to incoherent scattering from the diffracting

planes which degrade the DP quality. In the DP, the lattice distortion also results in small zone axes shifts detectable only from high-resolution images [88]. Similarly local chemical gradients caused by the precipitation of solute atoms from solid-solutions (e.g. Cr depletion along grain boundaries of Type 316 steels due to carbide precipitation) or chemical segregation on lattice defects such as dislocation may also degrade DP quality due to lattice distortion. As mentioned earlier, a degradation of DP quality will affect the accuracy of orientation measurement, increasing 'noise' in the data. Such local lattice distortions will not generally introduce lattice orientation changes equivalent to GNDs and will therefore have little effect on strain measurement based on such orientation changes. For chemical segregation occurring on GNDs their contribution to lattice orientation changes may not be obvious.

The quality of a DP is expressed through a band contrast (BC) parameter which assesses the average intensity of the diffracted pattern against the overall background intensity. However, this is a relative measure of quality since the intensity of a diffraction pattern also depends on other factors such as the diffracting plane involved and the phases present at the interaction volume. The pattern quality is also quantified using a band slope parameter which assesses the maximum intensity gradient between the band's edges.

2.4.3.9. EBSD system Calibration

Since the indexing of the diffraction patterns depends on the measurements of interplanar angles and bands' widths, calibration of the EBSD system is important to ensure accuracy of orientation measurement. For this purpose a single crystal of known interplanar spacing and interplanar angle is used to produce a diffraction pattern on an EBSD system of known working distance (WD) allowing determination of the detector distance (DD) and the pattern centre (PC) [89] as shown schematically in Fig. 2.17. Typically, DD is about 15-30mm [85] while WD is about a third of the image diameter

formed at a solid angle of ~60° [90]. PC is the closest point on the projection plane to the pattern source on the specimen. Essentially, the location of any point (x) on the projection plane is related to the PC through:

$$x = OU \tan \psi \qquad \text{Eq. 2.11}$$

where OU is the normal distance from the specimen to the projection plane and ψ is the angular displacement of x from the PC. During calibration the coordinates of point U (PC) and the distance OU are defined and any subsequent changes made on them requires a re-calibration of the system. The accuracy of the orientation measurement therefore depends on the precise location of the PC on the projection plane. Any instability in the detector system which displaces the PC position also introduces errors in the orientation measurement.

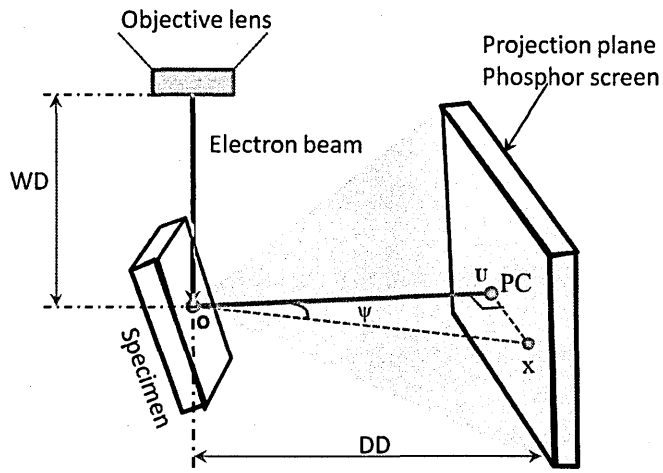

Fig. 2.17. Schematic diagram of an EBSD diffraction geometry showing working distance (WD), detector distance (DD) and pattern centre (PC).

2.4.4. Orientation mapping

The concept of orientation mapping [68, 70, 71, 87] came into existence owing to the automation of DP detection and indexing. This made it possible to acquire spatially resolved orientation data over a predefined area thus opening up many new possibilities of interrogating materials. Through orientation mapping studies, it is now possible to appraise

a material's texture, grain boundary statistics and phase distributions. Orientation mapping therefore plays a key role in the application of EBSD in material characterisation and the following section will review how it is implemented considering factors such as surface requirements, measurement modes, measurement resolution, orientation descriptions and measurement speed.

2.4.4.1. Surface requirements

Since the generation of the diffraction patterns occurs at depths much less than 1μm [73, 75] their quality is largely influenced by the condition of the surface. As discussed previously, the quality of the DP has a direct effect on the reliability of the automated indexing and thus the accuracy of the orientation measurement. The surface preparation procedures adopted for orientation mapping should therefore aim at achieving the best possible DP quality through minimising preparation-induced plastic deformation, surface contamination and oxidation. To reduce the loss of DP quality through beam defocusing and shadowing effects, the surface should be smooth with minimal relief. The presence of surface oxides and other non-conductive surface contaminants, create charging effects due to electron accumulations. These lower the DP quality owing to focus and image drifts.

Acceptable surface conditions for orientation mapping are normally realised through the conventional metallographic procedures of grinding and polishing but a final preparation is often needed to eliminate any surface deformation arising from the grinding and polishing processes. For metallic materials, the commonly used final treatments are colloidal silica polishing and electropolishing. Surfaces have also been prepared through ion milling [91] although this method is not generally used as it requires a DualBeam (combined focussed ion beam and SEM) fitted with EBSD.

Colloidal silica suspension which consists of silicon oxide particles in the sub-micron size range (~0.04μm) stabilised in an alkaline medium [92] removes the damaged

layer through both mechanical and chemical processes owing to the particle's abrasion and the slight etching effects of the stabilising medium, respectively. Electropolishing removes the damaged layer through anodic dissolution in an electrolytic cell thus avoiding any deformation that arises from the mechanical processes. A detailed account of electropolishing can be found in books [93, 94].

2.4.4.2. Measurement modes

Once the surface has been adequately prepared the orientation mapping is carried out in either beam scanning [95] or stage scanning mode [96]. In the beam scanning mode the SEM stage is kept stationary while a focused electron beam is scanned over the sample's surface at predefined intervals (step-size) following a given grid. This mode is fast but due to the specimen tilt it is limited by the beam defocus and shift from the optic axis which may introduce errors in the orientation measurements, particularly at low magnifications and short working distances [74, 97]. This is mitigated by employing a dynamic focus feature [98] which ensures the beam remains in focus everywhere in the region of interest. Additionally, the tilt causes the diffraction geometry to change from point to point requiring implementation of dynamic calibration feature [99] to allow accurate orientation mapping.

In the stage scanning mode the SEM stage is mechanically translated while the electron beam remains stationary. This minimises the beam defocusing problem, thus improving the accuracy of orientation measurement. This mode also allows measurements over a large area and its step-size calibration is independent of SEM magnification. Most importantly its diffraction geometry remains identical for all measured points. However, due to the intricate control required it is 3-5 times slower than the beam scanning and has poor positional accuracy [84, 97, 100].

Orientation mapping over a large area is realized by combining the two modes, whereby the beam scanning allows rapid measurement in a given field while the stage scanning translates from one field to the next.

2.4.4.3. Measurement resolution

To ensure the accuracy of the orientation measurement and to account for most of the microstructural features on the specimen, it is necessary to consider angular, spatial, and depth resolutions during the orientation mapping.

2.4.4.3.1. Spatial Resolution

The spatial resolution of an EBSD system determines the smallest microstructural features that can be detected during the orientation mapping. The resolution is dependent on both the electron excitation volume and the beam spread which are functions of material, specimen tilt angle, accelerating voltage and probe current [73, 84, 100]. The probe size determines the smallest distance which can be taken between the EBSD measurement points.

Tilting of a specimen leads to an elliptical probe spot with the ratio of major to minor axis being ~3:1 [73, 84] and so the spatial resolution along these axes varies similarly.

Increasing the accelerating voltage raises the beam energy which then spread more and penetrate deeper into the specimen. This reduces the spatial resolution due to an increase in electron excitation volume [84]. Decreasing the accelerating voltage reduces the electron penetration depth and thus improves the depth resolution which is reported as 50nm for aluminium studied at 20keV [73]. However, there is a corresponding decrease in pattern intensity since the energy required by an electron to penetrate a phosphor screen with and without an aluminium coating is about 20keV [73] and 3keV [84], respectively, and these are typical minimum accelerating voltages for EBSD systems with such screens.

The errors in the orientation measurements owing to poor pattern quality are therefore expected to increase as the accelerating voltage is reduced below the stated minimum values. Increasing the number of frames averaged for a solution increases the pattern quality and thus the spatial resolution at a given accelerating voltage but this is at the expense of the acquisition time [74].

The quality of the DP increases with increasing probe current owing to an increase in the beam current density. The spatial resolution therefore increases with the beam current, particularly in the field-emission gun SEM (FEGSEM) where the beam size does not vary much with the probe current [74, 101]. Increasing the probe current can also increase the specimen contamination due to polymerisation of hydrocarbons under the beam [102] which may lead to a reduction in the pattern quality and thus the spatial resolution. The optimal spatial resolution is therefore obtained at intermediate probe currents.

Since the electron backscattering yield increases with increasing atomic number [82], a higher spatial resolution is expected in materials of high atomic number than of low atomic number owing to their better pattern quality when subjected to similar conditions [100]. The electron interaction volume reduces with increasing atomic number [83] and so better spatial resolution is expected in heavier than in lighter material.

2.4.4.3.2. Angular resolution

The angular resolution of an EBSD system defines the smallest orientation difference it can measure in spatially resolved orientation data. During orientation mapping, the angular resolution influences the precision of the orientation measurements and so contributes to the development of orientation 'noise' in the acquired data. Most of the factors which influence the quality of diffraction patterns also affect the achievable angular resolution. As mentioned earlier the detection and indexing of DP depends on their

quality. Increasing the probe current and the number of frames averaged for a solution raises the DP quality and so improves the achievable angular resolution. The resolution also increases with increasing accelerating voltage owing to increased accuracy of narrow band detection/location on the phosphor screen [74].

Apart from the pattern quality, the angular resolution is also influenced by the actual number of pixels in the CCD camera used for pattern acquisition, with higher resolution obtainable with finely rather than coarsely digitised patterns. Cameras with higher pixel resolution record finer displacements in the patterns thus giving better assessment of orientation changes between the measurement points than cameras with low pixel resolution. However, their higher angular resolution comes at an expense of the measurement speed since more time is required for acquiring and analysing finely digitised patterns [103, 104].

From the above discussion it is clear that there are many factors which influence the achievable angular resolution and thus the precision of the orientation measurement. An inherent orientation 'noise' is therefore expected in most orientation data acquired using EBSD systems. This can be quantified from the point-to-point orientation variations in an otherwise deformation-free single crystal where such variations are not expected.

2.4.4.4. Orientation description

Indexing a diffraction pattern allows determination of the crystallographic orientation as mentioned earlier. In an orientation map this is done in a two dimensional space thus allowing visualisation of grains owing to their lattice orientation differences. Crystallographic orientation is defined as the rotation needed to bring a fixed/specimen coordinate system into coincidence with a crystal coordinate system [78, 79]. It is expressed either as Euler angles, in axis-angle notation or in terms of a rotation matrix.

Crystallographic orientation can be expressed in terms of three Euler angles [105] which map a fixed coordinate system onto a crystal coordinate system. A two dimensional mapping of the Euler angles can be used to generate an orientation map as shown in Fig. 2.18. Since grains in polycrystalline material vary in their average orientations, they appear distinct in this orientation map. The main limitation in the use of Euler angles is the existence of symmetry orientation spread or discontinuities. This is where the same orientation is represented by different Euler angles all of which are valid solutions for the diffraction pattern [106].

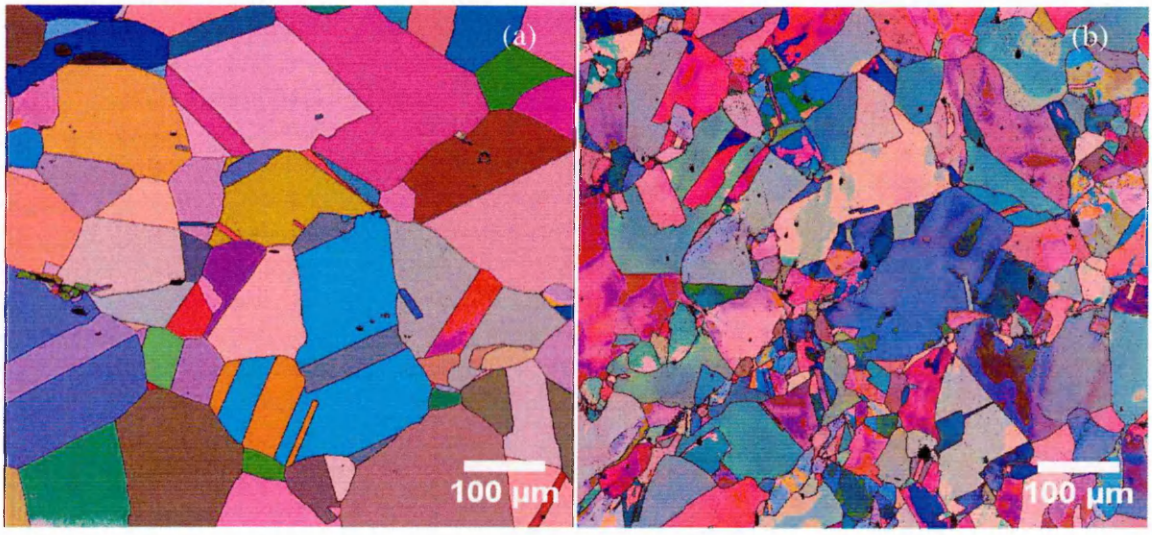

Fig. 2.18. Euler angle maps of service-aged Type 316H stainless steel in: (a) undeformed state, and (b) deformed state. Grain distinction is evident in (a) than in (b).

In the axis-angle notation the transformation that maps a fixed coordinate system onto a crystal coordinate system is defined by a rotation angle about a specific common axis between the two systems. This notation is commonly used to describe the orientation difference (misorientation) between two crystals or data points that share a common axis. Due to cubic crystal symmetry, each orientation has 24 equivalents and so the misorientation is normally represented by the smallest rotation angle among the rotation angles that can bring the two crystals into exact coincidence [79].

A rotation matrix maps a fixed coordinate system onto a crystal coordinate system or one lattice onto a reference lattice. The matrix is derived from the cosine of angles between the two coordinate systems [78, 79, 107].

2.4.4.5. Measurement speed

The speed of orientation measurement depends on both pattern acquisition and processing times. The acquisition time is mainly a function of the material and the SEM operating conditions. Essentially the acquisition time depends on the quality of DP while the pattern processing time depends on the computer's processing speed, the speed of the pattern-solving algorithm and the number of patterns averaged for a solution [97].

An improvement in the measurement speed can be obtained through CCD camera pixel binning. As mentioned previously this increases the sensitivity of the camera so lowering its exposure time and thus the acquisition time but reduces the quality of the measured DPs.

2.4.5. EBSD data analysis and presentation

In this thesis the analysis and presentation of the orientation data was performed using HKL Channel-5 software. The spatially resolved orientation data was acquired on a square grid. The main focus here will be on how the data can be analysed to extract information about plastic stain, grain size and texture of the material.

The raw data obtained at each measurement point contain information about its orientation, phase, position in the image space and its DP quality expressed in band contrast and band slope values. This information is only available from the measurement points where the DP indexing is possible otherwise a zero solution is returned. This non-indexing is mostly due to patterns overlapping particularly at grain boundaries, the presence of phases not selected for indexing, the presence of an amorphous contamination layer and/or severe deformation which inhibit coherent diffraction.

Some data points are also incorrectly indexed as their orientation differs significantly, typically by more than 5°[87], from those of their immediate neighbours without being part of a different grain. They form spurious grains and result from the poor indexing of DP. These points can be avoided by the use of high quality DP, accurate calibration of the EBSD system and by increasing the number of bands detected for a pattern solution.

The non-indexed and incorrectly indexed data points in an orientation map can be replaced by copies of immediate neighbouring points that are correctly indexed through the application of data cleaning procedures that are installed in the analysis software. However, excessive data cleaning can distort the original data, particularly if the presence of such data points arises from the treatments applied to the material. For materials with no deformation the orientation 'noise' in the data can also be reduced by applying the orientation averaging routines available in the analysis software. These routines assign an average orientation to each measurements point based on the orientations of the neighbouring points using kernels of varying sizes as detailed in [108].

2.4.5.1. Orientation data analysis

One of the advantages of the EBSD measurement is that the orientation data can be presented to show the distribution of strain, grain size and texture in the measured material. This is a useful visual tool particularly when characterising strain distribution e.g. around a crack tip or within a grain. In this section, the application of orientation data for qualitative strain assessment, grain size and texture measurement will be reviewed.

2.4.5.1.1. Qualitative assessment of strain

The presentation of orientation data in the form of image quality maps and the inverse pole figure maps is normally used for qualitative assessment of strain accumulations.

(a) Image quality (IQ) maps

These are maps reconstructed from the EBSD raw data using the band contrast (BC) values (see section 2.4.3.8) of the measurement points. The BC values are scaled from 0 to 255 in an increasing order of the DP quality. When the BC values are grey scaled, the darkest and brightest shades of grey corresponds to 0 and 255 values, respectively. Since the quality of DP along the grain boundaries is low, the boundaries are clearly outlined with a dark contrast on the IQ maps as seen in Fig. 2.19. In undeformed material, grains have uniform contrast since their measurement points have comparable DP qualities. Dark shades in the IQ maps can also represent regions of high deformation since the presence of dislocations lower the DP quality as mentioned previously. For microstructural features such as voids and cracks no diffraction pattern is obtained from them and so they appear as black features on the IQ maps. However, this is a relative assessment of deformation since other factors such as the crystallographic orientation (see section 2.4.3.6) and the phases present in the material also influences the DP quality. Despite the stated limitations, the IQ maps have been used in several studies [109-111] to visualise features arising from the deformation processes.

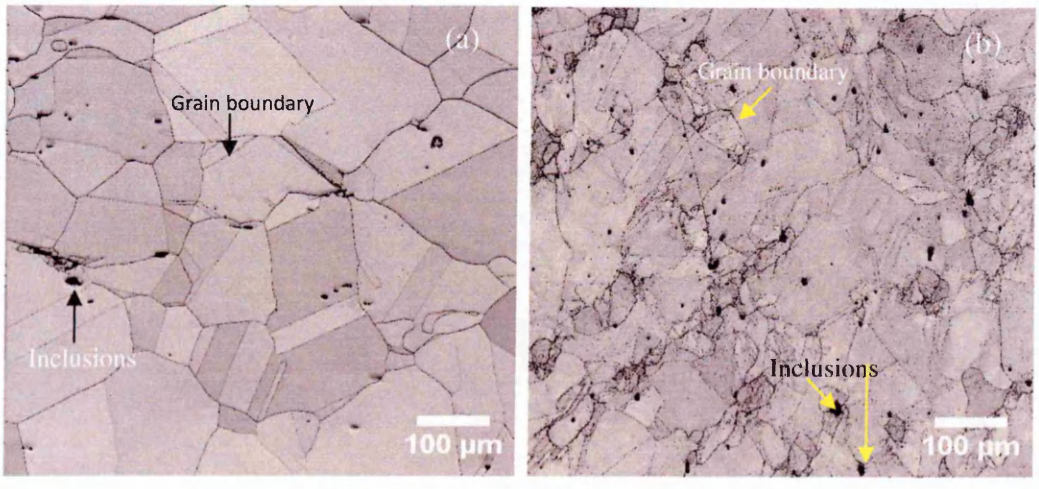

Fig. 2.19. Image quality maps of service-aged Type 316H stainless steel in: (a) undeformed state, and (b) deformed state. Uniformity of grain's contrast is more evident in (a) than in (b).

(b) Inverse pole figure (IPF) maps

Inverse pole figures are used to shows the distribution of crystallographic directions parallel to either the normal, rolling or transverse direction in the specimen [78, 79]. An orientation map can be constructed to show the crystallographic direction of each point on the surface of every grain in the field of view that is parallel to the specimen normal direction. These maps can be used for qualitative assessment of plastic strain since in an undeformed material, each grain will have a uniform crystallographic orientation relative to the specimen normal direction (see Fig. 2.20a). This may be compared to the grains in a deformed material (see Fig. 2.20b). The lattice rotations arising from the accumulation of GNDs within the grains can alter the crystallographic directions parallel to the specimen normal direction at each point in the grain. This makes the distribution of orientations within the grain non-uniform. These maps have been used for qualitative assessment of plastic and creep strain accumulations in Type 316 stainless steel [63].

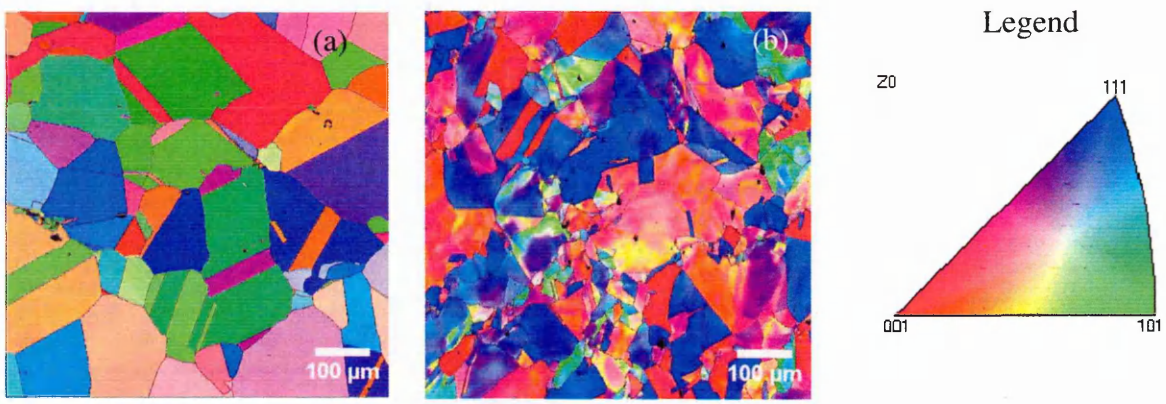

Fig. 2.20. Orientation maps of service-aged Type 316 stainless steel in: (a) undeformed state, and (b) deformed state. Intragranular colour gradation is more evident in (b) than in (a). Colour coding is based on crystal directions parallel to specimen's normal direction.

2.4.5.1.2. EBSD grain size measurement

An important application of the orientation measurement is in grain size determination, since for the spatially resolved orientation data it is possible to define grains

as regions of comparable orientations [74]. A grain boundary is defined as region where misorientation between two adjacent measurement points exceeds a certain value. Since orientation can be expressed in axis-angle notation, grain boundary misorientation axis can also be determined allowing characterisation of special boundaries such as twins [33]. An orientation map shows all the grains in the microstructure that are equal or larger than the size of the beam probe. This leads to detection of many spurious grains arising from the incorrectly indexed data points. These points therefore need to be removed from the orientation data before the measurement of the grain size. To obtain the true area covered by the grains, the orientation data also need to be corrected for non-indexing [74].

2.4.5.1.3. EBSD texture measurements

The distribution of crystallographic orientation within a material defines its texture. A non-textured material has a random distribution of crystallographic orientations for all the different grains mapped, while a textured material shows a 'preferred orientation'. A material's texture can give information about its deformation history since the distribution of lattice orientation is influenced by manufacturing processes such as rolling. Texture also influences the mechanical properties of materials with a textured material having anisotropic properties [112]. Texture is commonly assessed through pole figures generated from the orientation data [79]. The pole density in these figures shows the strength of the poles clustering relative to a completely random distribution and is expressed quantitatively in terms of multiples of uniform density (MUD) [79] (see Fig. 2.21).

Micro-texture measurements sample the orientation variation within individual grains, while macro-texture measurements sample many grains without reference to the location of individual grains and so provide volumetric information associated with each orientation [79]. By sampling a sufficient number of grains it is possible to apply EBSD for macro-texture measurement [72, 113]. Since oversampling of individual grains affects

the pole density, it is common to use single grain orientation [79] when assessing macro-texture from the EBSD data. This approach is better suited for materials of comparable grain sizes.

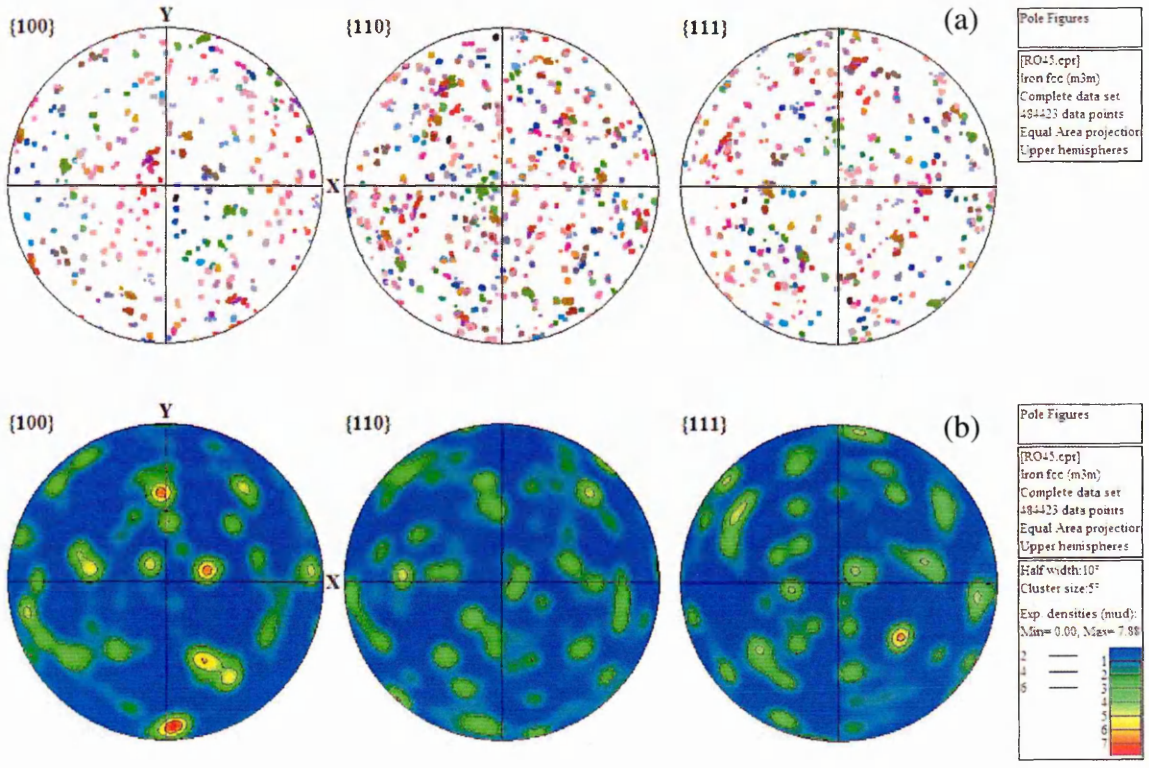

Fig. 2.21. (a) Pole figures of deformed service-aged Type 316 stainless steel. (b) Corresponding normalised pole figures of (a) showing presence of preferred orientation.

2.4.5.2. Quantitative assessment of strain

Discussion in this section will focus on how crystal orientation data obtained from commercial EBSD systems can be used for quantitative assessment of strain in materials. Since EBSD does not measure plasticity but rather the effects of plasticity, the term 'assessment of strain' rather than 'measurement of strain' will be used in this thesis. The generation and accumulation of GNDs during plastic deformation result in lattice rotations. This leads to local changes in crystal orientations which are measured through EBSD. The assessment of plasticity using EBSD therefore does not give full account of the total dislocation content in deformed materials since the SSDs are not accounted for.

As mentioned in section 2.4.4.4 crystallographic orientation can be expressed in several ways. In this discussion the axis-angle notation will be used and the term 'misorientation' will be used in reference to the rotation angle component of the notation.

Two approaches for assessing plastic strain using misorientation measurements will be reviewed here. Firstly the local misorientation approach which evaluates the orientation differences among adjacent measurement points and secondly, the average misorientation approach which considers the average orientation changes within a region of comparable orientations e.g. a grain.

2.4.5.2.1. Local misorientation approach

In this approach the spatially correlated misorientations are evaluated in several different ways to assess strain in the measured area. In this section the commonly used metrics in the literature based on this approach will be reviewed. These include Kernel Average Misorientation (KAM), Grain Average Misorientation (GAM) and Grain Boundary Fractions.

a) Kernel Average Misorientation (KAM)

KAM is a metric that assess the orientation differences between a measurement point and its neighbouring points. As the name suggests this is an averaging kernel (set of points surrounding a point of interest) which calculate an average misorientation for each measurement point based on the misorientations between the point and its neighbours (see Fig. 2.22). To represent the local misorientation, the smallest kernel size of 3x3 data points is used. Increasing the kernel size smoothen the local misorientations.

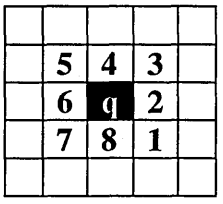

Fig. 2.22. Schematic drawing of a 3x3 kernel (shaded) about a central pixel (q).

KAM represent the small lattice rotation between adjacent measurement points brought about by the accumulation of GNDs. However, this is only true when misorientations associated with the grain and subgrain boundaries are excluded during the KAM computation. In many EBSD studies [75, 77, 79, 88, 114] a misorientation of 2° has normally been used as the lower limit of the subgrain boundary due to the limitations in the angular resolution of EBSD systems.

Owing to the inherent orientation 'noise' in the orientation data (see Fig. 2.23 and section 2.4.4.3) a finite KAM always exists, although theoretically for a perfect crystal the KAM should be zero. It is clear that the KAM metric can only be used to assess plastic strain which introduces misorientations greater than those introduced by the orientation 'noise'. Another important attribute of the KAM metric is that its values are not absolute since they depend on the distance between the measurement points (i.e. step-size). Increasing the step-size is analogous to increasing the kernel size which samples a large area leading to a relatively high KAM values. The chances of sampling multiple regions belonging to different subgrains increases with increasing sampling area and this would ultimately increase the local misorientation measured. This dependence has been reported previously [88].

Mapping the KAM of all the points in an orientation map gives a qualitative assessment of the strain distribution (see Fig. 2.23). The KAM maps tends to be noisy owing to the presence of orientation 'noise' and the fact that they are constructed using all data points in an orientation map. In 10Cr-1Mo-1W-VNbN steel, the KAM metric was used to characterise creep deformation where its values were related to creep time fractions [115, 116]. Similarly, in Alloy 600 cross-weld KAM values were used to represent plastic strain [117]. Another metric which is computed similarly to the KAM metric is the Kernel Orientation Spread (KOS) [88].

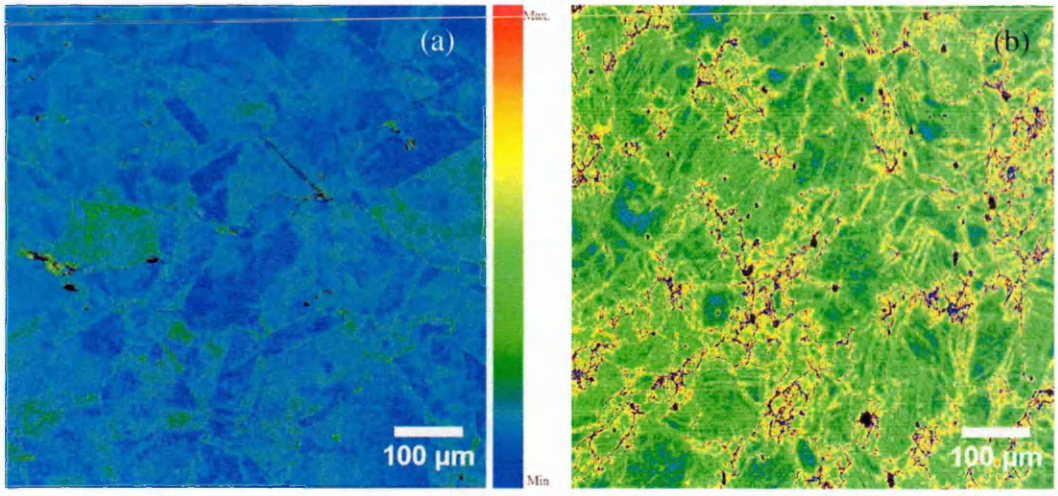

Fig. 2.23. KAM maps of service-aged Type 316H stainless steel in: (a) undeformed state, and (b) deformed state. Rainbow colours from blue to red shows minimum to maximum strain. Orientation 'noise' is evident in (a).

b) Grain Average Misorientation (GAM)

GAM [118] metric calculates the average misorientation based on misorientations between each pair of neighbouring measurement points within the grain. In Alloy 690TT deformed at room temperature in tension, GAM showed strong linear correlation with the applied strain of up to 0.25 [64]. Similar linear correlation has been reported in Type 316 stainless steel [63] deformed at room temperature in tension and in compression to about 0.1 strains. In that work the GAM was also found to increase with increasing creep damage ratio.

c) Grain Boundary Fractions

In an orientation map boundaries are defined as regions where misorientation between neighbouring points is above a certain threshold. Typically, local misorientations >15° defines the high angle grain boundaries (HAGBs) [74, 75, 119, 120] and those <15° are considered as the low angle grain boundaries (LAGBs) [15, 77, 114]. HAGBs arise from the orientation differences among the grains while LAGBs evolve as an array of discrete lattice dislocations which display local strain gradients and are arranged so as to

minimise their total line and strain energies [15]. The development of LAGBs is therefore associated with deformation and their densities have been used to qualitatively assess the extent of plastic deformation around a fatigue crack tip in Type 304 stainless steel [111].

Since in spatially resolved orientation data all local misorientations can be defined, the fraction of LAGBs in the microstructure can be used to characterise deformation e.g. in [121] LAGB fractions were used to track microstructural evolution during hot compression of Type 304 stainless steel while in [122] they were evaluated as a function of cold rolling extent and annealing temperature during the characterisation of Alloy 718 (IN718) tensile-creep properties.

2.4.5.2.2. Average Misorientation Approach

In this approach spatially uncorrelated misorientations within a grain are calculated and an average value determined. In this section the commonly used metrics in the literature based on this approach will be reviewed. These metrics include Average Intragrain Misorientation (AMIS), Grain Orientation Spread (GOS), Deformed Grain Fraction (DGF), Crystal Deformation and Modified Crystal Deformation (MCD).

AMIS is a metric that computes an average misorientation from misorientations between the measurement points in a grain and a reference point. The mean grain orientation is used as the reference orientation. AMIS therefore gives a measure of the average crystal rotation due to build-up of GNDs. The overall AMIS for the whole orientation map is obtained by averaging AMIS from the individual grains in the map. Since AMIS is computed from spatially uncorrelated misorientations, it is relatively insensitive to the measurement step-size. The GOS [88] metric is computed in a similar manner as the AMIS.

DGF [123] is a metric that computes the fraction of deformed grains in an orientation map. The deformed grains are defined as those having an average intragrain misorientation above a certain value, typically taken as the overall AMIS of an orientation

map of undeformed sample. The main attributes of this metric include insensitivity to measurement step-size and to microstructural variations.

Crystal Deformation (C_d) [124] metric differs from the AMIS metric in the way the reference point is selected. For this metric, the reference is the measurement point in the grain with the lowest summed misorientation among the points. The overall C_d for the whole orientation map is evaluated from the summation of all uncorrelated misorientations divided by the number of grains considered. A method proposed in [111] works in the same way and uses uncorrelated misorientations computed from a reference identified as the point in the grain with the lowest KAM.

Modified Crystal Deformation (*MCD*) [125] was a further development of the C_d metric and is quite similar to AMIS in that the uncorrelated misorientations are calculated from a reference which is identified as the mean orientation of the grain. However, the overall *MCD* of an orientation map is defined as the mean of the lognormal distribution of all uncorrelated misorientations. The important attributes of this metric include insensitivity to electron beam conditions, to SEM type and to measurement step-size.

Most of the metrics proposed, particularly those based on the average misorientation approach, show strong linear correlations with the applied plastic strain. However, these correlations are based on room temperature tests on materials that are well characterised. The use of these correlations for strain assessment in materials that are deformed at elevated temperatures and/or in materials with non-uniform microstructures (particularly those with varying grain sizes and precipitate densities), may give erroneous strain estimates since the evolution of misorientations under these conditions may be different.

One of the objectives of the current study was to develop a universal metric based on lattice orientation measurement that is generally applicable for strain assessment in materials of varied microstructures and different deformation histories.

CHAPTER 3

EXPERIMENTAL TECHNIQUES

3.1. Introduction

In this chapter various experimental techniques adopted in the current study are discussed in detail. In section 3.2 uniaxial tensile, compression and creep testing techniques are described in terms of the machine specifications, specimen geometries, Standards, strain measurements, temperature control and data analysis. Mechanical tests were performed to introduce controlled deformation in steels studied, as a preliminary stage in the development of an EBSD-based strain assessment technique. Hardness measurement, which was used as a complimentary technique for the assessment of deformation in the steels studied, is also discussed in this section in terms of sample preparation requirements, Standards, hardness range measured and in terms of data analysis.

In section 3.3 there is a discussion of the microstructural assessment techniques applied in the current study. These included optical microscopy, scanning electron microscopy, energy dispersive X-ray spectroscopy, optical emission spectroscopy and transmission electron microscopy. The discussion focuses on their working principles, lateral resolutions, optimal operating conditions and sample preparation requirements.

EBSD was used in the present study to develop strain assessment methods for Type 316 austenitic stainless steels and in section 3.4 this strain assessment technique is elaborated. Discussion focuses mainly on the equipment available and its optimal operating conditions, sample preparation requirements, EBSD measurement parameters and data analysis for strain assessments. A summary of the key points in this chapter is given in section 3.5.

3.2. Mechanical testing

3.2.1. Uniaxial tensile tests

Uniaxial tensile tests at ambient (~24°C) and elevated temperatures (550°C and 675°C) were used for characterising the tensile properties of the steels studied and also for controlled deformation of specimens under different conditions. The tests were conducted in accordance with BS EN ISO 6892-1:2009 [126] and BS EN 10002-5:1992 [127] for the ambient and the elevated temperature tensile tests, respectively. The geometry of the cylindrical specimen used is shown in Fig. 3.1. The diameters of the machined specimens were accurately measured from five equidistant locations along their gauge lengths to derive an average value.

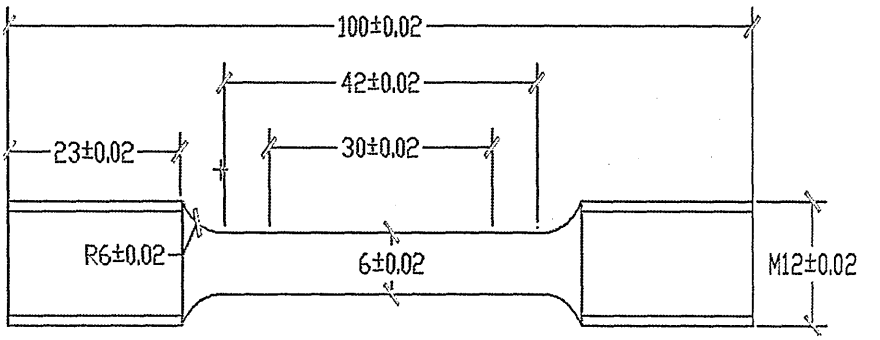

Fig. 3.1. Tensile specimen geometry (schematic): all dimensions in mm.

The tests were conducted on an Instron 8862 machine with a load capacity of 100kN and fitted with a single screw electromechanical actuator, capable of very slow strain rate tests (see Fig. 3.2a). The machine was controlled through built-in Instron Bluehill software and tests were performed at constant displacement rates of 0.5mm min^{-1} and 0.075mm min^{-1} for the ambient and the elevated temperature tensile tests, respectively.

Strain was externally monitored via a high temperature extensometer (Instron 2632-054) interfaced with Instron's controllers and mounted onto the specimen gauge length using ceramic cords as seen in Fig. 3.2b. The extensometer gauge length was 12.5mm with a maximum travel of 2.5mm and was fitted with chisel-ended alumina rods which served

to transmit mechanical displacement on the specimen to the strain gauge housed in the extensometer body. The conversion of mechanical displacement into electrical signal by the strain gauge allows strain monitoring on the specimen. The accuracy of strain measurements was enhanced through extensometer calibration before every test using an Instron calibrator unit.

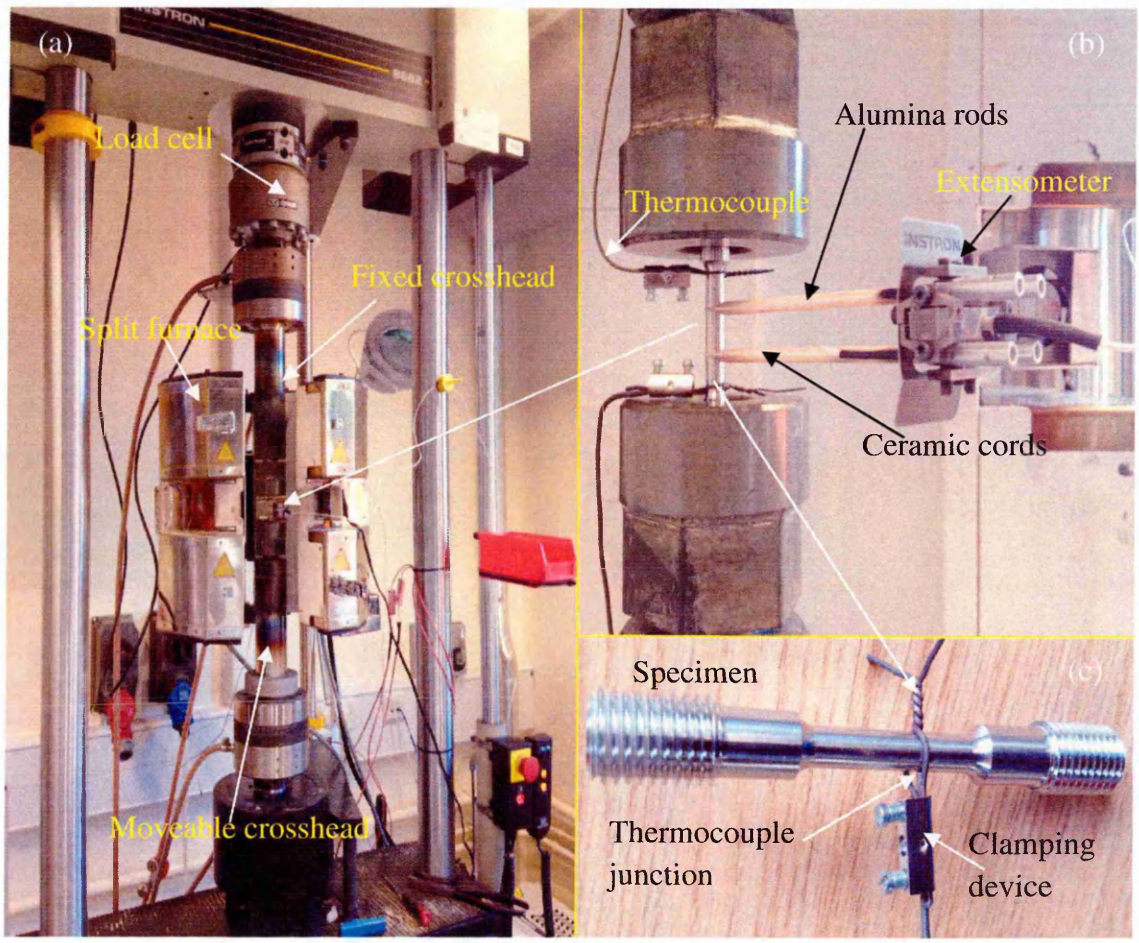

Fig. 3.2. Photographs of (a) Instron 8862 machine fitted with a split furnace, (b) Instron 2632-054 extensometer and type-N thermocouples mounted on a specimen, and (c) thermocouple clamping device.

A furnace of split construction and with a side window was used for high temperature tests as it allowed easy specimen loading and extensometry attachment. A Eurotherm 3216 controller was used to manage the temperature of the furnace, which was independently heated at three zones through resistance wires wound on a re-crystallised

alumina tube. Furnace temperatures were manually adjusted to give uniform specimen heating through a combination of convection and radiation heat transfer. The specimen temperature was monitored by means of type-N thermocouples attached directly at two locations along its gauge length through an improvised clamping device shown in Fig. 3.2c. Before the specimens were deformed, they were held for 1 hour at the test temperature to allow temperature homogenisation. The resultant temperature gradient along the gauge was <1°C and the variation from the test temperature within ±1°C. This was achieved through careful setting of the furnace temperatures and through proper insulation of its open areas to minimise heat loss. However, during the test some variations in specimen temperature were observed, particularly for highly strained specimens. This was attributed to loose connections between the thermocouples and the specimens owing to their diminishing diameters. At the end of the tests the specimens were unloaded and allowed to cool in the air to ambient temperature.

To enhance the repeatability of tests performed under similar conditions, specimens were extracted from the same locality of the parent material, in an endeavour to limit their variability in terms of chemical and mechanical properties.

The important raw data logged continuously by the software during the test included; test time, crosshead extension, load and strain. The true strain (ε) was computed from the nominal strain (e) using the equation $\varepsilon = \ln(e + 1)$, while the true strain rate was given by the gradient of the true strain versus time curve. Nominal stress (s_σ) was derived from the applied load (P) and the original specimen diameter (d) using the equation $s_\sigma = 4P/\pi d^2$ while the true stress (σ) was given by $\sigma = s_\sigma(e + 1)$.

Tensile tests at a constant strain rate of ~0.015s^{-1} were also performed on Type 316 stainless steel tubes at room temperature, using the method described in [128]. The strain was monitored by side-mounted extensometer and the tubes were deformed to specific

strain levels as will be detailed in Chapter 5. In this thesis, only the true strain and stress values are reported.

3.2.2. Uniaxial compression tests

Uniaxial compression tests were performed on specimens of service-aged steel, mainly to introduce controlled deformation under different conditions. Tests were conducted on cylindrical specimens 10mm in diameter (D) and 15mm high (H) at 24°C and at 550°C. The dimensions were chosen so that the ratio of H/D was 1.5 as stipulated in ASTM Standard E9-89a [129]. The specimens were extracted from the parent material by wire electric discharge machining (EDM) with a resultant surface roughness (R_a) of about 2.2μm. After machining the average dimensions of the specimens were determined with a high precision micrometer screw gauge. Each D value was taken as the average of four measurements at the midpoint of the specimen taken 45° to each other. The H values were derived by taking the average of four measurements, one taken at the centre and three on the circumference each separated by 120°.

The tests were conducted on a MTS-810 servo-hydraulic machine with a load capacity of 100kN. The machine's moving crosshead applied the load which was measured by a load-cell fitted on the fixed crosshead. The machine platens were made from high strength PM1000 alloy which ensured that only the specimen deformed even at 550°C. The machine was controlled through built-in MTS Teststar II software and the compression tests were performed at constant displacement rates of 0.5mm min^{-1} and 0.075mm min^{-1} at 24°C and 550°C, respectively.

For room temperature tests the strain was measured using an extensometer (MTS 634.31F-25, maximum travel 6mm) attached directly onto the specimen's gauge length and interfaced with MTS controllers. The other data logged continuously during the test included the test time, axial displacement and the axial load.

Compression tests at 550°C were conducted using a split furnace which allowed easy specimen access. The absence of a side window on this furnace made direct strain measurement using an extensometer impossible. The furnace, controlled by a Eurotherm 2216e unit, was resistively heated in three zones, allowing a uniform temperature to be obtained along the specimen. The specimen temperature was monitored by type-N thermocouples attached directly at the top and bottom of its gauge length. Before the test the specimen was held at 550°C for 1 hour, to allow temperature homogenisation, at which point the gradient along the gauge length was <1°C and the variation from the test temperature within ±2°C. At the end of the test the specimen was unloaded and allowed to cool in the air.

To reduce the contact friction at the interface between the specimen and the machine's platens, and thus the specimen's tendency to barrel during the test, molybdenum disulphide- and boron nitride-based lubricants were used in the room and high temperature tests, respectively.

The average dimensions of the deformed specimens were determined as previously described in the case of undeformed specimens. The true strain (ε) was calculated using equation $\varepsilon = ln(H_f/H_0)$ where H_f and H_0 are the final and initial average specimen heights, respectively [31, 130]. The data was also used to calculate the barrelling coefficient (B), the height coefficient (H_c) (which assesses the parallelism of the specimen during deformation), and the ovality coefficient (O_v) (which gives an indication of the influence of texture and microstructure on the deformation behaviour). These coefficients are expressed as follow:

$$B = \frac{H_f d_f^2}{H_0 d_0^2} \quad , \quad O_v = \frac{d_{fmax}}{d_{fmin}} \quad , \quad H_c = \frac{Sh_f}{H_f} \qquad \text{Eq. 3.1}$$

where Sh_f is the standard deviation of the deformed specimen heights, d_f and d_0 are the final and initial specimen diameters, measured at the midpoint, while d_{fmax} and d_{fmin} are the maximum and minimum diameters of the deformed specimen, respectively [126].

The true stress and true strain values were also derived from the raw data using the equations described in section 3.2.1 and were used to generate true stress-true strain curves. There was good agreement between the global true strain obtained from the extensometer measurements and that from the H differences, for tests at 24°C. For 550°C curves, the strain values were calculated from the axial displacement of the crosshead, after making allowance for the machine compliance at this temperature. The compliance was calculated in accordance with the procedures given in [130, 131] and was 1.4 x10^{-5}mmN^{-1} at 550°C.

3.2.3. Uniaxial creep tests

Uniaxial constant load creep tests were performed to introduce a controlled amount of creep strain in specimens as a preliminary stage in the development of an EBSD-based strain assessment technique. The tests were performed at 550°C and at 675°C in accordance with BS EN ISO 204:2009 [132]. The geometry of the creep specimen used is shown in Fig. 3.3. The new diameters of the deformed specimens (prestrained) were accurately measured from five equidistant locations along their gauge lengths to derive an average value. Similarly, an average value was computed for the new gauge length.

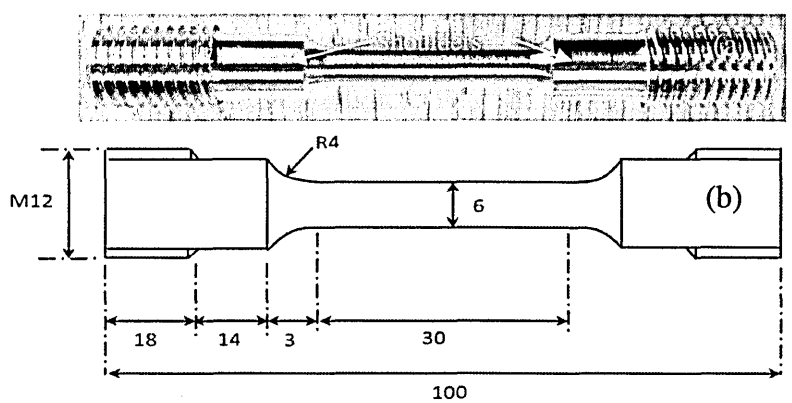

Fig. 3.3. Creep specimens' (a) photograph, and (b) geometry (in mm).

Uniaxial creep tests were conducted on a constant load creep frame shown schematically in Fig. 3.4. The main sections of the frame were involved with either driving or loading. The driving section consisted of an electric motor linked to the connecting rods (pull rods) through a worm-wheel gear mechanism, and drove the pull rods up and down. The pull rods were connected to the specimen through universal coupling joints, which minimised bending forces on the specimen. The loading section consisted of a hanger, holding disks of known weight (dead weight) and connected to the driving section through a 10:1 levering system. The connections were made flexible by using knife edges. The frames were fitted with a limit switch, which triggered the motor to drive the system up or down when changes in the specimen gauge length caused the lever arm to deviate from the horizontal. This maintained the lever arm ratio and ensured a constant load on the specimen throughout the creep test. All pivots and knife edges were well lubricated to minimise frictional effects.

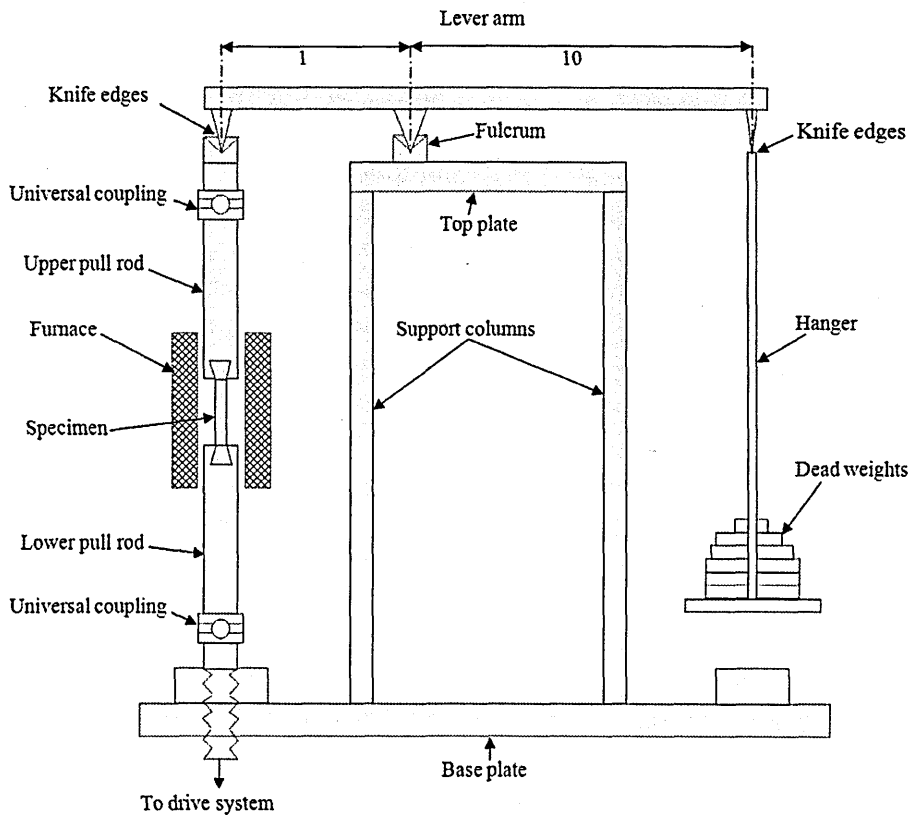

Fig. 3.4. Schematic representation of a constant load creep frame.

The creep frames were fitted with furnaces which could be moved up and down to allow easy access to the specimen. Each furnace was independently resistance heated in three zones and its temperature monitored by type-N thermocouples. Three Eurotherm 3216 controllers governed the furnace temperature using control loop feedback.

The displacement along the specimen gauge length was monitored by a Linear Variable Displacement Transformer (LVDT) which works on the principle of electromagnetic induction. The LVDT consists of a primary coil, secondary coils and a core, as shown schematically in Fig. 3.5b. The primary coil is connected to an alternating current and produces an alternating magnetic field which induces current in the secondary coils depending on the core's position. Within limits, the induced current is linearly proportional to the mechanical movement and so displacement can be measured. The LVDTs used in the current work had a maximum travel of 5mm and a displacement resolution of 1μm. The LVDT was calibrated before every test using an Instron calibrator unit to improve the accuracy of the displacement measurements. The LVDTs were linked to the specimen through a pair of rigid frames which were screw fastened around the specimen shoulders, and the whole unit connected to the pull rods through the nose caps and collets as shown in Fig. 3.5a. All threaded connections exposed to high temperatures were coated with copper-based anti-seize agent to prevent their seizing up during tests.

The specimen temperature was monitored by type-N thermocouples attached directly at three locations (see Fig. 3.5a) along its gauge length through the improvised clamping device previously discussed (see Fig. 3.2c). The temperature was recorded regularly using Picolog software. Before the specimens were loaded, they were held for 1 hour at the test temperature to allow temperature homogenisation. The resultant temperature gradient along the gauge length was <1°C and the variation from the test temperature within ±1°C. This was achieved through correct setting of the furnace temperatures and through proper insulation of its open areas. The ambient temperature in

the creep laboratory was maintained at 20°C±0.5°C by air conditioning. All loadings took <120 seconds and when the required creep strain was reached, the tests were interrupted by stopping the heating, removing the furnace and cooling the specimen rapidly to ambient temperature while still loaded. This was meant to minimize recovery of the dislocation structures.

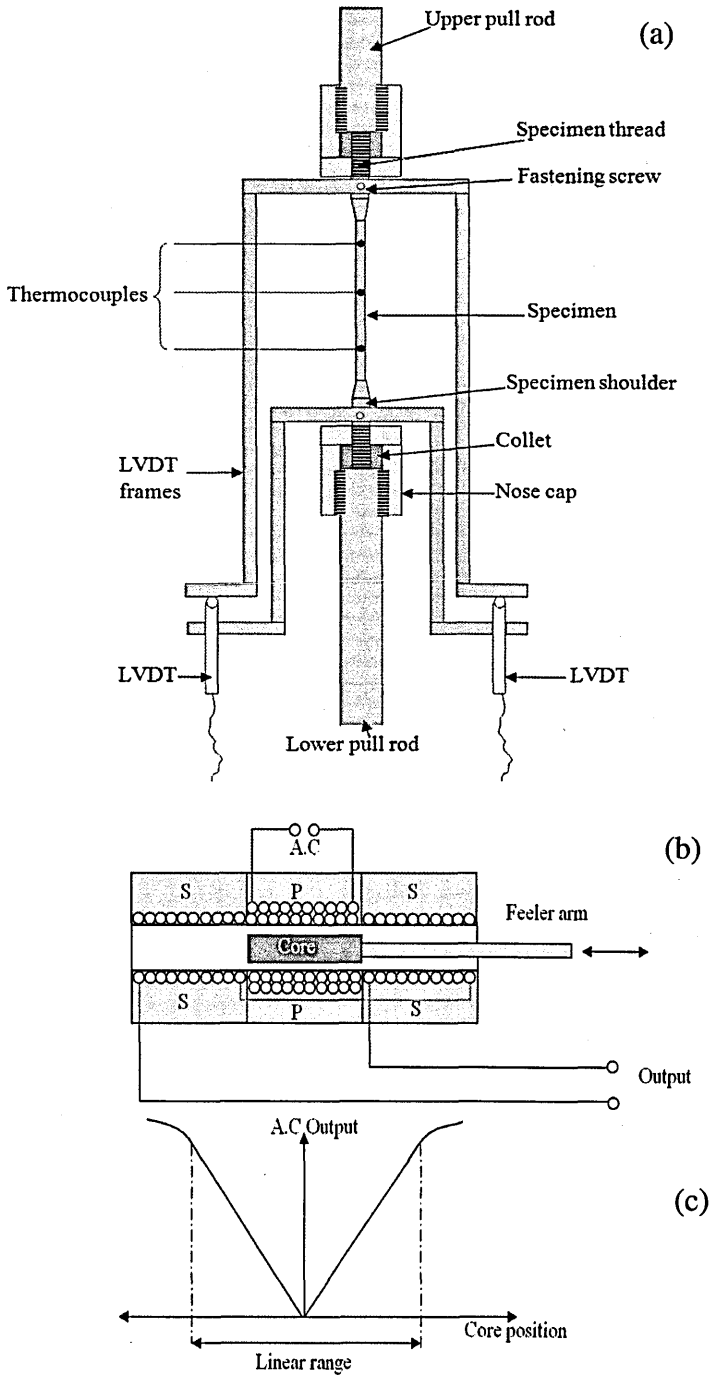

Fig. 3.5. Schematic drawing of: (a) specimen set-up on a creep machine, (b) LVDT main components, and (c) LVDT output voltage versus core position.

To improve the accuracy of the applied loads a load cell was connected on the frame in the specimen's position and the actual load applied by each dead weight determined taking into consideration the lever arm ratio. All dead weights were subsequently labelled with their corresponding frame number and actual loads. At the beginning of this process the lever arm was ensured to be horizontal and all slackness in the pull-rod connections eliminated by applying a 20N load on the hanger.

In-house software was used to record the following raw data during the test; accumulated displacement (l) on the specimen (which was an average of the two LVDTs values), test time elapsed, and accumulated creep strain (ε_c) (computed from the specimen gauge length L using, $\varepsilon_c = l/L$). The frequency of data recording was high during loading and primary creep stages (every 1 second) but gradually reduced as the test progressed into the secondary stage (every 5-30 min) before being increased again to every 5 min as the tertiary stage was approached. The initial stress (σ) applied during the test was calculated from the specimen's diameter (d) and the applied loads (P) using equation $\sigma = 4P/\pi d^2$. From the creep strain (ε_c) versus time (t) curve (see Fig. 2.7), the creep rate at any given time was given by $d\varepsilon_c/dt$ [8]. The minimum creep rate corresponded with the smallest rate calculated.

3.2.4. Uniaxial tensile test in SEM for in-situ EBSD measurements

In-situ tensile tests at 24°C were performed to study the evolution of plastic deformation in a localised area as a preliminary stage in the development of an EBSD-based strain assessment technique. The tests were performed on 1mm thick flat specimens whose geometry is shown in Fig. 3.6.

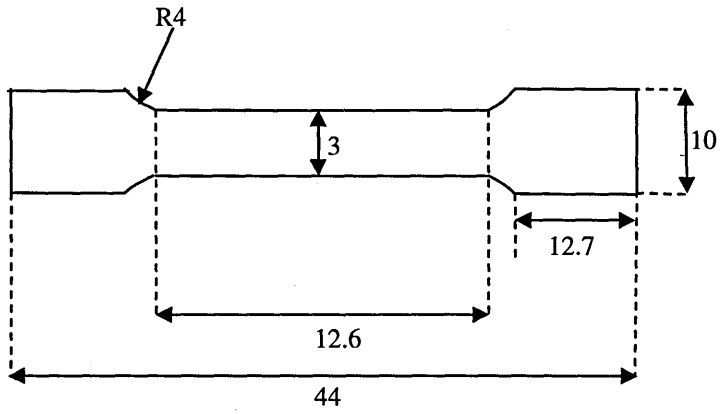

Fig. 3.6. Tensile specimen geometry (mm) used for *in-situ* EBSD studies (schematic).

The tests were conducted on a MTI/Fullam SEMtester machine with a maximum load capacity of 4.5kN and fitted with two movable crossheads driven by a direct current motor through a worm gearing system as shown in Fig. 3.7. The machine was controlled through Material Testing Software (MTS) that complies with ASTM specifications and tests were performed at a constant crosshead displacement rate of 0.5mm min^{-1}. The machine was equipped with self-locking grips, a sample holder tilt-able by 30° from horizontal and a resistive heater capable of attaining 1200°C.

All the tests were performed inside a scanning electron microscope (SEM) under vacuum and the data logged regularly by the MTS software included the test time elapsed, the load applied and the crosshead displacements. From the displacement and gauge length values the nominal strain was calculated while nominal stress was computed from the load and specimen cross-sectional area data as described previously. The position transducer was calibrated in accordance with the manufacturer's instruction.

To facilitate EBSD measurement, one side of the specimen was ground, polished and electropolished following the procedures given later in section 3.3. The specimen was then loaded onto the SEMtester machine tilted at 30° while the SEM stage was tilted by 40° giving a total tilt of 70°, necessary for the EBSD measurements. Due to the large size of the SEMtester machine the EBSD camera was only inserted by 160mm instead of the

normal distance of 175mm and this necessitated recalibration of the EBSD system at this distance to enable correct detection and indexing of the diffraction patterns (see section 2.4.3.9). The calibration procedures are given in [133]. The tensile test was interrupted at specific strain levels to allow EBSD measurements, after which the test was allowed to continue and this was repeated until the specimen ruptured. EBSD measurements were carried out in the middle of the specimen's gauge length while the load was still on. Only room temperature tests were performed since the available EBSD detector was only designed for ambient temperature applications.

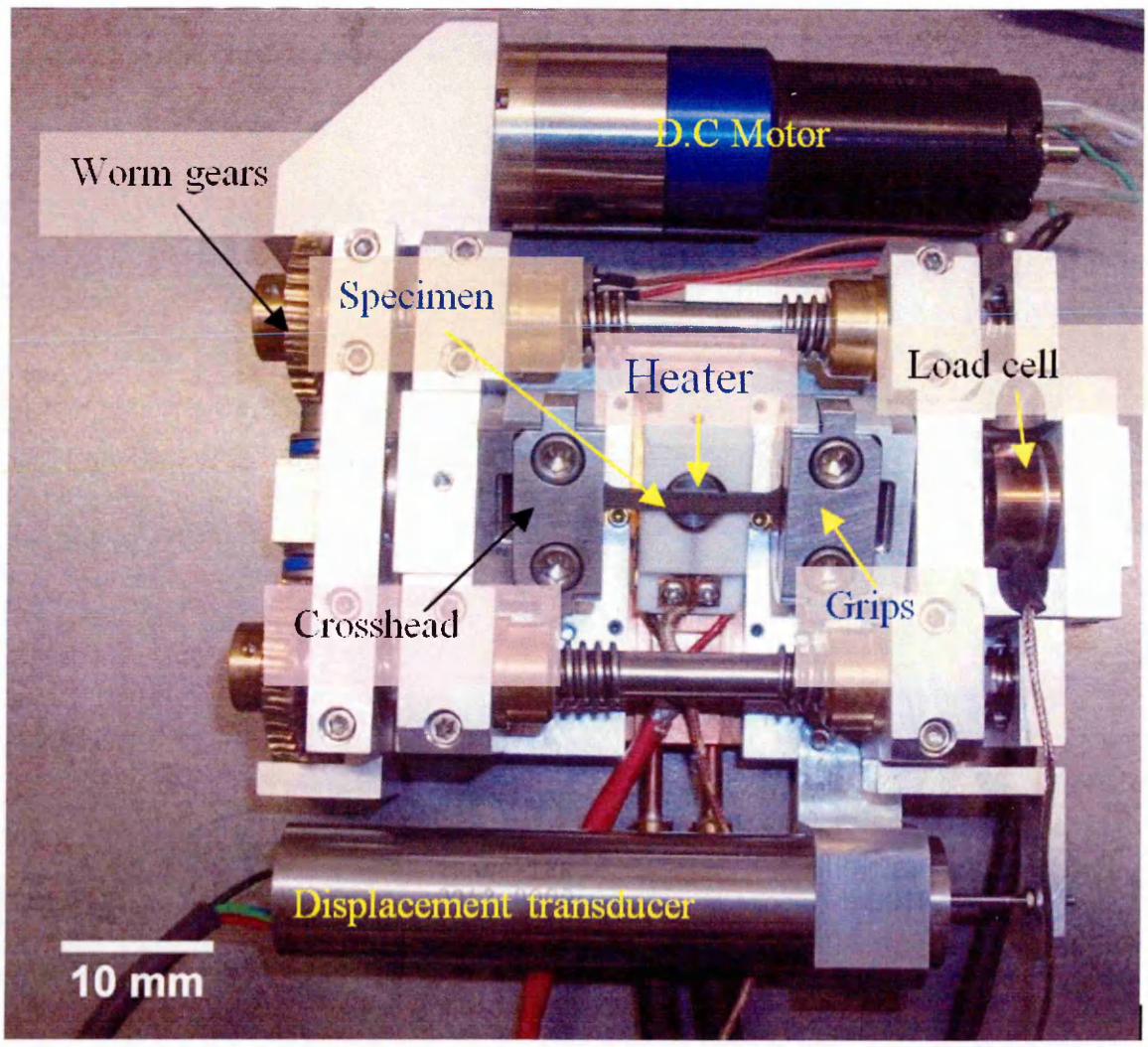

Fig. 3.7. Photograph of MTI/Fullam SEMtester machine used for *in-situ* EBSD studies.

3.2.5. *Hardness measurement*

The hardness of materials refers to their resistance to permanent penetration by another harder material. Hardness only provides relative information about material's properties, since it is measured using different techniques with different scales. For measurements based on indentation tests, the hardness is determined in the macro range when the applied forces are between 2 and 30kN, in the micro range when the forces are <2N and the indentation depth >0.2μm, and in the nano range when indentation depths are ⩽0.2μm [61].

The macro-hardness in the current study were determined using Vickers hardness testing, which uses a square-base diamond pyramid indenter with 136° between its opposite facets. The measurements were performed in accordance with BS EN ISO 6507-1:2005 [134], on a Struers Duramin-A300 machine, using a maximum force of 5kgf for 10s and an indenter spacing of 0.5mm on a surface that had been prepared for electron microscopy studies as described later in section 3.3. The macro hardness tests were mainly used to assess the hardness variations across weldments. The hardness was expressed in terms of the Vickers hardness number (*HV*) given by [31]:

$$HV = \frac{2P\sin(\omega/2)}{L^2} = \frac{1.854P}{L^2} \qquad \text{Eq. 3.2}$$

where P is the applied load in kg, ω is the angle between indenter's opposite facets and L is the average length in mm of indentation diagonals (determined from the microscopic measurements of the indent). The indent spacing's were all >3L to avoid overlapping of the indentation strain fields [134].

Hardness measurements at the nano range were made with an MTS Nano Indenter XP, fitted with a diamond indenter and controlled by TestWorks-4 software [135]. The measurements were carried out in accordance with BS EN ISO 14577-1:2002 [61] using a maximum force of 49mN for 5s at a rate of 3.3mNs^{-1} and an indenter spacing of 18μm. The

surface tested was prepared as for electron microscopy, to minimize preparation-induced surface hardness. To ensure sampling of multiple grains, line measurements over a total length of 700μm were made on each sample and the mean hardness determined. The nano hardness measurements were mainly made on small samples derived from the mechanically deformed specimens where hardness (H_n) was expressed in terms of N/mm^2 and given by [61]:

$$H_n = \frac{F_{max}}{A_p}, \quad A_p = 24.5{h_c}^2 \qquad \text{Eq. 3.3}$$

where F_{max} is the maximum applied force in N, h_c is the unloaded indentation depth, and A_p is the projected area in mm^2 of the contact between the indenter and the sample (determined from the force-displacement curve (see Fig. 3.8) and the indenter area function).

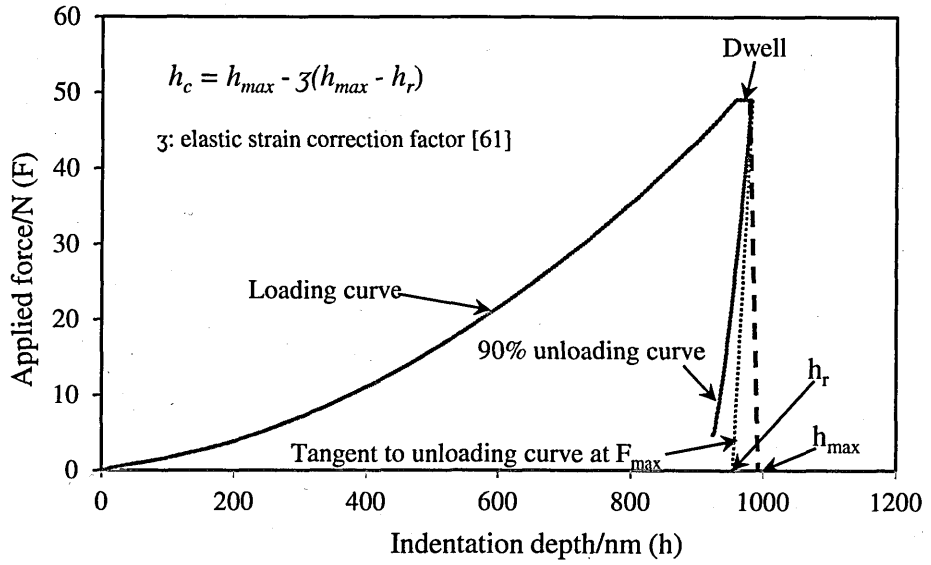

Fig. 3.8. Load versus indentation depth curve used in nanohardness measurement.

3.3. Microstructural assessment techniques

3.3.1. Optical Microscopy (OM)

Optical microscopy (OM) is usually the preferred starting tool for microstructural assessments at low magnifications. In the present study a Leica DMI 5000M reflected light

optical microscope fitted with Leica DFC280 digital camera was used for capturing and processing of optical images through the Leica Application Suite software. This is an inverted microscope and so only the sample surface facing the objective lens needs be perfectly flat. The microstructural assessments were conducted in the bright field (BF) mode where the polished surface appears bright and surface irregularities such as grain boundaries, precipitates, inclusions, slip bands, pit etc. appears dark as their reflected light does not go back to the objective. The micrographs were captured at different levels of magnifications to allow effective analysis of the features of interest.

3.3.1.1. Sample preparation procedure

The dependence of OM on reflected light requires a well-polished surface 'mirror finish' and features that are well defined. This is achieved through a number of sample preparation treatments which in the present study included;

Sectioning: samples were extracted from the bulk material or from the deformed specimens by wire EDM. The average roughness (R_a) of the resultant surface was around 3.3μm for sectioning based on 3mm diameter wire.

Mounting: to ease handling of the extracted samples they were hot-mounted using phenolic thermosetting resin which is electrically conductive and thus allowed samples to be examined also in an electron microscope without any charging effects. The mounting was performed at 0.21MPa using 25mm diameter mounts and a maximum moulding temperature of 150°C, with the whole process taking 15min per sample. Only samples <25mm long were mounted and subsequently prepared on automated machines, while longer samples were not mounted and their preparation was carried out manually.

Grinding: the mounted samples were ground sequentially using increasingly fine SiC grinding paper. Grinding which was meant to remove the damaged layer introduced at the sectioning stage was conducted on a Buehler semiautomatic grinding machine under

the conditions given in Table 3.1. Several samples were ground together under similar conditions. A contra-rotation at 150rpm was maintained between the grinding platen and the sample holder with running water used for both cooling and lubrication purposes. After each grinding stage the samples were thoroughly rinsed in running water so as to remove all the loose particles on the surface before commencing the subsequent grinding stage at a different grit size.

Table 3.1: Grinding conditions adopted in the current study.

Grinding paper	Grit size/μm	Applied load/sample	Time/min.
P220	68	10N	5
P500	30	10N	5
P800	22	10N	5
P1200	14	10N	10
P2500	8.5	10N	10

Polishing: the ground samples were ultrasonically cleaned for 5 minutes in water containing ordinary washing detergents to ensure all remnant loose particles from the grinding process were removed. This was followed by a two-step polishing process aimed at removing grinding artefacts but very little material. This was conducted on Struers TegraForce-5 automatic machine using metal-backed napped cotton (MD-Nap) cloths impregnated with diamond abrasives. The polishing conditions summarised in Table 3.2 were carried out under a high viscosity propylene glycol-based lubricant (RedLube^{TM}) at 150rpm with contra-rotation between the sample holder and the polishing platen. Moderate injection rates were maintained for both the diamond suspension and the lubricant throughout the polishing process. After each polishing step samples were thoroughly cleaned in running water, rinsed with isopropanol and air dried before their surface conditions were checked under a low magnification microscope to ensure they were as free as possible from any preparation-induced artefacts. Care was taken not to contaminate polishing cloths at each step with different particle sizes. Detailed information on sample preparation for metallographic examination can be found in [136].

Table 3.2: Polishing conditions based on diamond particle suspensions.

Particle size/μm	Applied load/sample	Time/min.
6	10N	10
1	10N	20

The final preparation procedure performed on the polished samples was dependent on the subsequent characterisation technique to be employed. For OM, room temperature electrolytic etching was used, to highlight special features in the steels currently studied. For as-received steels (see later in Chapter 4) an electrolyte consisting of 60% nitric acid applied at 2V potential for 5 seconds yielded good results while for the service-aged steel an electrolytic etching at 6V potential for 5 seconds using an electrolyte comprising of 10% oxalic acid was found to be satisfactory. Nitric acid electrolytic etching on service-aged steel resulted in a preferential attacks within some grains.

3.3.2. Scanning Electron Microscopy (SEM)

Microstructural examination at resolutions better than those attained in OM are achieved under SEM which uses a beam of electrons of much shorter wavelength than that of the visible light. The SEM uses secondary electrons (SEs) produced at the beam's interaction volume (see section 2.4.3.1) for topographical imaging and so its resolving power is in the order of a few nanometres. It also has deeper depth of field than OM thus allowing observation of topographical features without losing focus. The spatial resolution of an SEM is a function of the probe size and usually improves with increasing beam energy since it can then be focused into a smaller spot. However, the increased interaction volume at higher energies, due to deeper penetration, degrades the image resolution owing to the increased SEs production by the backscattered electrons (BSE) from regions far outside the one defined by the incident probe. SEs images taken at 5keV are usually satisfactory [137].

In the present work a FEGSEM (Zeiss Supra 55VP) operated at 5keV with a 30μm objective aperture was used in the SE imaging mode for the microstructural examination of the etched samples and fractured surfaces. When the SEM was used to examine the presence and distribution of precipitates in Type 316 stainless steels, the samples were ground and polished following the procedure outlined for the OM samples, but the final preparation stage entailed electropolishing at room temperature for 60-120 seconds at 22V potential using Struers A21 electrolyte. This treatment highlighted both intra- and intergranular precipitates, facilitating good SE imaging, while at the same time removing most of the preparation-induced surface deformation, as is required for good diffraction of backscattered electrons. Further details on electropolishing are provided in section 3.4.1.2.

3.3.3. Energy Dispersive X-ray Spectroscopy (EDS)

EDS is an analytical tool for near surface chemical characterisation of materials. It works on the principle that each atom produces a characteristic X-ray photon on interacting with a high energy beam of electrons. By analysing the emitted X-rays, a qualitative and quantitative chemical analysis can be obtained [137]. The EDS detector used in the present study was an X-Max 50mm^2 attached to the Zeiss Supra 55VP FEGSEM. The measurements were conducted in spot mode on various microstructural features such as inter- and intra-granular precipitates, at an accelerating voltage of 20keV using a 30μm objective aperture and a working distance of 8.5mm. The spectra were acquired and analysed using Aztec software [138].

3.3.4. Optical Emission Spectroscopy (OES)

OES is an analytical tool for chemical characterisation of bulk material. The technique works through excitation of atoms by a high energy spark produced between the sample and an electrode. The excited atoms emit characteristic light whose wavelengths are unique to the particular elements of interest. The linear variation of the emitted lights

intensities with elemental concentrations [137] allows both qualitative and quantitative compositional analysis via calibration curves. The technique gives a reflection of the bulk composition since it analyses a certain amount of material ablated from the sample by spark discharges over a relatively large surface area ~1cm^2 [137]. In the present work the OES analysis was mainly used for the determination of bulk elemental composition of the service-aged steel. The analysis was conducted externally at Inspiratech 2000 Ltd.

3.3.5. Transmission Electron Microscopy (TEM)

TEM allows microstructural characterisation at higher resolution than those attainable with SEM. It works by directing a focused beam of electron onto a thin (<200nm) sample. The transmitted, elastically and inelastically scattered electrons (see Fig. 2.13) are directed onto a detector through a series of electromagnetic lenses, to provide both imaging and diffraction information. In the diffraction contrast mode, structural defects can be imaged due to scattering of the incident electron wave. The transmitted and diffracted beams form the bright field (BF) and the dark field images, respectively. In the diffraction mode, an electron diffraction pattern from a selected area illuminated by the electron beam is projected onto a detector enabling crystal structure analysis.

The lateral spatial resolution of TEM increases with the accelerating voltage due to a reduction in the electron wavelength. The resolution is improved by using thin samples which limits the electron scattering and thus the spread of the probe as it traverses the thin sample. The depth resolution is limited since image information originating from a three-dimensional sample is projected onto a two-dimensional detector plane which superimposes the microstructural features along the beam direction at the image plane. Nevertheless, it is possible to obtain limited depth information through sample tilting. The other main limitations of the TEM are its small sampling area which may not be representative of the bulk, their image interpretation which requires considerable expertise,

the damage of the sample due to high energy electron beam and the specimen preparation required, which may lead to modification of the original microstructure.

In the present study a JEOL JEM 2100 transmission electron microscope with a LaB_6 emitter and a maximum lateral resolution of 0.25nm was used. It was operated at 200keV with images acquired using a Gatan Orius SC1000 digital camera mounted in-line with the TEM optics. TEM was mainly used to characterise the dislocation structures in the deformed specimens. On each sample the measurements were done at different locations and with different imaging vectors using a double tilt specimen holder. This was to increase the statistical representation of the bulk and also to ensure dislocations of different Burger's vectors were account for. Imaging was carried out in the BF mode and the corresponding diffraction pattern recorded using selected area diffraction mode.

In order to produce electron transparent samples for TEM studies the following preparation procedure was adopted;

Sectioning: this entailed machining 0.3mm thick slices from the deformed specimens by wire EDM.

Punching: this was performed using a Gatan Disc Punch model-659 which produced 3mm diameter discs from the sectioned slices to fit appropriately in the standard TEM specimen holders.

Grinding: this was carried out using a Gatan Model 623 disc grinder and involved fixing the punched discs onto a specimen mount, using a low melting point wax, and grinding sequentially, using 40μm, 15μm and 5μm grit SiC paper lubricated with water. This was followed by re-melting the wax, turning over the discs, re-affixing, and grinding their other side until a thickness of about 100μm was achieved. It is not advisable to produce very thin discs as the preparation-induced deformation could spread throughout the thickness, distorting the original dislocation structures.

Electropolishing: this was performed on a Metalthin Mk4 machine designed to constantly bombard the sample on both sides with a jet of electrolyte while maintaining a potential difference on it. The electropolishing was carried out at -50±5°C using a potential difference of 20V and an electrolyte consisting of 5% perchloric acid in methanol. The process was terminated when a hole was created on each sample.

3.4. Strain assessment technique

3.4.1. Electron Backscatter Diffraction Technique (EBSD)

EBSD was used in the current study to characterise plastic and creep strain in Type 316 stainless steels deformed under controlled conditions. The objective was to develop an EBSD-based strain assessment technique. The working principle of the technique was explained in Chapter 2 and this section will be devoted to the experimental and data analysis aspects.

3.4.1.1. Sample extraction

The EBSD samples were extracted from the deformed specimen gauge length (*L*) by wire EDM at 0.5L and 0.3L for tensile and compression specimens, respectively. These were regions where average specimen deformation was expected and the measurements were conducted on the mid-planes parallel (*PL*) and normal (*NL*) to the loading direction as shown in Fig. 3.9.

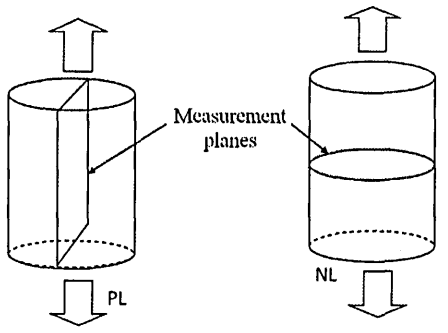

Fig. 3.9. Schematic drawing showing EBSD measurement planes parallel (PL) and normal (NL) to specimen loading direction.

3.4.1.2. Sample preparation

EBSD is a surface sensitive technique since signals collected come from the top few nanometres of material and so it requires a preparation procedure that minimises the preparation-induced surface deformation. To achieve this, the samples were ground and polished following the procedures outlined for the electron microscopy samples. The final preparation step involved electropolishing even though colloidal silica treatment was also experimented with but yielded a surface with a relatively high level of surface deformation than an electropolished surface.

The electropolishing was conducted using a Struers LectroPol-5 machine and the main parameters controlled were the electropolishing time, voltage and temperature. A standard electrolyte consisting of ethanol, 2-butoxyethanol, perchloric acid and water (Struers A21) was used and its temperature maintained at about 24°C during the process. The electropolishing voltage of 22V was selected from the plateau of the current versus voltage curve (see Fig. 3.10) generated by the machine. The process was carried out for 120 seconds, which was found to be adequate to give a relatively flat surface. The electropolishing area was limited to 0.8cm^2 on all samples through masking the unwanted regions with a chemical resistant tape. The theory behind electropolishing and colloidal silica polishing is briefly given in section 2.4.4.1.

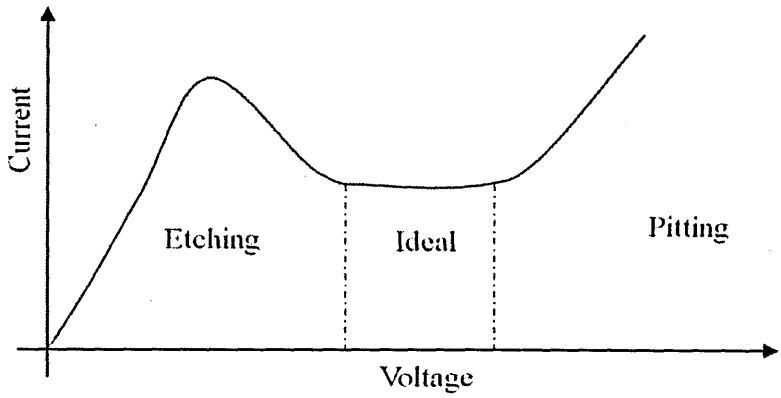

Fig. 3.10. Schematic drawing showing an ideal electropolishing curve where low and high voltage leads to etching and pitting, respectively [93].

3.4.1.3. EBSD measurements settings

In the present work the EBSD measurements were made on a Zeiss Supra 55VP FEGSEM fitted with a NordlysF EBSD detector. The data acquisition was carried out using HKL fast acquisition software [103]. The measurements were performed using an accelerating voltage of 20keV, a working distance (WD) of 15±0.1mm, a detector distance (DD) of 15mm and a 120μm objective aperture in the high current mode on samples pre-tilted by 70° from horizontal. Based on the Faraday cup measurements the probe current was around 9.5nA. All measurements were performed in the beam scanning mode under dynamic focus conditions using SEM magnification of x400.

Orientation maps based on iron *f.c.c* crystal structure (Space Group 225, F m3m) were obtained from all deformed samples over an area 700μm x 700μm using 1μm step-size in a square grid and each took about 2 hours. The relatively large area measured in the current study was necessary to accommodate the deformation inhomogeneity as seen in Fig. 5.5. Only maps with more than 100 grains (good statistical representation of an infinite population of grains) and indexing rates >96% were used for the strain analysis. For multiple measurements on the same sample, the SEM stage was programmed to shift automatically to a new location once the previous measurements were done. This movement was only limited to the *x*-direction of the stage in order to maintain the WD and the image focus since the sample was tilted.

For *in-situ* EBSD measurements, the DD was increased to 30mm to accommodate the *in-situ* device in the SEM chamber and the measurement area was reduced to 350μm x 350μm to allow the whole test program to be completed within a reasonable time (about 10 hours).

3.4.1.4. Optimisation of EBSD measurement parameters

The EBSD parameters adopted in the current study were derived from an optimisation process based on unstrained service-aged steel and a germanium single

crystal. The EBSD measurements were performed on the same region under different settings as summarised in Table 3.3.

Table 3.3: EBSD measurement parameters studied and the associated KAM_a values.

Sample	BD	HR	CB	FA	IR/%	AT/ms	AS/μm	AV/kV	KAM_a
Aged 316H	5-7	60	4x4	4	99	16.2	120	20	0.335
Aged 316H	5-7	80	4x4	4	99	16.2	120	20	0.305
Aged 316H	5-7	100	4x4	4	99	16.2	120	20	0.335
Aged 316H	**5-7**	**120**	**4x4**	**4**	**99**	**16.2**	**120**	**20**	**0.286**
Aged 316H	6-8	120	4x4	4	98.7	16.4	120	20	0.279
Aged 316H	9-11	120	4x4	4	95.8	16.5	120	20	0.268
Aged 316H	3-5	120	4x4	4	99.5	16.2	120	20	0.328
Aged 316H	5-7	120	2x2	4	99.2	72.5	120	20	0.276
Aged 316H	5-7	120	4x4	6	99.1	24.2	120	20	0.280
Aged 316H	5-7	120	4x4	8	99	32.2	120	20	0.283
Aged 316H	5-7	120	4x4	4	99.6	80.6	60	20	0.290
Aged 316H	5-7	120	4x4	4	98.3	16.2	120	17	0.307
Aged 316H	5-7	120	4x4	4	99	32.2	120	15	0.322
Germanium	5-7	120	2x2	4	98	32.4	120	20	0.243
Germanium	5-7	120	4x4	4	98.2	16.1	120	20	0.280

Unstrained service-aged steel used; Parameters in bold were adopted in the present study; Abbreviations explanation given in text;

The settings that yielded the lowest KAM_a value were selected since for a perfect crystal the mean spread in orientation about each point in the grain should theoretically be zero. However, as seen in Table 3.3, a finite minimum value of KAM_a was measured due to the limitation of the angular resolution of the standard EBSD system as explained in section 2.4.4.3. The measured KAM_a reduces with increases in the number of bands detected (BD), the Hough resolution (HR), the number of frames averaged (FA), the aperture size (AS), the accelerating voltage (AV) and as the camera binning (CB) is reduced. The conditions highlighted in Table 3.3 are the best compromise for high angular resolution (i.e. relatively low KAM_a), high indexing rate (IR) and low acquisition time (AT) per measurement point and were used in the present study. KAM_a values from an unstrained germanium single crystal and unstrained service-aged steel were very similar confirming that for the undeformed material, KAM_a is mainly determined by the accuracy of the orientation measurement. The small differences in their KAM_a values can be

attributed to differences in their sample preparation, mechanical history and the number of crystals analysed. KAM_a from the strain free germanium single crystal was therefore used as a measure of the orientation 'noise' in the current measurements.

3.4.1.5. EBSD data analysis

The post-processing of the EBSD raw data was carried out using HKL Channel-5 software [133]. One of the pieces of information contained in the raw data collected at each measurement point is its orientation with respect to the specimen coordinate system. In the present study the orientation data was used in the assessment of both plastic and creep strains, and no data cleaning was performed to avoid losing details associated with the deformation. In this section an explanation is given on how the raw data were processed to obtain quantifiable values representing the relative orientation changes as a function of the induced strain. In this thesis, average metric's values from at least four orientation maps are reported.

(a) Local misorientation measurement by Kernel Average Misorientations (KAM)

The orientation data were collected in a square grid pattern giving a finite number of equidistant measurement points. KAM is an in-built metric in HKL Channel-5 software that assigns an average misorientation to every measurement point in an orientation map derived from the mean misorientation between the point and its neighbouring points. In the present study the KAM was computed using a 3x3 kernel for all misorientations in the range 0°-2°. As explained in section 2.4.5.2, misorientations >2° are associated with the subgrain and grain boundaries and the higher kernel sizes conceals the local deformation information. The amount of KAM data (n) in an orientation map was given by:

$$n = \left(\frac{L}{\varsigma}\right) * \left(\frac{W}{\varsigma}\right) * IR \qquad \text{Eq. 3.4}$$

where L and W are the length and width of an orientation map while ş and IR are the measurement step-size and the percentage indexing rate, respectively. The data were binned using 0.1° class width giving 20 classes between 0°-2°. It was exported into an excel spreadsheet where the absolute frequencies (f) in each class (i) and the corresponding midpoint misorientation values were used to calculate the overall Kernel Average Misorientation (KAM_a) in an orientation map. Reducing the binning interval increases the number of classes and thus the 'noise' in the distribution as seen in Fig. 3.11. An example of KAM data obtained under the current measurement conditions is given in Table 3.4.

Table 3.4: Frequency distribution of KAM data binned at 0.1°.

KAM/deg Midpoint	Absolute frequency	KAM/deg Midpoint	Absolute frequency	KAM/deg Midpoint	Absolute frequency	KAM/deg Midpoint	Absolute frequency
0.05	3456	**0.55**	33115	**1.05**	3572	**1.55**	188
0.15	63029	**0.65**	18224	**1.15**	2201	**1.65**	112
0.25	144347	**0.75**	11389	**1.25**	1377	**1.75**	68
0.35	120544	**0.85**	7570	**1.35**	764	**1.85**	35
0.45	67114	**0.95**	5359	**1.45**	403	**1.95**	12

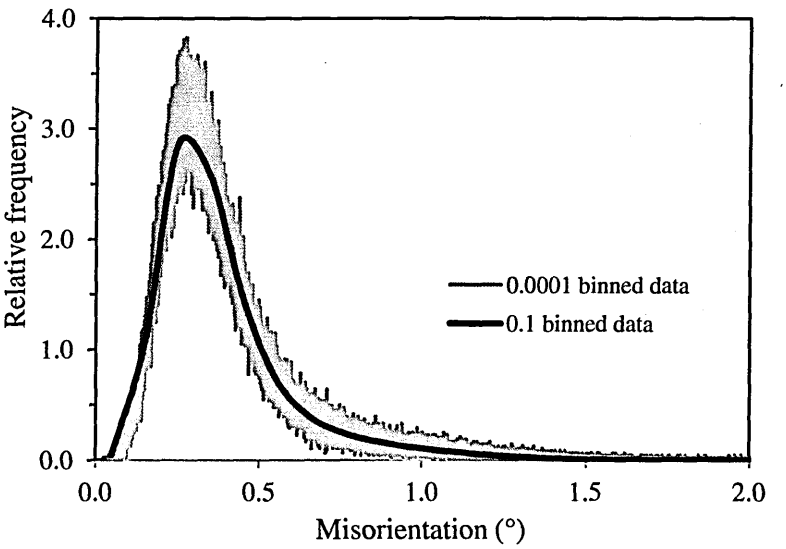

Fig. 3.11. Distribution of KAM data showing increased 'noise' at 0.0001° than at 0.1° binning.

The simplest way of calculating KAM_a was through arithmetic mean of the KAM frequency distribution using:

$$KAM_a = \frac{\sum_{i=1}^{i=20} f_i * KAM_i}{n} \quad \text{Eq. 3.5}$$

However this computation did not provide any information concerning the nature of misorientation evolution with the strain. The KAM_a was therefore expressed as the mean of a theoretical probability density function (PDF) that best fitted the KAM frequency distribution at a given strain level. This reduced the sensitivity of the KAM_a values to erratic variations in the KAM data and enabled the prediction of their values through modelling of the misorientation behaviour with the strain.

The KAM distributions at different strains were therefore compared with a variety of theoretical skewed PDFs including Rayleigh, log-logistic, Weibull, lognormal and gamma distributions. The lowest statistical variances were given by the gamma and lognormal PDFs which were then used to fit the KAM frequency distributions from the orientation maps. The gamma distribution is given by:

$$f(x; s, \Lambda) = \frac{1}{\Lambda^s \Gamma(s)} x^{s-1} e^{\frac{-x}{\Lambda}} \quad \text{For } x \geq 0 \text{ and } s, \Lambda > 0 \quad \text{Eq. 3.6}$$

where x is the variable (the KAM value in present case); s is the shape parameter; Λ is the scale parameter and Γ is the gamma function [139]. The lognormal distribution takes the form:

$$f(x; \mu, \delta) = \frac{1}{x\delta\sqrt{2\pi}} e^{\frac{-(lnx-\mu)^2}{2\delta^2}} \quad \text{For } x > 0 \quad \text{Eq. 3.7}$$

where μ and δ represents the logarithmic mean and the standard deviation of the distribution, respectively [140]. For the lognormal distribution the mean was given by:

$$KAM_a = exp\left(\frac{\sum_{i=1}^{n} ln\, x_i}{n} + \frac{\delta^2}{2}\right) \quad \text{Eq. 3.8}$$

and for the gamma distribution the mean was given by $KAM_a = s\Lambda$.

The precision of the theoretical PDF fitting was judged using both the statistical variance from the experimental KAM distribution and the linearity of probability plots as

will be discussed later in section 6.2.4.1. The KAM_a was calculated only from misorientations >0.15° to reduce the effects of orientation 'noise'. The change in KAM_a per unit strain was given by:

$$\Delta KAM_a/\varepsilon = \frac{KAM_{ah} - KAM_{a0}}{\varepsilon_h} \quad \text{Eq. 3.9}$$

where KAM_{a0} and KAM_{ah} represented the KAM_a values at 0 strain and higher strains, respectively while ε_h was the true strain corresponding to KAM_{ah}.

(b) Local misorientation measurement by Low Angle Misorientation Fraction (LAMF)

The low angle misorientation fraction was based on misorientation assessment between a measurement point and its neighbour to the right and one directly below it in an orientation map. The total number of misorientations was therefore double the number of measurement points in a map less the points with zero solution. In the HKL Channel-5 software the minimum grain boundary angle was set to 2° using the general preferences component and the software set to detect all misorientations >2° in the orientation data using the grain boundary component. The detected misorientation data were exported into an excel spreadsheet where LAMF was computed as follows:

$$LAMF = \frac{N(\theta_{2-15})}{N(\theta_{>2})} \quad \text{Eq. 3.10}$$

where $N(\theta_{2\text{-}15})$ is the number of misorientations with angles between 2°-15° and $N(\theta_{>2})$ is the total number of misorientations in the orientation map with angles >2°. The selection of these particular values was based on fact that a misorientation range of 2°-15° represented the evolution of low angle misorientations (LAM) with the increase in plastic strain well as seen Fig. 3.12. Also as discussed in Chapter 2, a misorientation of 2° is usually taken as the lower limit of a subgrain boundary and those >15° are regarded as high angle boundaries.

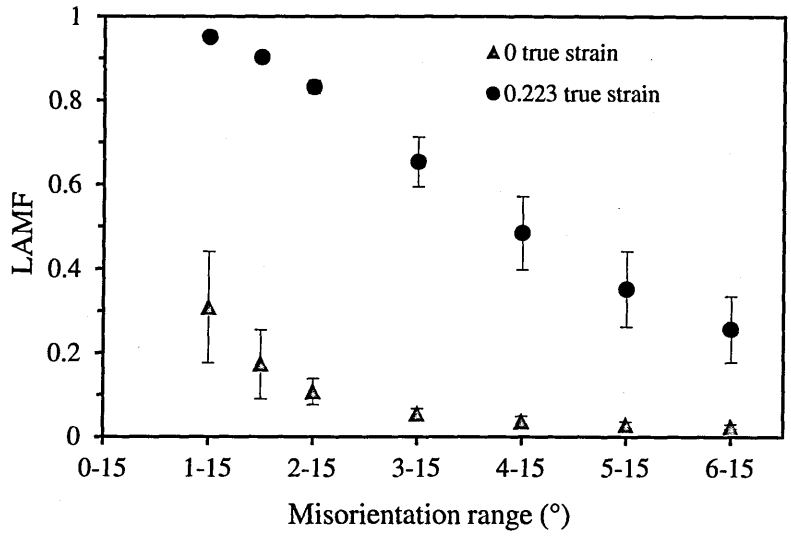

Fig. 3.12. LAMF versus included misorientation ranges for samples with 0 and 0.223 strain showing LAMF saturation beyond 2°-15° range.

(c) Long-range misorientation measurement by Average Intragrain Misorientation (AMIS)

The calculation of AMIS was based on the arithmetic mean of all spatially uncorrelated misorientations within each grain as explained in section 2.4.5.2.2. From the HKL Channel-5 software, the grain detection component was used to reconstruct all grains in an orientation map using a critical misorientation angle of 15°. All incomplete boundaries with misorientations starting from 0° were allowed to complete and twin boundaries were regarded. With these settings, the software generated the grain's statistic data for each orientation map analysed, giving information about the grains' areas, equivalent circle diameters (ECD), mean misorientations (Θ) and mean orientations. The data was exported into an excel spreadsheet and used to compute an overall average intragrain misorientation ($AMIS_a$) in an orientation map containing m grains using the following equation:

$$AMIS_a = \frac{1}{m}\sum_{j=1}^{m}\Theta_j \qquad \text{Eq. 3.11}$$

In this calculation, only grains with ECD >11μm were considered. This was mainly to avoid spurious grains arising from the incorrectly indexed points (see section 2.4.5) since no data cleaning was performed, but also to maintain consistency with the minimum grain size adopted for the steels studied (see later in section 4.3.2). At true strains above 0.1 some grains showed high orientation spread and their mean misorientations were determined through the procedures given in Appendix 1.

(d) Long-range misorientation measurement by Deformed Grain Fraction (DGF)

The calculation of DGF was based on the grain statistic data obtained in the computation of $AMIS_a$. The DGF was computed using an equation of the form:

$$DGF = \frac{m_d}{m_a} \qquad \text{Eq. 3.12}$$

where m_d is the total number of grains with Θ above the grain deformation threshold (Θ_d) and m_a is the total number of grains in an orientation map with ECD >11μm. The selection of Θ_d was based on the $AMIS_a$ of undeformed service-aged steel which was ~1.5. The selection of Θ_d should be such that it is above the misorientation level due to the orientation 'noise' in the data which in the current case was ~0.3°. Since the metric assesses the fraction of the deformed grains and not the severity of the deformation, it is less sensitive to local misorientations variations compared to the other metrics. Its strain sensitivity can be adjusted by changing the value of Θ_d.

(e) Measurements of Twin Boundary Fractions (TBF)

The perfect twin boundary is described by a misorientation of 60° about the <111> axis (see section 2.2.2). However, by introducing a tolerance angle of 8.66° [141] to the perfect twin boundary orientation, it is possible to use orientation mapping to identify all near-twin boundaries. In the current study, the assessment of TBF was based on the boundary component in HKL Channel-5 software, which identified all the near-twin

boundaries in an orientation map. The TBF was then calculated as the length fraction of the identified twin boundaries to the total lengths of all boundaries with misorientations >15° in a map.

(f) Effects of measurement step-size

The numerical values of both KAM_a and LAMF depend on the measurement step-size used since they are based on spatially correlated misorientations (see section 2.4.5.2.1). This was demonstrated by reconstructing the same orientation map from an unstrained sample using different step-sizes, which ensured that only effects due to the step-size change was investigated. As shown in Fig. 3.13, both LAMF and KAM_a increased almost linearly with the step-size while $AMIS_a$ and DGF remained constant as they are based on spatially uncorrelated misorientations. This underpins the importance of keeping the step-size constant when performing comparative misorientation studies among different samples.

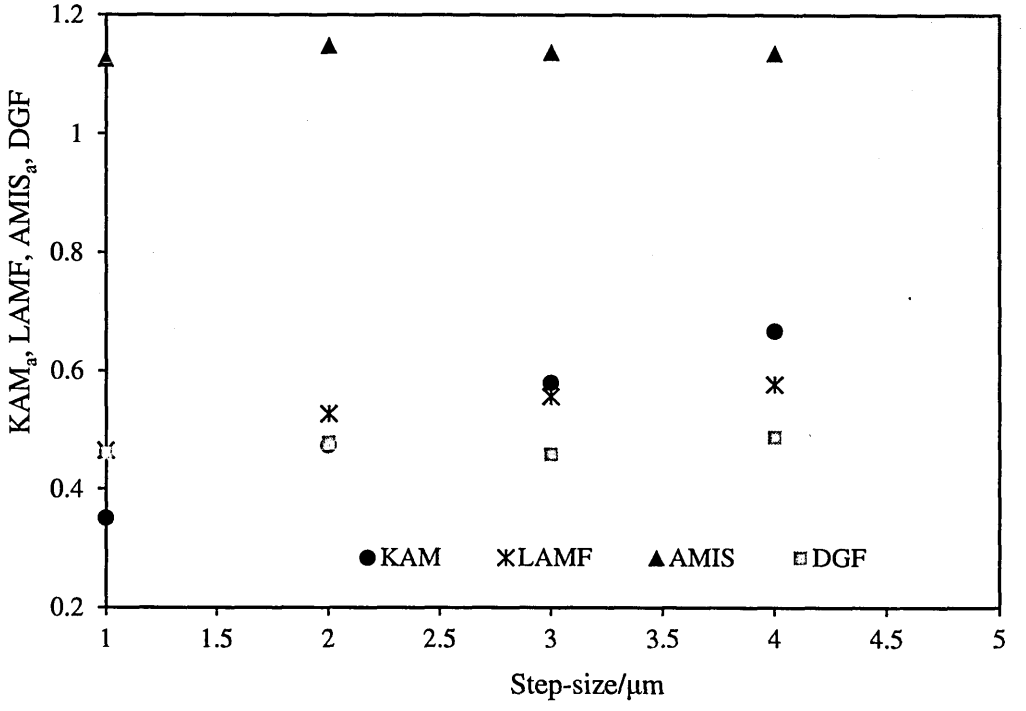

Fig. 3.13. Step-size dependence of the EBSD metrics as assessed from an undeformed stainless steel sample.

3.5. Summary

The key points in this chapter can be summarised as follows;

- The procedures used for mechanical testing to achieve repeatable and controlled deformation have been presented.
- The sample preparation procedures used for EBSD measurements were standardised to improve comparative misorientation studies.
- The microstructure assessment techniques selected to allow the examination of chemical, microstructure and dislocation structure of the deformed materials have been described.
- The methods adopted for analysing raw data from a commercial EBSD system have been outlined and discussed for the purpose of assessing strain in deformed material.

CHAPTER 4

MATERIAL CHARACTERISATION

4.1. Introduction

The materials studied in this work were made of AISI Type 316H austenitic stainless steel supplied in the form of an ex-service steam header, ex-service weldments, crept specimens and as-received steel bars and tubes. These materials are described in terms of their heat treatment histories, service histories, chemical compositions and their mechanical properties. The chapter provides details about grain size characterisation of the steels based on both Optical Microscopy (OM) and EBSD through Orientation Imaging Microscopy (OIM). It presents the deformed steels' microstructures and dislocation structures as examined through Scanning Electron Microscopy (SEM) and Transmission Electron Microscopy (TEM), respectively. Details are also provided about the local chemical composition of various microstructural features in ex-service steel based on Energy Dispersive X-ray Spectroscopy (EDS) and the bulk elemental composition derived from Optical Emission Spectroscopy (OES) analysis. The chapter concludes with a summary of the key findings.

4.2. Materials

The materials investigated within this work are summarised in Fig. 4.1 and their details provided in the following sections.

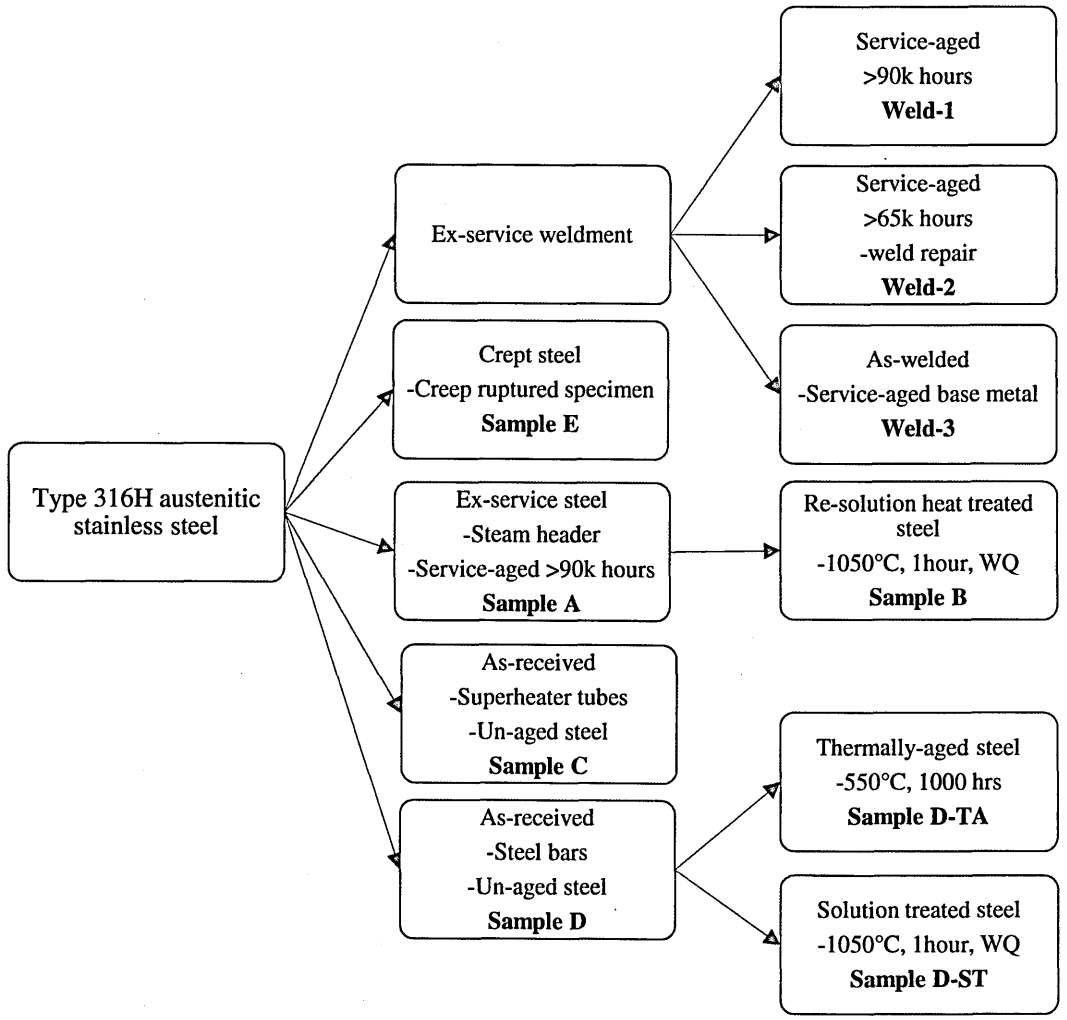

Fig. 4.1. Summary of Type 316H austenitic stainless steels studied (WQ: water quenched).

4.2.1. Ex-service Type 316H austenitic stainless steel

The ex-service steel available for the current study was part of a power plant steam header (HRA 2B2/1 cast 69431) (see Fig. 4.2a) supplied by EDF Energy and is denoted as "Sample A" in the present work. It was in service for 90,930 hours at about 516°C and under internal steam pressure of around 16MPa. Its internal diameter and thickness was 304.8mm and 63.5mm, respectively. The chemical composition in weight percentage of the header after service based on OES analysis is given Table 4.1. The specimens for mechanical testing were extracted from the marked blocks *HRA 1a*, *HRA 1b* and *HRA 1c* shown in Fig. 4.2b, which were located remote from the header's nozzle.

Table 4.1: Chemical composition (weight %) of service-aged Type 316H stainless steel.

C	Si	Mn	P	S	Cr	Ni	Mo	Al	Cu
0.066	0.42	1.00	0.029	0.015	17.82	11.81	2.33	0.003	0.23
Sn	**V**	**W**	**Co**	**Pb**	**B**	**N**	**Nb**	**Ti**	**Fe**
0.016	0.031	0.068	0.093	0.003	0.0051	0.096	0.007	0.004	Bal.

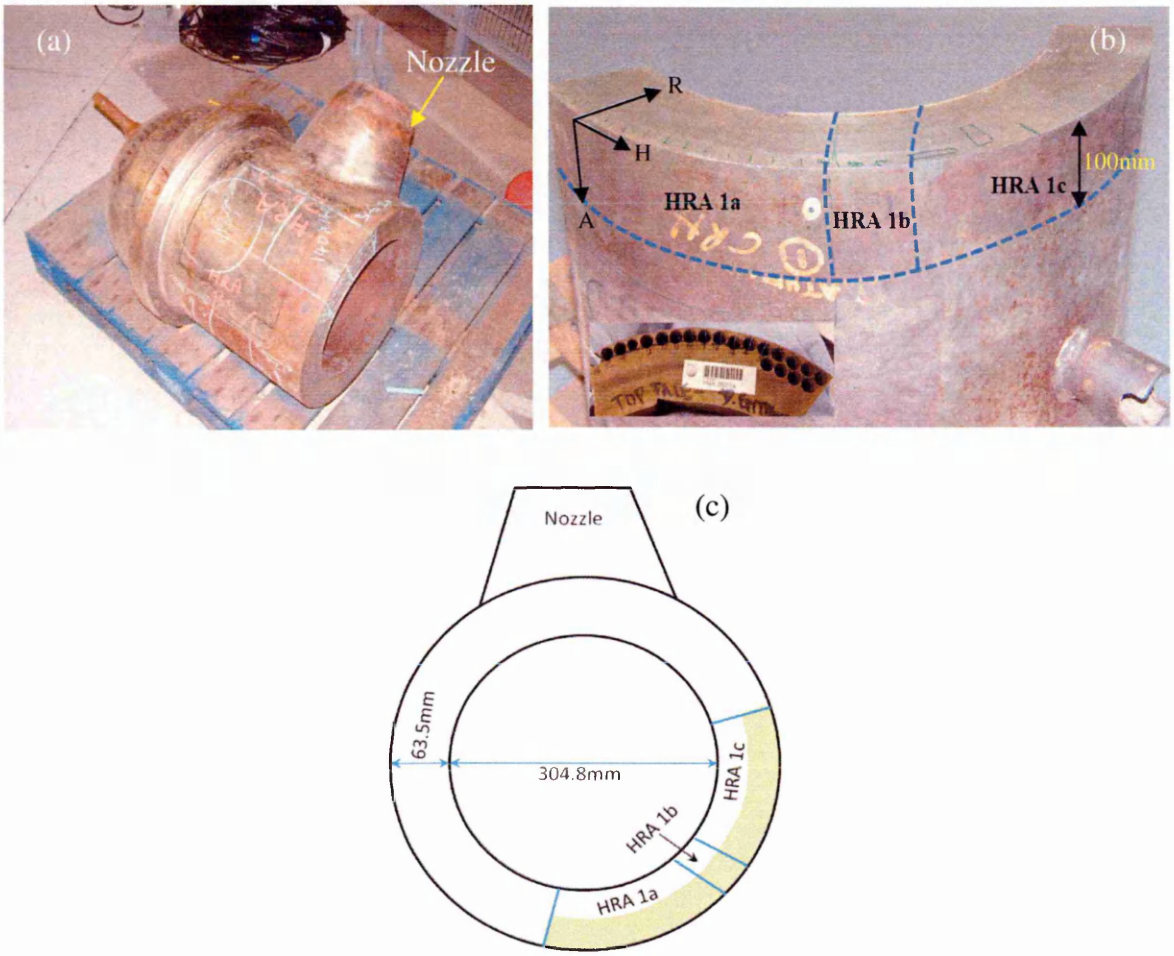

Fig. 4.2. Photographs of (a) service-aged Type 316H austenitic stainless steel steam header (Sample A) supplied by EDF Energy, (b) steam header section showing demarcation of three blocks used for specimens extraction as shown in the insert, and (c) schematic end view of (a) illustrating locations used for specimens extraction (shaded region). (RHA: Radial, Hoop and Axial directions).

Investigations were also conducted on Sample A material which was re-solution heat treated at 1050°C for 1 hour followed by water quenching. This material denoted as "Sample B" in the present work, was used in Chapter 5 to study the influence of both

carbide precipitation and grain size on the strain-induced misorientation development. Specimens derived from Sample A were used in Chapter 6 to investigate the development of strain-induced misorientations in materials that have seen long service life.

4.2.2. As-received Type 316H austenitic stainless steel

The influence of microstructure, thermal aging and grain size on the development of strain-induced lattice rotations was investigated in Chapter 5 by considering two types of steels which had not seen service. The first type, referred to as "Sample C" in the present work, was supplied by EDF Energy in the form of superheater tubes which were 38mm in diameter and 4mm thick. The tubes were manufactured through extrusion and solution annealed at 1100°C followed by water quenching. The tubes chemical composition in weight percentage is given in Table 4.2 (provided by Sandvik Material Technology Ltd).

The second type of steel, presently designated as "Sample D", was sourced from Power Metal Suppliers in the form of steel bars which were 12.5mm in diameter. The bars were solution annealed by the manufacturer at 1100°C for 90 minutes followed by water quenching before being cold drawn. Their chemical composition in weight percentage based on the EDS measurement is given in Table 4.2. In the present study, Sample D specimens which were thermally-aged at 550°C for 1000 hours followed by air cooling to ambient temperature are denoted as "Sample D-TA" while those which were solution treated at 1050°C for 1 hour followed by water quenching are designated as "Sample D-ST".

Table 4.2: Chemical composition (weight %) of un-aged Type 316H austenitic stainless steels and weld metal.

Material	C	Si	Mn	P	S	Cr	Ni	Mo	N	Co
Sample C	0.05	0.53	1.55	0.029	0.005	16.89	11.25	2.04	-	0.089
Sample D	0.08	0.5	0.7	0.04	0.05	17.2	10.0	1.94	-	-
Weld metal	0.03	0.28	1.16	0.01	0.012	18.4	12	2.6	<0.01	-

4.2.3. *Creep deformed Type 316H austenitic stainless steel*

Creep ruptured stainless steel specimens were supplied by EDF Energy for validation of the strain assessment methods developed here. These specimens, referred to in the current work as "Sample E", were deformed by the supplier at 550°C using the constant load creep conditions summarised in Table 4.3. The specimens had different amounts of prior and accumulated creep strains and were all made from cast 69431. The reported strain values were measured along the specimens' gauge lengths during the creep tests.

Table 4.3: Constant load creep data at 550°C for Type 316H austenitic stainless steel (*source EDF Energy*).

Test ID	Header	σ	$\dot{\varepsilon}_m$	ε_p	ε_c	ε_t	t_p	t_r
R0385	2C23	360	1.39E-07	0.133	0.080	0.213	29	79
IRD CWW	2B13 HAR	260	7.38E-09	0.024	0.103	0.127	550	2032
IRD CWP	2C23	240	3.36E-09	0.025	0.149	0.174	890	6839
R0453	2C23	200	3.02E-10	0.015	0.211	0.226	1448	6360
R0452	2C23	160	1.55E-12	0.001	0.002	0.003	2871	10760

(σ: applied stress/MPa, $\dot{\varepsilon}_m$: true minimum creep strain rate (s^{-1}), ε_p: true plastic loading strain, ε_c: true creep strain, ε_t: true total strain, t_p: time to primary creep end (hours), t_r: time to failure)

4.2.4. *Ex-service Type 316H austenitic stainless steel weldments*

Welding is one of the main methods used for joining structural components in many power plants. It is also employed for the repair of aged components already in service. In the current study, three categories of weldments supplied by EDF Energy were investigated. The weldments consisted of service-aged base metals welded together by manual metal arc (MMA) welding. The first category referred to as Weld-1 (see Fig. 4.3) in the present study, consisted of weldments that had been exposed to 90,930 hours of service at around 516°C as detailed in Table 4.4.

Table 4.4: Welding and service details of Type 316H stainless steel weldment (Weld-1) (*Source EDF Energy*).

Preparation	J
Geometry	Nozzle
Thickness	63.5mm sleeve, 62.7mm nozzle
Weld process	MMA
Weld metal	Babcock Type S
Condition	Ex-service with creep damage
Base metal service life	90,930 hours
Service temperature	516°C
Cast / Header	69431 / 2B2/1
Reactor -HRA	Hartlepool

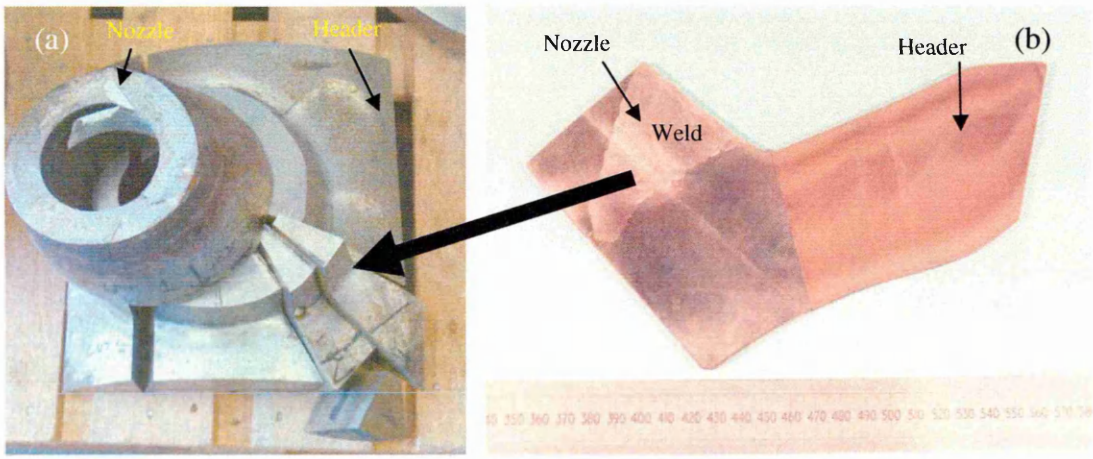

Fig. 4.3. Photographs of ex-service Type 316H stainless steel weldment (Weld-1) showing: (a) weld location on the component, and (b) the weld profile.

The second category denoted as Weld-2 (see Fig. 4.4) was composed of weldments that had been exposed to 65,015 hours of service at 490°C to 530°C followed by a single repair as detailed in Table 4.5.

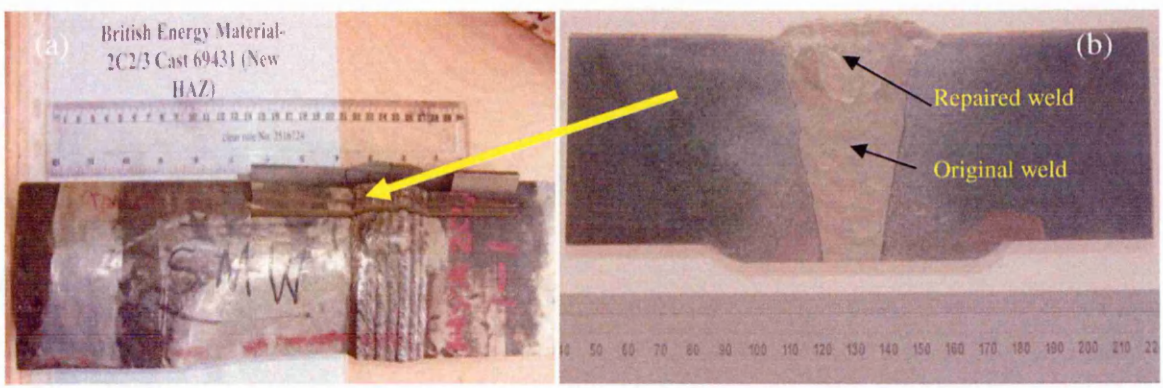

Fig. 4.4. Photographs of ex-service Type 316H stainless steel weldment (Weld-2) showing: (a) weld location on the component, and (b) the weld profile.

Table 4.5: Welding and service details of Type 316H stainless steel weldment (Weld-2) (*Source EDF Energy*).

Preparation	V and V root
Geometry	Girth
Thickness	63.5mm
Weld process	MMA
Weld metal	Babcock Type S
Condition	Repair welded
Comments	Repaired once, HAZ not removed
Repair depth	75% of original weld thickness
Repair length	100mm @ 45° tilt
Repair root	6mm
Number of beads repair 1 and 2	35 and 41
Base metal service life	65,015 hours
Service temperature	490-530°C
Service life after repair	0
Cast / Header	69431 / 2C2/3
Reactor - HYA	Heysham 1

The last category identified as Weld-3 (see Fig. 4.5) consisted of two service-aged steels (from headers 1D2/4 and 2D2/2) welded together by MMA as summarised in Table 4.6. The chemical composition in weight percentage of the weld metal is listed in Table 4.2. It is derived from the Babcock-S electrodes used in MMA welding and is typical of 316L austenitic steel weld filler. These weldments were used to assess the applicability of the strain characterisation methods developed in the current work, in estimating local strains in the HAZs of welds.

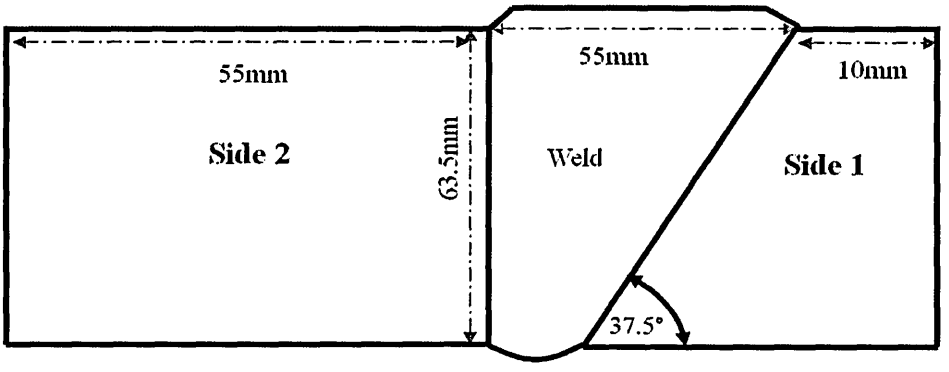

Fig. 4.5. Weld geometry of Type 316H stainless steel weldment (Weld-3).

Table 4.6: Welding and service details of Type 316H stainless steel weldment (Weld-3) (*Source EDF Energy*).

	Side 1	**Side 2**
Preparation	37.5° inclined face	straight (0°)
Geometry	Girth	Girth
Thickness	63.5mm	63.5mm
Outer diameter	430mm	430mm
Weld process	MMA	MMA
Weld metal	Babcock Type S	Babcock Type S
Pre-heat condition	19°C	19°C
Number of layers	26	26
Number of passes	129	129
Base metal service life	-	65015 hours
Service temperature	490-530°C	490-530°C
Weld service life	0	0
Cast	-	55882
Reactor - HYA	HYA 1D2/4	HYA 2D2/2

4.3. Material Characterisation

4.3.1. Tensile properties

The characterisation of tensile properties of the steels studied was based on a series of tensile tests carried out at room and at high temperature (550°C and 675°C) at a strain rate of $2.0x10^{-4}s^{-1}$ and $3.5x10^{-5}s^{-1}$, respectively. The testing details are provided in Chapter 3. The Young's modulus was calculated from the inclination of the linear-elastic region of the flow curves. The 0.2% and 1% proof stresses were determined by the intersection of a line offset by 0.2% and 1% true strain, respectively from the linear region of the curves shown in Fig. 4.6. The results are summarised in Table 4.7. The proof stress obtained in the current study agrees well with the reference values provided by EDF Energy for the same cast as Sample A. The proof stress reduced with increasing temperature and was higher in Sample A than in Sample B.

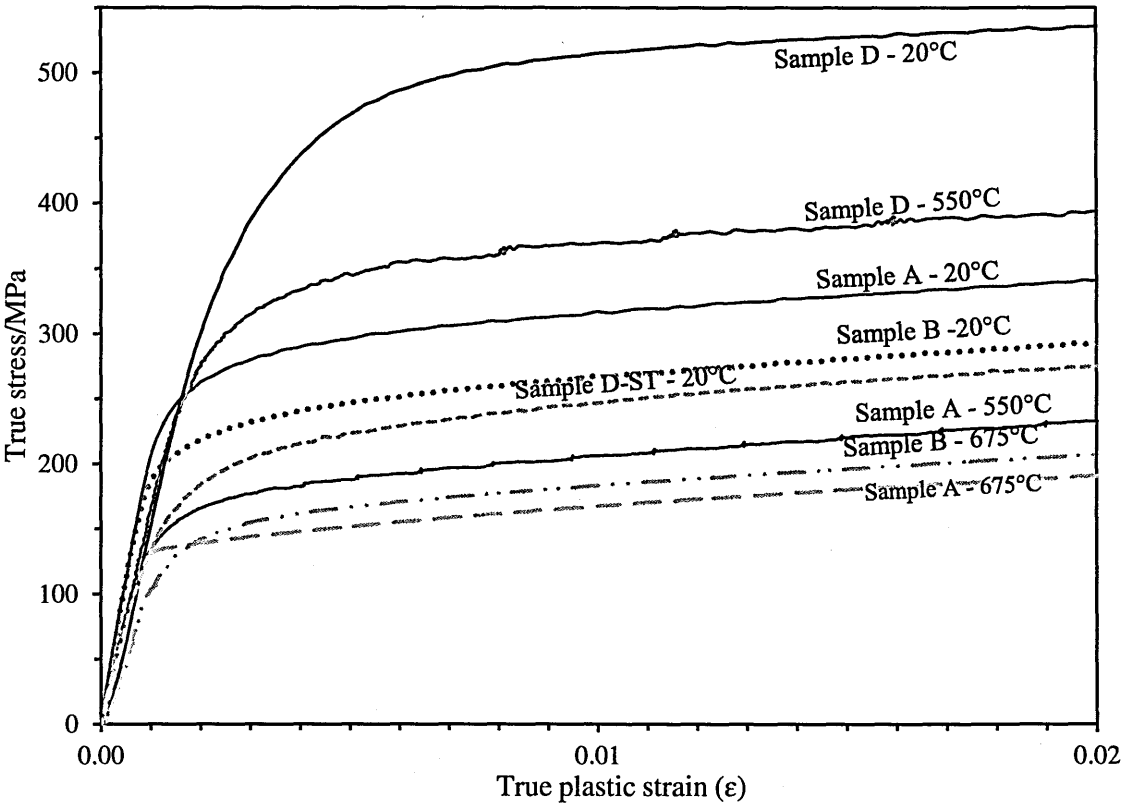

Fig. 4.6. Tensile flow curves at different temperatures for Type 316H stainless steels studied.

Table 4.7: Proof stress/MPa and Young's modulus/GPa of Type 316H stainless steels studied.

Temp. (°C)	Sample A	Sample B	Sample C	Sample D	Sample D-ST	Sample A reference
20	285[1]/325[2]/207[3]	225/275/193	*379[2]	450/520/174	210/250/163	-
550	185/230/158	-	*158[1]/*191[2]	330/380/165	-	180[1]/150[3]
675	165/175/151	155/190/130	-	250/280/131	-	-

*Key: [1]0.2% proof stress, [2]1% proof stress, [3]Young's modulus, *proof stresses provided by the manufacturer*

The mechanical properties of the service-aged steel (Sample A) showed no pronounced mechanical anisotropy relating to its yield stress when tested at room temperature under compression in hoop, axial and radial directions of the steam header as seen in Fig. 4.7. The isotropic properties can be attributed to weak texture (see Fig. 4.8) exhibited by Sample A based on crystallographic orientation assessment over an area measuring 11.7mm x 2.9mm.

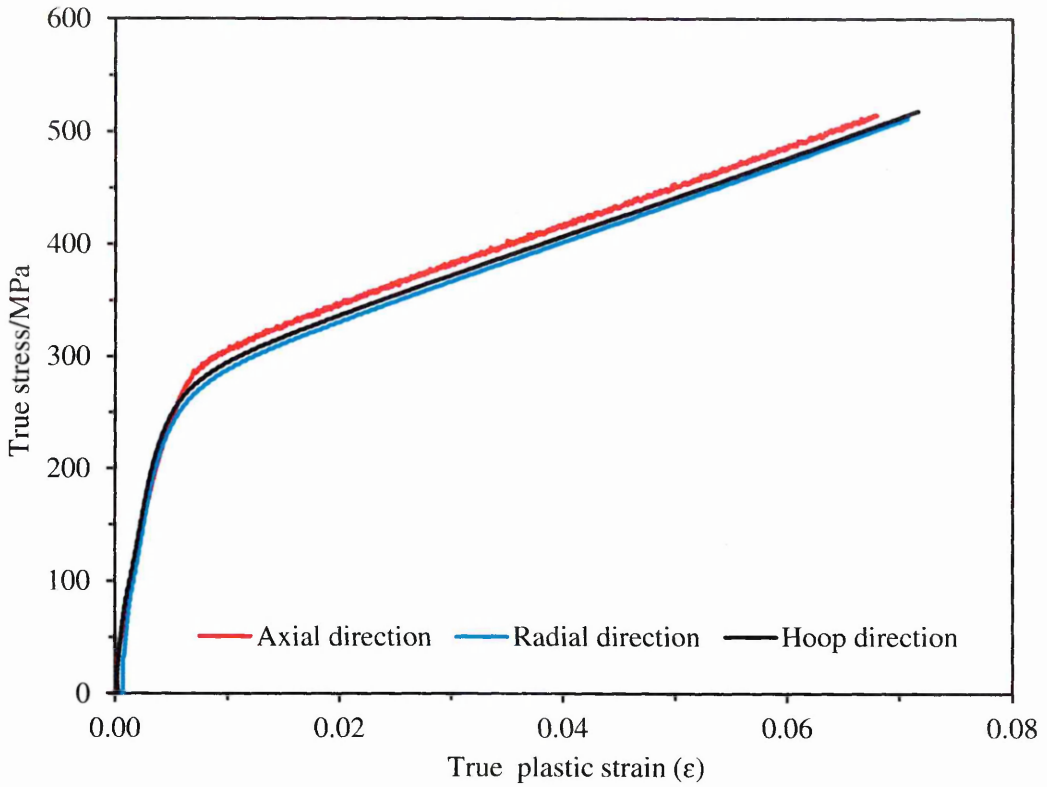

Fig. 4.7. Compressive flow curves for service-aged Type 316H stainless steel at 24°C exhibiting marginal mechanical anisotropy.

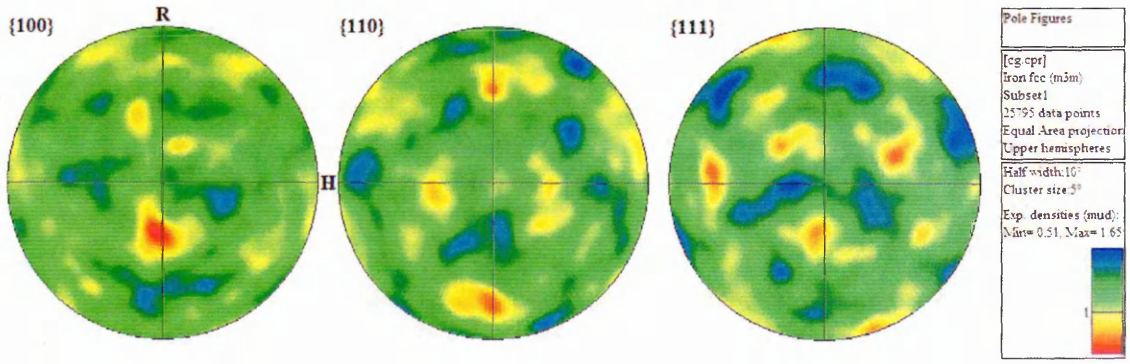

Fig. 4.8. Normalised pole figures plots of undeformed service-aged Type 316H stainless steel exhibiting weak texture with a maximum MUD of 1.65. (RHA: Radial, Hoop and Axial (centre) axes).

The flow curves of Sample D and Sample D-ST specimens (see Fig. 4.6) exhibited significant differences, indicating the presence of work hardening in Sample D. The

mechanical properties of Sample C were provided by the supplier as detailed in the test certificate given in Appendix 2.

4.3.2. Characterisation of average grain sizes

The influence of grain size on the misorientation development was investigated in the current study and therefore proper characterisation of the grain sizes in the steels studied was essential. The characterisation was based on both OM and OIM methods which required different sample preparation procedures as described in Chapter 3. For OM method it was necessary to etch the samples to reveal most of the grain boundaries, as shown in Fig. 4.9, while for the OIM method the aim was to obtain a pristinely flat surface with minimum preparation-induced plastic deformation.

The optical grain size determination was based on the linear intercept method as described in the ASTM Standard E112-12 [142]. The measurements were made using ImageJ software [143] and entailed superimposing straight test lines of known length (L) vertically and horizontally on the optical micrographs of known magnification and counting the total number of intersections (N) between the test lines and the visible grain boundaries. The spacing and lengths of the test lines was such that N was >50 in all micrographs examined. The grain size was expressed in terms of the mean lineal intercept (MLI) value using equation:

$$MLI = \frac{L_t}{N} \qquad \text{Eq. 4.1}$$

where L_t is the total lengths of all tests lines superimposed on the micrographs. The reported grain size represents the average intercept of a minimum of 500 grains.

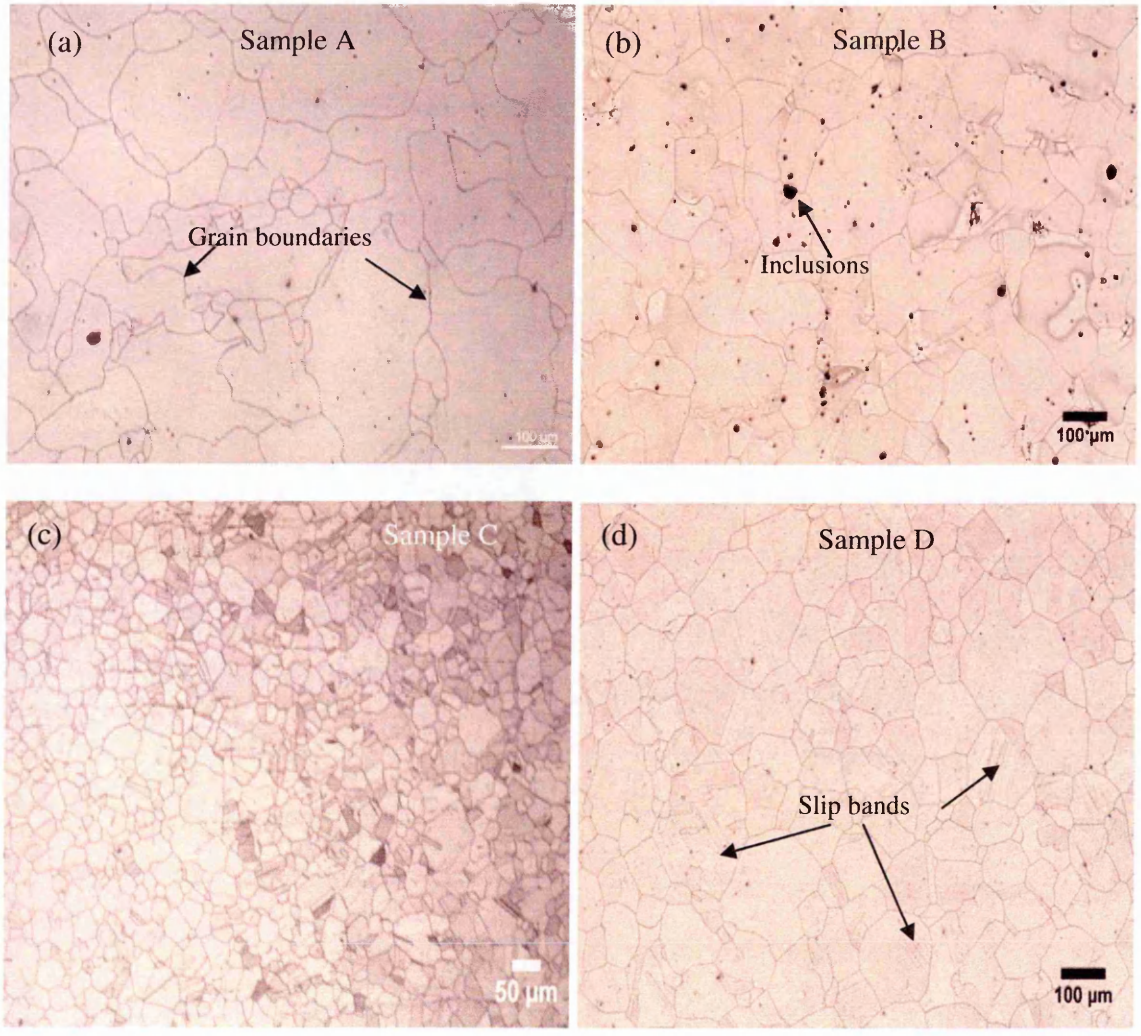

Fig. 4.9. Optical micrographs showing etched out grain boundaries used for grain size determination in Type 316H stainless steels studied. Slip bands and inclusions are evident within some grains as shown in (b) and (d).

The assessment of the grain size using OIM was based on the equivalent circle diameter (ECD) and the MLI methods. In both methods, orientation maps acquired at 1µm step-size at indexing rates better than 96% and containing >50 whole grains were used. The grain boundaries were defined by misorientation >15° (see section 2.4.5.2.1) and twin boundaries were disregarded. The grain size in terms of ECD was given by:

$$\zeta = \sqrt{\frac{4A}{\pi}} \qquad \text{Eq. 4.2}$$

where ζ is the grain size in micron and A is the grain area given by the total number of measurement points per grain. In the current study the grains were defined by a minimum of 100 measurement points as explained in section 3.4.1.5c and in [144].

The grain size assessment based on the MLI method also utilised the orientation maps on which several lines were drawn in both x and y directions and their intercepts with the grain boundaries counted. The distance between the superimposed lines was selected such that the oversampling of the large grains and missing out of smaller grains was minimised (see Fig. 4.10). The mean lineal intercept grain size (L_x) in x-direction was given by [74]:

$$L_x = \frac{R_x \varsigma P_x}{N_x} \qquad \text{Eq. 4.3}$$

where R_x is the number of rows scanned in the x direction, N_x is the number of complete boundaries intercepted, P_x is the number of pixels in the x direction and ς is the distance between pixels. The procedure was repeated in the y-direction and the corresponding mean lineal intercept grain size (L_y) determined. The overall grain size was then obtained from the mean value of L_x and L_y in each orientation map.

Fig. 4.10. Grain boundary orientation map showing vertically superimposed lines used for OIM-MLI grain size determination.

In the present study, the average grain sizes of Samples A, B, C and D based on the OM and OIM methods were comparable as seen in Table 4.8. To improve the comparativeness of the grain size determination among the steels studied, similar EBSD settings were used and more than 500 grains analysed in each case. The minimum grain size considered for Sample A, B, C and D based on ECD measurement was 11μm [144] but the maximum size obtained was 650μm, 563μm, 140μm and 355μm, respectively.

Table 4.8: Average grain size/μm for Type 316H stainless steels studied.

Method	Sample A	Sample B	Sample C	Sample D	Sample D-TA
OM -MLI	88±9	92±5	28±3	65±3	-
OIM -MLI	98±5	97±12	27±1	69±6	64±8
OIM -ECD	98±8	93± 12	35±1	73±6	73±5

Limit (±) at 95% confidence level

4.3.3. Characterisation of microstructures

The microstructural characterisation of the steels was performed using Zeiss Supra 55VP FEGSEM. The experimental procedures concerning sample preparation and imaging conditions are given in Chapter 3.

4.3.3.1. Microstructure assessment of Sample A and Sample B

The microstructure of Sample A exhibited extensive intra- and inter-granular precipitation as seen in Fig. 4.11a. The intergranular precipitate appeared relatively large with high aspect ratio compared to the intragranular precipitates which displayed a circular morphology. The observed morphologies are common in over-aged 316 steel [22, 26, 145]. The distribution of intragranular precipitates was not even on all grains as seen in Fig. 4.12. This could have resulted from the differences in nucleation and growth of precipitates between grains owing to differences in their deformation behaviour. It is possible that grains with higher overall Schmid factor accumulated more creep strain during service and thus had more nucleation sites for precipitation.

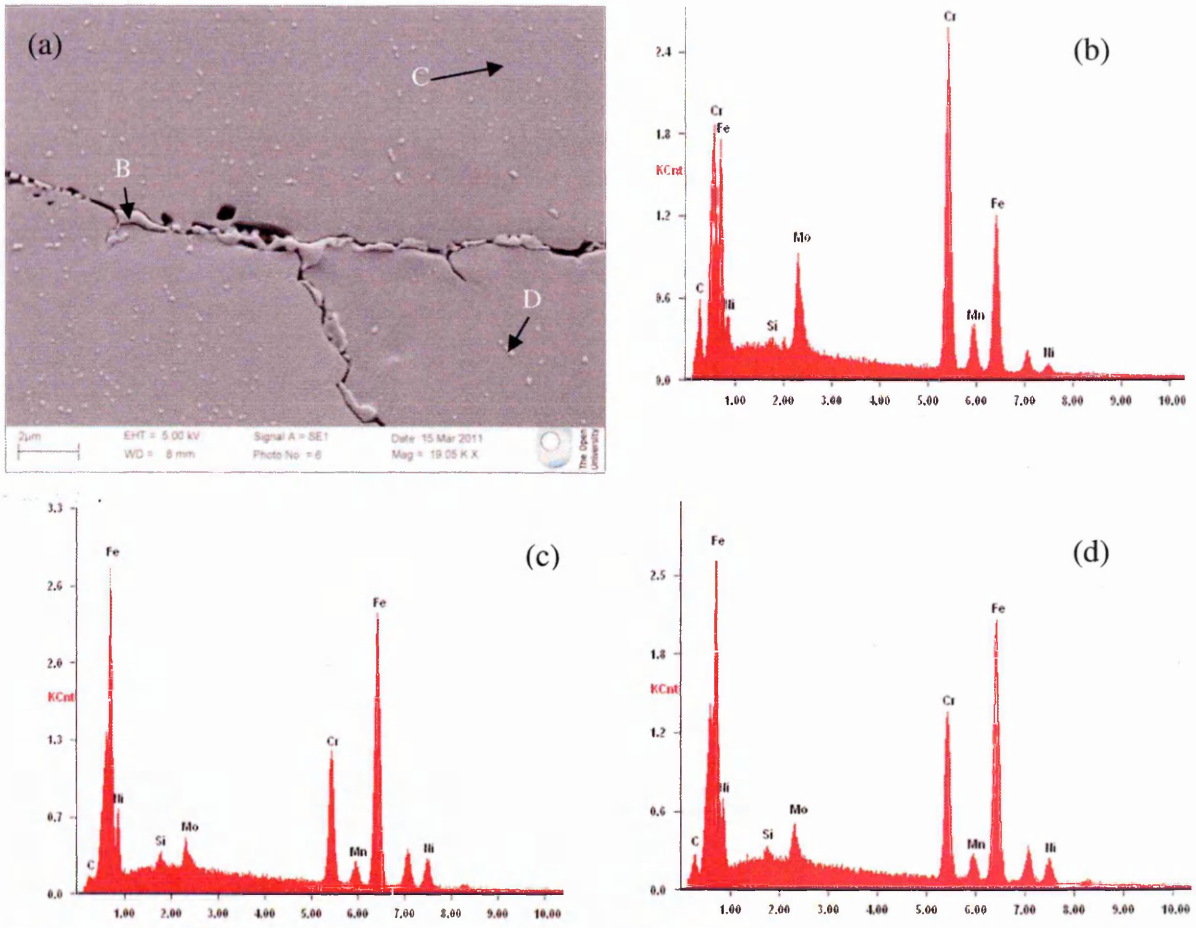

Fig. 4.11. (a) SEM micrograph of service-aged Type 316H stainless steel showing inter- and intra-granular precipitates with the mean compositions of regions marked B, C and D given in Table 4.9 and their corresponding EDS spectrum in (b), (c) and (d). Spectra display count per second/eV versus X-ray energies/keV.

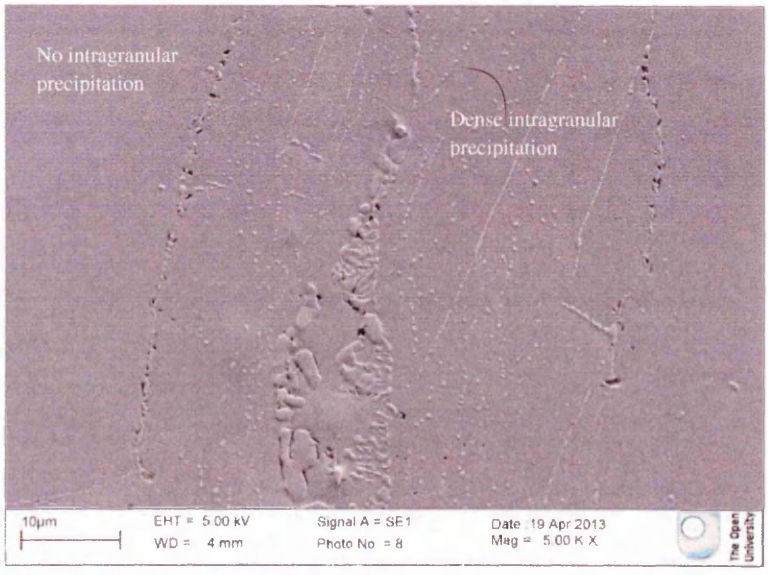

Fig. 4.12. SEM micrograph showing non-uniform distribution of intragranular precipitates in service-aged Type 316H stainless steel.

Based on the local EDS analysis, the mean concentration of Cr and Mo as measured from 5 different locations was higher on the intergranular precipitates than on the intragranular precipitates as shown in Table 4.9. This can be ascribed to the fact that Sample A was in service for more than 90,000 hours at around 516°C where the predominant carbides are $M_{23}C_6$ ($M = Cr, Fe, Mo$) for un-stabilised steel [26], which precipitate first at grain boundaries and then intragranularly [21, 22]. It should be noted that this assessment is unreliable for exact composition analysis of very small precipitates as the electron interaction volume incorporates a significant volume of the metal too.

The matrix carbon composition from the EDS analysis was significantly higher than that expected for 316H steel and this could have resulted from sample contamination during handling and also due carbon build up in the SEM chamber as result of hydrocarbon molecules breakdown on interaction with high energy beam of electrons (see section 2.4.4.3). However, from the high carbon content of the precipitates they may be assumed to be $M_{23}C_6$ carbides.

Table 4.9: Local composition of service-aged Type 316H stainless steel in regions marked in Fig. 4.11.

Elements	Bulk* composition	B Wt%	SD* Wt%	C Wt%	SD Wt%	D Wt%	SD Wt%
C	0.07	14.1	0.5	3.7	0.3	7.5	0.1
Si	0.42	0.4	0.1	0.6	0.1	0.5	0.1
Mo	2.33	5.4	0.2	2.6	0.2	2.7	0.2
Cr	17.82	29.9	0.2	18.5	0.2	19.1	0.2
Mn	1.00	0.9	0.1	1.1	0.1	1.0	0.1
Fe	65.95	43.1	0.3	63.7	0.3	67.0	0.3
Ni	11.81	6.2	0.2	9.9	0.2	9.7	0.2

**Bulk composition is based on OES analysis. SD: standard deviation*

The microstructure of Sample B as seen in Fig. 4.13a, was free of precipitates mainly due to solution treatment (ST). Sample B was therefore an ideal candidate material

for studying the effects of precipitation on the evolution of strain-induced misorientations since it had comparable composition and grain size to Sample A.

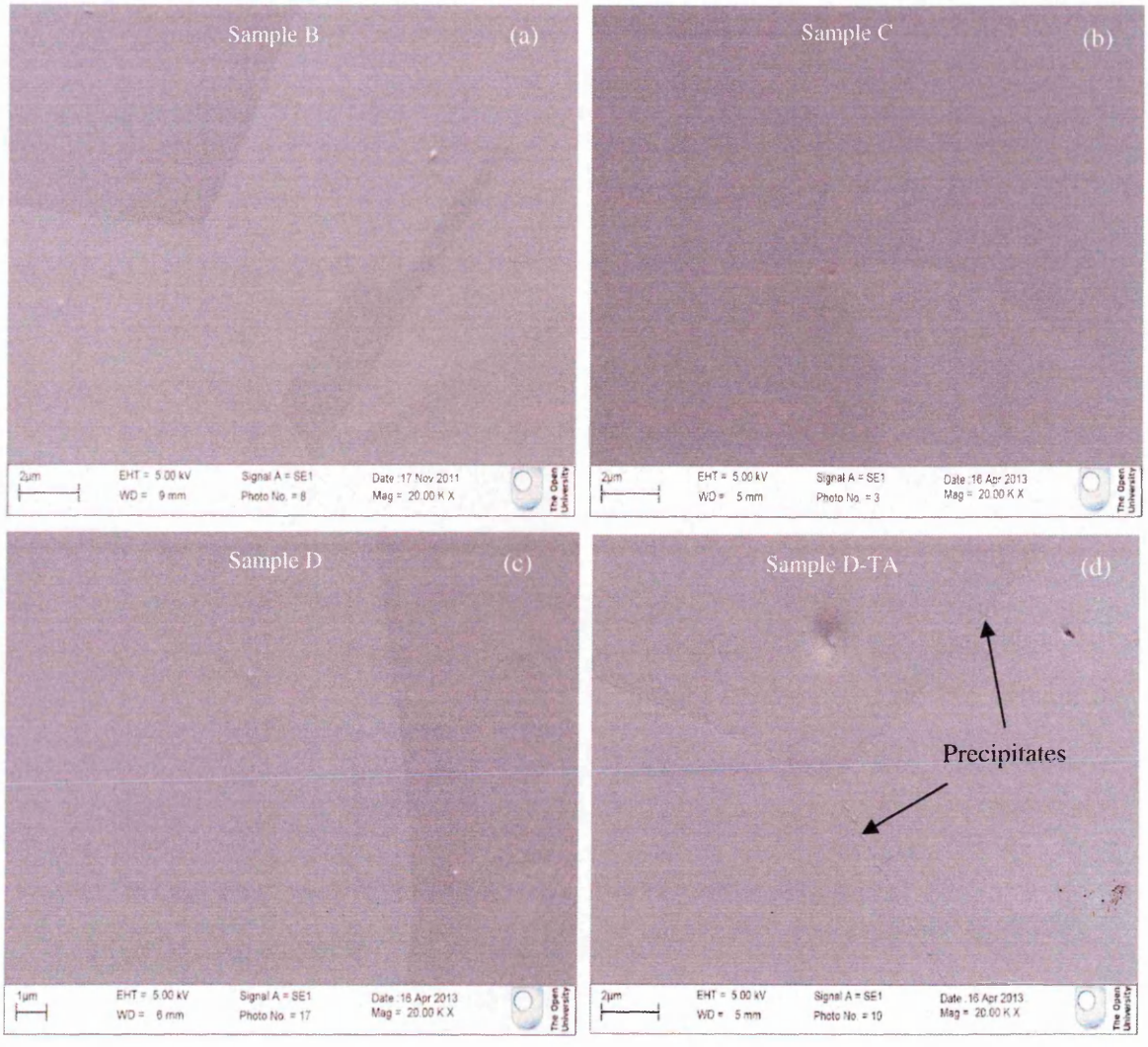

Fig. 4.13. SEM micrographs showing microstructures of Type 316H stainless steels studied. Precipitation is only evident in thermally-aged steel (d).

4.3.3.2. Microstructure assessment of Sample C

The microstructure of Sample C showed no precipitation as seen in Fig. 4.13b. This can be credited to the ST performed on the material by the manufacturer. The effects of the precipitates and other aging phenomenon on the development of strain-induced misorientations in Sample C were therefore minimal, particularly during the room temperature deformation where no precipitation occurs.

4.3.3.3. Microstructure assessment of Sample D

The as-received microstructure of Sample D is shown in Fig. 4.13c. The material was supplied in solution annealed state and this is attested by the lack of precipitation in its microstructure. As seen in Fig. 4.9d, slip bands were evident in some grains indicating existence of plastic deformation possibly from the cold drawing process. The microstructure of Sample D-TA exhibited both inter- and intra-granular precipitation as shown in Fig. 4.13d.

4.3.4. Characterisation of dislocation densities

As explained in Chapter 2, the generation and accumulation of GNDs during deformation introduces lattice rotations and since EBSD measures crystallographic orientations, it indirectly assesses the dislocation content. Characterisation of dislocation densities was therefore important in ascertaining their relationship with the lattice orientation changes. Dislocations rarely occur in isolation but rather as an irregular array with a mean density ρ described as the total length of dislocation line per unit volume.

In the current study the calculation of dislocation densities was based on diffraction contrast TEM images obtained from electron transparent thin foils of the deformed materials. A minimum of three foils were examined from each specimen, and the assessment of dislocation densities from each region of interest (at least five regions per foil) was carried out with several different imaging vectors to account for dislocations with different Burgers vectors [15]. The calculation was based on the following equation [146]:

$$\rho = \frac{2N}{Lt} \qquad \text{Eq. 4.4}$$

where N is the total number of intersections between dislocations and straight test lines superimposed randomly on the TEM micrograph while L and t represents the total length of all test lines and the foil thickness at the region of interest, respectively. The assessment was carried out using ImageJ software and involved superimposing five straight lines on a

micrograph in random directions. For all micrographs examined N was >50. The thickness t at each region of interest was estimated from the projected length (under two-beam imaging conditions) of a dislocation emerging on both surfaces of the foil, as shown schematically in Fig. 4.14, where q is the angle between the incident beam and the plane of the defect, α is the foil tilt angle and w is the projected length of the dislocation line.

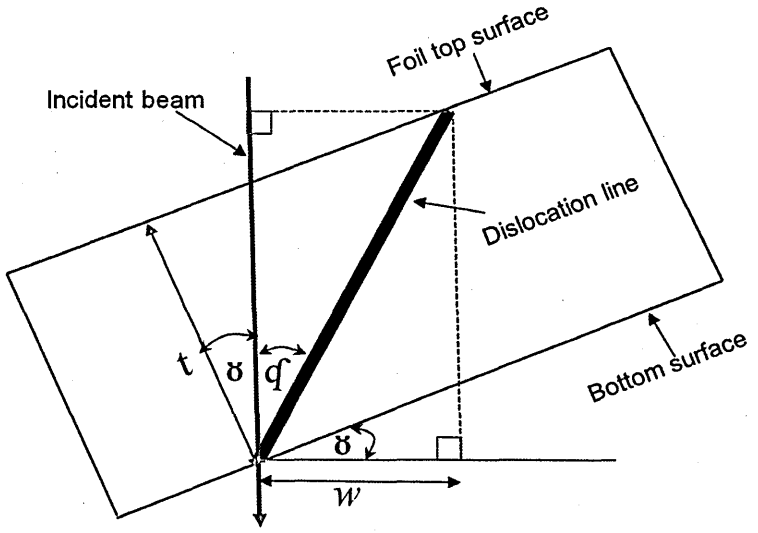

Fig. 4.14. Schematic diagram showing parameters required for TEM foil thickness t measurement from a planar defect of projected length w, inclined to the incident beam by angle q and foil tilted through an angle α.

By indexing the diffraction pattern from each region of interest, the plane containing the defect and the zone axis were determined following the procedures given in [147]. The angle between the zone axis and the plane containing the defect gave φ. The thickness t was then calculated using the following expression:

$$t = w(\cot\varphi - \tan\alpha)\cos\alpha \qquad \text{Eq. 4.5}$$

The main difficulty of this method is the determination of φ. Error in the determination of φ introduces error in the calculated thickness which can be as much as 18% for a deviation of 5° in φ. Other possible methods of estimating t include contamination spot separation, X-ray spectrometry, electron energy-loss spectrometry and convergent-beam diffraction

methods [137, 148]. Each has its own advantages and disadvantages and overall none is superior to the other [137, 148]. Foil thickness should be determined at each region of interest since the foil thinning process results in a wedged edge rather than a parallel sided specimen. In the present study the calculated foil thickness ranged from ~95 to 300nm within the TEM micrographs studied.

The calculated average dislocation densities for Sample A specimens deformed under different conditions is summarised in Table 4.10. The dislocation density increases almost linearly with the increase in strain as seen in Fig. 4.15. The error bars in this figure represent statistical error at 95% confidence level. The accumulation of dislocations about obstacles such as precipitates also influences the distribution of dislocations as shown in Fig. 4.16. The presence of dense network of dislocations at high strains seen in Fig. 4.18b limits the determination of the dislocation densities.

Table 4.10: Average dislocation densities ρ (m^{-2}) in service-aged Type 316H stainless steel based on TEM measurement and calculation using Eq. 4.6.

Sample ID	True strain	Max. Flow stress/MPa	Strain rate (s^{-1})	ρ by TEM	ρ by Taylor
HTST1	0.098	401	$3.5x10^{-3}$	3.3E+14	7.3E+14
HTST2	0.098	383	$3.0x10^{-5}$	3.1E+14	7.1E+14
HTST3	0.098	391	$4.0x10^{-6}$		6.9E+14
HTST4	0.098	354	$4.0x10^{-7}$		5.6E+14
HTT1	0.011	206	$3.5x10^{-5}$		1.9E+14
HTT3	0.030	258	$3.5x10^{-5}$		3.0E+14
HTT5	0.058	339	$3.5x10^{-5}$	1.9E+14	5.2E+14
HTT10	0.102	413	$3.5x10^{-5}$		7.7E+14
HTT15	0.140	463	$3.5x10^{-5}$		9.7E+14
HTT20	0.176	484	$3.5x10^{-5}$	5.1E+14	1.1E+15
HTT25	0.229	542	$3.5x10^{-5}$		1.3E+15

Specimens deformed in tension at 550°C

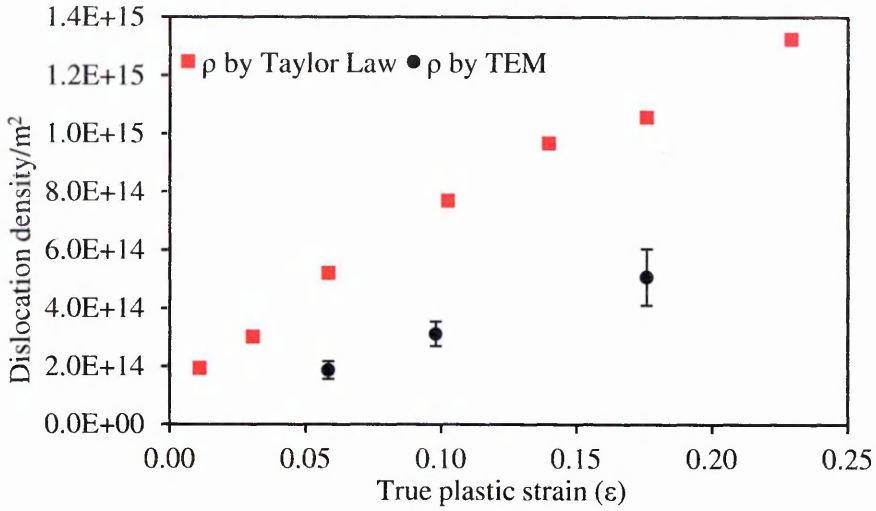

Fig. 4.15. Variation of dislocation density (ρ) with true plastic strain for specimens deformed as in Table 4.10. ρ is measured through TEM and calculated from Eq. 4.6.

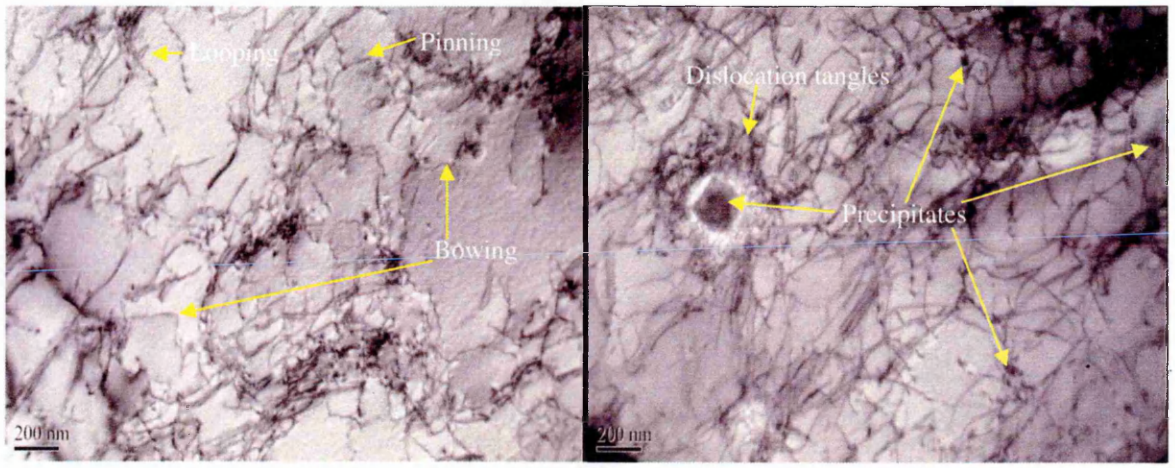

Fig. 4.16. TEM BF micrographs showing dislocation looping, bowing and interactions with precipitate in service-aged Type 316H stainless steel deformed to 0.058 strain at a strain rate of $3.5 \times 10^{-5} s^{-1}$.

It is clear that the TEM measurement of dislocation densities is a time consuming procedure that is prone to considerable experimental errors. However, this method allows both qualitative and quantitative assessment of dislocation density, and also provides information about dislocations characters and distributions. The calculated dislocation densities are not absolute values as some dislocations may have been lost during specimen preparation while others may not be fully accounted for due to overlapping [82]. Also the

foil thickness per micrograph is assumed to be constant which is not the case as a slight taper does exist toward the foil hole and this introduces errors in the calculation of the dislocation densities. Additional errors result from the determination of the foil thickness due to difficulties of finding an appropriate dislocation that projects on both surfaces of the foil and also from the use of random lines superimposed on micrographs which may lead to over- or under-sampling of dislocations, if they are not randomly distributed. However the biggest uncertainty comes from the limited volume sampled which may not be representative of the bulk's dislocation densities. The relative values of the dislocation densities given in Table 4.10 are expected to be more reliable than the absolute values as many of the errors in their determination apply to all the specimens investigated.

Total dislocation densities accumulated in deformed material can also be estimated by applying Taylor's equation [15, 149, 150]:

$$\rho = \rho_{GND} + \rho_{SSD} = \left(\frac{\sigma}{\alpha G b}\right)^2 \qquad \text{Eq. 4.6}$$

Where ρ_{GND} and ρ_{SSD} represent geometrically necessary and statistically stored dislocations (see section 2.2.2.4) while σ, G, b and α represent the flow stress, shear modulus, Burgers vector magnitude and a constant (~1), respectively. In the current study, the flow stresses were obtained from the true stress-true strain curves while the shear modulus was calculated from the Young's modulus (E) and Poisson ratio (v_p) of Type 316 stainless steel using the equation $G = E/2(1 + v_p)$ [31]. The value of b used was 2.58 x10^{-10}m calculated from iron *f.c.c* lattice parameter (a) of 0.365nm [16] assuming $b = \frac{a}{2} < 110 >$.

The calculated dislocation densities at different level of strains and strain rate based on the TEM measurements and on Taylor's equation are given in Table 4.10. The values obtained are of the same order of magnitude although the TEM values are lower, which can be attributed to the systematic errors discussed previously. The main assumption in the

application of Taylor's equation was that α equals 1, which is an ideal value for precipitation-hardened material [38] and may not be generally applicable to the service-aged steel studied. In this equation, the friction stress is also assumed which makes the calculated ρ an upper bound. In a similar application, Taylor's equation was used by [42] to calculate the density of mobile dislocations in 316 steel deformed in creep at 593-816°C and 240-55MPa. The dislocation density was found to increase with increasing applied stress which is consistent with the current work as deduced from Table 4.10.

4.3.5. Characterisation of dislocation structures

Dislocations are linear defects in metallic materials whose motion produces plastic deformation. In austenitic stainless steel the predominant dislocation structure is closely related to the main deformation mechanism, which depends on the test temperature, strain and strain rate [151]. Consequently, characterisation of these structures is important in giving a mechanistic explanation of the observed macroscopic behaviour of the deformed material. In the current study, TEM bright-field imaging was used to characterise dislocation structures in Sample A specimens, deformed plastically and in creep at 550°C. Although the small volume sampled using TEM could raise concern about its statistical representation of the bulk, every effort was made to ensure the results obtained were representative by examining different regions of the sample under study.

4.3.5.1. Dislocation structures under tensile deformation

As seen in Fig. 4.17a, dislocation structures in the specimen with no deformation consisted of individual dislocations which were fairly randomly distributed. For the specimens deformed at $3.5x10^{-3}s^{-1}$ to 0.098 strain, the structures consisted of both individual and tangled dislocations particularly in regions close to grain boundaries as seen in Fig. 4.17b. After 0.058 strain at a strain rate of $3.0x10^{-5}s^{-1}$, the distribution of dislocation structures was still fairly random with evidence of dislocation bowing, looping, pinning,

and dislocation-precipitate interactions as shown in Fig. 4.16. However, as the strain was increased to 0.098 (see Fig. 4.18a) and 0.176 (see Fig. 4.18b) at the same strain rate, there was evidence of diffuse cell-wall structures and localised dislocation tangles which became more pronounced as the strain rate was further reduced to $4.0x10^{-6}s^{-1}$ and $4.0x10^{-7}s^{-1}$ as seen in Fig. 4.19.

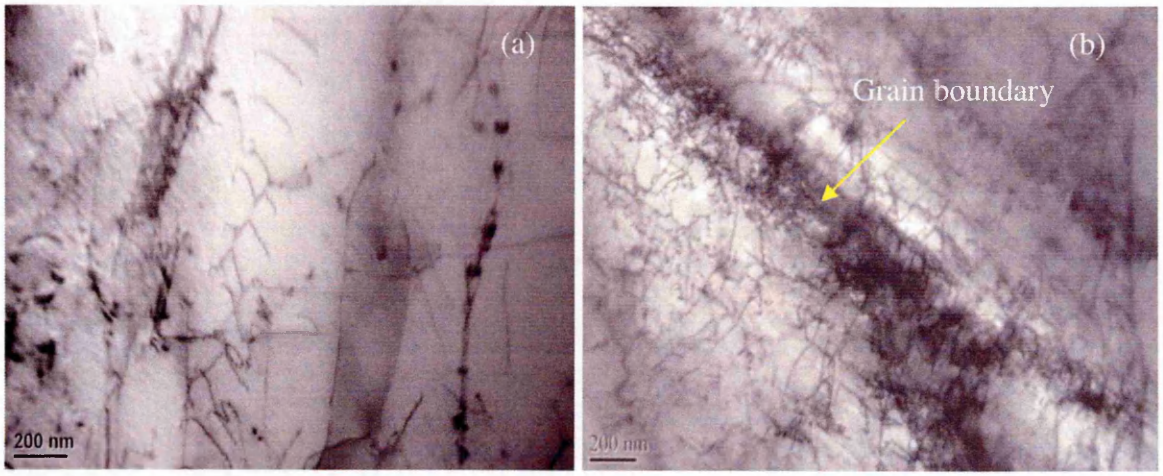

Fig. 4.17. TEM BF micrographs of service-aged Type 316H stainless steel showing: (a) relatively random dislocation distribution in undeformed sample, and (b) dislocation tangles in regions close to grain boundaries for specimen deformed to 0.098 strain at a strain rate of $3.5x10^{-3}s^{-1}$.

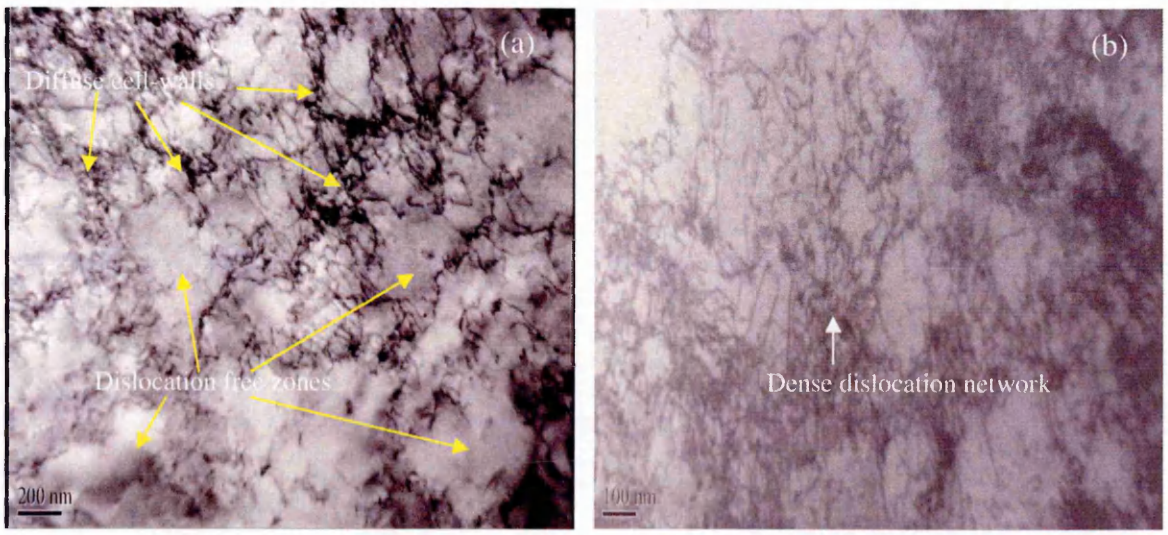

Fig. 4.18. TEM BF micrographs of service-aged Type 316H stainless steel showing: (a) diffuse cell-wall structures in specimen deformed to 0.098 strain at a strain rate of $3.0x10^{-5}s^{-1}$, and (b) localised regions of dense dislocation networks in specimen deformed to 0.176 strain at a strain rate of $3.5x10^{-5}s^{-1}$.

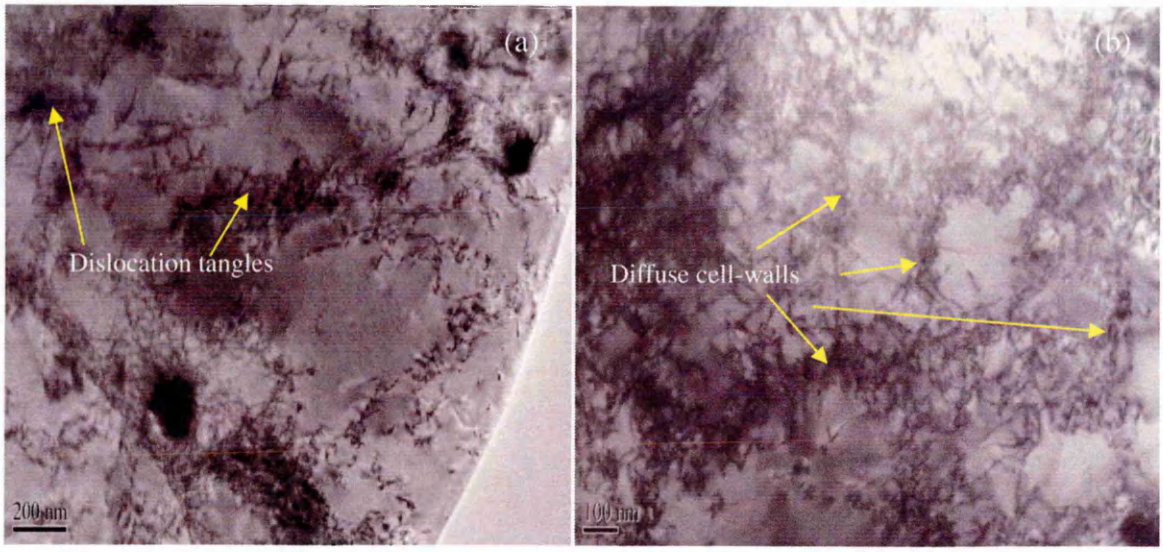

Fig. 4.19. TEM BF micrographs showing dislocation tangles and diffuse cell-wall structures in service-aged Type 316H stainless steel deformed to 0.098 strain at strain rates of (a) $4.0x10^{-6}s^{-1}$, and (b) $4.0x10^{-7}s^{-1}$.

As explained in Chapter 2, the high density of intragranular precipitation favours formation of diffuse cell-wall structures (see section 2.2.2.3) and hinders subgrain formation (see section 2.2.3.2). The development of cell-like structures have been reported in an annealed Type 316H steel whose thickness had been reduced by 15% through warm-rolling at 400-600°C [152]. In agreement with the current work, substructures in Type 316L steel deformed at 400°C at a strain rate of about $10^{-3}s^{-1}$ were found by [151] to vary from random distribution of dislocations at 0.02 strain to cell-like structures at 0.24 strain. In Type 316 steel the formation of subgrain structures occurs at temperatures above *0.5Tm* due to increased recovery rate while deformation below this temperature gives substructure comprising of tangled dislocation cell-wall structures [153] which is in agreement with the current findings.

4.3.5.2. Dislocation structures under creep deformation

In this section, the examination of dislocation structures in specimens deformed in tension at 550°C to 0.079 strain at a rate of $3.5x10^{-5}s^{-1}$ followed by constant load creep

deformation at 550°C using an initial stress of 320MPa is reported. All specimens had a similar amount of prior plastic strain but their accumulated creep strains were different.

For the specimen with an accumulated creep strain of 0.011, there was evidence of stacking faults (errors in atomic plane stacking sequence caused by plastic deformation) characterised by their typical fringe patterns (see Fig. 4.20a). These can be attributed to the low SFE of Type 316 stainless steel [43] which allows dissociation of perfect dislocations into widely separated partials with a stacking fault between them. In the same specimen, the dislocation cell-like structures were also evident (see Fig. 4.20b) in which dense networks of dislocations surrounded regions of relatively low dislocation density. Fig. 4.20 (c and d) captured from the same specimen shows evidence of slip bands and dislocation-precipitate interactions, respectively. Similar banded structures have been reported in 316 steel deformed at 600°C using an initial stress of 230MPa, and were attributed to gliding and agglomeration of dislocations into walls parallel to {111} planes [154]. In the current case, it is possible that these structures were introduced during the prestraining stage since there was little accumulated creep strain in this sample.

Since extensive intergranular precipitation in Type 316 stainless steel hinders the formation of subgrain structures [42], it is possible that the cell-like structures seen in Fig. 4.19 and Fig. 4.20b could have resulted from other mechanisms such as chequered configuration of slip bands or from dense dislocation walls owing to dislocation-precipitate interactions.

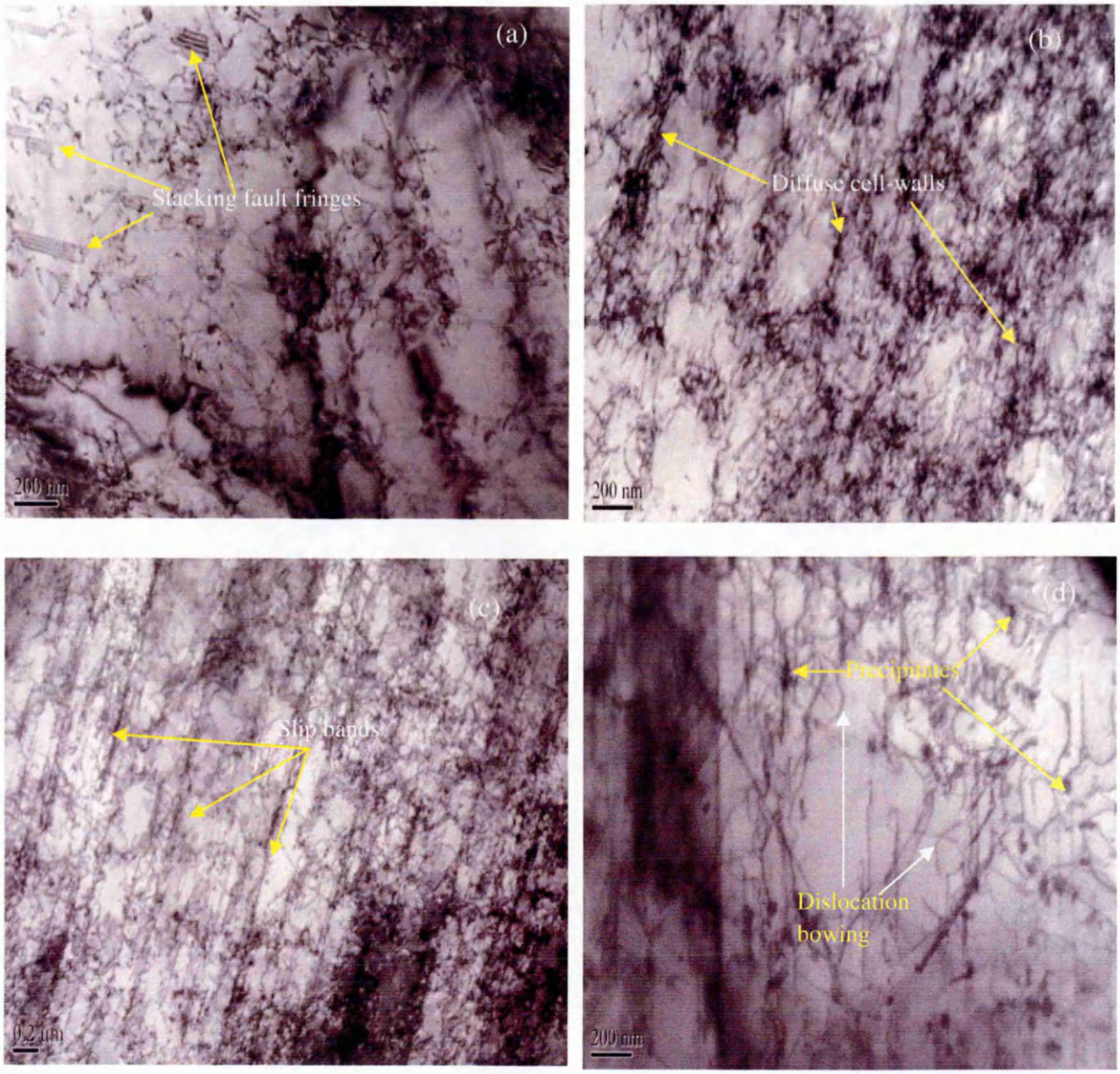

Fig. 4.20. TEM BF micrographs showing stacking faults, slip bands, dislocation bowing and diffuse cell-wall structures in service-aged Type 316H stainless steel prestrained to 0.079 followed by 0.011 creep strain.

The substructures formed at an accumulated creep strain of 0.023 and 0.043 consisted of dislocation free cells bordered by regions of high dislocation densities on which carbide precipitation had occurred as seen in Fig. 4.21 (a and b). This is in agreement with the previous explanation in which it was postulated that intragranular precipitates assist in the formation of cell-like structure consisting of diffuse dislocation walls. As explained in section 2.2.2.3 this may have resulted from dislocations forming

loops on precipitates as they glide. The high dislocation density developed after 0.068 creep strain (see Fig. 4.22) can be attributed to increased deformation in the necking region of the creep specimen before failure.

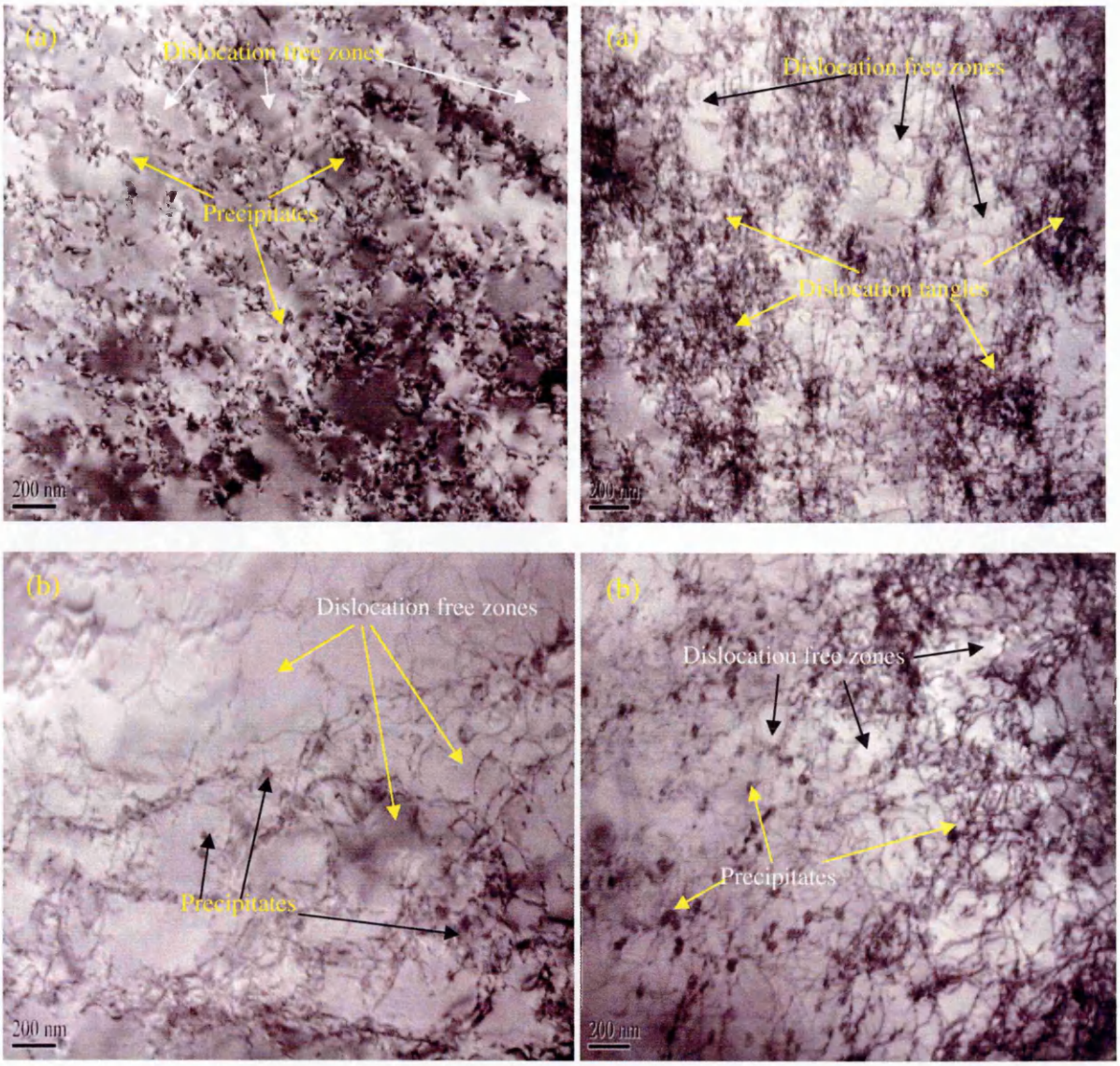

Fig. 4.21. TEM BF micrographs showing large dislocation free zones, dislocation tangles and carbide precipitation on dislocations in service-aged Type 316H stainless steel prestrained to 0.079 followed by (a) 0.023, and (b) 0.042 creep strains.

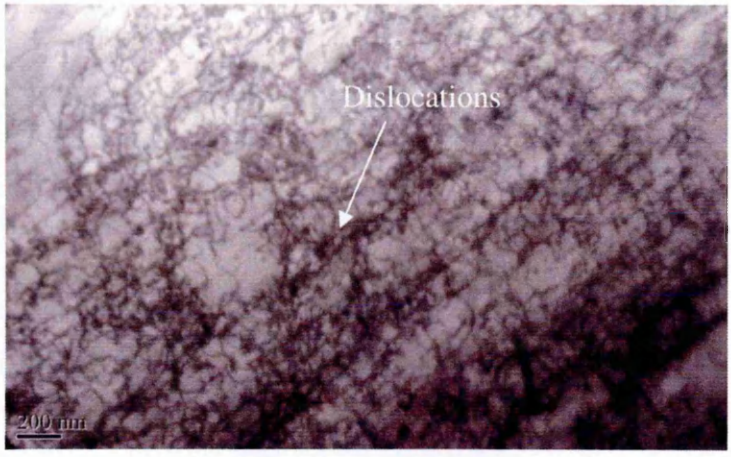

Fig. 4.22. TEM BF micrograph showing high dislocation density in service-aged Type 316H stainless steel prestrained to 0.079 followed by 0.068 creep strain.

It is clear from the current results that the dislocation structures developed vary with the deformation conditions from a relatively uniform distribution at low strains to cell-like structures at high strains. Similar variations in dislocation structures occur with a reduction in the deformation strain rate. From the observed dislocation-precipitates interactions, it is possible that the extensive intragranular precipitation in the service-aged steel played a major role in the evolution of these dislocation structures.

4.4. Summary

The key findings in this chapter can be summarised as follows;

- The characterisation of grain size based on the OM and OIM were found to give comparable results.
- The service-aged steel had extensive inter- and intra-granular precipitation which varied between the grains and had a higher 0.2% proof stress compared to re-solution heat treated steel.
- The dislocation density in the service-aged steel was found to increase with increasing strain and strain rate.
- The development of dislocation structures at 550°C was found to vary from relatively uniform distribution at low strains to cell-like structures at high strains. The distinctness of the cell-like structures was found to increase as the rate of deformation was reduced.

CHAPTER 5

THE INFLUENCE OF MICROSTRUCTURE, THERMAL AGING AND GRAIN SIZE ON STRAIN-INDUCED MISORIENTATION DEVELOPMENT

5.1. Introduction

The influence of microstructure and grain size on the mechanical properties of metallic material is well established in the literature [19, 31, 155, 156]. However, little information is available about their influence on misorientation development under different deformation conditions. In this chapter, the influence of intergranular and intragranular precipitates in the development of strain-induced misorientation is systematically investigated firstly by comparing results obtained from the service-aged (Sample A) and re-solution heat treated steel (Sample B) deformed under similar conditions and secondly, by assessing the development of misorientation in the Sample D-TA which was thermally-aged without load at 550°C for 1000 hours followed by deformation under different conditions. The influence of grain size on strain-induced misorientation development is also investigated in this chapter by analysing results obtained from Sample B and Sample C (solution annealed steel in as-received condition) which had different average grain sizes and microstructures free of precipitates. The chapter concludes with a summary of the key findings.

5.2. The influence of precipitation on strain-induced misorientation development

5.2.1. Service-aged steel versus re-solution heat treated steel

5.2.1.1. Mechanical tests

The effect of carbide precipitation on misorientation development was investigated through a series of room temperature tensile tests carried out on Sample A and Sample B. The solution treatment (ST) was carried out on blanks (12mm in diameter and 100mm long) machined from the service-aged steel and involved heating the blanks to 1050°C for

1 hour followed by water quenching. The average grain size after ST based on ECD measurement was 93±12μm which was comparable to 98±8μm of the service-aged steel and hence the influence of the grain size on the subsequent misorientation development during deformation was assumed to be negligible. Tensile specimens machined from Sample A were denoted as RTT and those from Sample B ST blanks as STRTT. The tensile tests were conducted using the procedures outlined in Chapter 3 and the conditions given in Table 5.1. The correspondence in the deformation conditions facilitated comparative misorientation studies while the use of room temperature avoided the re-precipitation of the carbides. The flow stresses were significantly higher in Sample A than in Sample B at equivalent strains as seen in Fig. 5.1. Similar observations attributed to the presence of precipitates in aged Type 316 stainless steel have been made by [157].

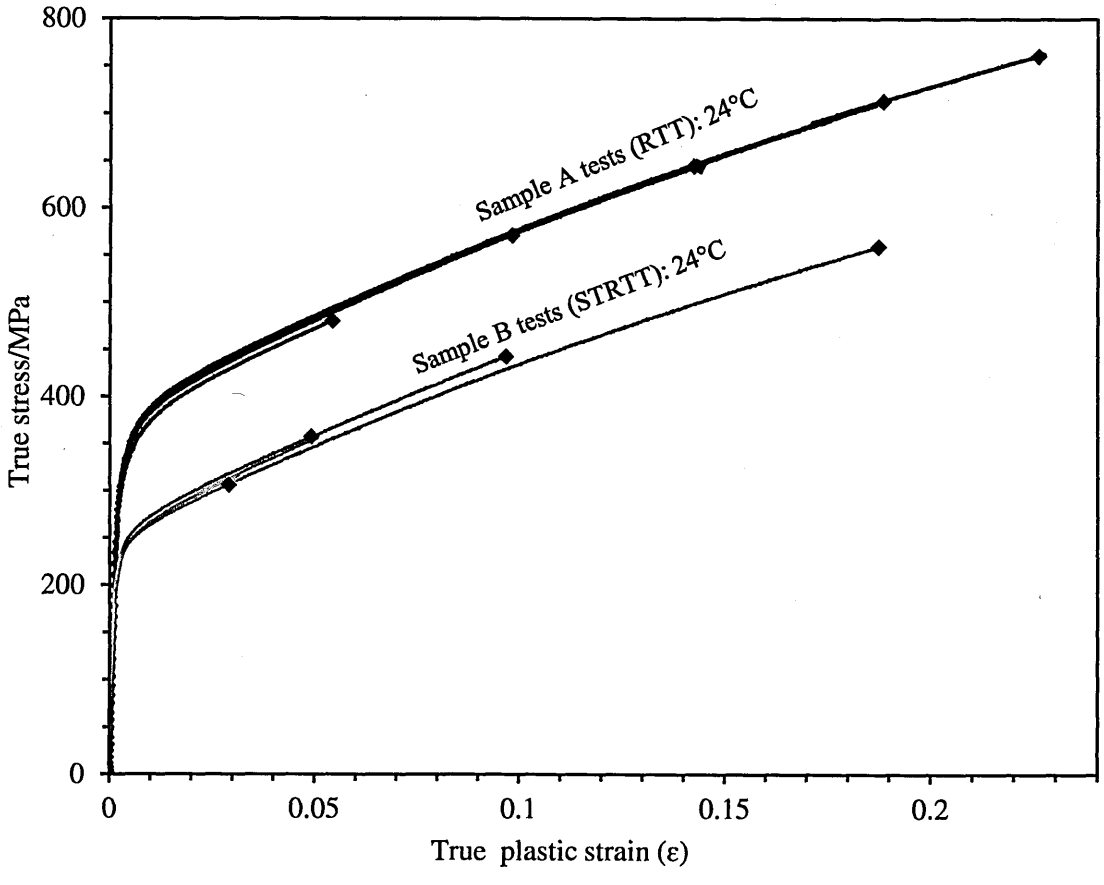

Fig. 5.1. Flow curves for Type 316H stainless steel deformed as in Table 5.1 in service-aged (RTT) and re-solution heat treated (STRTT) conditions.

Table 5.1: Tensile tests conditions at 24°C for Type 316H stainless steels studied.

Steels	% true plastic strain (ε)	Strain rate (s^{-1})	Grain size(μm)	Specimen ID
Sample A	5.4, 9.8, 14.3, 18.7, 22.7	$2.0x10^{-4}$	98±8	RTT
Sample B	3.1, 5.1, 9.7, 18.7	$2.0x10^{-4}$	93±12	STRTT
Sample C	9.5, 14.0, 18.2, 22.3	$1.5x10^{-3}$	35±1	

5.2.1.2. EBSD measurements

EBSD measurements were carried out on the deformed specimens using the procedure outlined in Chapter 3. The misorientation development as a function of the applied strain was assessed at the local scale using the LAMF and the KAM_a metrics and at the long range scale using the $AMIS_a$ and the DGF metrics.

5.2.1.3. Results and discussion

The evolution of misorientations in both Sample A and Sample B showed similar trends (see Fig. 5.2 and Fig. 5.3) but at equivalent strain and strain rate, the build-up was significantly faster in the Sample A than in the Sample B. This can be ascribed to the effects of long-term aging during service which yielded extensive intragranular and intergranular precipitation. These precipitates not only harden the metal by creating additional obstacles to dislocation flow (see Fig. 5.4) but their interfaces provide additional dislocation sources and sinks.

The back stresses (see section 2.2.2.3) resulting from dislocations accumulating at precipitates on given slip planes may have necessitated higher flow stresses in Sample A than in Sample B for similar levels of deformation as seen in Fig. 5.1. Since at room temperature dislocation motion is limited to the glide planes (see section 2.2.2), it is expected that the aged material will have more dislocations generated to achieve the same level of strain as the solution treated material. Accumulation of dislocations on precipitates may increase GNDs locally leading to higher local misorientations owing to larger lattice

curvature. The lattice distortions arising from chemical gradients due to carbide precipitation will not contribute to the measured misorientation as explained in section 2.4.3.8). As seen by comparing Fig. 5.5 (a-b) grain boundary precipitates also complicate the transfer of slip across grain boundaries and initiate complex slip earlier than clean grain boundaries. The service-aged steel in this case exhibits more deformation (demonstrated by the low angle misorientations) along grain boundaries than the ST steel.

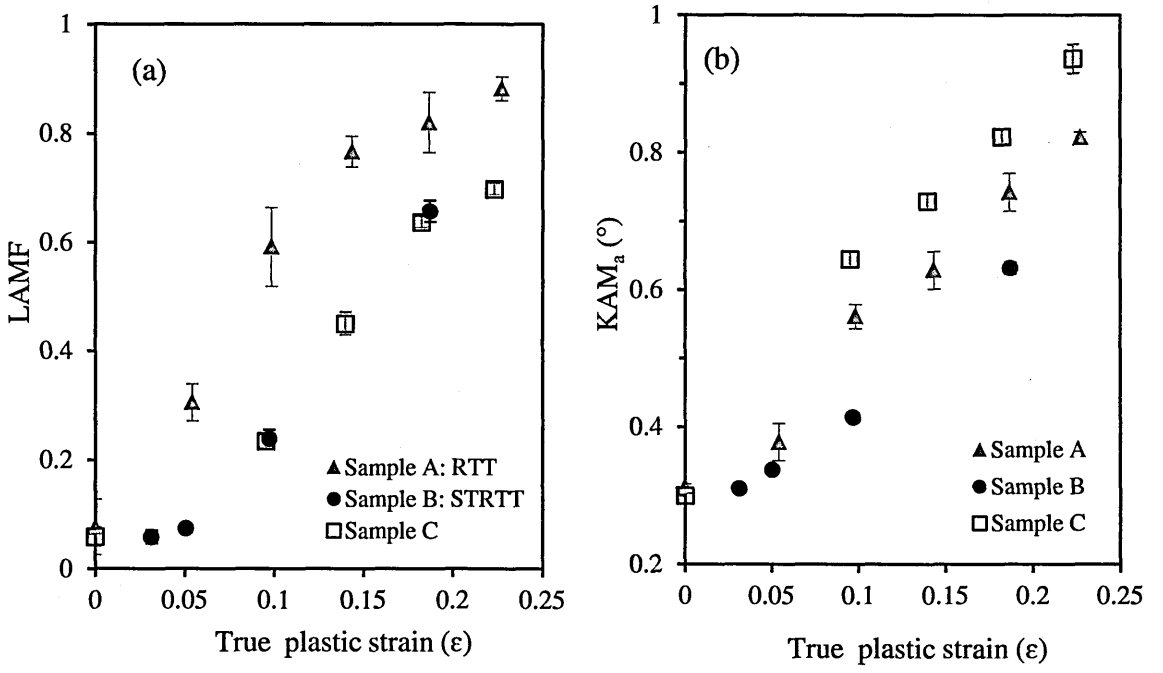

Fig. 5.2. Variations of (a) LAMF, and (b) KAM_a with true plastic strain for Type 316H stainless steels deformed as in Table 5.1. Effect of precipitation and grain size on measured local misorientation is evident.

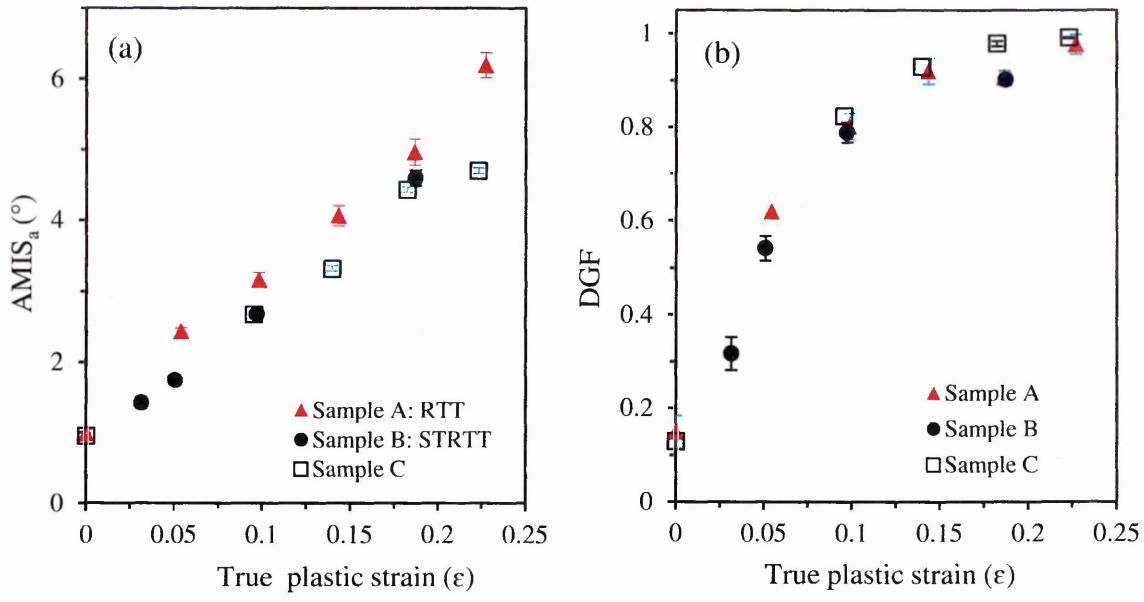

Fig. 5.3. Variations of (a) $AMIS_a$, and (b) DGF with true plastic strain for Type 316H stainless steels deformed as in Table 5.1. Effect of precipitation and grain size on measured long-range misorientation is marginal.

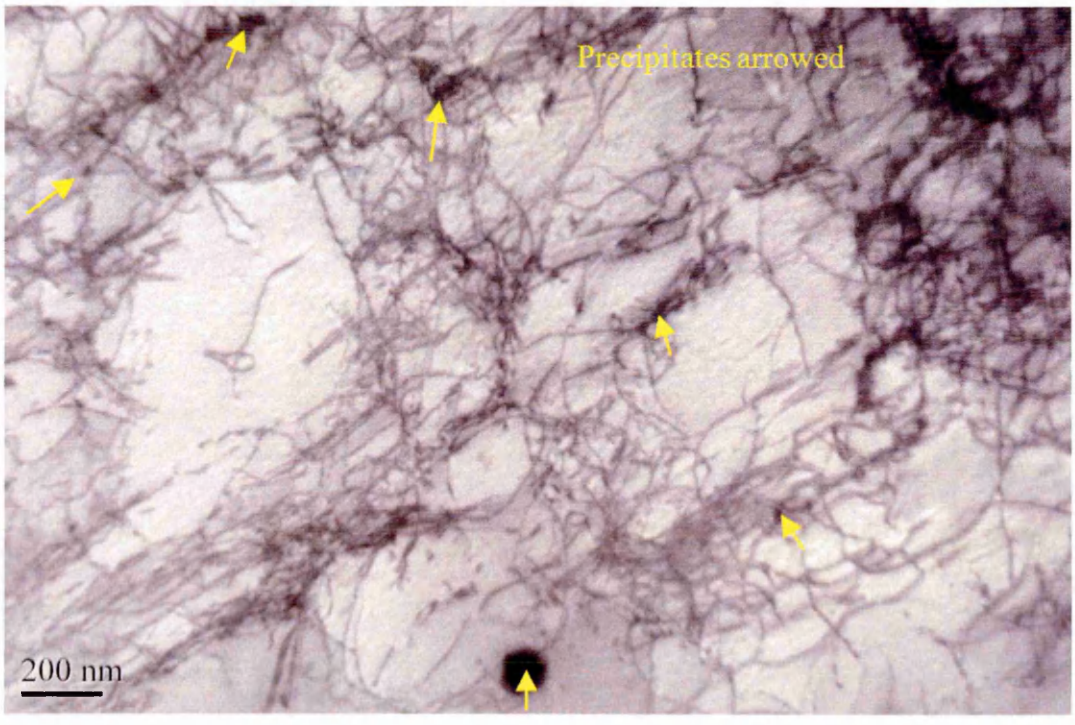

Fig. 5.4. TEM BF micrograph showing precipitate-dislocation interactions in deformed service-aged Type 316H stainless steel.

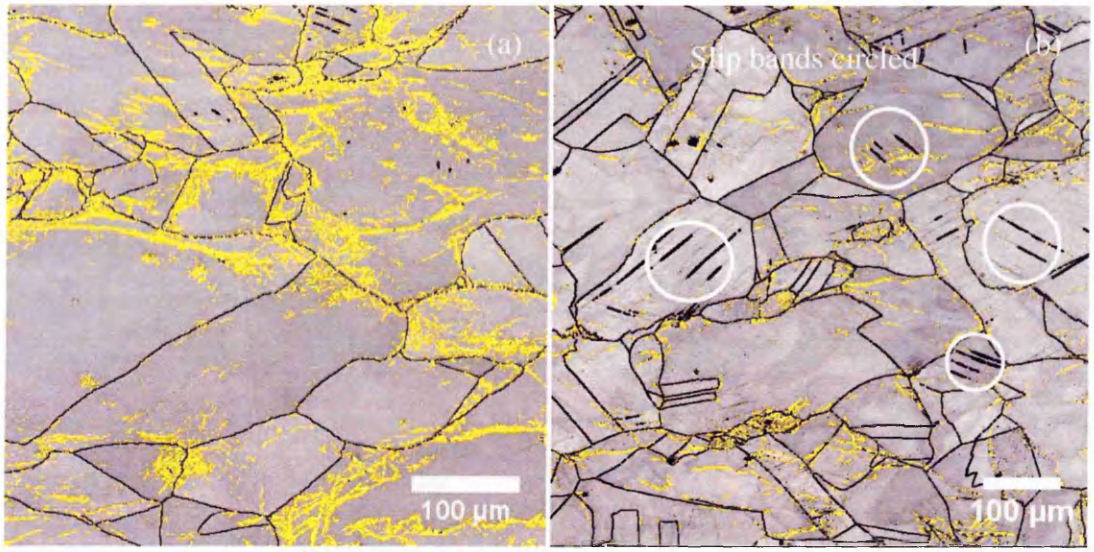

Fig. 5.5. Image quality maps of Type 316H stainless steel deformed to ~0.187 at 24°C showing dense deformation zones ('yellow patches') in close proximity to grain boundaries in service-aged steel (a) than in re-solution heat treated steel (b). Slips bands are evident in (b).

The effect of precipitation on the development of local misorientation becomes clearer when the misorientation distributions from Sample A and Sample B specimens deformed to ~0.18 true strain are compared as shown in Fig. 5.6. The misorientation distribution from Sample A exhibited a wider spread than that from Sample B which can be attributed to an increase in the rate of dislocation accumulation as a result of the extensive precipitation.

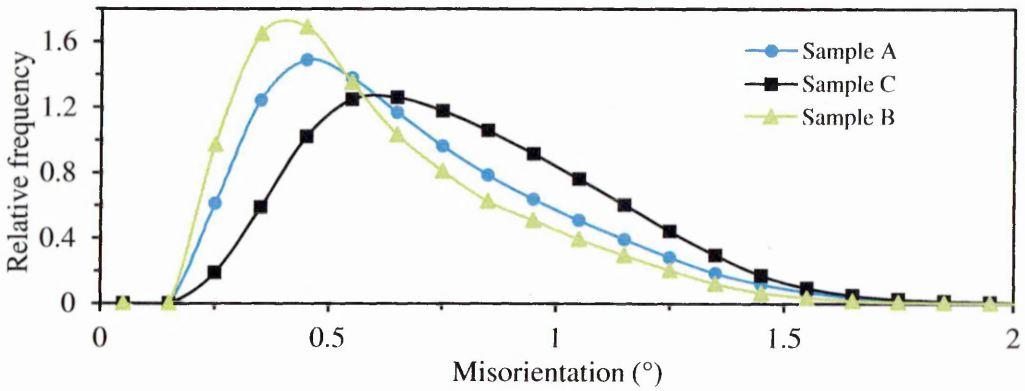

Fig. 5.6. Effects of precipitation and grain size on local misorientation distribution for Type 316H stainless steels deformed to ~0.18 true strains at 24°C.

The sensitivity of the EBSD metrics to the effects of precipitates in the material is dependent on their sensitivity to local misorientation variations, which decreases as the number of measurement points considered in their computation increases. As seen in Fig. 5.2a, LAMF has the highest sensitivity since it is based on point-to-point misorientation assessment and so it detects lattice rotations among adjacent measurement points. Slip bands and dislocation pile-ups at precipitates tend to concentrate misorientation locally, giving more misorientations with values ranging from 2° to 15° between points 1μm apart in Sample A than in Sample B and so increasing the measured LAMF. However, this assessment is influenced by the presence of orientation 'noise' in the data giving relatively large scatter as depicted by the error bars in Fig. 5.2a. By considering average misorientation values, as in the case of KAM_a and $AMIS_a$, the influence of orientation 'noise' is reduced but at the same time their sensitivity toward local deformation due to dislocation accumulations on precipitates diminishes, as is evident from the much smaller differences between their values from Sample A and Sample B in Fig. 5.2b and Fig. 5.3a, respectively. However, the higher KAM_a values in the service-aged steel than in the ST steel of a similar grain size reflects the concentration of dislocation tangles around the precipitates in the service-aged steel which results in higher local misorientations.

The increase in $AMIS_a$ caused by aging shows that precipitation assists the generation and accumulation of GNDs during deformation. It is possible that dislocation tangles around precipitates (see Fig. 4.16) and the generally greater complexity of deformation in grains containing harder particles may make it easier for differences to arise in the activation of different slip systems in local volumes of the grain and so might stabilize a smaller cell size in the deformation structure of the service-aged steel than in the ST. As AMIS is a measure of the longer range misorientations across a grain, if the misorientation change at each diffuse cell boundary is similar this could explain the increased AMIS.

The DGF metric, which only considers a fraction of grains in an orientation map with AMIS values above a certain threshold value, is least sensitive to local deformation associated with the precipitate-dislocation interactions. For instance, a grain may have large variations in local deformation owing to precipitate-dislocation interactions, but if its AMIS value is below the threshold value it will be considered un-deformed. For this reason the values of DGF show the least scatter (Fig. 5.3b) and can be a good gauge of the global macroscopic strain in austenitic stainless steels, regardless of their thermal histories. However, caution is needed when generally assessing plastic strain in Type 316H stainless steels using the LAMF, KAM_a and $AMIS_a$ metrics as they are sensitive to aging effects particularly the presence of precipitates. For accurate assessment of plastic strain using these metrics, a good correspondence in microstructure is needed between the calibration material and the measured material.

5.2.2. Thermal aging effects on strain-induced misorientation development

Type 316 stainless steel is widely used in power generating plants because of its good high temperature strength, oxidation and creep resistance [17, 18] but long term exposure to service temperature of about 550°C can degrade its mechanical properties [17, 158, 159] through extensive precipitation both intragranularly and at the grain boundaries.

5.2.2.1. Measurement conditions

In this section, the effect of thermal aging at 550°C for 1000 hours on misorientation development under different deformation conditions is reported. Table 5.2 summarises the conditions under which the current study was conducted, which included: room temperature deformation (RTD), high temperature deformation (HTD), high temperature plastic deformation followed by aging (HTDA), high temperature aging followed by plastic deformation (HTAD), high temperature plastic deformation followed by creep deformation (HTDC) and lastly high temperature aging followed by plastic and

creep deformation (HTADC). The specimens in their as-received solution treated condition were denoted by ARST. The variation of the temperature over the whole aging duration was within ±1°C of the targeted temperature of 550°C. At the end of the aging period the specimens were allowed to cool in air to ambient temperature.

Table 5.2: Mechanical test conditions for thermally-aged Type 316H stainless steel.

Specimen ID	Condition	True Plastic strain	Strain rate (s^{-1})
ARST	As-received no thermal aging	0.00	-
HTA	Thermally-aged	0.00	-
RTD	Deformed at 24°C	0.08	$3.0x10^{-4}$
HTD	Deformed at 550°C	0.08	$4.0x10^{-5}$
HTAD	Thermally-aged + deformation at 550°C	0.08	$4.0x10^{-5}$
HTDA	Deformed at 550°C + thermally-aged	0.08	$4.0x10^{-5}$
HTDC	Deformed at 550°C + crept at 550°C by 0.35%	0.08	$4.0x10^{-5}$ $3.9x10^{-10}$
HTADC	Thermally-aged + deformed at 550°C + crept at 550°C by 0.35%	0.08	$4.0x10^{-5}$ $7.4x10^{-10}$

5.2.2.2. Mechanical tests

The tensile tests were conducted at 24°C and at 550°C under the conditions given in Table 5.2 following the procedures outlined in Chapter 3. The tests were terminated after 0.08 strain in all cases. The creep tests were conducted as described in Chapter 3 at 550°C using an initial stress of 320MPa. The tests were terminated after an accumulated creep strain of about 0.35%.

5.2.2.3. EBSD measurements

To assess the thermal aging effects on the misorientation development, EBSD measurements were conducted using the procedures specified in Chapter 3, on the specimens listed in Table 5.2. Strain-induced misorientations were assessed both at the local and long-range scales. This ensured that both the subtle differences in lattice orientations among adjacent measurement points and the long-range changes in lattice orientations were investigated.

5.2.2.4. Results and discussion

The microstructure of the material after thermal aging indicated the presence of intergranular precipitates (see Fig. 5.7a) which were not evident before the thermal aging (see Fig. 5.7b). This is expected since intergranular precipitation of $M_{23}C_6$ carbides at 550°C starts after about 10 hours of aging based on temperature-time precipitation (TTP) diagram for solution annealed Type 316 stainless steel (see Fig. 2.2).

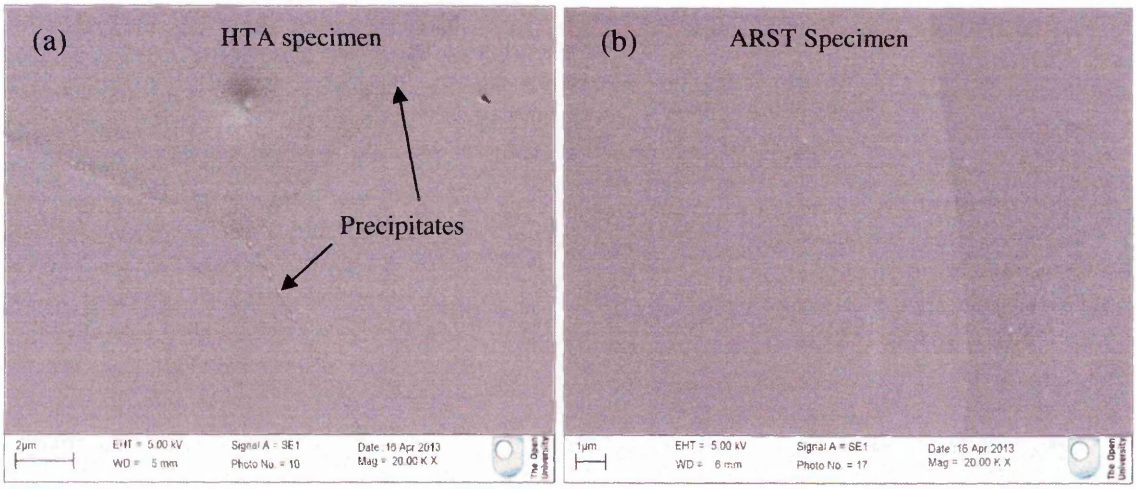

Fig. 5.7. SEM micrographs of Type 316H stainless steel showing intergranular precipitation in thermally-aged specimen (a), and none in un-aged specimen (b).

The flow curves for the tensile tested specimens are shown in Fig. 5.8. It can be noted that at equivalent strains, the thermally-aged specimen had a higher flow stress at 550°C compared to the un-aged specimen. As explained in section 5.2.1 this can be attributed to the presence of precipitates in the thermally-aged specimen (see Fig. 5.7). At equivalent strains the room temperature flow stresses for the un-aged specimens were significantly higher than those at 550°C mostly due to differences in the deformation mechanisms at these two temperatures. In summary, the increased thermal activation at high temperatures facilitates the processes of dislocation climb over obstacles and cross-slip (see section 2.2.3.1.2). This reduces dislocation pile-ups on barriers and thus the

amount of back stresses generated along the slip planes. Consequently, the flow stress needed to achieve a given deformation is lower at 550°C than at 24°C.

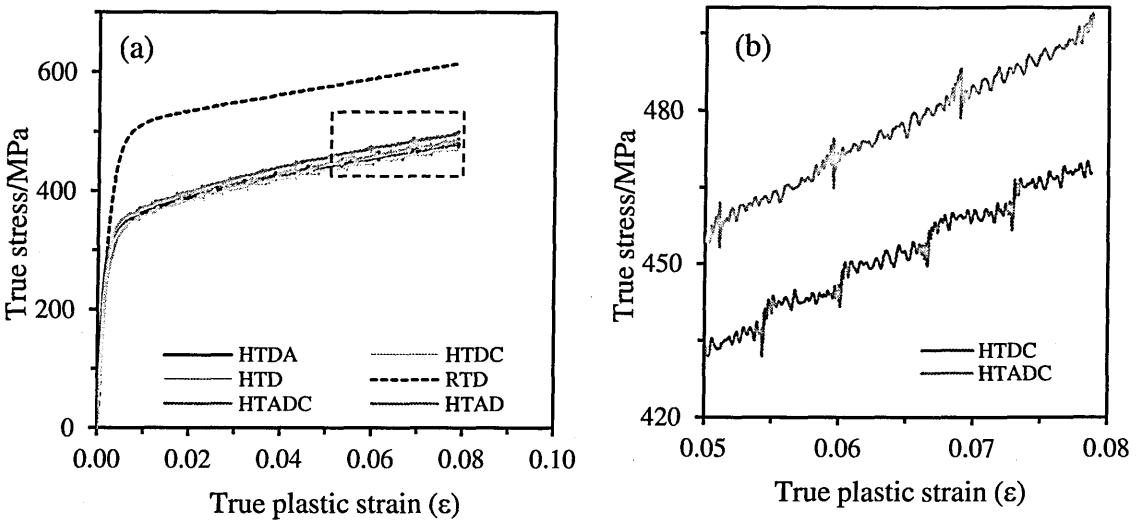

Fig. 5.8. Flow curves for Type 316H stainless steel deformed as in Table 5.2, and (b) magnification of the dotted section in (a) showing the effect of thermal aging on flow stress.

The creep responses for the plastically deformed specimens with (HTADC) and without (HTDC) prior thermal aging are shown in Fig. 5.9. The HTADC specimen had significantly reduced creep resistance despite its marginally higher flow stress curve as seen in Fig. 5.8.

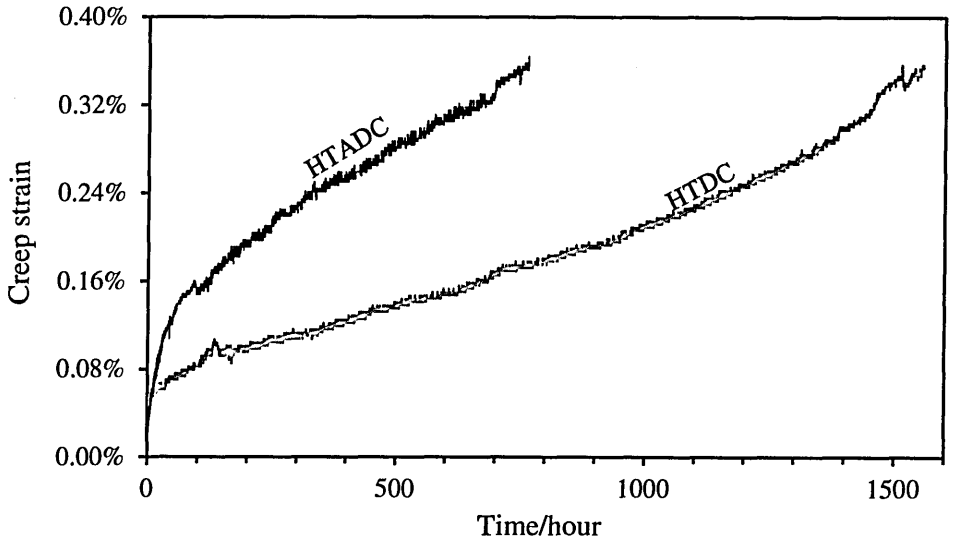

Fig. 5.9. Creep responses of Type 316H stainless steel crept as in Table 5.2 showing the effect of thermal aging on creep resistance.

Thermal aging had little effect on the existing misorientations as shown by metrics values from the ARST and HTA specimens seen in Fig. 5.10 and Fig. 5.11. The misorientation build-up at the local scale during the room temperature deformation (RTD) was higher than that at 550°C (HTD) (see Fig. 5.10) but lower at the long-range scale (see Fig. 5.11). This can be attributed to the difference in deformation mechanism at these two temperatures. At room temperature, dislocation movement is restricted to the glide planes causing local accumulations (e.g. along the slip bands seen in Fig. 5.12a), leading to higher local misorientations. However, as seen in Fig. 5.12b, at higher temperature the increased ability of dislocations to climb and cross-slip limits the development of slip bands and accumulations therefore occur over much longer length scales, mostly at grain boundaries if no other obstacles are present.

At 550°C misorientation accumulated at a faster rate in the thermally-aged specimen (HTAD) than in the un-aged specimen (HTD) deformed under similar conditions. This can be attributed to the presence of precipitates in the microstructure as explained previously. By comparing Fig. 5.12 (b and c) for HTD and HTAD specimens it is evident that precipitation enhanced the random distribution of local deformation. However, when the misorientation build-up was assessed at longer range, the effects of precipitation were not obvious as seen in Fig. 5.11b, in agreement with the observations in section 5.2.1. The misorientations built in the HTD and HTDA specimens were similar both at the local and longer scale, implying that thermal aging at 550°C has minimal effects on the misorientations already pre-existing in the material. This shows that static recovery is minimal at this aging temperature.

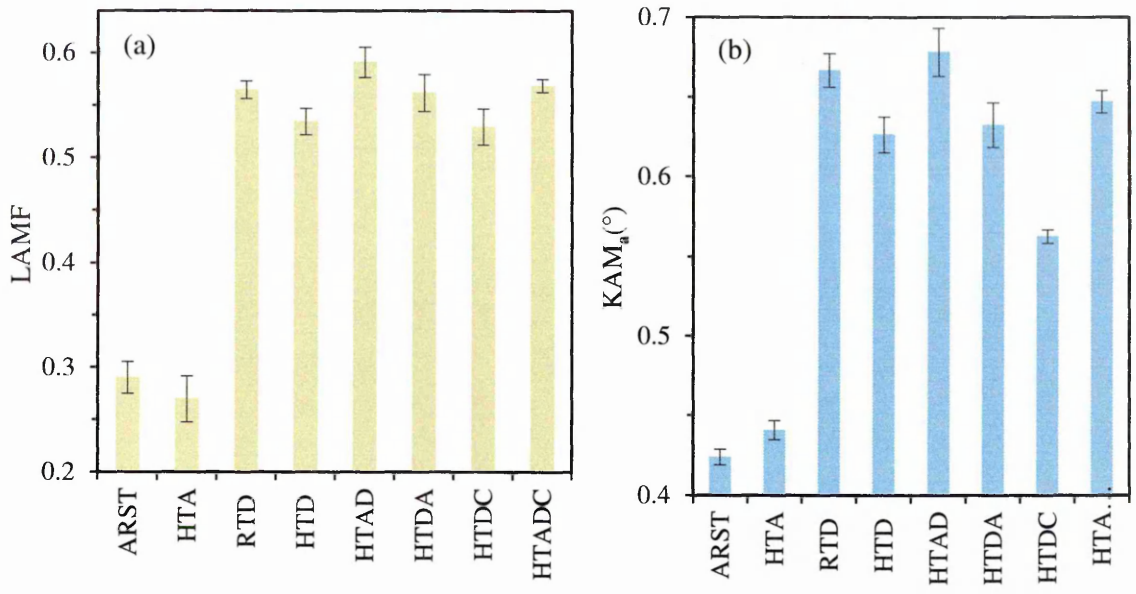

Fig. 5.10. Development of (a) LAMF, and (b) KAM_a in Type 316H stainless steel deformed as in Table 5.2.

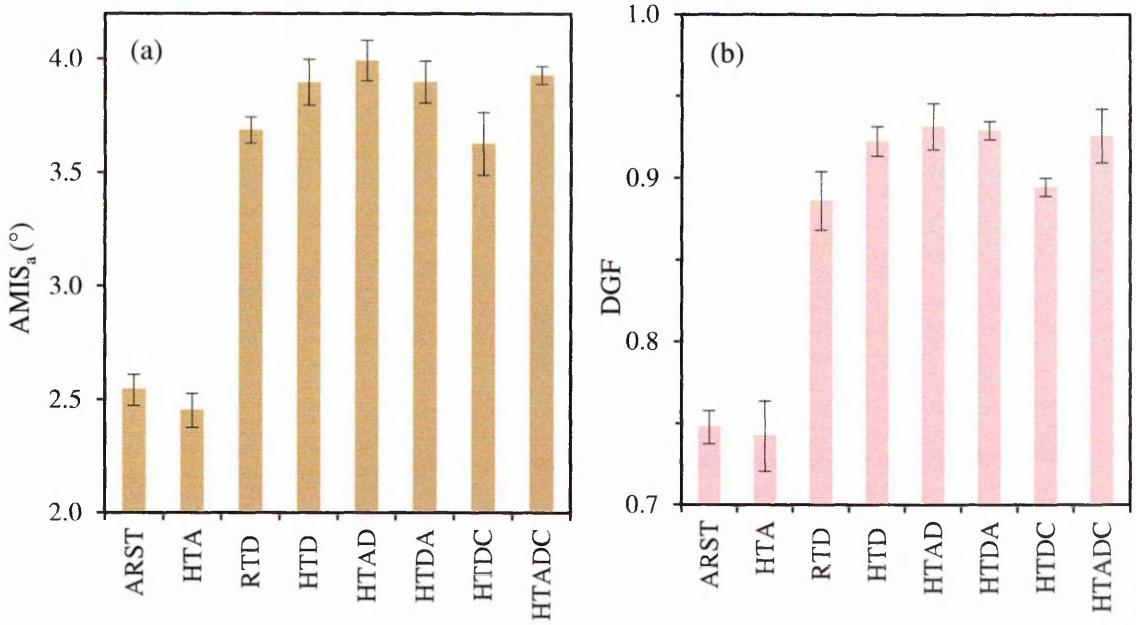

Fig. 5.11. Development of (a) $AMIS_a$, and (b) DGF in Type 316H stainless steel deformed as in Table 5.2.

Comparison between the misorientation development in the HTDC and HTADC specimens (see Fig. 5.10) indicates that during creep deformation, the local misorientation builds at a significantly faster rate in the thermally-aged steel than in un-aged steel. This

trend is also seen at the macroscopic scale (see Table 5.2) where the thermally-aged specimen exhibits a higher minimum creep strain rate than the un-aged specimen. At a longer scale, the misorientation build-up in thermally-aged steel is still faster than in un-aged steel as seen in Fig. 5.11. This can again be attributed to the effects of precipitates in the thermally-aged steel as explained previously.

The comparison between the un-aged specimens (HTD and HTDC) and the thermally-aged specimens (HTAD and HTADC) indicates that the misorientation built-up is less in creep than in plastic deformation. As seen in Fig. 5.10 and Fig. 5.11, this reduction is captured by all metrics meaning it exists at both short- and long-range scales, albeit not so obviously for the thermally-aged specimens at the longer scale. It is shown later in Chapter 7 that the accumulated misorientations resulting from creep deformation only adds to the existing misorientations. It is possible, therefore, that during creep deformation the balance between the hardening and recovery processes at the time the test was interrupted influenced the resultant values of the misorientations, with hardening expected to give higher values. This assertion is supported by the way local deformation is distributed in the deformed specimens. As seen in Fig. 5.12 (d and e) the distribution of deformed zones within grains in crept specimens is different from that of plastically deformed specimens shown in Fig. 5.12 (b and c). This may imply that when the creep test was interrupted, dislocations were bypassing obstacles within the grains, through the thermally activated processes of climb and glide, and causing accumulations at much longer length scales. It is possible that the slight decline in the accumulated misorientation resulted from reduced dislocation densities within the grains. In the current study it was not possible to accumulate large creep strain within a reasonable time since the specimens exhibited high creep resistance as revealed by Fig. 5.9.

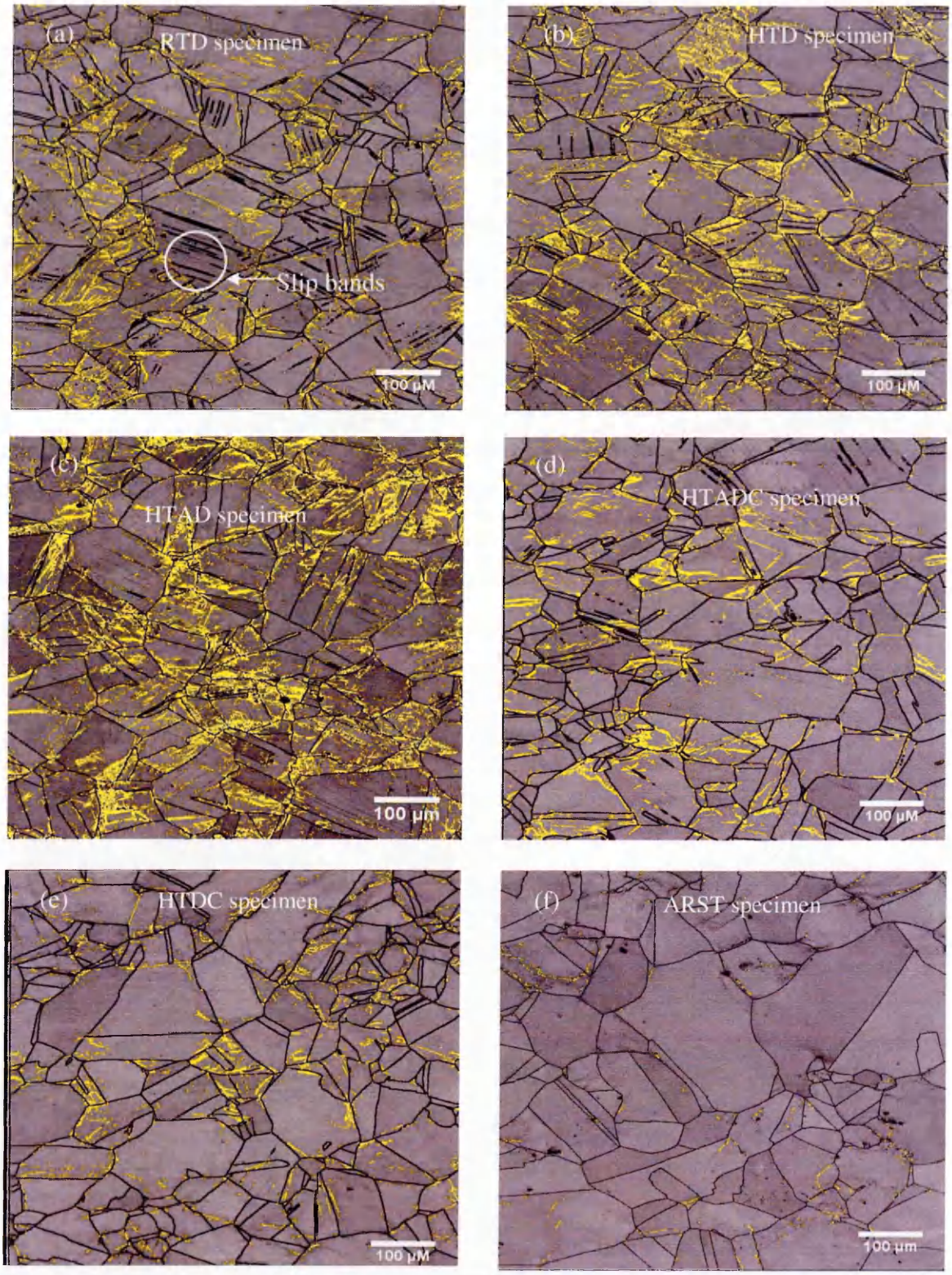

Fig. 5.12. Image quality maps of Type 316H stainless steel showing distribution of deformed zones ('yellow patches') in specimens deformed as in Table 5.2. Less deformation within grains in the crept specimens (d) and (e) than in the plastically deformed specimens (a), (b) and (c). Deformed zone are represented by misorientations between 2° and 15° while grain boundaries by misorientations >15° (continuous black line).

The thermal aging of Sample D at 550°C for 1,000 hours introduced detectable intergranular precipitates (see Fig. 5.7) while none were detected in the HTD specimen (see Fig. 5.13) whose test took about 0.5 hours. Limited precipitation following pre-straining of an annealed Type 316 stainless steel at 400-600°C has also been reported in the literature [62]. It is likely, therefore that the precipitation seen in the HTAD (see Fig. 5.14a) and the HTDA (see Fig. 5.14b) specimens developed during the thermal aging stage. The application of stress on Type 316 steel at 550°C for prolonged times (e.g. 1550 hours in the current case) promotes intergranular precipitation as seen in the HTDC specimen (see Fig. 5.15a) which was crept by 0.004 strain at 320MPa. The combined effects of thermal aging and creep in the HTADC specimen could therefore have led to an increased precipitation as seen in Fig. 5.15b.

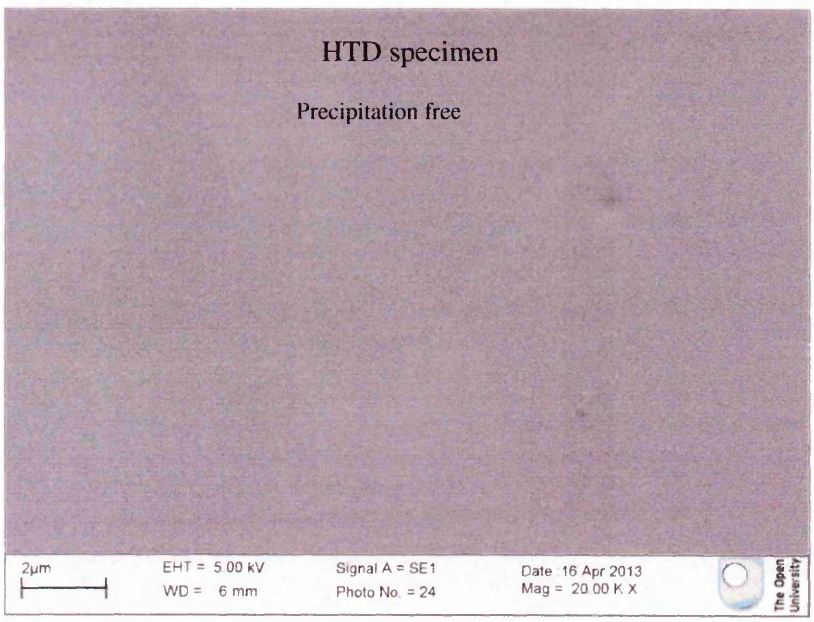

Fig. 5.13. SEM micrograph of Type 316H stainless steel deformed at 550°C showing a precipitation free microstructure.

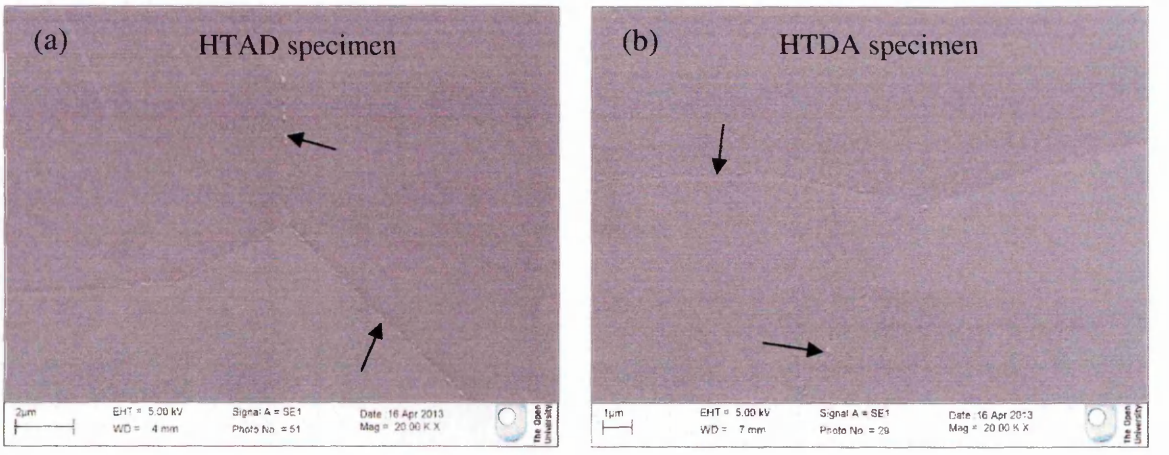

Fig. 5.14. SEM micrographs showing intergranular precipitation (arrows) in Type 316H stainless steel plastically deformed as in Table 5.2.

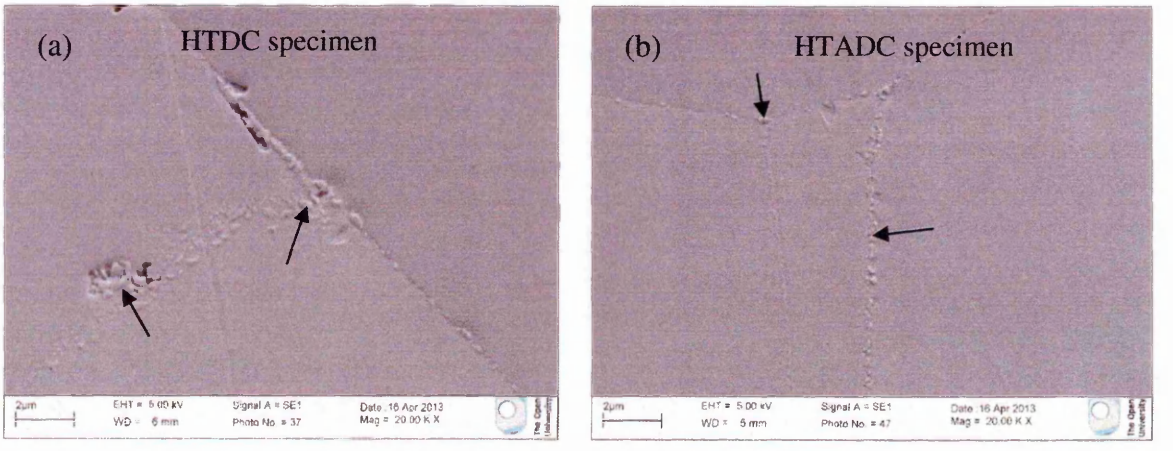

Fig. 5.15. SEM micrographs showing intergranular precipitation (arrows) in Type 316H stainless steel crept as in Table 5.2.

The reduced creep resistance of the HTADC specimen (see Fig. 5.9), despite showing higher strength than the HTDC specimen during the tensile test is surprising and may be attributed to grain boundary sliding (GBS) owing to the intergranular precipitates coarsening. GBS is considered to increase with increasing temperature and/or reducing strain rate, and so is expected to be more prevalent in creep deformation above the equicohesive temperature (ECT) [31]. At ECT the grain's interior and boundary have comparable shear strength. In Type 347H stainless steel, improvement in the creep rupture time due to an increased number density of fine $M_{23}C_6$ intergranular precipitates has been reported by [47] who also observed a reduction in the mean grain boundary displacement

as the number density of intergranular precipitates increased. It is possible that an optimum precipitate size and spacing exists which offers the best creep resistance through a microscopic grain boundary locking mechanism. This locking mechanism may be related to the actual grain boundary contact area and therefore its effect reduces with increasing size and spacing of intergranular precipitates.

In the present case it is plausible that the precipitates that developed in HTADC specimen during the thermal aging stage continued to coarsen during the subsequent creep deformation [17]. This was not the case for the HTDC specimen deformed similarly; since its starting microstructure did not have any detectable intergranular precipitates (see Fig. 5.13). It is therefore logical to assume that there was nucleation of precipitates in the HTDC specimen and coarsening of precipitates in the HTADC specimen during the period of creep deformation making the latter more susceptible to GBS and increased creep strain rate. As explained in section 2.2.2.3, resistance to dislocation movement reduces with the coarsening of precipitates. The thermal history of the HTADC specimen could also have resulted in relatively high sensitisation, weakening the regions bordering the grain boundaries [17, 160] and so making them more susceptible to accelerated creep deformation. The extensive deformation near the grain boundaries in the HTADC specimen (Fig. 5.12d) unlike in the HTDC specimen (Fig. 5.12e) may indicate occurrence of GBS since such deformations would be necessary in maintaining continuity at the grain boundaries as described in section 2.2.2.4. However, this evidence is not conclusive as the dislocations can also accumulate along the grain boundaries from the grain's interior through the climb and glide process during deformation.

The propensity for GBS decreases with increasing strain rate, and so its effect is minimal during relatively fast tensile tests. It is possible that the intragranular precipitation in the HTADC specimen offered additional obstacles to dislocation motion necessitating

the application of higher stresses to generate similar deformation to that in the HTDC specimen (see Fig. 5.8).

5.3. The influence of grain size on strain-induced misorientation development

The mechanical properties of metals are frequently related to the grain size through the well known Hall-Petch equation [31] which shows an inverse relation between the yield stress and the square root of the grain size. Strain hardening is closely associated with changes in the dislocation density (ρ) which can in turn be related to the flow stress using equation $\sigma = \sigma_i + \alpha G b \rho^{0.5}$ (see section 2.2.2.1). A plausible implication of the two equations is that at a given flow stress level, grains of different sizes will have different dislocation densities and therefore different degrees of lattice orientation changes.

5.3.1. Materials

In the current study the investigation of grain size effects on the misorientation development was based on Sample B and Sample C whose average grain sizes were 93±12μm and 35±1μm, respectively. In this section, Sample B and C will also be referred to as the course- and fine-grained steel, respectively. The two steels exhibited no evidence of precipitation in their microstructures and so the influence of precipitates on the misorientation development was assumed to be negligible. However, it should be noted that, even though the two steels are classified as Type 316H stainless steels, their chemical compositions are slightly different, as given in Chapter 4. Although the difference in the misorientation evolution that may arise due to compositional variations has been assumed to be negligible in the present study, it is possible that small differences in misorientation may exist due to solute-dislocation interactions in the solid-solution (see section 2.2.2.2). For instance, the addition of nitrogen in austenitic steels affects their mechanical properties [161], as it favours planar dislocation slip by lowering stacking fault energies [162].

5.3.2. *Mechanical tests and EBSD measurements*

Specimens from Sample B and Sample C were deformed at room temperature under the conditions given in Table 5.1 and following the procedures given in Chapter 3. EBSD measurements were carried out on the deformed specimens as outlined in Chapter 3 and the accumulation of misorientations as a function of strain was quantified through the LAMF, KAM_a, $AMIS_a$, and DGF metrics.

5.3.3. *Results and discussion*

From Fig. 5.2b it is evident that the local misorientations as measured by KAM_a built at a faster rate in the fine-grained steel (Sample C) than in the coarse-grained steel (Sample B). As explained in section 2.2.2.4, a homogeneous deformation is typically found in fine-grained materials whereas in coarse-grained materials, large discrepancies in strain distribution exist between the core and the regions bordering the grain boundaries [31]. The uniformity and higher density of dislocations in fine-grained materials would give relatively high local misorientation values as the possibility of lattice rotations between adjacent measurement points is high. In the case of coarse-grained materials, the low densities of dislocation and their non-uniform distribution may limit the dislocation-dislocation interactions. This would result in relatively low local misorientation values. However, when the local misorientation development was assessed through LAMF, no significant difference was observed between the fine- and coarse-grained steels at equivalent strains, as seen in Fig. 5.2a. Generally, a high local misorientation is expected in fine-grained steel but its larger fraction of high angle misorientations (>15°) per unit volume than that of coarse-grained steel, serves to reduce its LAMF. This mean that LAMF correlation with the applied strain can only be used for assessing strain in materials of comparable average grain size with the calibration material.

From Fig. 5.6 it is evident that the fine-grained steel (Sample C) exhibited a wider spread in the local misorientation distribution than the coarse-grained steel (Sample B) at comparable strain levels. The wider spread is an indication of a greater accumulation of GNDs (see section 2.2.2.4) which have increased both the number and the magnitude of the available misorientations.

The grain size had little effect on the development of long-range misorientations as shown in Fig. 5.3, where the $AMIS_a$ and DGF values from the fine- and coarse-grained steels were comparable. This is possibly due to the way AMIS is computed, where uncorrelated misorientations are averaged within the grain.

5.4. Summary

The key findings in this chapter can be summarised as follows;

- Intergranular precipitates were found in Sample D after thermal aging at 550°C for 1000 hours without load while no detectable precipitation was found following a tensile deformation at 550°C using a strain rate of $4.0x10^{-5}s^{-1}$ over a period of 0.5hrs. Intense intergranular precipitation occurred after a constant load creep for 1550 hours at T= 550°C and σ = 320MPa. Precipitation at 550°C in the Type 316 stainless steel studied is therefore judged to be time and stress dependent.
- Lower creep resistance was observed at 550°C and 320MPa in material with prior thermal aging compared to material with no prior thermal aging.
- Thermal aging at 550°C for 1000 hours had little effect on the local and long-range misorientations already built in the steels studied.
- The grain size had little effect on the long-range misorientation build-up but at a local scale the build-up was faster on fine-grained steel than coarse-grained steel.

- The evolution of long-range misorientations during plastic deformation was little influenced by precipitate-dislocation interactions, but on a local scale, misorientation development during deformation was faster in aged steels than in un-aged steels.
- The DGF metric had least sensitivity to either grain size or precipitation effects and can therefore be used to characterise global macroscopic strain in Type 316 stainless steel regardless of its thermal history.

CHAPTER 6

THE INFLUENCE OF PLASTIC STRAIN AND STRAIN RATE ON MISORIENTATION DEVELOPMENT

6.1. Introduction

The assessment of plastic deformation in materials in high temperature applications is important since such deformation influences their creep behaviour [17, 48, 50], their susceptibility to stress-corrosion cracking [17] and their corrosion resistance owing to carbide precipitation on dislocation structures [24].

This chapter discusses the influence of plastic strain on the development of strain-induced misorientations in service-aged Type 316 austenitic stainless steel. Section 6.2 describes the mechanical tests, EBSD measurements and data analysis performed on the service-aged steel. The section discusses the influence of deformation mode, temperature, strain, and strain rate on the development of misorientation. The statistical approach adopted in the analysis of the strain-induced misorientation development is also discussed in this section. Section 6.3 reports on the evolution of strain-induced misorientation within specific grains in a sample as assessed through *in-situ* EBSD measurements. Section 6.4 describes a model that predicts the distribution of local misorientations as a function of strain, strain rate and measurement step-size. Finally, section 6.5 provides a summary of the key findings in this chapter.

6.2. Studies on the influence of plastic strain and strain rate on misorientation development

The investigations were based on the service-aged steel (Sample A) and the main drive for using this material was the fact that there is little published work on the evolution of strain-induced misorientations in aged materials. The current research is aimed at providing insights on this area.

6.2.1. Mechanical tests

In order to determine how misorientation evolves as a function of induced plastic strain, a series of uniaxial tensile and compressive tests were conducted both at room temperature and at 550°C. A summary of the mechanical tests performed is listed in Table 6.1. The tests which were carried out at constant strain rate and interrupted at specific strains included: room temperature tensile (RTT), high temperature tensile (HTT), room temperature compression (RTC), high temperature compression (HTC), and high temperature strain rate (HTST) tests. The geometries of the tensile and compression specimens are given in Chapter 3. The specimens were extracted from the service-aged steel by wire EDM and deformed uniaxially in tension and compression using the procedures outlined in Chapter 3 and the conditions listed in Table 6.1. To ensure all specimens had almost similar chemical composition and mechanical properties, they were extracted at adjacent locations from the same block of Sample A denoted as *HRA 1a* in Chapter 4.

Table 6.1: Mechanical tests condition for service-aged Type 316H stainless steel.

Test	True plastic strains (ε)	Strain rate (s^{-1})	T (°C)
RTT	0.054, 0.098, 0.143, 0.187, 0.227	2.0×10^{-4}	24
HTT	0.011, 0.031, 0.058, 0.102, 0.14, 0.176, 0.223	3.5×10^{-5}	550±1
RTC	0.065, 0.081, 0.145, 0.19, 0.226	5.0×10^{-4}	24
HTC	0.06, 0.087, 0.142, 0.179, 0.231	4.0×10^{-5}	550±1
HTST 1	0.098	3.5×10^{-3}	550±1
HTST 2	0.098	3.0×10^{-5}	550±1
HTST 3	0.098	4.0×10^{-6}	550±1
HTST 4	0.098	4.0×10^{-7}	550±1

6.2.2. EBSD measurements

EBSD measurements were carried out on all deformed specimens as described in Chapter 3. To ensure good representation of the misorientation development in each

deformed specimen, at least four orientation maps were taken at different locations on the mid-plane and average values reported.

The accumulation of misorientations as a function of induced plastic strain was quantified using the LAMF, KAM_a, $AMIS_a$ and DGF metrics described in Chapter 3. The first two metrics were used to assess the development of short-range misorientations that were spatially correlated (local misorientations) while the other metrics assessed the development of long-range misorientations that were spatially uncorrelated. In this chapter the error bars on the EBSD/strain correlations are ± the standard error of the mean metric value of at least 4 orientation maps from each of the deformed samples. A sample of orientation maps are provided in Appendix 3 (A and B).

6.2.3. Mechanical tests results

The flow curves obtained in HTT and RTT tests are shown Fig. 6.1. The uniformity of flow behaviour at each temperature and strain rate is demonstrated by the overlay of the curves indicating that the deformed samples are representative of the plastic strain at each condition. Flows curves at 550°C were characterised by serrations (owing to dynamic strain aging, see later in section 6.2.5.1) and a lower flow stress at a given strain than the 24°C curves. The strain hardening rates ($d\sigma/d\varepsilon$) calculated from the true stress (σ) vs. true strain (ε) curves at 0.05 strain were about 2140MPa and 2670MPa for the HTT and RTT tests, respectively. Further details on the mechanical properties are provided in section 4.3.1.

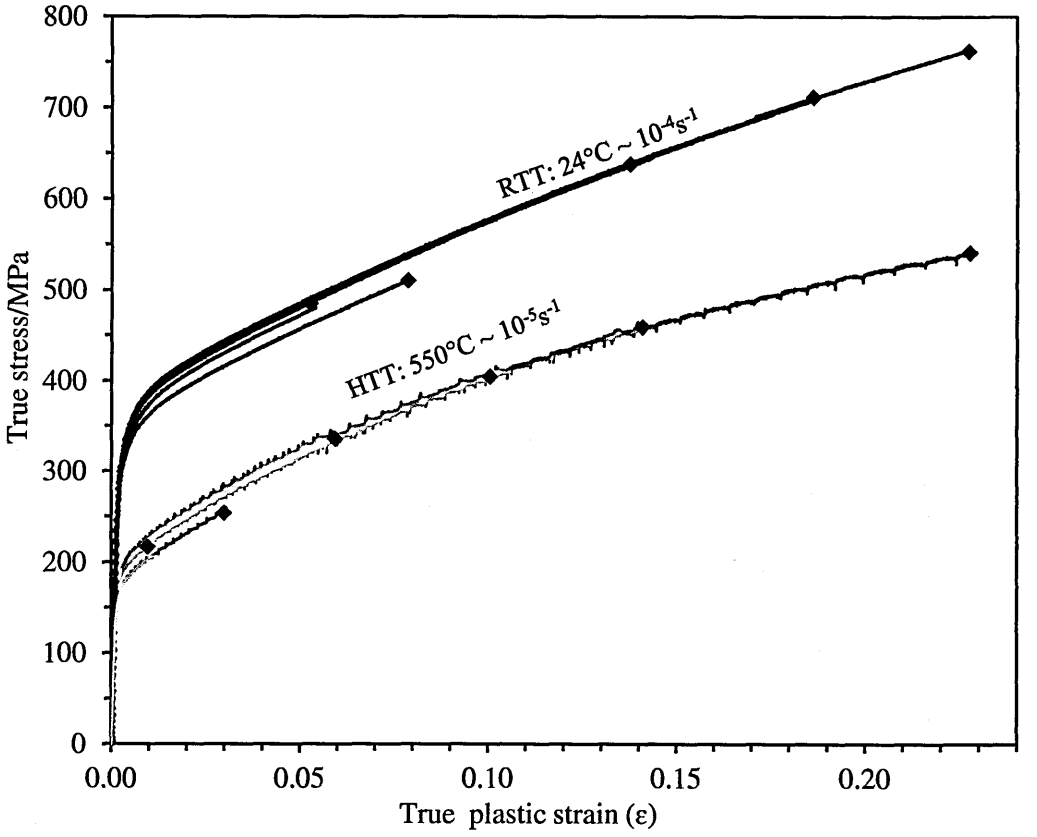

Fig. 6.1. Tensile flow curves at 24°C and at 550°C for service-aged Type 316H stainless steel.

The flow behaviour was similar in compression as seen in Fig. 6.2 with a strain hardening rate of about 2760MPa at a true strain of 0.05 at 24°C. It should be noted that the flow curves for the RTC tests were based on extensometry measurements while those for the HTC tests were based on the crosshead displacement measurements (see section 3.2.2), which could have given them different profiles. The use of an extensometer in the RTC tests enabled direct comparison of the strain hardening rate with the RTT tests.

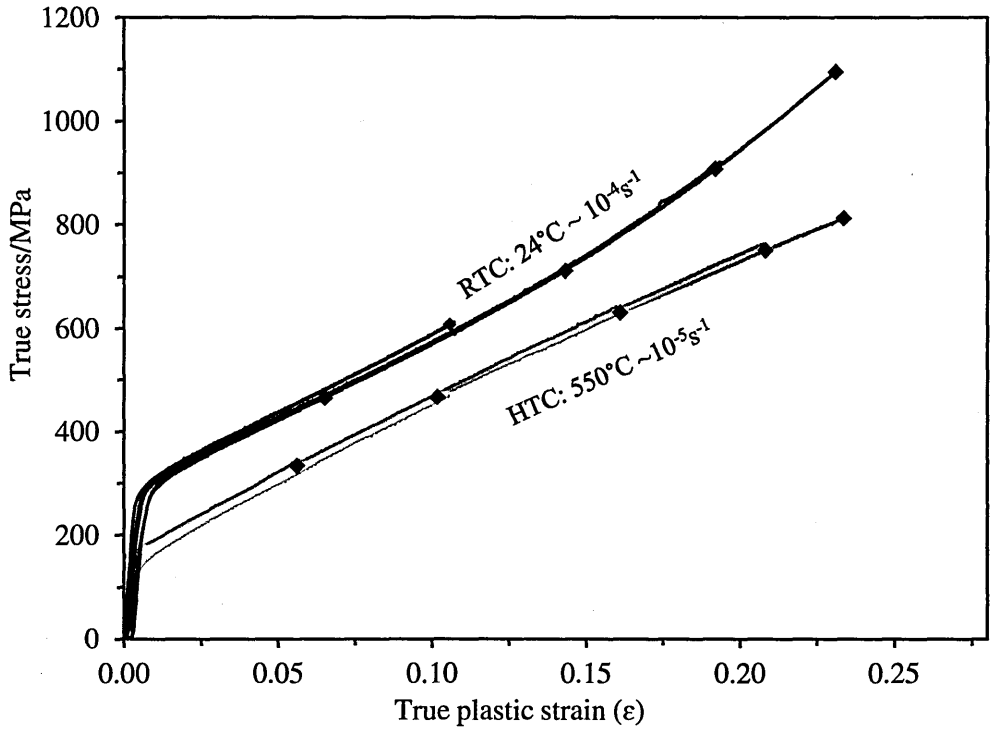

Fig. 6.2. Compressive flow curves at 24°C and at 550°C for service-aged Type 316H stainless steel.

In the current study, the coefficients associated with barrelling, height and ovality of the HTC specimens were all within the allowed limits as specific in [130] even though they increased slightly with the applied compressive strain as summarised in Table 6.2. The values of ovality coefficient indicated minimal effects of texture and the microstructure on macroscopic deformation behaviour while the height coefficient showed that parallelism of the specimen was maintained during the test. For RTC tests no changes were detected in these coefficients.

Table 6.2: Compression coefficients at 550°C for service-aged Type 316H stainless steel.

True strain	Barrelling coefficient (1.1)*	Height coefficient (0.04)*	Ovality coefficient
0.065	1.010	0.002	1.003
0.087	1.014	0.001	1.004
0.142	1.021	0.001	1.005
0.179	1.023	0.002	1.012
0.231	1.044	0.002	1.007

**Upper limits for valid tests [130]*

Fig. 6.3 shows the flow curves from specimens deformed in tension at 550°C to 0.098 strain at strain rates ranging from $3.5x10^{-3}s^{-1}$ to $4x10^{-7}s^{-1}$. The flow stress at 0.098 strain remained very similar as the strain rate was reduced from $3.5x10^{-3}s^{-1}$ to $4.0x10^{-6}s^{-1}$ whereas a large reduction was seen at $4.0x10^{-7}s^{-1}$. There were conspicuous serrations on the flow curves at the intermediate strain rate of $3.0x10^{-5}s^{-1}$ which were barely detectable at high ($3.5x10^{-3}s^{-1}$) and low ($4.0x10^{-7}s^{-1}$) strain rates. The calculated strain hardening rates at 0.05 true strain were about 2250MPa and 1580MPa for tensile deformation at strain rates of $3.5x10^{-3}s^{-1}$ and $4.0x10^{-7}s^{-1}$, respectively. The 0.2% and 1% proof stresses for the HTST tested specimens are listed in Table 6.3.

Table 6.3: Proof stresses/MPa at 550°C for service-aged Type 316H stainless steel.

Strain rate (s^{-1})	0.2% proof stress	1% proof stress
3.5×10^{-3}	180	220
3.0×10^{-5}	195	225
4.0×10^{-6}	180	220
4.0×10^{-7}	175	215

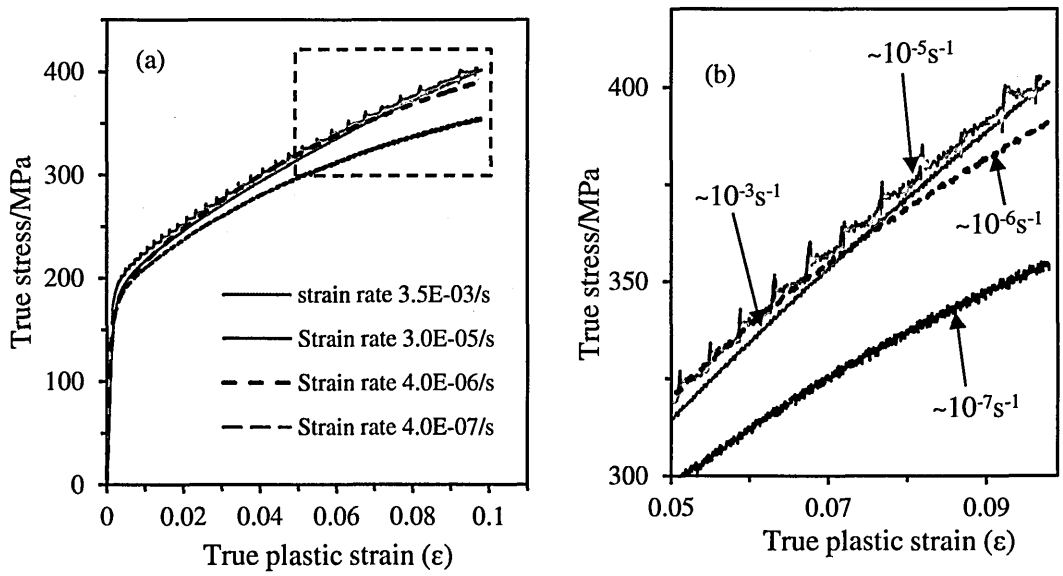

Fig. 6.3. (a) Strain rate dependence of the flow stress at 550°C for service-aged Type 316H stainless steel. (b) Magnification of the dashed region in (a).

6.2.4. *EBSD measurement results*

6.2.4.1. Local misorientation distribution

Fig. 6.4 (a and b) show comparisons between the fit of the lognormal distribution and the gamma distribution to the KAM frequency distributions obtained from samples deformed in tension to 0.102 and 0.223 strain, respectively at 550°C. The mean of the theoretical distribution approaches the sample mean as its data fit improves.

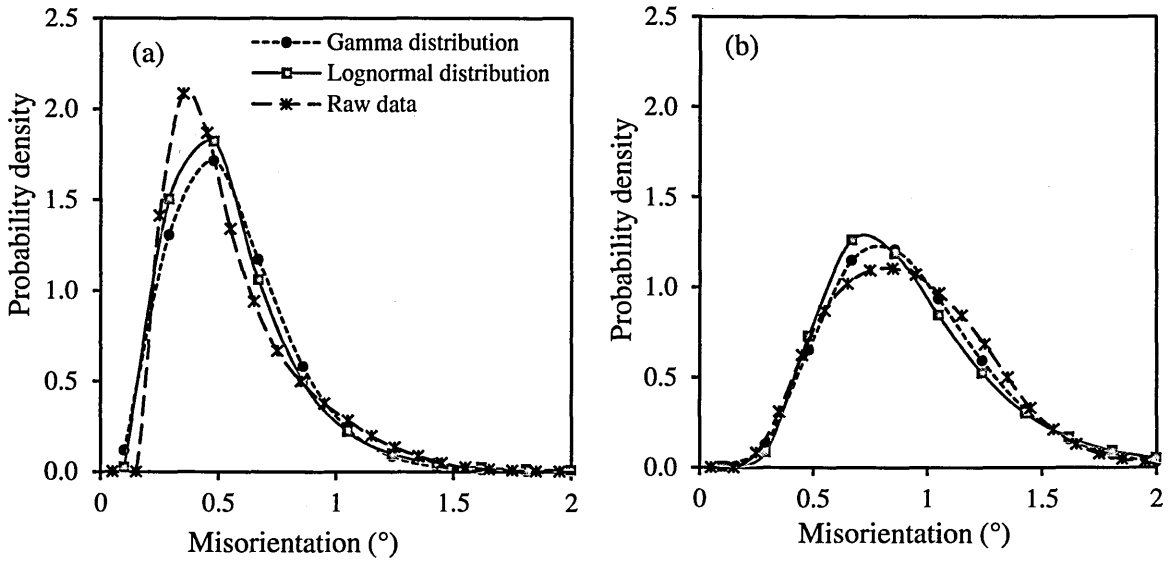

Fig. 6.4. Gamma and lognormal PDF fits to the KAM frequency distribution for service-aged Type 316H stainless steel deformed in tension at 550°C to (a) 0.102, and (b) 0.223 strain.

The quality of the fit of the theoretical PDF was judged using both the statistical variance from the true KAM distributions and the probability plots [163, 164]. For KAM data fitted with gamma, Rayleigh and lognormal PDFs the variance increased almost linearly as the true plastic strain was raised from 0 to 0.223, as shown in Fig. 6.5.

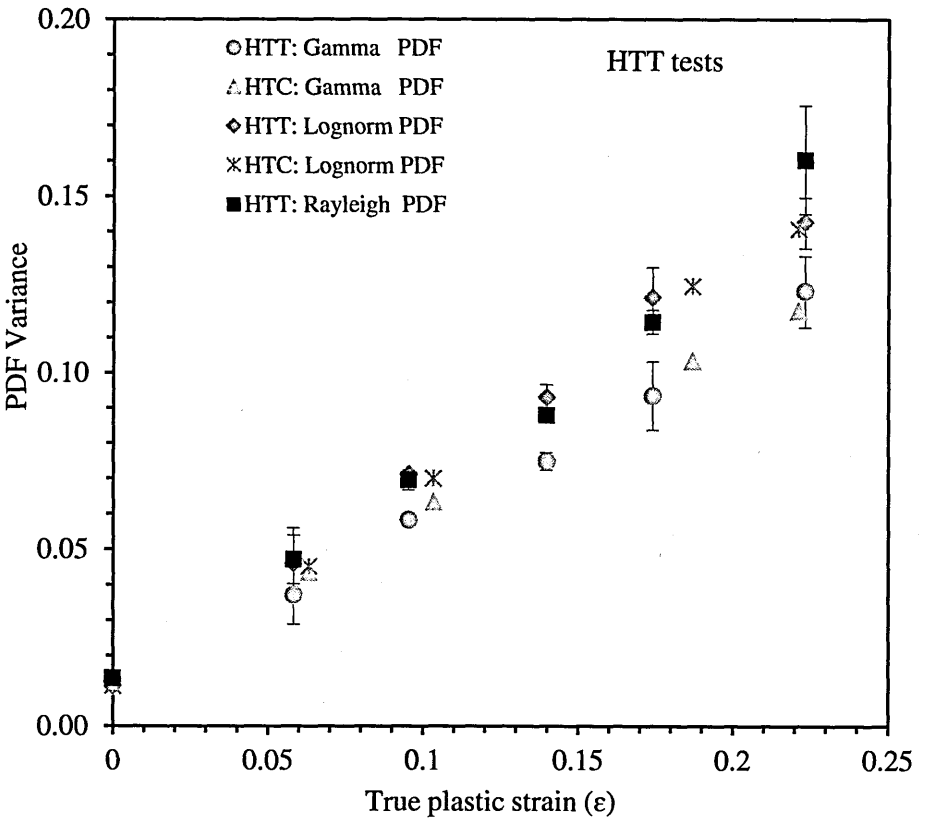

Fig. 6.5. Statistical variance versus true plastic strain at 550°C for KAM data fitted with gamma, Rayleigh and lognormal PDFs.

The gamma PDF fit had consistently lower variance from the experimental data at all strain levels. For true strain >0.1 the divergence in the variances was significant indicating a clearly better fit of the gamma distribution while the difference was not significant for true strain <0.1. However from the probability plots shown in Fig. 6.6, the deviation from linearity of the experimental KAM data indicated that for strains <0.1, a lognormal PDF provided the best fit while the gamma PDF was better for strains >0.1. To obtain a single value to accurately represent the degree of plastic deformation, allowance should be made for the variation of local misorientation distributions with the level of plastic strain in the material. However, in this thesis the calculation of KAM_a was based on the lognormal PDF since the main interest of the study was on the characterisation of small strains (<0.1[13]) such as those associated with creep deformation.

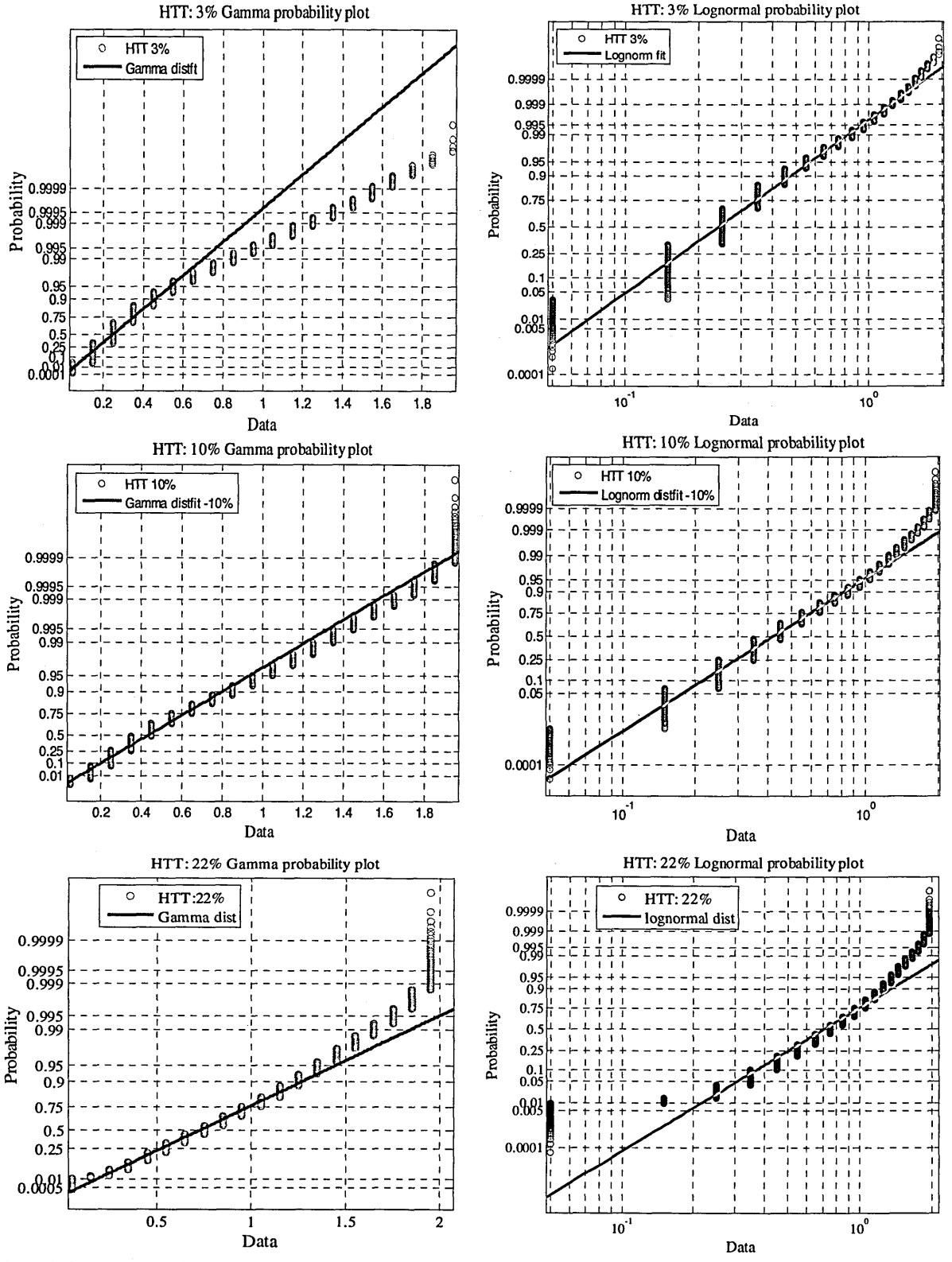

Fig. 6.6. Probability plots of KAM data from service-aged Type 316H stainless steel deformed at 550°C to 0.031, 0.102 and 0.223 strains as in Table 6.1. The reference lines represent the probability plots from theoretical gamma PDF (blue line) and lognormal PDF (red line). The best fitting PDF to the KAM data produces a linear plot.

The frequency distribution of local misorientations acquired from an orientation map showed a spread which increased with increasing strain and strain rate as shown in Fig. 6.7. The local misorientation distributions from HTT and RTT tested specimens deformed to ~0.05 and ~0.18 strains indicated little differences in the skewness as seen in Fig. 6.8.

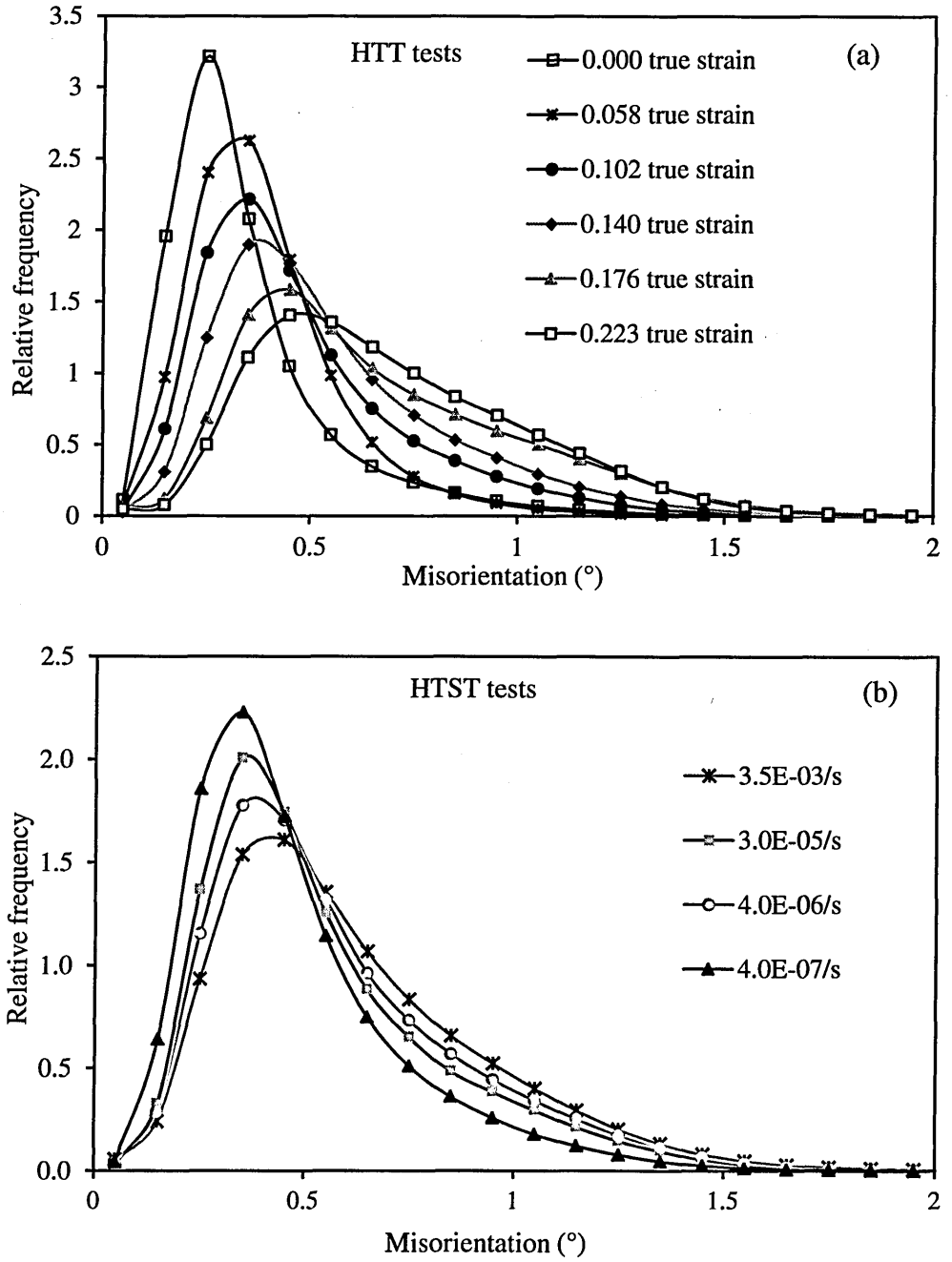

Fig. 6.7. Effects of (a) strain and (b) strain rate on local misorientation distribution for service-aged Type 316H stainless steel deformed in tension at 550°C as in Table 6.1.

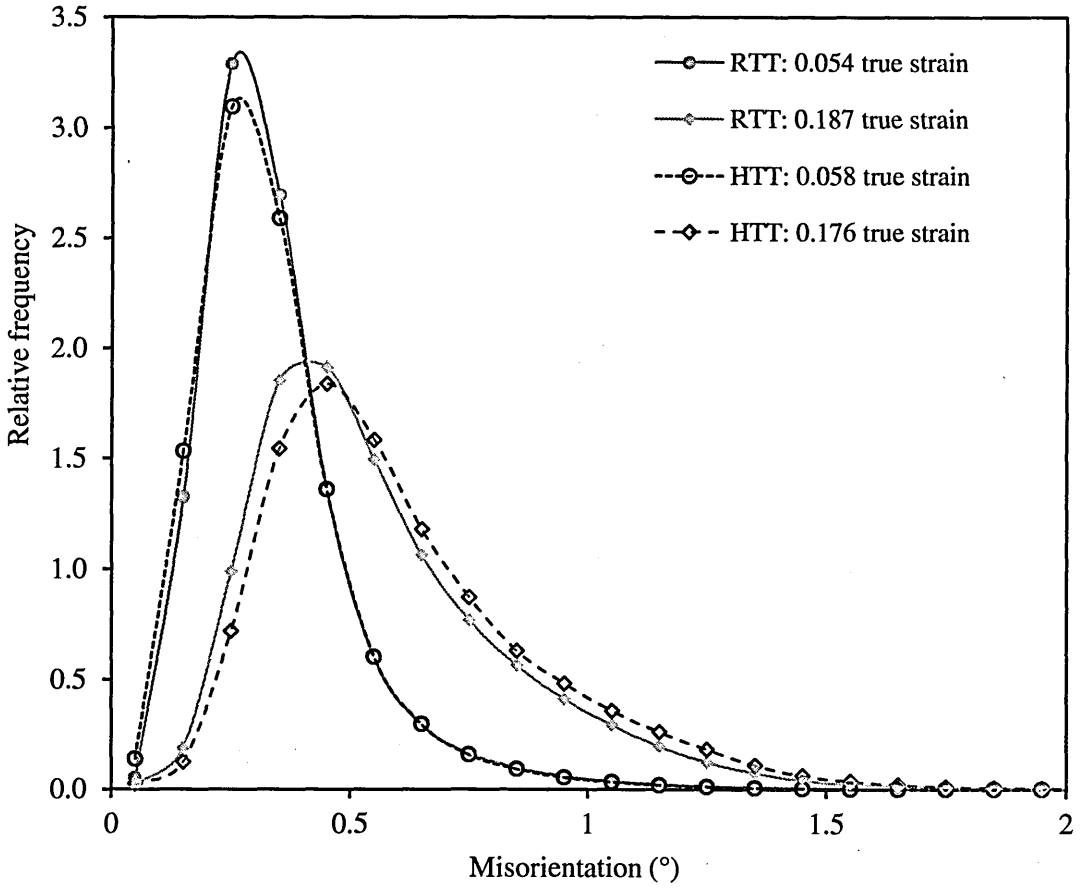

Fig. 6.8. Effect of temperature on local misorientation distribution for service-aged Type 316H stainless steel deformed at 24°C and at 550°C as in Table 6.1.

6.2.4.2. Development of strain-induced local misorientation

The correlation between the KAM_a and the true plastic strain produced at different temperatures, deformation modes and strain rates down to $10^{-5}s^{-1}$ is shown in Fig. 6.9. The KAM_a increased with strain and at a given strain level no significant difference was seen between the values obtained under the different deformation conditions. For strains >0.1 the rate of increase was slightly less and the HTC samples had slightly higher KAM_a than the other service-aged samples.

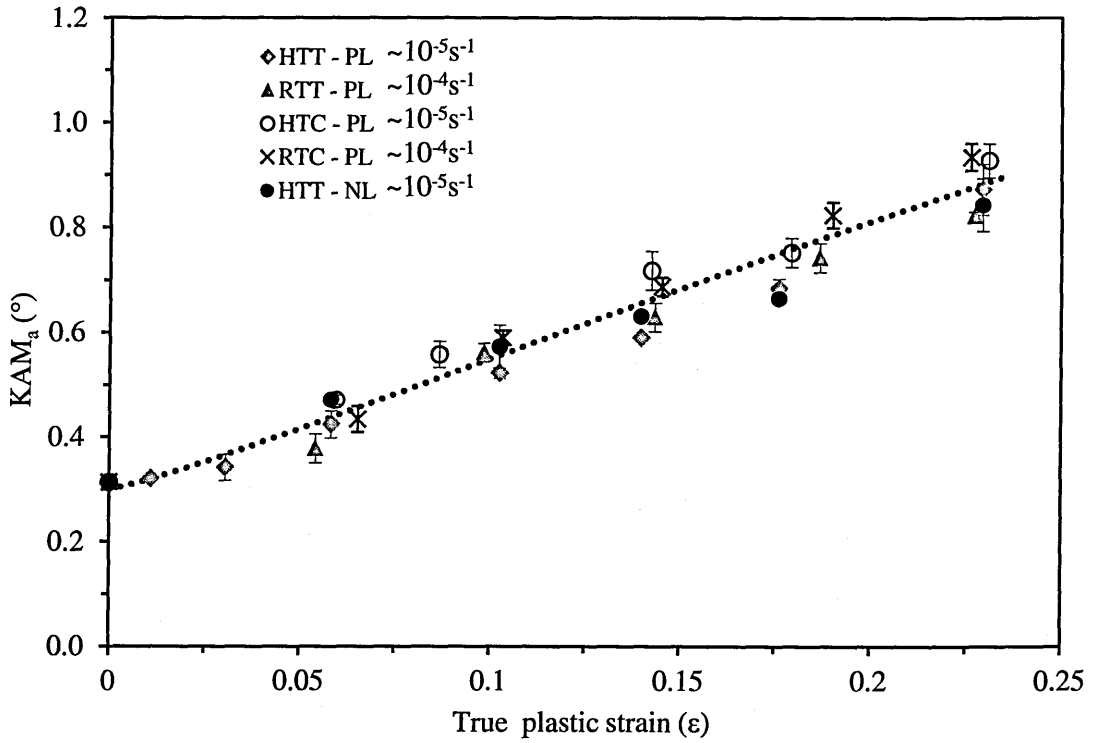

Fig. 6.9. KAM_a versus true plastic strain for service-aged Type 316H stainless steel deformed as in Table 6.1.

The change in KAM_a per unit strain (see Eq. 3.9) increased with increasing strain up to 0.1 and remained relatively constant beyond this as seen in Fig. 6.10.

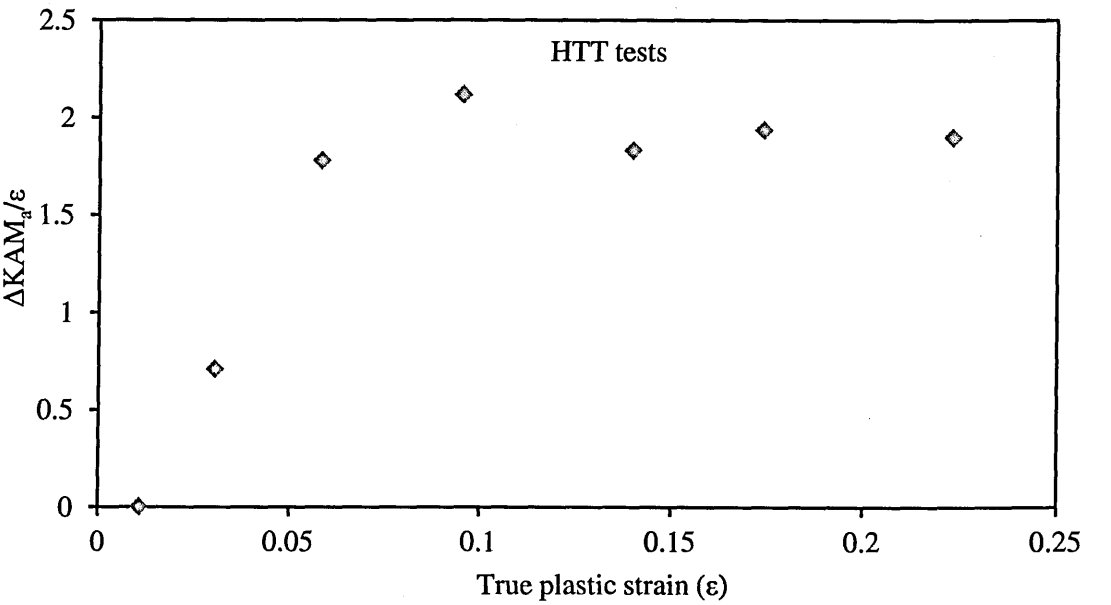

Fig. 6.10. Variation of $\Delta KAM_a/\varepsilon$ with true plastic strain for service-aged Type 316H stainless steel deformed at 550°C in tension.

The orientation of the measurement plane had little effect on KAM_a as the values obtained from the mid-planes parallel (PL) and normal (NL) to the loading axis showed no significant difference. However, KAM_a was dependent on the misorientation range considered during KAM computation as shown in Fig. 6.11.

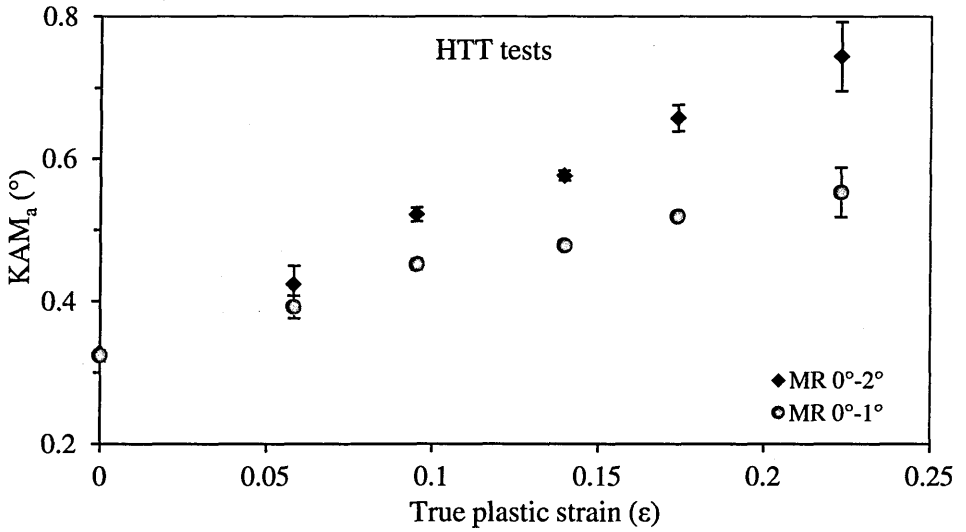

Fig. 6.11. Dependence of the calculated KAM_a on the included misorientation range (MR) for service-aged Type 316H stainless steel deformed at 550°C in tension.

The line in Fig. 6.9 was fitted using a Rodbard function [165] which gave smaller values of residual variance and higher coefficient of determination (R^2) than a linear fit (see Table 6.4). The estimated dislocation densities based on the TEM investigation increased almost linearly with the KAM_a for specimens deformed in tension to strains of 0.058, 0.098 and 0.176 at 550°C as shown in Fig. 6.12.

Table 6.4: Fit statistics for the data shown in Fig. 6.9, Fig. 6.13, Fig. 6.15 and Fig. 6.16.

Metric	Fit statistics	Linear function	Rodbard function
KAM_a	Residual variance	0.002	0.001
	R^2	0.971	0.990
LAMF	Residual variance	0.007	0.001
	R^2	0.950	0.999
$AMIS_a$	Residual variance	0.191	0.208
	R^2	0.942	0.942
DGF	Residual variance	0.018	0.001
	R^2	0.867	0.999

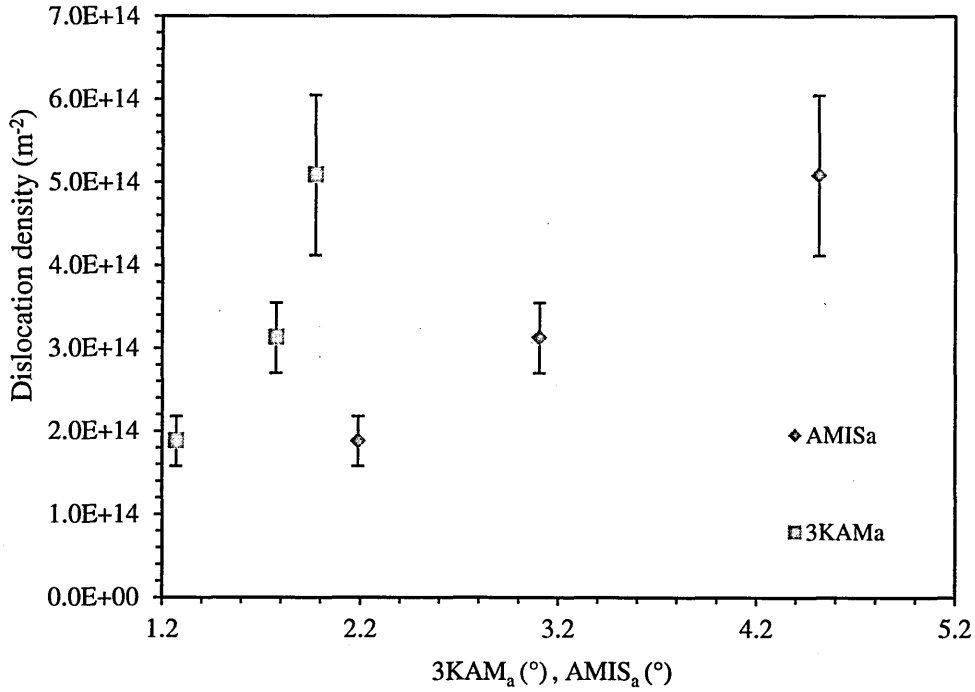

Fig. 6.12. Variations of dislocation densities with KAM_a and $AMIS_a$ for service-aged Type 316H stainless steel deformed to 0.058, 0.098 and 0.176 strains at 550°C.

The relationship between the LAMF and the true plastic strain obtained under different conditions of temperature, deformation mode and strain rate down to ~$10^{-5}s^{-1}$ is shown in Fig. 6.13. Above 0.03 strains, the LAMF increased with the strain at a decreasing rate leading to saturation at strains >0.15. At any given strain level, LAMFs from samples deformed under the different conditions were similar. The LAMF was insensitive to the loading direction as the values obtained from the mid-planes parallel and normal to the loading axis were comparable.

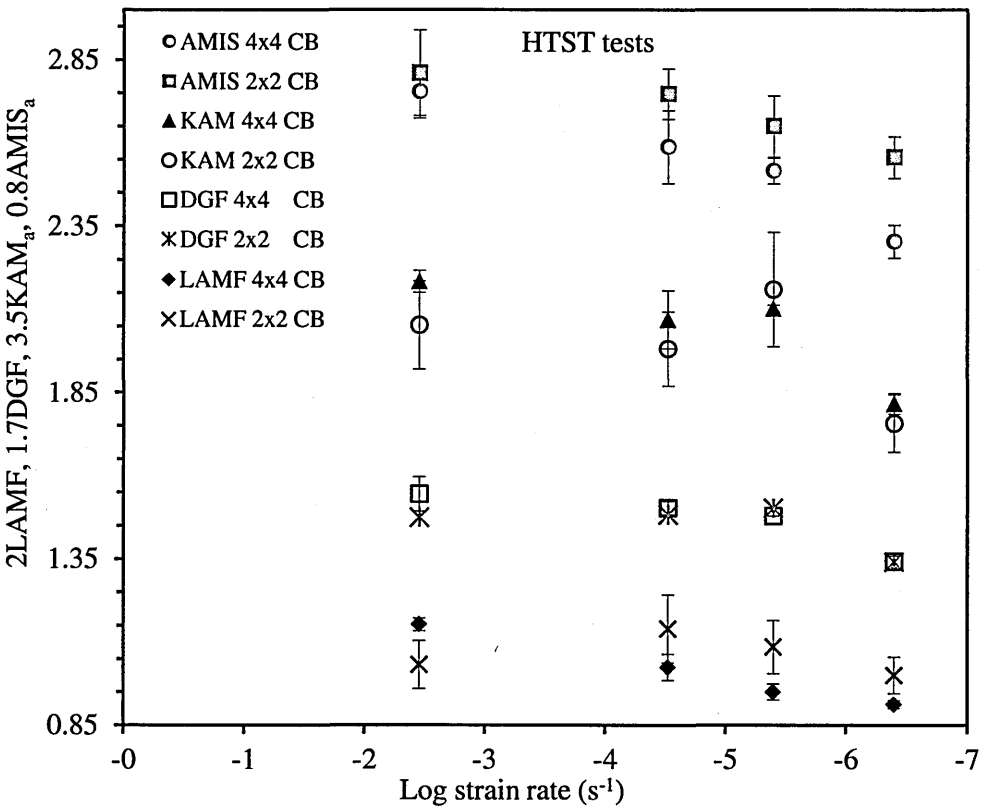

Fig. 6.14. Strain rate dependence of the LAMF, DGF, KAM_a and $AMIS_a$ for service-aged Type 316H stainless steel deformed as in Table 6.1. (CB: EBSD camera binning).

6.2.4.3. Development of strain-induced long-range misorientations

The relationship between the $AMIS_a$ and true plastic strain under different conditions of temperature and deformation mode for strain rates down to ~$10^{-5}s^{-1}$ is shown in Fig. 6.15. The $AMIS_a$ increased linearly with the plastic strain, although there was more scatter in the data for strains beyond 0.1. At each strain level, the variations in $AMIS_a$ obtained under the different deformation conditions were not significant although the values from the HTC samples appeared slightly higher for strains above 0.1. Measurements carried out on mid-planes parallel and normal to the loading axis gave similar $AMIS_a$ values. Dislocation densities based on the TEM investigations increased almost linearly with the $AMIS_a$, as seen in Fig. 6.12 for specimens deformed in tension to strains of 0.058, 0.098 and 0.176 at 550°C.

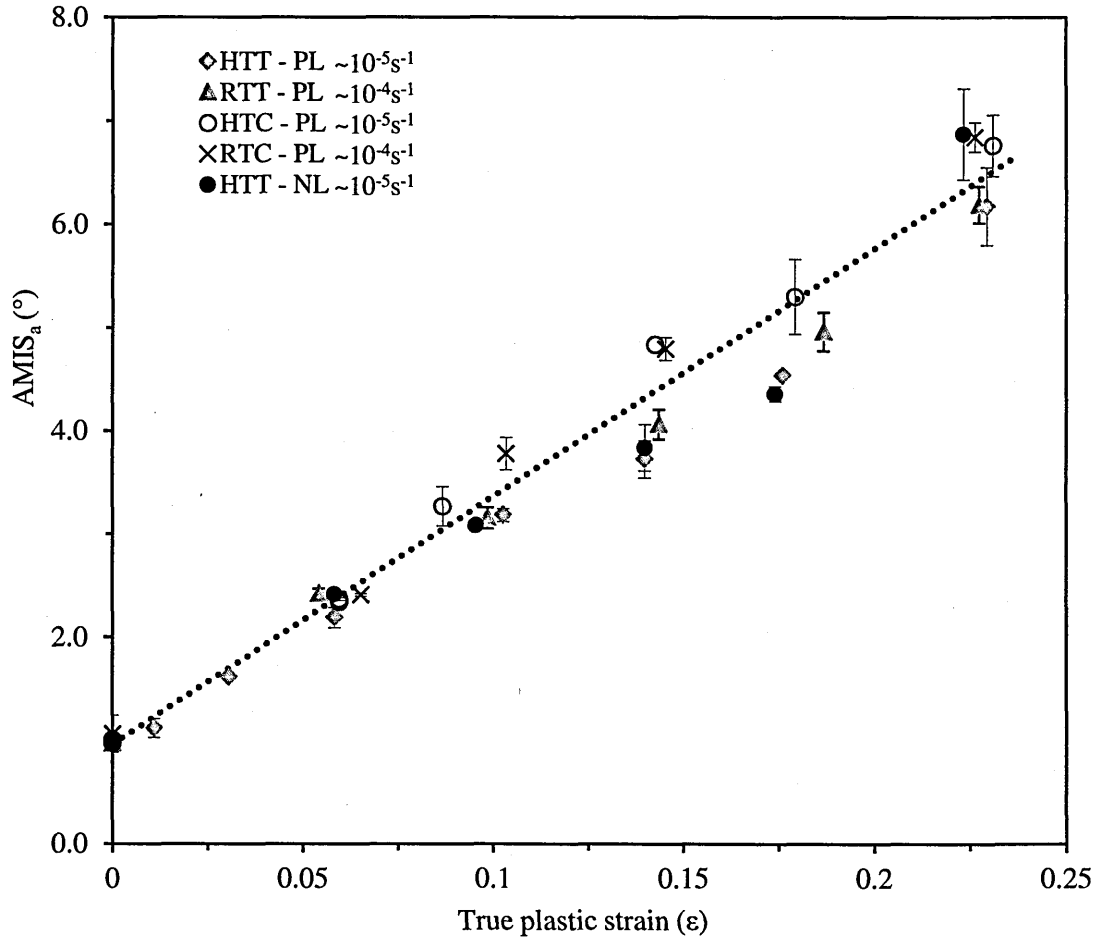

Fig. 6.15. AMIS$_a$ versus true plastic strain for service-aged Type 316H stainless steel deformed as in Table 6.1.

The variation of DGF with the plastic strain under different deformation conditions is shown in Fig. 6.16. DGF increased monotonically with the strain and for strain rate down to ~$10^{-5}s^{-1}$ it appeared insensitive to deformation temperature, mode and orientation of the measurement plane.

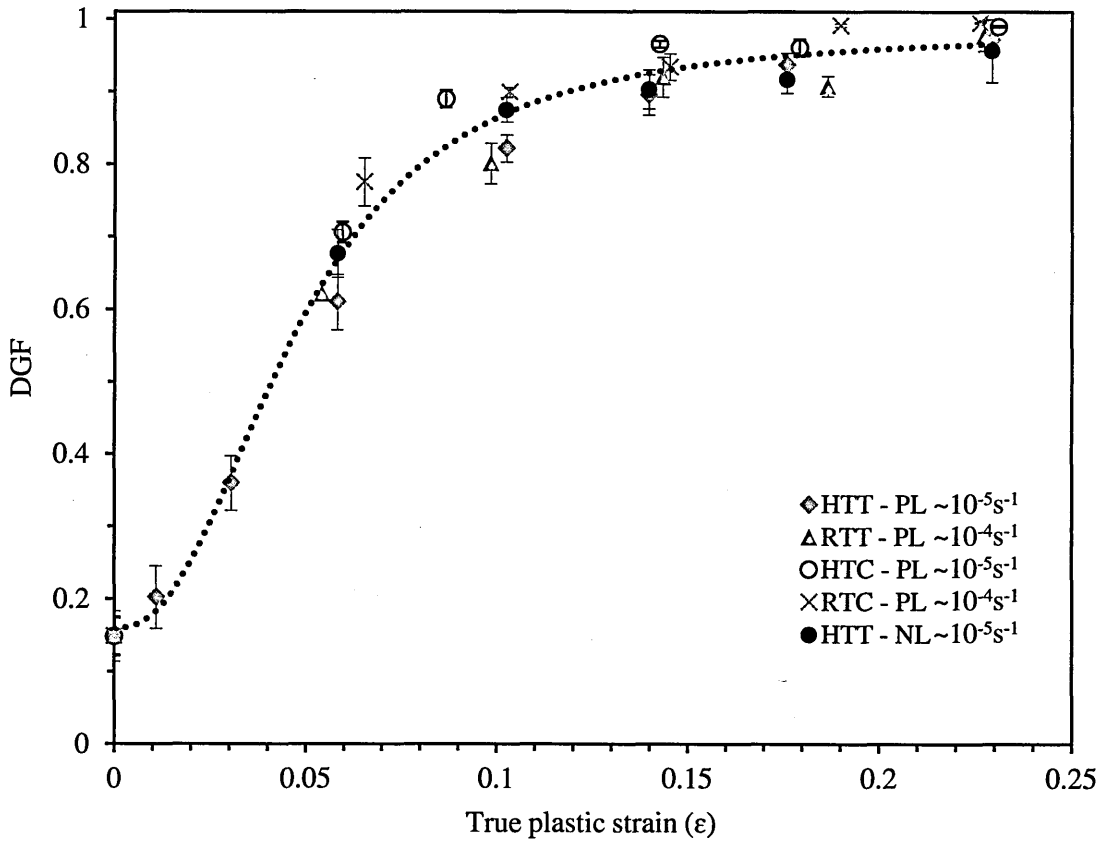

Fig. 6.16. Variation of DGF with true plastic strain for service-aged Type 316H stainless steel deformed as in Table 6.1.

Fig. 6.14 shows $AMIS_a$ as a function of strain rate for samples deformed in tension to 0.098 at 550°C. The $AMIS_a$ reduced monotonically as the strain rate fell from ~$10^{-3}s^{-1}$ to ~$10^{-7}s^{-1}$. The reduction of EBSD camera binning from 4x4 to 2x2 increased the measured $AMIS_a$ but still showed the same trend of variation with the strain rate. In the same figure, DGF decreased with decreasing strain rate and was little affected by the camera binning.

6.2.5. Discussion

6.2.5.1. Flow behaviour of service-aged 316 steel

As shown in Fig. 6.1, Fig. 6.2 and Fig. 6.3 the deformation behaviour of the different samples is consistent and reproducible. The flow behaviours at 24°C and 550°C differ in the values of the flow stress, the presence of serrations and also in the rate of strain hardening, as previously observed [166]. Strain hardening is associated with changes

in the dislocation density (ρ) which can be related to the flow stress using equation $\sigma = \sigma_i + \alpha G b \rho^{0.5}$ [37] so these different flow stresses and strain hardening rates suggest that similar strain levels produced by deformation at different temperatures may be associated with different dislocation densities and therefore different degrees of lattice orientation changes.

When at 550°C the strain rate is decreased from $3.3x10^{-3}s^{-1}$ to $3.0x10^{-5}s^{-1}$ (see Fig. 6.3) the flow stress increases and serrations appear on the flow curve characterised by a pattern of spikes with smaller variations in between, during which period the strain hardening rate is lower than it is overall. A further decrease in strain rate to $4x10^{-6}s^{-1}$ has a marginal effect on the flow stress but almost eliminates the serrations. 550°C is known to be within the dynamic strain aging (DSA) regime for austenitic stainless steel deformed at about $10^{-4}s^{-1}$ [167, 168] and the effects seen here are considered to result from DSA. During DSA dislocation motion is interrupted by segregation of substitutional solute atoms (e.g. Cr) resulting in repeated yielding as the dislocations are unlocked from their solute atmospheres. Similar serrations in Type 316 stainless steel have been observed by [158, 168-170]. The serrations seen here at $3x10^{-5}s^{-1}$ are typical of those seen at the high strain part of the DSA regime arising from the repeated unlocking and passage of deformation bands while at lower strain rates DSA of dislocations moving within the bands [171] produces smaller more regular serrations. Reducing the strain rate to $4.0x10^{-7}s^{-1}$ gives a smoother flow curve with a markedly reduced work hardening rate because at very low strain rates dislocations have more chance of climbing past obstacles.

6.2.5.2. Distribution of local misorientation

Fig. 6.4 and Fig. 6.5 shows that after deformation at 550°C the local misorientation distributions from Type 316 steel strained to <0.1 were closer to lognormal while for strains >0.1 they were better fitted by a gamma distribution (although the variances from

both distributions increased with the applied strain). Similar observations were made from the probability plots (see Fig. 6.6) where deviations from linearity indicated a poor fit of the applied PDF at a given strain level. A lognormal distribution arises from a random variable which can have only positive values. At low strains where dislocation densities are low and local misorientation values may be assumed to have a random occurrence the distribution will be close to lognormal and be strongly skewed towards zero as seen in Fig. 6.7a. As strain and dislocation density increase more misorientations arise and both the mean and the spread of the distribution increase while the skew decreases. If the distribution of local misorientations remained random with increasing strain the distribution would be expected to approach a normal distribution for highly strained coarse-grained material. Accordingly, the variance from the lognormal distribution can be used as a rough measure of the dislocation content of a deformed structure. As seen in Fig. 6.5 the variance from this PDF increases with the plastic strain.

KAM is sensitive to very local changes in orientations and the change towards the gamma distribution with increasing strain found in the present work may reflect both the increased contributions from multiple slip and the greater interaction between dislocations as their density increases and they tend more and more towards a diffuse cellular arrangement. As shown in section 4.3.5, the dislocations in the service-aged steel deformed at 550°C were fairly homogeneously distributed in the grains and at grain boundaries at lower strains but as the strain was increased, dislocations in the grains were arranged in diffuse cell-walls. These observations are consistent with the previous results [151, 172] of Type 316 steel deformed at room and intermediate temperatures ($0.3\text{-}0.5T_m$).

TEM measurements of misorientation angle distributions in deformed metals [173, 174] have been exclusively on materials which form a well developed subgrain deformation structure. The distributions have been determined on the basis of the number of boundaries of a particular misorientation irrespective of their area rather than the result

of sampling the misorientation distribution between points uniformly distributed in space as in EBSD. When attempting to fit the distributions to a Rayleigh distribution, [173, 175] noted a difference between the shape of the distributions (scaled by the mean misorientation) in Al cold rolled to 5% or 10% reduction compared to when it was deformed by 30% or 50% .

Although on the basis of TEM studies [176] it has been concluded that the distribution of misorientations is independent of strain level, careful examination of the compilation of data from Al and Ni tested at room temperature, and Type 304 steel tested at 1000°C show that the measured misorientation distributions are not exactly the same at different strain levels, appearing more skewed at lower strains than at higher strains. Although the local dislocation arrangements differ in subgrain boundaries and diffuse cell-walls and their energies and behaviour will be different, they are equivalent in terms of GNDs and so indistinguishable by EBSD.

As seen in Fig. 6.5, the variances of the Rayleigh, lognormal and gamma distributions from that of the local misorientations were similar at low strains but at plastic strains above 0.1 the gamma distribution gave a much better fit. The relationship between local misorientations and the extent of deformation is very complex. Although in polycrystals five independent active slip systems are necessary to accommodate the macroscopic shape changes of general plastic deformation, local regions within grains frequently deform by fewer slip systems and misorientations arise from different slip systems operating in neighbouring regions of a crystal or from differences in activity on the same slip system [177]. Most work has been on materials with medium to high stacking fault energies so is difficult to apply to 316 steels.

The increasing tendency to a gamma distribution for strains above 0.1 may result from sampling the misorientations from a dislocation structure increasingly organized into

diffuse cells of rather larger size than the separation of the measurement points (see section 4.3.5).

TEM measurements of misorientations have a higher angular resolution than those of EBSD and can reliably detect misorientations <0.1° but sample only a very small volume, making it difficult to get representative results when deformation is highly inhomogeneous, as seen in Fig. 5.5. The strength of EBSD in studying deformation is its ability to sample much larger volumes.

As seen in Fig. 6.7b the evolution of the local misorientations distributions in the service-aged Type 316 steel with imposed plastic strain at 550°C shows a progressive change with strain rates of ~$10^{-3}s^{-1}$, ~$10^{-5}s^{-1}$ and ~$10^{-7}s^{-1}$. The misorientation distribution sharpens towards the lower misorientations as the strain rate is reduced but the result for $10^{-6}s^{-1}$ seems anomalous. There are two possible explanations for the overall change; firstly that dynamic recovery takes place so that dislocations rearrange to lower energy configurations and the misorientation distribution sharpens or secondly that at lower strain rates thermally activated deformation mechanisms other than dislocation generation and accumulation in the body of the grain contribute to the overall strain. In the latter case the reduced dislocation density would account for the observed reduction in both the mean and the spread of the distribution at lower strain rates. In agreement with this explanation, measured dislocation densities were shown in section 4.3.4 to reduce with reducing strain rate. Since the flow curves show that DSA occurs at 550°C, solute interactions with dislocations may also be affecting the distribution of misorientations, which could, depending on the time constants for diffusion of the solute concerned, account for the anomalous behaviour around $10^{-6}s^{-1}$.

Comparison of the misorientation distributions of HTT and RTT tested samples deformed to around 0.18 allows the effect of deformation temperature to be ascertained. The RTT and HTT samples show very similar behaviour with a slight reduction in both the

mean and the spread of the distributions from the HTT as compared to the RTT as shown in Fig. 6.8. The small variations in the distributions are attributable to slight disparities in the applied strains.

6.2.5.3. Influence of strain on local misorientation development

As shown in Fig. 6.9 the relationship between KAM_a and strain is independent of deformation temperature and mode for strain rates down to ~$10^{-5}s^{-1}$. This suggests a similar evolution of the lattice misorientations with strain at 550°C to that at 24°C despite the much lower flow stresses at any given strain (see Fig. 6.1). TEM studies [178] showed a much more rapid increase in overall dislocation density both at the grain boundaries and in the body of the grains of 316L steel deformed at 20°C rather than 400°C. Here the similarity of KAM_a after deformation to the same strain at the two different temperatures despite the difference in flow stresses suggests that locally the GND densities are similar even though the overall dislocation densities may be different.

KAM_a is little affected by the orientation of the measurement plane, suggesting that the spatial distribution of misorientations is independent of the loading direction for true strains up to 0.223. Accordingly, KAM_a can be applied for strain assessment in components where the stress axes are unknown e.g. in weldments.

From the findings of Chapter 5, the development of misorientations in un-aged steel (Sample D) was shown to be different for both room and high temperature deformation. It is plausible that the presence of precipitates in the service-aged steel complicated the development of misorientations resulting in the observed subtle differences in the built misorientations at the two temperatures in the current case.

The strain sensitivity of KAM_a reduces slightly for plastic strains >0.1 as seen in Fig. 6.9 by diminishing increments in KAM_a with increasing strain. It is evident from Fig. 6.10 that change in KAM_a per unit strain remains relatively constant beyond 0.1 strain. The

dislocation density was shown in section 4.3.4 to increase linearly with strain, so this saturation in KAM_a is due to the nature of the metric rather than changes in dislocation behaviour. As seen in Fig. 6.11, KAM_a saturation is dependent on the misorientation range included in its calculation. In the current study, KAM_a was found to increase with increasing dislocation density as seen in Fig. 6.12, although only a limited number of samples were examined. However, since KAM_a is calculated considering only misorientations between 0.15°- 2°, its value saturates at high strains, as more of the local misorientations approach the upper limit. Therefore, the nature of the correlation in Fig. 6.9 depends on the metric's definition, as shown in Fig. 6.11: reducing the included misorientation range makes KAM_a saturate at lower strains. These results demonstrate that the relationship between bounded EBSD metrics such as KAM_a and strain is not always linear at the extremes of the strain range. The saturation tendency introduces an asymptotic region in the graph of KAM_a against true plastic strain (ε) and the data can be fitted by a Rodbard function described by:

$$KAM_a = d + \frac{(a - d)}{\left[1 + \left(\frac{\varepsilon}{c}\right)^b\right]} \qquad \text{Eq. 6.1}$$

where a, b, c and d are constants determined by the position of the lower asymptote, the slope of the linear region, the location of the transition region and the position of the upper asymptote, respectively [179]. The relationship between KAM_a and strain derived from all the data from ex-service material in Fig. 6.9 is described by:

$$KAM_a = 3.314 - \frac{3.014}{\left[1 + \left(\frac{\varepsilon}{0.770}\right)^{1.178}\right]} \qquad \text{Eq. 6.2}$$

Lattice misorientations resulting from GNDs such as arrays of dislocations accumulated at obstacles in the microstructure contribute to the low angle misorientation fraction. Fig. 6.13 shows that as the global plastic strain increases LAMF increases at a reducing rate. This is because at high strains, high angle misorientation (>15°) develop

which reduces LAMF. At low strains the metric's sensitivity is reduced by the orientation 'noise' and by the presence of real low angle boundaries in the microstructure which prevent the LAMF value falling to zero at 0 strain. Like KAM_a, the LAMF is insensitive both to deformation mode and the orientation of the measurement plane.

The relationship shown in Fig. 6.13 suggests that the sensitivity of LAMF to the applied plastic strain is best between 0.03 and 0.15 true strains. The correlation between LAMF and strain can be fitted with a Rodbard function which for all the data from the service-aged material is given by:

$$LAMF = 0.938 - \frac{0.855}{\left[1 + \left(\frac{\varepsilon}{0.089}\right)^{2.818}\right]} \quad \text{Eq. 6.3}$$

As seen in Fig. 6.14, reducing the camera binning, which improves the detection of low angle misorientations, increases the numerical value of LAMF.

6.2.5.4. Influence of strain on long-range misorientation development

Whereas KAM is a very local measure of misorientation, AMIS is a measure of the longer range misorientations across the grain. In contrast to the bounded metrics e.g. KAM_a and LAMF, the whole range of possible misorientations are included in $AMIS_a$ and it increases monotonically with plastic strain as seen in Fig. 6.15. This result suggests a constant increase in crystal/grain deformation resulting from the generation and storage of GNDs as the strain increases from 0 to 0.23, at 24°C and 550°C and at strain rates down to $10^{-5}s^{-1}$. However, at strains >0.1 greater scatter is observed in the data, owing to the slightly higher $AMIS_a$ values of HTC and RTC tested samples. This is attributable to non-uniformity in the deformation due to barrelling, as indicated in Table 6.2. There is also good correspondence between $AMIS_a$ and the TEM-observed dislocation densities as they relate almost linearly as shown in Fig. 6.12 for HTT tested samples. As seen in Fig. 6.14, reducing the camera binning, which improves the EBSD angular resolution, increases the

measured $AMIS_a$ because increasing the accuracy of each orientation measurement improves the detection of very low angle misorientations. Fig. 6.15 indicates that the sensitivity of $AMIS_a$ in assessing plastic strain is good at all strain levels investigated. For the service-aged steel the relationship can be fitted by a straight line of the form:

$$AMIS_a = 24.02\varepsilon + 0.96 \qquad \text{Eq. 6.4}$$

The variation of DGF with the applied strain appears unaffected by deformation temperature, mode or orientation of the measurement plane as seen in Fig. 6.16. The metric is insensitive to local deformation as it considers only the proportion and not the severity of the grains' deformation (see sections 3.4.1.5d and 5.2.1). Although further work is necessary to establish how DGF depends on texture, it seems to offer a very simple way to follow deformation particularly for strains <0.1. From all the data in Fig. 6.16:

$$DGF = 0.985 - \frac{0.825}{\left[1 + \left(\frac{\varepsilon}{0.048}\right)^{2.379}\right]} \qquad \text{Eq. 6.5}$$

6.2.5.5. Influence of strain rate on misorientation development

As seen in Fig. 6.14, both LAMF and $AMIS_a$ decrease with reducing strain rate over the whole range studied, while the calculated KAM_a appears to have a rate sensitivity limit between $4.0x10^{-6}s^{-1}$ and $4.0x10^{-7}s^{-1}$ above which it is insensitive to strain rate. This difference in the metrics' behaviours is probably linked to their sensitivity to small differences in GND density. A decrease in the LAMF and AMIS indicates an overall reduction in spatially correlated and spatially uncorrelated misorientations, respectively (see section 2.4.5.2). This would result in a reduced number of misorientations >2° and also a reduced average misorientation within a grain. Since KAM assesses average local misorientation in the range of 0 - 2°, it is expected to be sensitive to small changes in local misorientation. The apparent insensitivity of KAM_a to constant deformation obtained at strain rates above $4.0x10^{-6}s^{-1}$ may indicate similarities in local GND densities at this strain

rate range. An increased tendency to grain boundary sliding (GBS) at ~$10^{-7}s^{-1}$ might also result in a reduced dislocation content away from the immediate vicinity of the grain boundaries and thus a lower KAM_a. Similarly, the DGF is seen to decrease as the strain rate decreases which again suggests that at lower strain rates a change in the deformation mechanism leads to an overall reduction in GNDs.

All these changes indicate that as the strain rate is reduced the number of GNDs at any particular strain level reduces, which is consistent with the findings of section 4.3.4. This must either be due to fewer GNDs being generated or more being annihilated. If a mechanism such as GBS, which is accommodated in a region close to the boundary, contributes to deformation this need not generate an excess of dislocations of a particular sign in the grain interiors. Observations of grain shape changes during deformation [180] have indicated that GBS can contribute significantly to deformation of 316L stainless steel at intermediate temperatures and low strain rates. At lower strain rates it is possible that thermally activated processes such as unpinning or climb of favourably oriented SSDs (see section 2.2.2.4) which then become mobile may make a greater contribution to the total deformation than at higher strain rates (and so reduce the number of GNDs that need to be generated). Alternatively thermally activated unpinning or climb of otherwise immobile GNDs may allow them to glide to sinks such as grain boundaries or precipitate-matrix interfaces or to annihilate with others of opposite sign.

The consistent indications of an effect of strain rate on the misorientations produced during plastic deformation to a particular strain found in this study are in contrast to previous comparisons on a 2.25%Cr-1%Mo steel between tensile and creep deformations at 600°C [181] which found no significant difference. However, the metric used in that case considered only a very limited number of measurement points in each grain which could have reduced its sensitivity to orientation changes, especially for the creep deformation which is heterogeneous [8]. The strain rate dependence of the strain-

induced misorientation shows that EBSD can be used to discern transitions between deformation mechanisms. It is important to note that all metrics showed a significant reduction in the measured misorientation only after the strain rate was reduced below 4.0 $x10^{-6}s^{-1}$. This can therefore be used as the strain rate limit for the developed empirical correlations between accumulated plastic strain and misorientation metrics (see Eq. 6.2 - Eq. 6.5).

6.3. In-situ studies of strain-induced misorientation development

6.3.1. Uniaxial tensile test in SEM

To investigate the evolution of misorientations within specific grains as a function of the applied strain, tensile tests were performed at 24°C inside SEM under the conditions given in Table 6.5 and following the procedures outlined in Chapter 3. These tests are denoted as ISRTT in this thesis. The specimens whose geometry is given in Chapter 3 were extracted from the block *HRA 1a* of Sample A to enable comparison of their misorientation development with those of the RTT tests (*ex-situ* tests).

Table 6.5: Test program for tensile test in SEM for *in-situ* EBSD measurements.

Interruption point	Interruption strain (ε)	Strain rate (s^{-1})	EBSD measurement time/min
1	0.030	5.6×10^{-4}	65
2	0.140	5.6×10^{-4}	65
3	0.207	5.6×10^{-4}	65
4	0.247	5.6×10^{-4}	65
5	0.285	5.6×10^{-4}	65
6	0.358	5.6×10^{-4}	65
7	0.432*	5.6×10^{-4}	65

**Rupture strain, Test conducted at 24°C*

6.3.2. In-situ EBSD measurements

In-situ EBSD measurements were conducted as described in Chapter 3 and only one orientation map was taken at each interruption of the tensile test. The same area was

re-measured at different strain levels. The accumulation of misorientations as a function of induced plastic strain was quantified using the LAMF, KAM_a, $AMIS_a$, and DGF metrics.

6.3.3. In-situ measurement results

The flow curve from the ISRTT test is shown in Fig. 6.17 on which the points at which the test was interrupted to allow EBSD measurements are indicated. There was a slight drop in the applied stress after each interruption caused by delays in the MTS feedback system while trying to maintain the applied load constant. Topographical changes were observed to develop on the specimen surface as the strain was increased as seen in Fig. 6.18, showing an increasing amount of displacement outwards and normal to the plane of the sample surface.

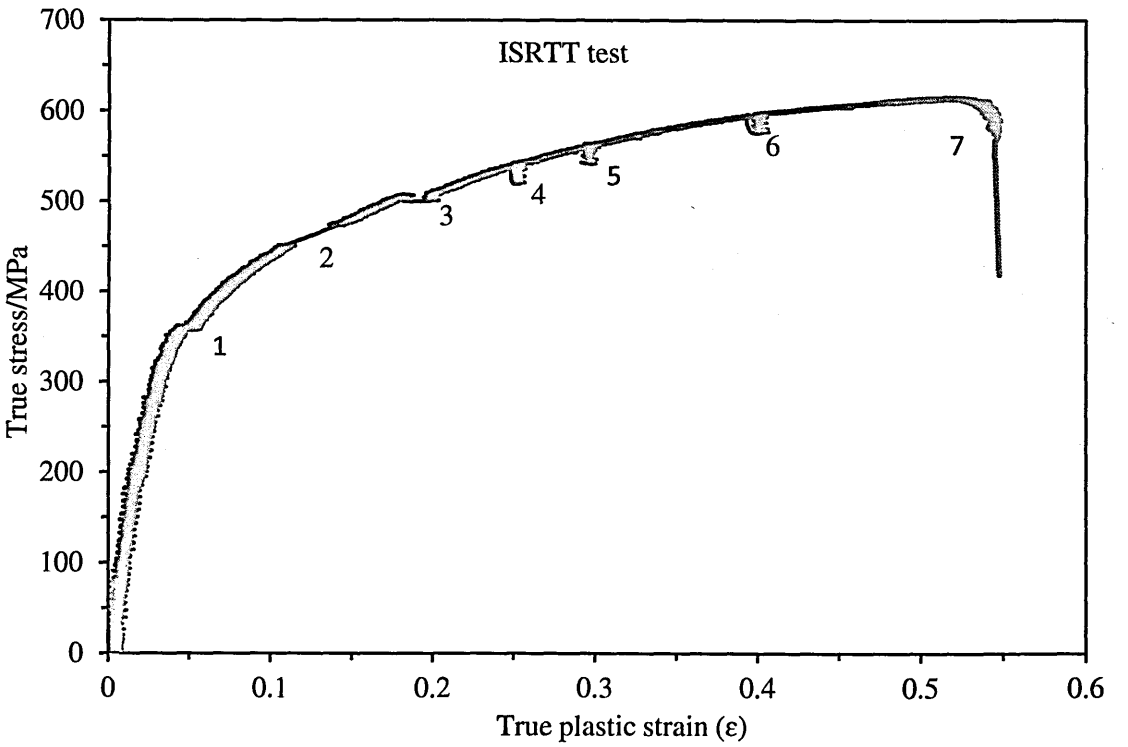

Fig. 6.17. Flow curve for service-aged Type 316H stainless steel deformed as in Table 6.5. Test was interrupted at points 1-7 to allow *in-situ* EBSD measurements.

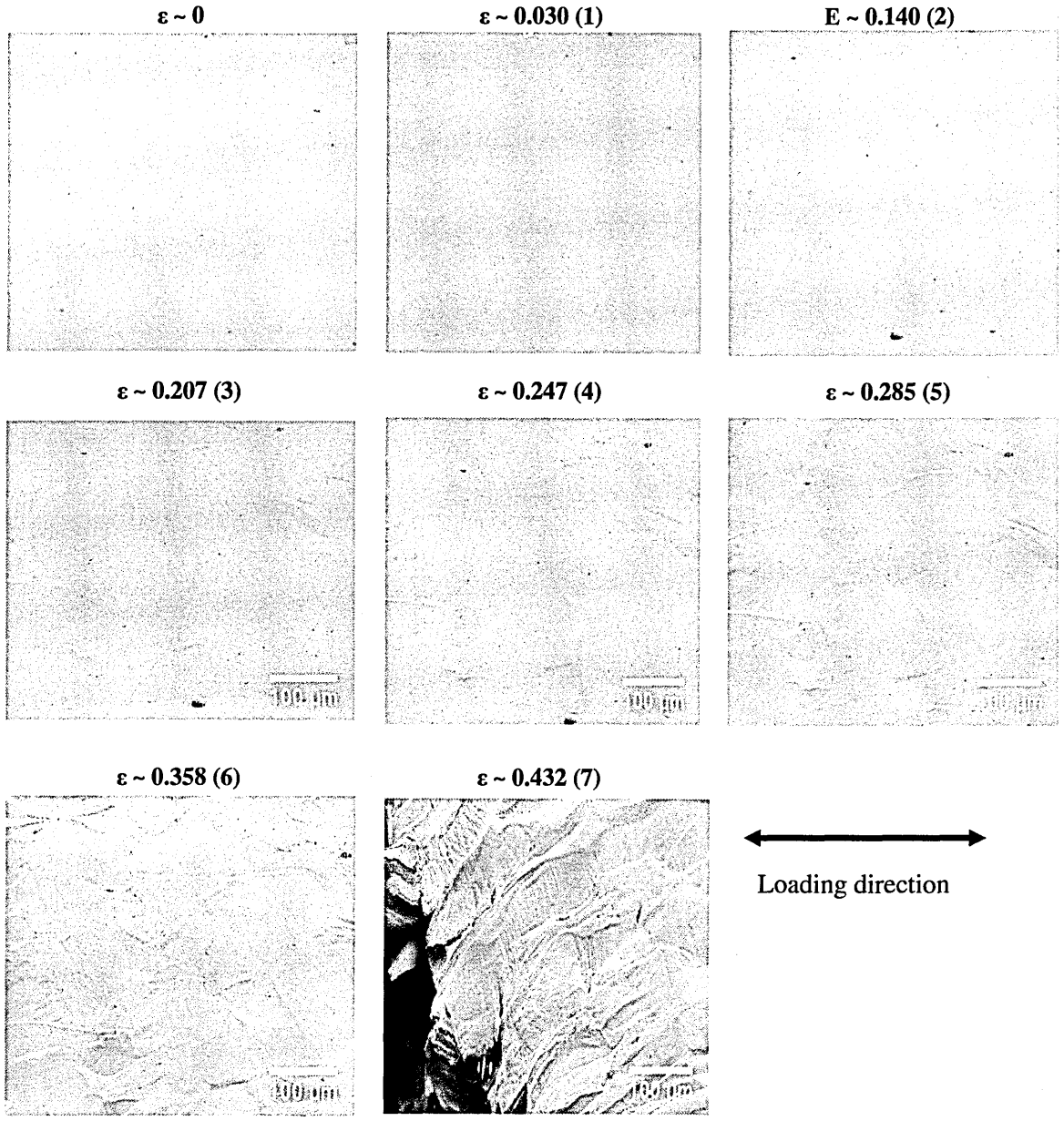

Fig. 6.18. SEM micrographs showing surface topographical changes with increasing applied strain for service-aged Type 316H stainless steel deformed as in Table 6.5.

Fig. 6.19a shows the comparison between the KAM_a correlation with the applied strain for ISRTT and RTT tested specimens. Apparently, the build-up of local misorientations was comparable under these two test regimes since as seen in Fig. 6.19b the LAMF correlation with strain gave similar results. The development of long-range misorientations with the applied strain under RTT and ISRTT test regimes showed similar

trends but different values as seen in Fig. 6.20. However, with the ISRTT test it was possible to track qualitatively the evolution of strain-induced lattice orientation changes within specific grains as shown in Fig. 6.21.

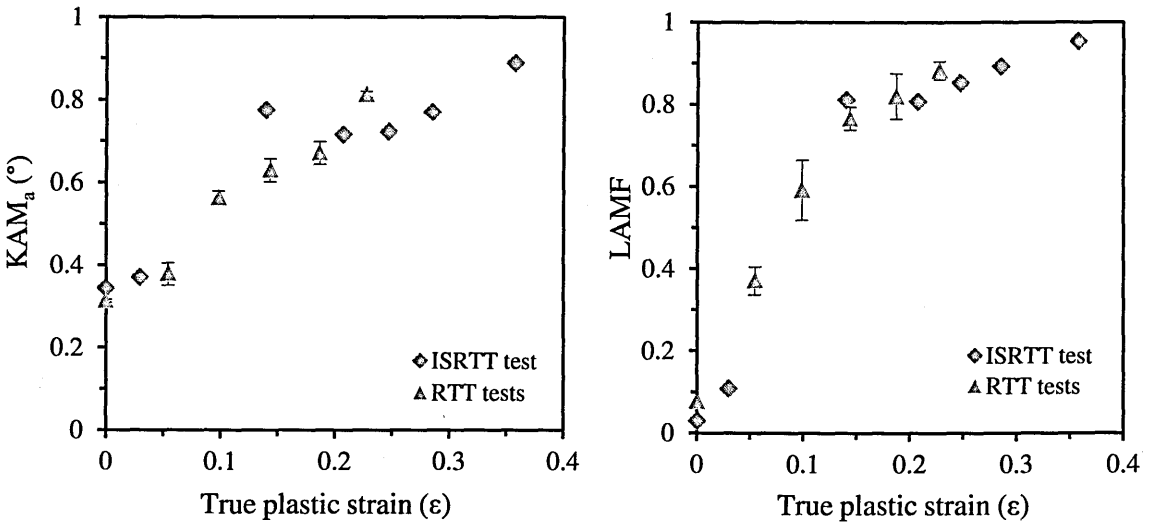

Fig. 6.19. Variations of (a) KAM_a and (b) LAMF with true plastic strain for service-aged Type 316H stainless steel deformed as in Table 6.1 and Table 6.5.

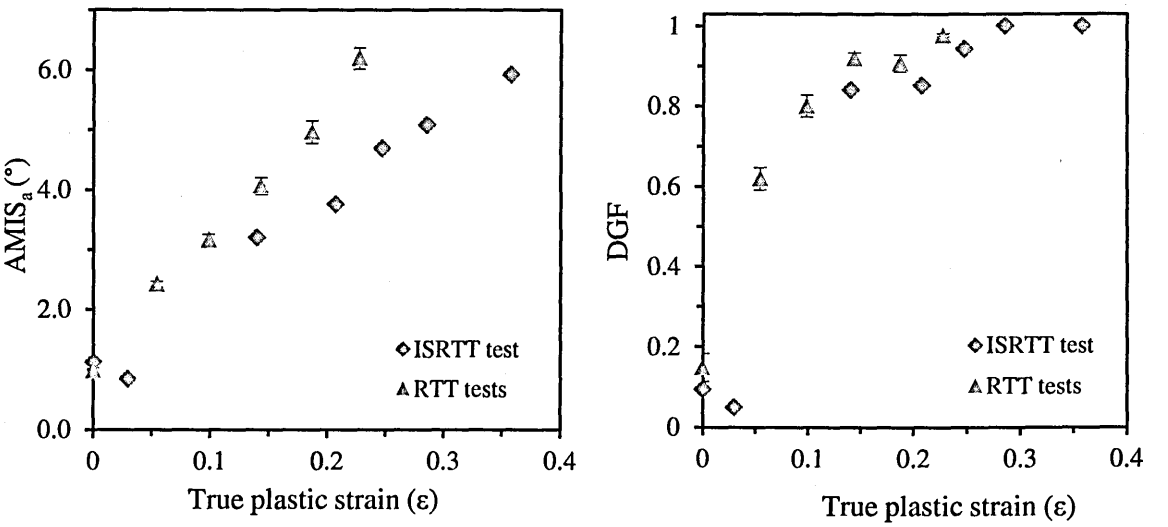

Fig. 6.20. Variations of (a) $AMIS_a$ and (b) DGF with true plastic strain for service-aged Type 316H stainless steel deformed as in Table 6.1 and Table 6.5.

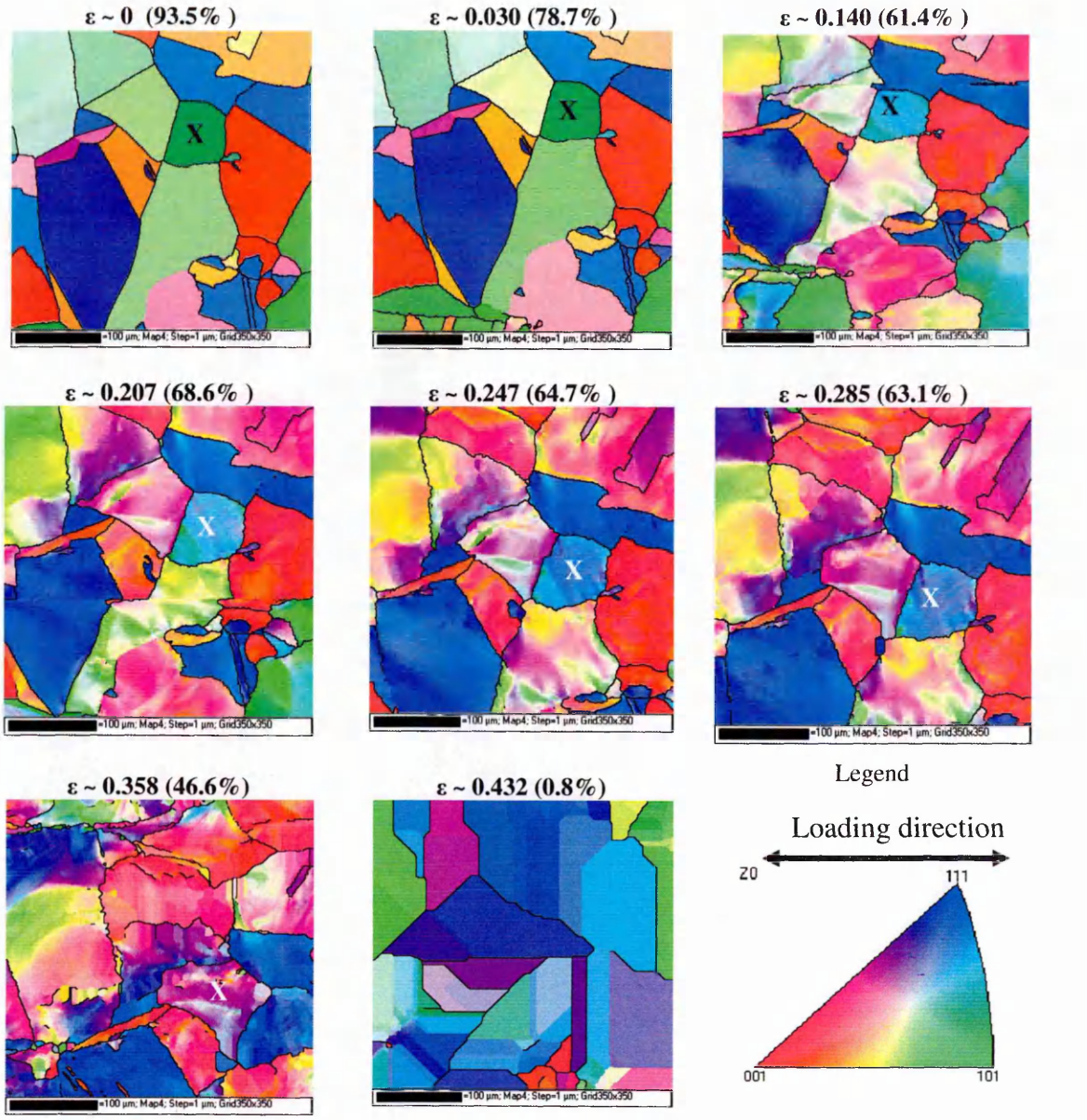

Fig. 6.21. Orientation maps for service-aged Type 316H stainless steel deformed as in Table 6.5 showing lattice orientation changes within grains as a function of the applied strain. Grains distortion increases with increasing strain and at rupture (ε ~0.432), grains structures are completely destroyed. Measurement indexing rates are indicated in brackets and colour coding is based on crystal directions parallel to specimen's normal direction.

6.3.4. Discussion

The comparison given in Fig. 6.19 clearly shows that the evolution of local misorientations with applied strain can be attributable to changes in dislocation densities since the correlations obtained from *in-situ* (single specimen) and *ex-situ* (several

specimens) tests were comparable. The evolution of long-range misorientations as a function of applied strain exhibited similar trends under *in-situ* and *ex-situ* tests as shown in Fig. 6.20.

A complete correspondence between misorientation measurement in *in-situ* and *ex-situ* tests is however not expected owing to development of surface topographical changes in the former tests. Since EBSD measurements are performed on a tilted specimen, one of the prerequisite conditions during orientation measurement is a flat and smooth surface which minimises variations in SEM working distance thus avoiding problems of beam defocusing and shadowing, which tends to degrade DP quality. The development of surface undulation during *in-situ* test therefore degrades DP quality and as mentioned in section 2.4.3.8, this reduces the reliability of DP detection and indexing, increasing uncertainty in orientation measurement. Additional error in orientation measurements arises from local changes in specimen tilt angle caused by surface roughness. Since EBSD system is calibrated using a specific specimen tilt angle (e.g. 70° from horizontal in the current study), the actual local angle between the incident electron beam and the specimen's surface may not be exactly 20°, which may introduce error in the measured orientation as the quality and geometry of DP may be altered locally.

The irregular geometry may yield a wrong solution for a DP thus influencing the measured misorientation values and hence the strain measurement. Surface roughness may also result in non-indexing of DP reducing indexing rates, as seen in the *in-situ* test, where indexing rate decreased with increasing strain owing to increasing surface topographical changes (see Fig. 6.18). These surface changes can be attributed to inhomogeneous deformation resulting from differences in the grains' sizes and orientations relative to the loading axis. In the literature, such changes in surface roughness for materials deformed in tension has been found to be a function of the applied strain [182, 183] and grain size [182].

It is apparent from the above discussion that the measured misorientation from *in-situ* and *ex-situ* tests should be compared only in qualitative terms. The difference in the long-range misorientation values (see Fig. 6.20) under the two test regimes can be attributed to the poor indexing rates and the lower numbers of grains analysed in the *in-situ* test, which could have led to a reduction in $AMIS_a$ and DGF values (which are computed at the grain level).

However, the similarities in the strain-induced misorientation development under *in-situ* and *ex-situ* tests, give assurance that the results given in Fig. 6.9, Fig. 6.13, Fig. 6.15 and Fig. 6.16 can be attributed to strain-induced lattice orientations changes and not to variations arising from the use of different specimens. From Fig. 6.21, it is evident that lattice orientation changes occurred within the grains as the applied strain was increased (e.g. in grain marked 'X', the crystallographic direction parallel to the specimen's normal direction changed from near [101] to near [111] as the strain was increased from 0 to 0.285). The use of multiple specimens in the development of the strain assessment method was meant to introduce scatter in the data, making it more representative of application in a real industrial context.

6.4. Modelling of misorientation distributions

6.4.1. Introduction

In this section, the development of an empirical model which predicts the local misorientation distribution in Type 316 stainless steels under different deformation and measurement conditions is described. The model will be useful in examining the agreement between the misorientation distribution derived from the estimated strain and those from the experimental data. Such assessment would be helpful in evaluating the contribution of other deformation conditions such as strain rate. In the present study, enough experimental data were available for building the model and validation. Apart from

the cause-and-effect between variables during model development, the physical principles behind various measured quantities has been explained in the previous sections thus linking the model output with the microstructural changes expected in the material under study. From discussions in Chapter 5 and section 6.2.5.2, the main factors affecting the nature of the local misorientation distribution include strain, strain rate, step-size, microstructure, and grain size. The current model is developed to take into account the effects of some of these factors and is validated using unseen misorientation data acquired under known conditions. The main phases of the development of this model are described below:

6.4.2. Data collection

The data available for the model development came from the HTT and HTST tests summarised in Table 6.1. EBSD measurements were conducted on all deformed material as described in Chapter 3 and the local misorientation data were expressed in terms of KAM and presented in an absolute frequency distribution format.

6.4.3. Model selection

The selection of a particular model is generally based on: experience of the particular type of data, an understanding of the mechanism giving rise to the data and/or observations made on the data. All these factors were considered during the model selection for the local misorientation distributions. The model was based on a theoretical PDF appropriate for non-negative variables with skewed distribution.

The distribution of local misorientation shows skewness toward zero misorientation which is a function of the strain level, strain rate, grain size and the measurement step-size. As explained in section 6.2.5.2 these distributions are best modelled using a lognormal distribution for true strains <0.1 and by a gamma distribution for higher strains. In developing a model that can predict the local misorientation distributions under different

deformation conditions, it is important to establish the appropriate parameters for the selected model.

The interest in the current study was more on the creep deformation which normally is low and so the model selected was based on the lognormal PDF described in Chapter 3 by Eq. 3.7. The scale of the distribution is determined by parameter μ while δ determines its shape which approaches a symmetric normal distribution as δ tends to zero. The mean (m) and variance (v) of a lognormally distributed variable x are related to parameters μ and δ by [164]:

$$(a)\quad m = e^{\mu+\frac{\delta^2}{2}} \qquad (b)\quad v = \left(e^{2\mu+\delta^2}\right)\left(e^{\delta^2}-1\right) \qquad \text{Eq. 6.6}$$

While the moment and the maximum likelihood estimates of the parameters μ and δ takes the form [164]:

$$(a)\quad \mu_m = ln\left(\frac{m^2}{\sqrt{v+m^2}}\right) \qquad (b)\quad \mu_L = \frac{1}{n}\sum_{i}^{n}\ln(x_i) \qquad \text{Eq. 6.7}$$

$$(a)\quad \delta_m = \sqrt{ln\left(\frac{v}{m^2}+1\right)} \qquad (b)\quad \delta_L = \sqrt{\frac{1}{n}\sum_{i}^{n}[\ln(x_i)-\mu]^2} \qquad \text{Eq. 6.8}$$

where n is the sample size while the parameter's subscripts m and L represents their corresponding moment and maximum likelihood estimates.

6.4.4. Model calibration

The model calibration entails finding the right parameters for the selected distribution. In the present case, parameter estimation for the lognormal distribution model was based on the method of moments. This involved creation of a lognormal PDF from the local misorientation data expressed in terms of frequency distribution and using Eq. 6.7 and Eq. 6.8 to estimate the μ and δ, respectively. In this study the factors that were considered during the model calibration included the strain level, strain rate and the

measurement step-size. The optimisation of the model parameters was carried out through training with the experimental data.

6.4.4.1. Effects of strain level on the model parameters

The estimation of the model parameters as a function of the accumulated strain was based on the local misorientation data obtained at 1μm step-size from tensile specimens deformed at 550°C using a strain rate of $3.5x10^{-5}s^{-1}$. The skew in the local misorientation distributions decreases with the increase in true strains as seen in Fig. 6.7a. The values of parameters μ and δ were estimated from the resultant lognormal distributions and plotted as a function of the applied strain as shown in Fig. 6.22 and Fig. 6.23. The variation of μ and δ with strain was modelled using a linear and a polynomial function, respectively:

$$\mu = 4.5\varepsilon - 1.3 \qquad \text{Eq. 6.9}$$

$$\delta = 2.8\varepsilon^2 - 0.5\varepsilon + 0.5 \qquad \text{Eq. 6.10}$$

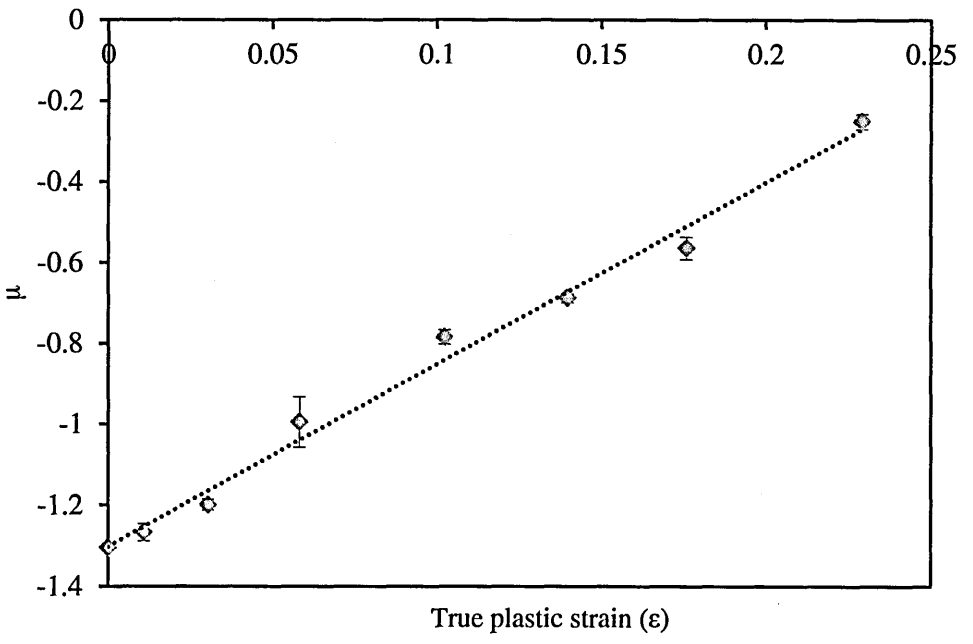

Fig. 6.22. Variation of μ with true plastic strain (ε) for service-aged Type 316H stainless steel deformed at 550°C in tension at a strain rate of $3.5x10^{-5}s^{-1}$.

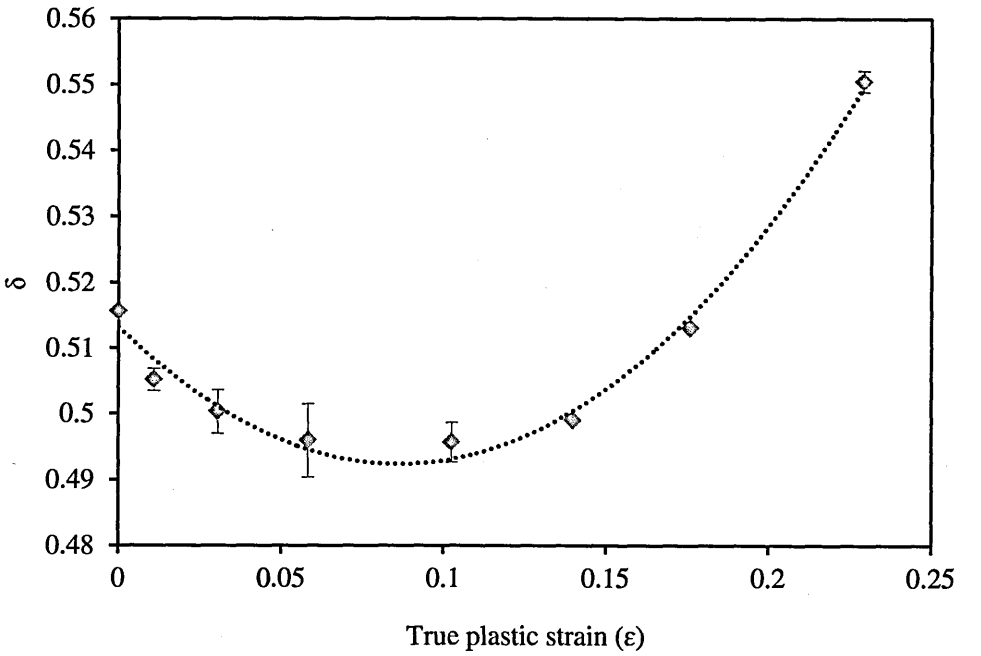

Fig. 6.23. Variation of δ with true plastic strain (ε) for service-aged Type 316H stainless steel deformed at 550°C in tension at a strain rate of $3.5x10^{-5}s^{-1}$.

6.4.4.2. Effects of the strain rate on the model parameters

The strain rate effect on the model parameters was investigated by considering the local misorientation distributions of tensile specimens deformed to 0.098 strain at 550°C using strain rates ranging from $3.5x10^{-3}s^{-1}$ to $4.0x10^{-7}s^{-1}$. The skew in the local misorientation distributions decreased though marginally with the increase in the strain rate as seen in Fig. 6.7b. To quantify these variations lognormal PDF were generated using Eq. 3.7 from which the parameters μ and δ were calculated for each of the strain rate using Eq. 6.7 and Eq. 6.8, respectively. To model the strain rate effect on the misorientation distribution, it was necessary to compute a factor by which the parameters μ and δ changed as a function of the applied strain rate. In the present case, the change in the parameters was generally represented by dr_i/dr_0 with dr_0 representing the parameters for specimens deformed at $3.5x10^{-3}s^{-1}$ and dr_i representing the parameters obtained at lower strain rates. The relationship between dr_i/dr_0 and the applied strain rate (see Fig. 6.24) was described

using a logarithmic function as it had better fit statistics (high R^2 and low residual variance) than a linear function. The resultant equations were therefore of the form:

$$\frac{d\mu_i}{d\mu_0} = 0.3ln\dot{\varepsilon} + 0.7 \qquad \text{Eq. 6.11}$$

$$\frac{d\delta_i}{d\delta_0} = -0.03ln\dot{\varepsilon} + 1 \qquad \text{Eq. 6.12}$$

where $\dot{\varepsilon}$ represent the logarithm of the strain rate. The μ and δ parameters associated with the local misorientation distribution at a given strain level were adjusted by a factor of $d\mu_i/d\mu_0$ and $d\delta_i/d\delta_0$, respectively to cater for the strain rate effects. The strain rate effect on the local misorientation distribution was only modelled for deformation at 550°C since at room temperature the strain rate has minimum effect on the deformation behaviour of steels (see section 2.2.2.5).

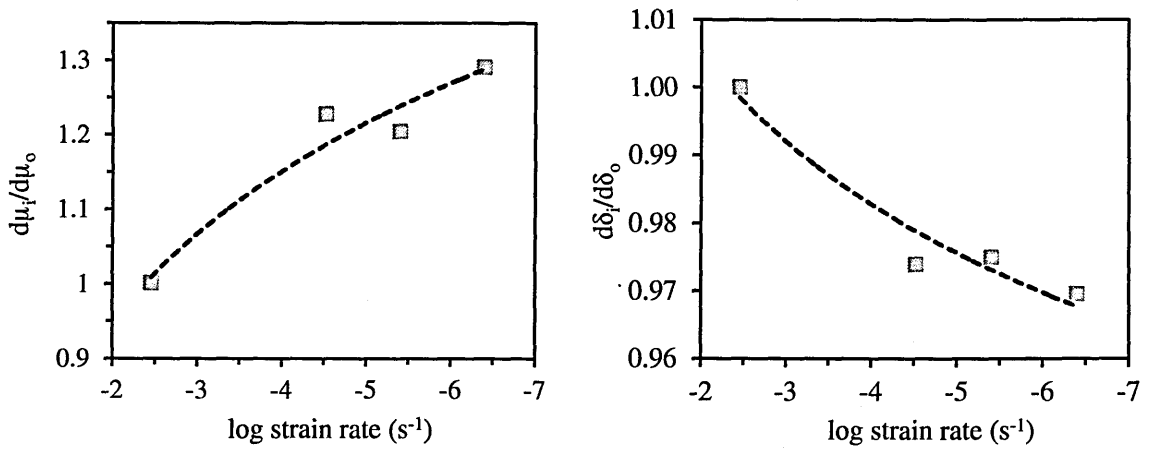

Fig. 6.24. Strain rate dependence of (a) $d\mu_i/d\mu_0$, and (b) $d\delta_i/d\delta_0$.

6.4.4.3. Effects of the step-size on the model parameters

The local misorientations are spatially correlated and therefore depend on the distance between the measurements points i.e. the step-size (s) as explained in section 2.4.5.2. As the step-size increases the local misorientation increases (see section 2.4.5.2.1a) and this is accompanied by a reduction in the skewness of the local misorientation distributions, as seen in Fig. 6.25. To investigate the effects of the step-size, measurements

were performed on an undeformed sample using step-sizes ranging from 0.2μm to 1μm. The measurements were conducted on the same area thereby eliminating variations arising from the sampling of different regions. To ensure all changes in the misorientation distributions were attributable to step-size variations, all the other EBSD settings were kept constant during the measurement.

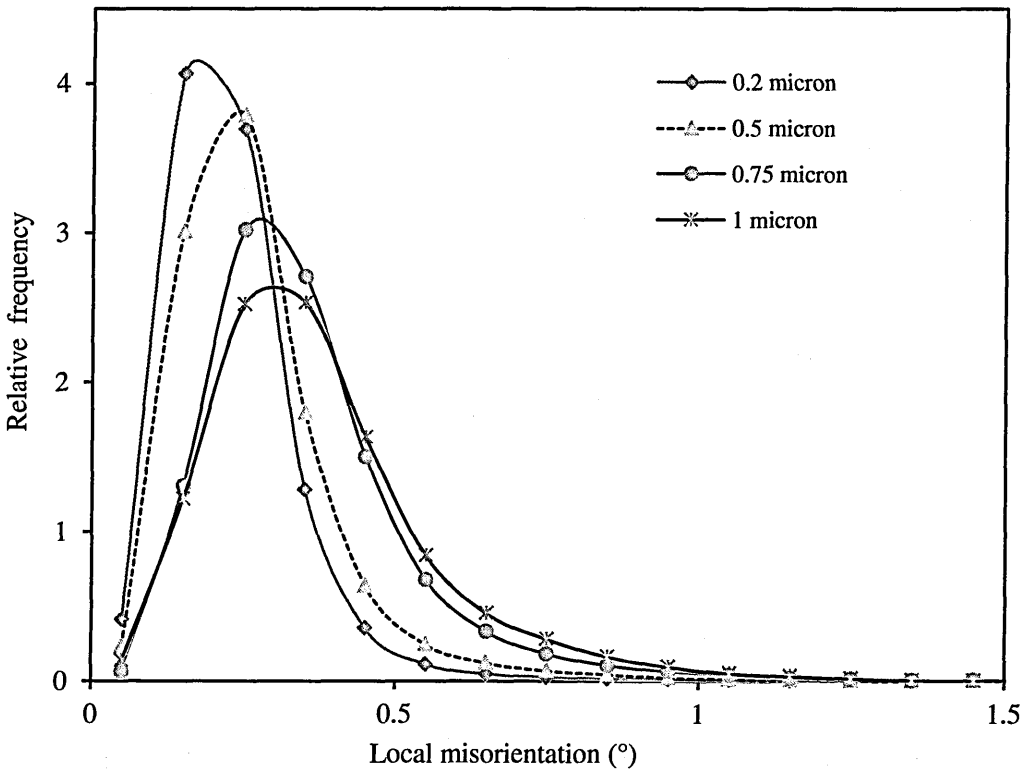

Fig. 6.25. Effects of measurement step-size on local misorientation distribution for undeformed service-aged Type 316H stainless steel.

The parametric changes in the distributions as a function of step-size were characterised by a factor ds_i/ds_0 in which ds_i represented the parameters from the data obtained at 0.2μm step-size and ds_0 for the data obtained at larger step-sizes. The variation of ds_i/ds_0 with the step-size is shown in Fig. 6.26 where $d\mu_i/d\mu_0$ varies almost linearly while $d\delta_i/d\delta_0$ is described by a logarithmic function.

The current model is based on data obtained using a step-size of 1μm. However, through adjustments of parameters μ and δ by a factor of $d\mu_i/d\mu_0$ and $d\delta_i/d\delta_0$,

respectively for distributions obtained at a particular strain and strain rate, it is possible to evaluate the nature of misorientation distributions likely to be achieved at step-sizes <1μm. These factors are represented by equations derived from the correlations in Fig. 6.26.

$$\frac{d\mu_i}{d\mu_0} = 0.4\varsigma + 0.9 \qquad \text{Eq. 6.13}$$

$$\frac{d\delta_i}{d\delta_0} = 0.03 \ln \varsigma + 1.1 \qquad \text{Eq. 6.14}$$

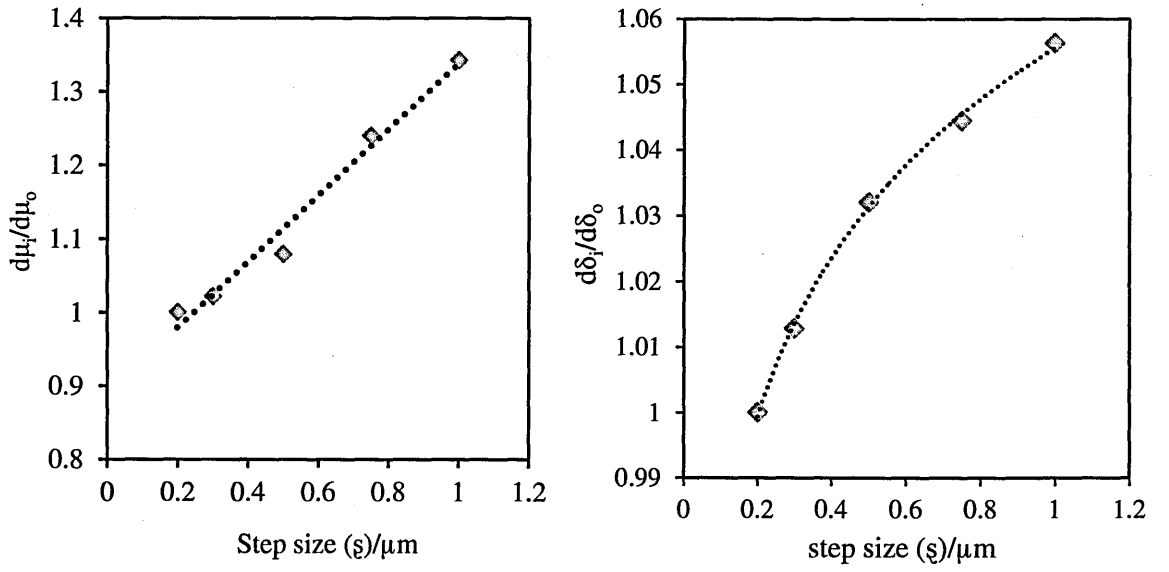

Fig. 6.26. Relationship between measurement step-size and: (a) $d\mu_i/d\mu_0$, and (b) $d\delta_i/d\delta_0$.

6.4.5. Model validation

To validate the efficacy of the model it was applied to unseen misorientation data whose deformation conditions, EBSD measurement conditions and material's average grain size were known. Table 5.1 and Table 6.1, summarise all the data available for the validation of the current model. The graphical representation of the modelled misorientation distributions under different conditions of strain (see Fig. 6.27), strain rate (see Fig. 6.28) and step-size (see Fig. 6.29) compare relatively well with the local misorientation distributions obtained from unseen raw data.

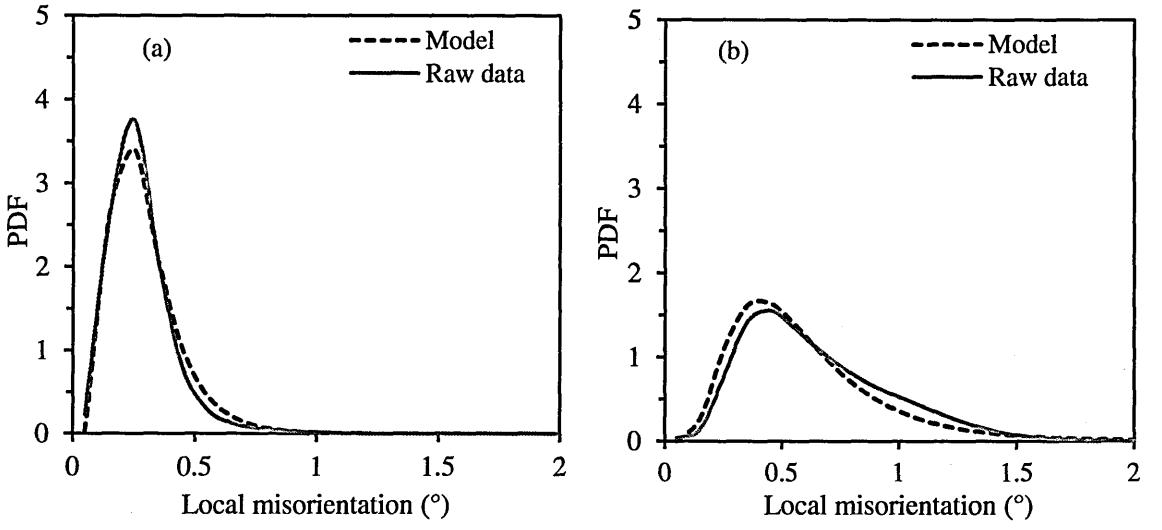

Fig. 6.27. Modelled and experimental local misorientation distributions for service-aged Type 316H stainless steel deformed at 550°C to: (a) 0.031 and (b) 0.176 strain at a strain rate of $3.5x10^{-5}s^{-1}$. Average grain size was ~98μm and measurement performed at 1μm step-size.

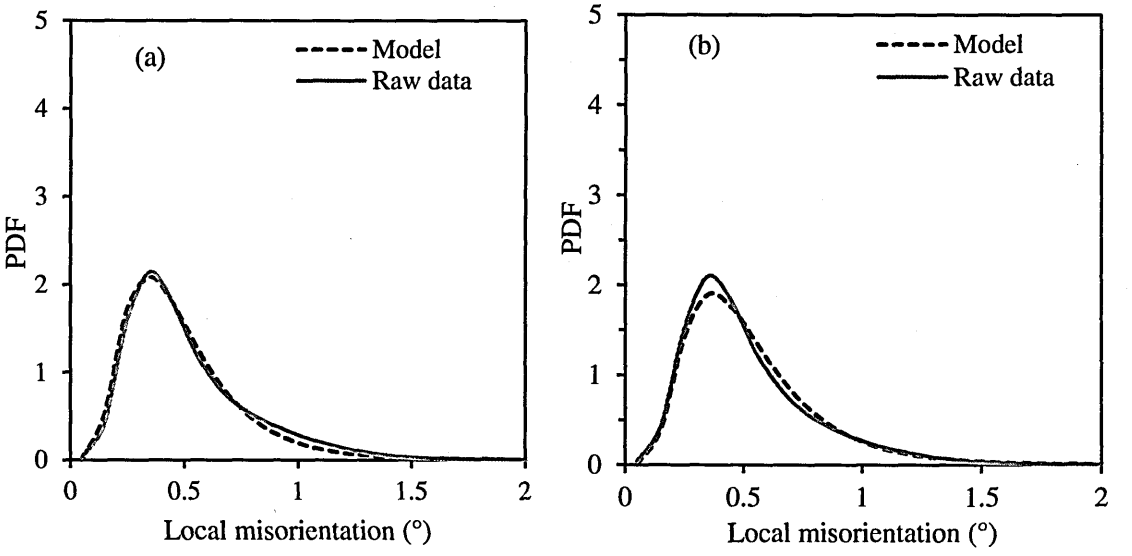

Fig. 6.28. Modelled and experimental local misorientation distributions for service-aged Type 316H stainless steel deformed at 550°C to 0.098 strain at a strain rate of (a) $3.5x10^{-5}s^{-1}$, and (b) $4.0x10^{-7}s^{-1}$. Average grain size was ~98μm and measurement performed at 1μm step-size.

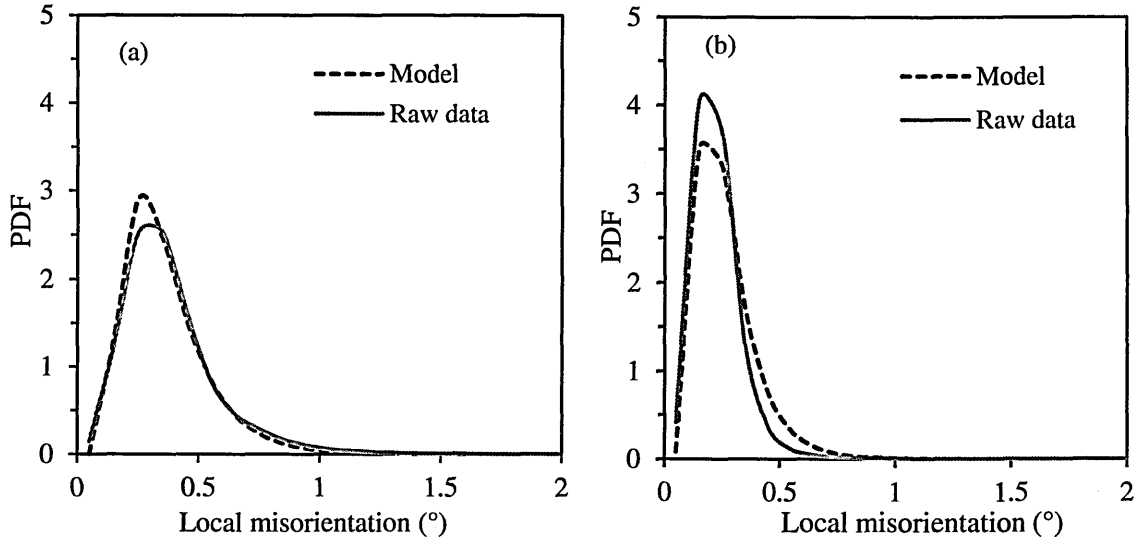

Fig. 6.29. Modelled and experimental local misorientation distributions for service-aged Type 316H stainless steel deformed at 550°C to 0.058 strain at a strain rate of $3.5x10^{-5}s^{-1}$ on a sample with an average grain size of ~98μm. Misorientation data collected at step-sizes of (a) 0.2μm and (b) 1μm.

6.4.6. Model application

To apply the developed model, the local misorientations data from unstrained material in the form of a frequency distribution is needed. Based on this, the model then generates a local misorientation distribution that is a function of the input variables which includes; strain, strain rate and measurement step-size of the material. In this way, the nature of the local misorientation distribution can be determined without necessarily having to carry out the mechanical testing and the subsequent EBSD measurements. By fitting the model onto the experimental data, it is possible to estimate the value of any input variable so long as the other variables are known.

Microstructure has significant influence on the local misorientation distributions as explained in Chapter 5. However, this influence cannot be modelled easily as the degree of microstructural influence on misorientation distribution is difficult to quantify. The grain size also has significant influence on the local misorientation development but its effects

were not modelled in the current work owing to unavailability of enough materials with varying grain sizes. Consequently, the application of the current model is limited to the service-aged steels with an average grain size of about 100μm.

6.5. Summary

The key findings in this chapter can be summarised as follows;

- The measured distribution of local misorientations (KAM) developing in Type 316H stainless steel under uniaxial isothermal loading has been shown to be a function of the applied strain, strain rate, grain size and the measurement step-size. An empirical model predicting the local misorientation distribution as a function of deformation conditions is proposed.
- The measured evolution of local and long-range misorientations in Type 316H stainless steel was found to be independent of the deformation temperature (24°C and 550°C) and deformation mode (tension vs compression) for strain rates down to $10^{-5}s^{-1}$ and empirical correlations between accumulated plastic strain and misorientation metrics (KAM_a, LAMF, $AMIS_a$ and DGF) developed for true strains up to 0.23. From strain rate assessment studies at 550°C it was shown that the correlations can be applied at strain rates down to $10^{-6}s^{-1}$.
- The strain sensitivities of the DGF and LAMF metrics were shown to vary with the applied strain, while for the KAM_a and $AMIS_a$ metrics, the strain sensitivity remained relatively constant between 0 and 0.23 strains.
- The development of strain-induced local and long-range misorientations at 550°C in Type 316H stainless steel was found to be independent of the measurement plane orientation with respect to the loading axis. This was postulated to arise from uniform spatial distribution of misorientations for true strains up to 0.23.

- The development of the local (KAM_a) and the long-range ($AMIS_a$) misorientations was found to correlate with the measured dislocation densities.
- The development of both local and long-range misorientations at 550°C was shown to vary with the applied strain rates below $4.0x10^{-6}s^{-1}$. This suggested a change in the deformation mechanism which gave rise to reduced dislocation densities as the strain rate was reduced.

CHAPTER 7

THE INFLUENCE OF CREEP STRAIN ON MISORIENTATION DEVELOPMENT

7.1. Introduction

Creep is the time dependent inelastic deformation of materials that are exposed to elevated temperatures, often $>0.4T_m$ [16], over long durations at relatively low stresses, mostly below the material's yield stress. In this chapter, the application of EBSD in the assessment of creep-induced lattice orientation changes in Type 316 stainless steel is discussed. The assessment is based on service-aged steel (Sample A) since it is likely to be similar to that found in service in UK Advanced Gas-cooled Reactor (AGR) power plants. Constant load creep tests at 550°C and 675°C, with and without prior plastic deformation, are described. A test temperature of 550°C was selected to correspond with the real service temperature of steam systems in AGR power plants. The test temperature of 675°C was used for accelerated creep tests at low applied stresses, where the initial loading strain is negligible and the substructures and work-hardening behaviours are similar to those at 550°C [153, 158]. The evolution of creep-induced local and long-range misorientations is examined and a distinction made between these and plastically-induced misorientations. Methodologies for quantifying the total strain and the accumulated creep strain are presented and elaborated. The chapter concludes with a summary of the key findings.

7.2. Studies on the influence of creep strain on misorientation development

7.2.1. Mechanical tests

To investigate the development of creep-induced misorientations in specimens with and without prior plastic deformation, a series of constant load creep tests were performed at 550°C and 675°C. The tests, which were carried out on the same creep frame under similar conditions of stress and temperature in each case, were interrupted at specific creep

strains. The interruption intervals were based on the accumulated creep strains and were aimed to cover primary, secondary and tertiary stages of the creep deformation.

The creep specimens, whose geometry was given in Chapter 3 (see Fig. 3.3), were extracted by wire EDM from the same *HRA 1c* block of Sample A (see Fig. 4.2) to minimise variability in their chemical compositions and mechanical properties. A few creep specimens extracted from the block *HRA 1a* of Sample A were also investigated.

7.2.1.1. Creep tests at 550°C

The creep tests were preceded by uniaxial tensile deformation on an Instron-8862 machine. These tensile tests were carried out at a constant strain rate of $3.5x10^{-5}s^{-1}$ and interrupted after 0.079, 0.102 and 0.115 true strains as indicated in Table 7.1. The tests were carried out as described in Chapter 3 and at the end of the test the specimens were generally unloaded and cooled in the air to room temperature. However, one specimen was cooled under load, to allow the effects of cooling on the creep response to be investigated.

Table 7.1: Constant load creep data for service-aged Type 316H stainless steel deformed at 550°C using an initial stress of 320MPa.

Specimen ID	Prestrain	Min. strain rate (s^{-1})	Loading strain	Creep strain
HRA 1C - 05	0.079	0	0.000	0.000
HRA 1C - 09	0.079	1.1E-08	0.003	0.005
HRA 1C - 10	0.079	5.3E-09	0.002	0.010
HRA 1C - 04	0.079	8.0E-09	0.003	0.014
HRA 1C - 06	0.079	7.5E-09	0.003	0.023
HRA 1C - 02	0.079	7.5E-09	0.002	0.042
HRA 1C - 03	0.079	7.3E-09	0.003	0.068
HRA 1A - 25	0.079	2.2E-08	0.005	0.130
HRA 1C - 29	0.079	1.1E-08	0.004	0.164
HRA 1C - 08	0.102	4.7E-09	0.004	0.019
HRA 1A - 09	0.041	2.7E-09	0.003	0.017
HRA 1A - 28	0.115	3.3E-09	0.003	0.011
HRA 1A - 30	0.086	2.6E-08	0.003	0.050
HRA 1A - 18	0.000	9.9E-08	0.072	0.180

Constant load creep tests were conducted on specimens with and without prestrain at T = 550°C and σ = 320MPa in accordance with the procedures outlined in Chapter 3. The final applied stress during the tensile tests ranged from 329MPa to 416MPa and so no plastic deformation was expected during the subsequent creep loading since the initial stress applied was 320MPa. However, as seen in Table 7.1 some loading strains were recorded most of which were recovered during the creep unloading, leaving a remnant strain of about 0.001 as seen in Fig. 7.1. Consequently, for all prestrained specimens the loading strains were not included in the final creep strain reported. For specimens without prestrain (in the as-received condition), the initial applied stress of 320MPa introduced an instantaneous plastic strain of ~0.072 and so this can be considered as a special case of prestraining with the difference only that the specimen is not cooled and unloaded before the creep test.

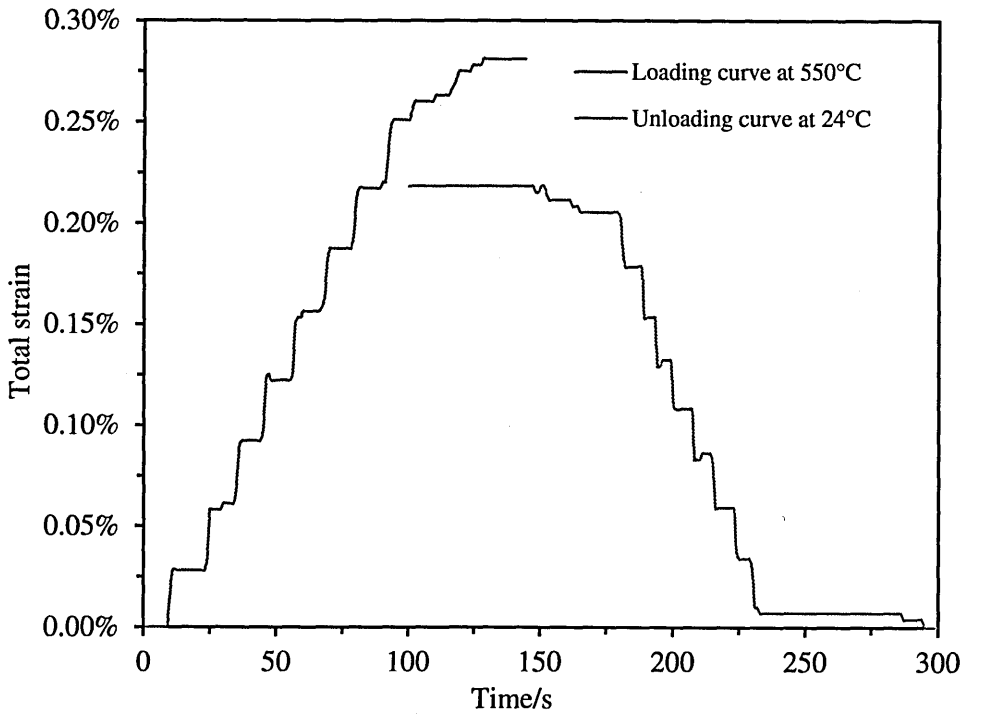

Fig. 7.1. Creep loading and unloading curves for service-aged Type 316H stainless steel showing recovery of the loading strain.

7.2.1.2. Creep tests at 675°C.

Constant load creep tests were also conducted at 675°C in similar way as those at 550°C but using an initial applied stress of 150MPa. The aim of this study was to investigate the development of misorientations under pure creep conditions. The 0.2% proof stress for the service-aged steel at 675°C was 165MPa (see Chapter 4), so minimal creep loading plastic strain was expected at an initial applied stress of 150MPa. However, some initial loading strains were recorded as summarised in Table 7.2. Most of these were recovered during the unloading stage and so they were excluded in the calculation of the accumulated creep strain from the total strain. Using creep specimens extracted from the adjacent locations on Sample A, and carrying out the tests on the same creep frame under the procedures outlined in Chapter 3 reduced the variability in the creep responses as seen in Fig. 7.9.

Table 7.2: Constant load creep data at 675°C for Type 316H stainless steel in service-aged and re-solution heat treated states.

Specimen ID	Stress/MPa	Min. strain rate (s^{-1})	Loading strain	Creep strain	Creep stage
HRA 1C – 11: A	150	1.2E-07	0.002	0.475	Rupture
HRA 1C – 12: A	150	1.0E-07	0.002	0.148	Tertiary (T_e)
HRA 1C – 13: A	150	1.1E-07	0.003	0.057	Secondary (S_e)
HRA 1C – 14: A	150	1.1E-07	0.003	0.033	Primary (T_e)
HRA 1C – 21: B	100	1.3E-08	0.002	0.050	Secondary

A constant load creep test was performed on Sample B (re-solution heat treated steel denoted here as RST) at T = 675°C and σ = 100MPa to investigate the effects of the starting microstructure on the creep-induced misorientations. Under these conditions, a creep strain of ~0.05 was accumulated, with minimal creep loading plastic strain, as the initial applied stress was below the 0.2% proof stress (155MPa) at this temperature.

Tensile tests were also conducted on Sample A and Sample B specimens at 675°C to 0.057 and 0.051 strains, respectively at a constant strain rate of $3.5 \times 10^{-5} s^{-1}$. The aim of

this study was to compare the misorientation development under pure creep and pure plastic strain conditions in both service-aged and RST steels.

7.2.2. EBSD measurements

EBSD measurements were performed on all crept specimens as described in Chapter 3. At least four orientation maps were obtained from each crept specimen studied and an average misorientation value reported. For the creep ruptured specimen (HRA 1C-11 in Table 7.2), measurements were made continuously along the gauge length starting at 0.7μm from the ruptured surface in the regions with fewer creep cracks. The presence of creep cracks reduced indexing rates in this specimen compared to the other crept specimens but repeat measurements were conducted in the adjacent areas and only maps with >96% indexing rates were considered for strain analysis.

The evolution of the misorientations as a function of the accumulated creep strain was investigated at both local and longer ranges. The development of local misorientations was based on the LAMF and KAM_a metrics while the long-range misorientations were characterised by the $AMIS_a$ and DGF metrics. A sample of orientation maps is given in Appendix 3 (C and D).

7.2.3. Mechanical tests results

7.2.3.1. Creep tests result at 550°C

Fig. 7.2 shows the flow curves obtained in tension at 550°C during the prestraining stage of the creep tests. The overlapping of flow curves indicates uniformity in both microstructures and deformation conditions amongst the specimens. However, specimens extracted from block *HRA 1a* exhibited relatively high flow stresses at a given strain compared with those from block *HRA 1c*. Since the two blocks belonged to the same parent material (Sample A) as explained in Chapter 4, it is possible that either their microstructure and/or their mechanical histories were different.

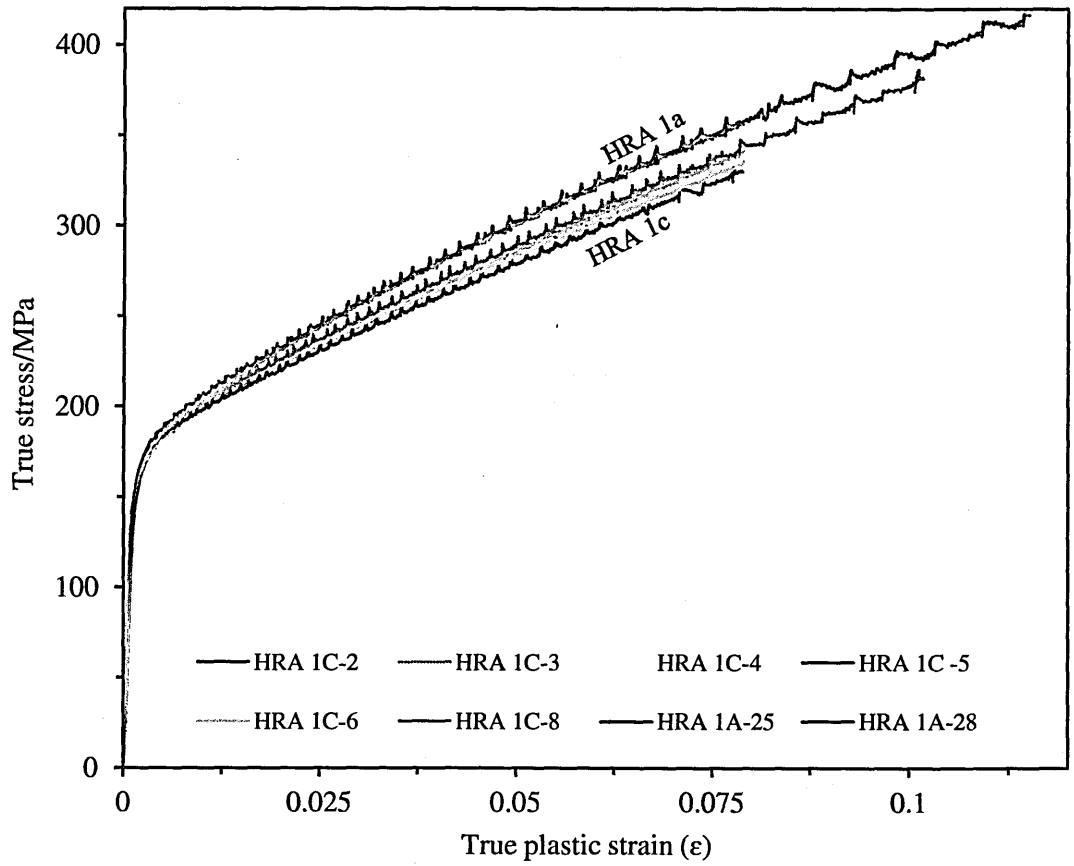

Fig. 7.2. Flow curves at 550°C for service-aged Type 316H stainless steel deformed to 0.079, 0.102 and 0.115 strains showing marginally higher flow curves in *HRA 1a* than in *HRA 1c* specimens.

The creep responses at T = 550°C and σ = 320MPa for specimens with and without prestrain, and crept to failure are shown in Fig. 7.3. Under these conditions, pretension increased the creep rupture life and reduced the overall creep strain and the minimum creep strain rate. The initial loading strain was also reduced significantly as indicated in Table 7.1.

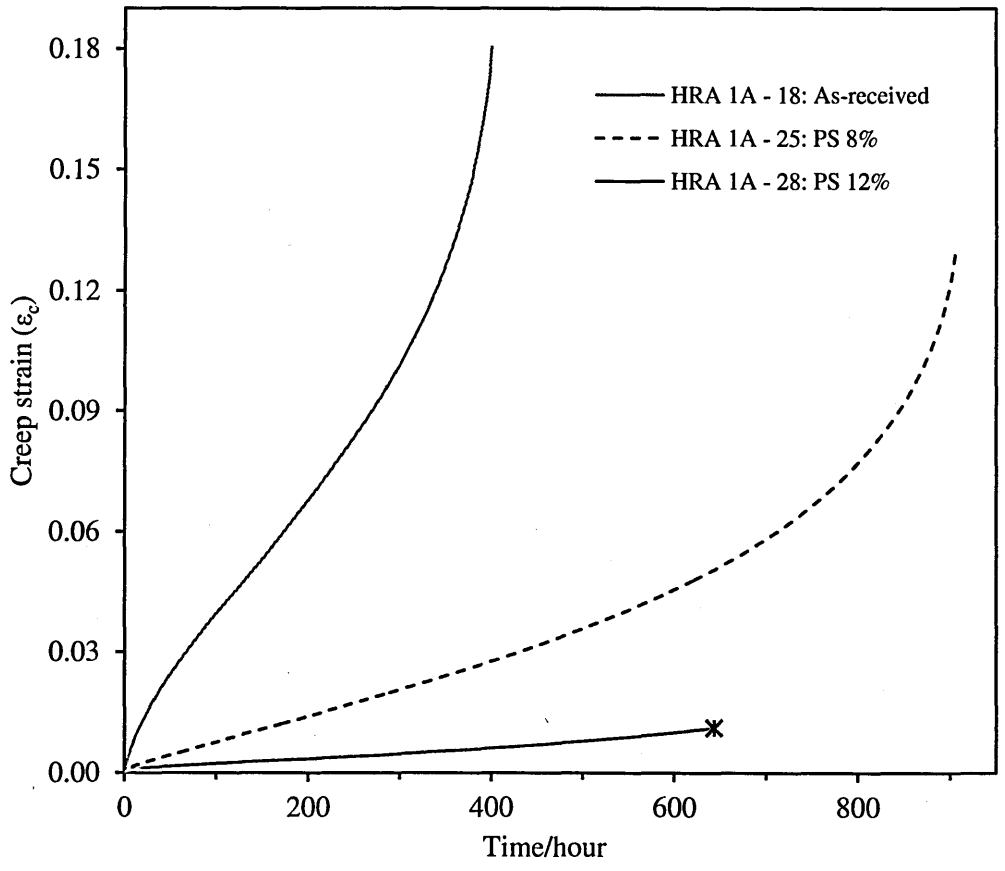

Fig. 7.3. Effect of prestrain on creep response of service-aged Type 316H stainless steel deformed as in Table 7.1. 12% PS curve was interrupted after 640 hours.

A variation in material properties in specimens extracted from different regions of the same component introduces scatter in measured creep response as seen in Fig. 7.4 for specimens exhibiting different flow behaviours during the prestraining stage (see Fig. 7.2). Specimens exhibiting relatively high flow stresses at a given strain during the prestraining stage had a lower creep resistance than those with lower flow stresses. This demonstrates that for creep behaviour reproducibility, it is essential to test material from the same region of a component where minimal variations in material's properties are expected.

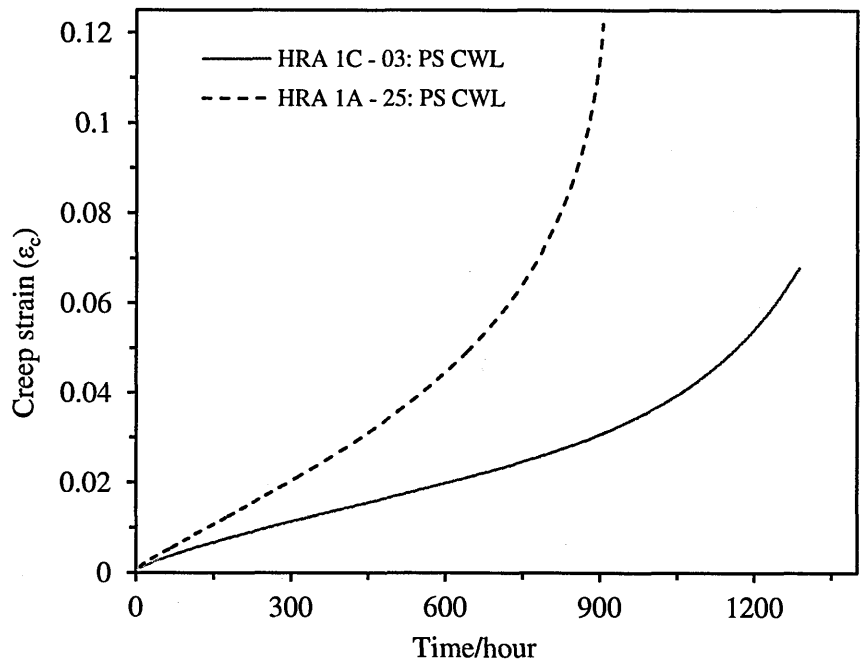

Fig. 7.4. Creep curves at T = 550°C and σ = 320MPa for service-aged Type 316H stainless steel extracted from *HRA 1c* and *HRA 1a* blocks shown in Fig. 4.2. (PS CWL: prestrained and cooled without load).

Cooling the specimens either with or without load during the prestraining stage influences their creep response. Specimens with similar flow behaviours at 550°C (see Fig. 7.5a) exhibited lower creep resistance when cooled under load than when cooled without the load as shown in Fig. 7.5b.

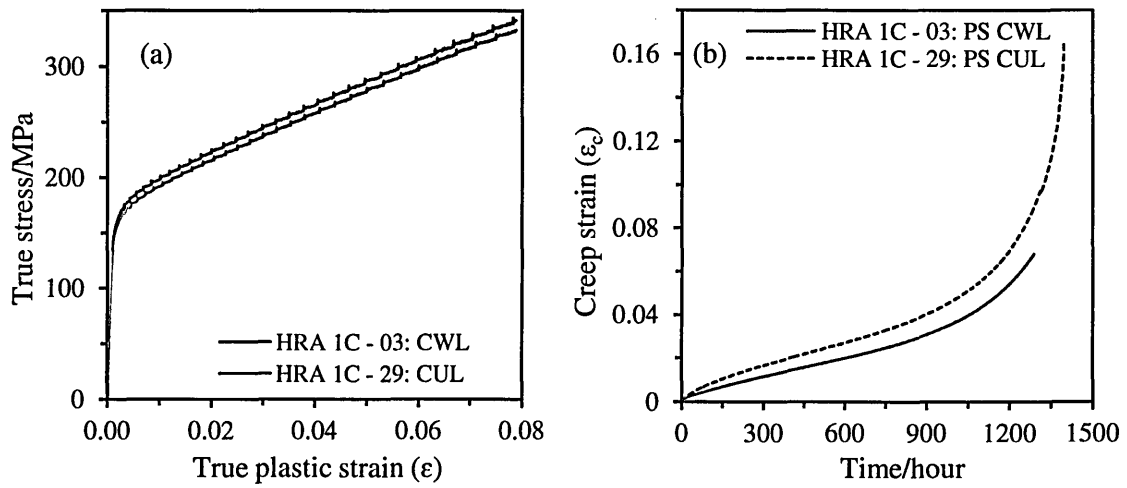

Fig. 7.5. (a) Flow curves at 550°C for service-aged Type 316H stainless steel deformed to 0.079 strain followed by cooling under load (CUL) and without load (CWL). (b) Creep rupture curves of (a) at T = 550°C and σ = 320MPa.

The creep responses at T = 550°C and σ = 320MPa, of specimens prestrained to 0.079 strain at 550°C followed by cooling without load, are shown in Fig. 7.6 and the corresponding creep strains in Table 7.1. The creep tests were interrupted at strains corresponding to primary (P_r), secondary (S_c) and tertiary (T_e) creep stages as seen in Fig. 7.7. Overlaying of the creep curves from different specimens indicates proper control of the test conditions such as temperature and the applied stresses and also uniformity of material's properties and deformation mechanisms. Creep failure was imminent after creep strain of 0.068 as evident by the macro-cracks seen in Fig. 7.8a.

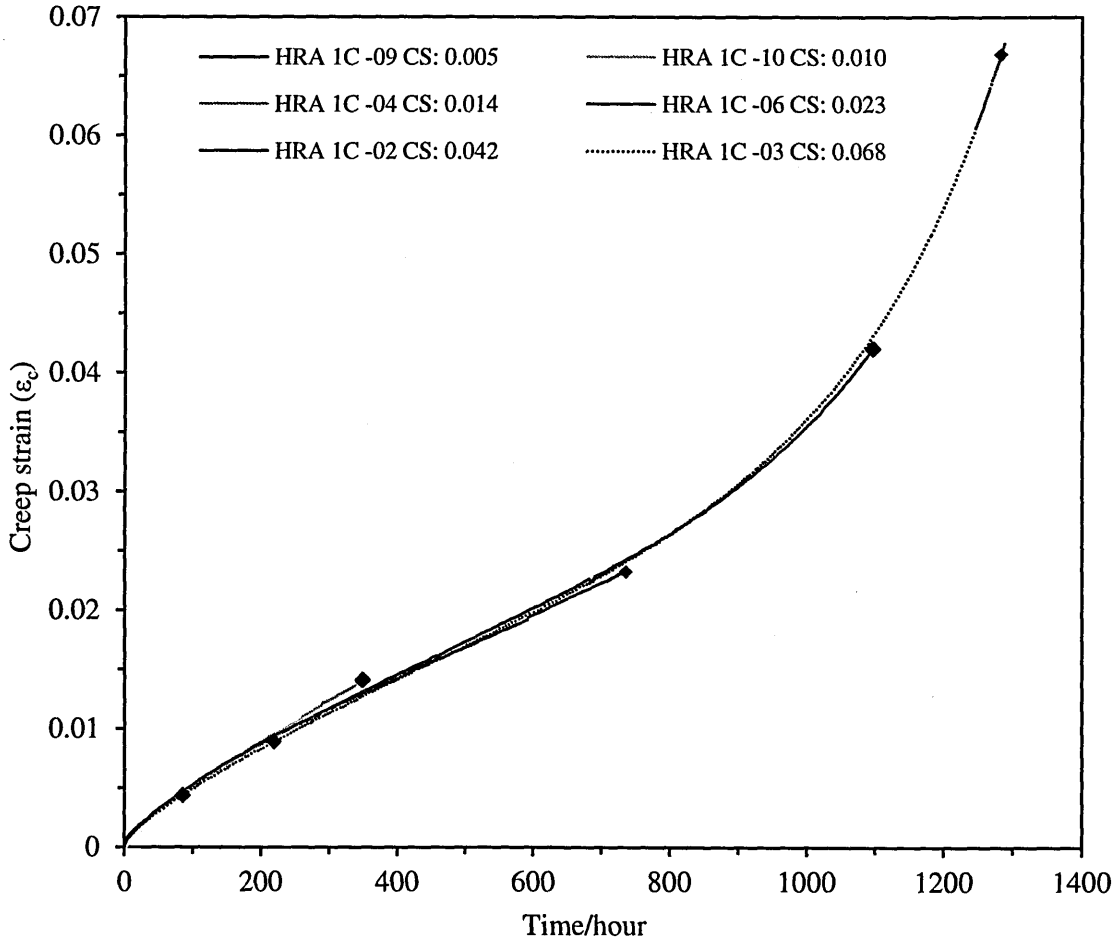

Fig. 7.6. Creep curves for service-aged Type 316H stainless steel crept at 550°C as in Table 7.1. (CS: creep strain).

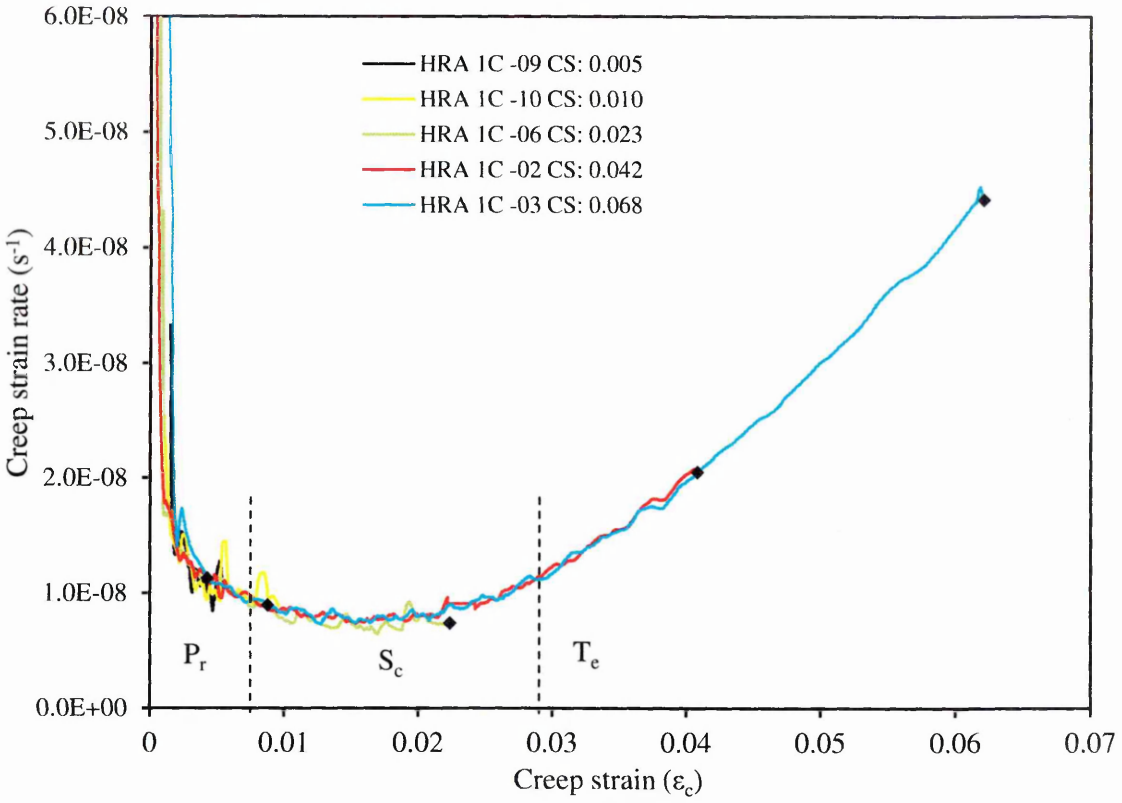

Fig. 7.7. Creep strain rate versus creep strain for service-aged Type 316H stainless steel crept at 550°C as in Table 7.1.

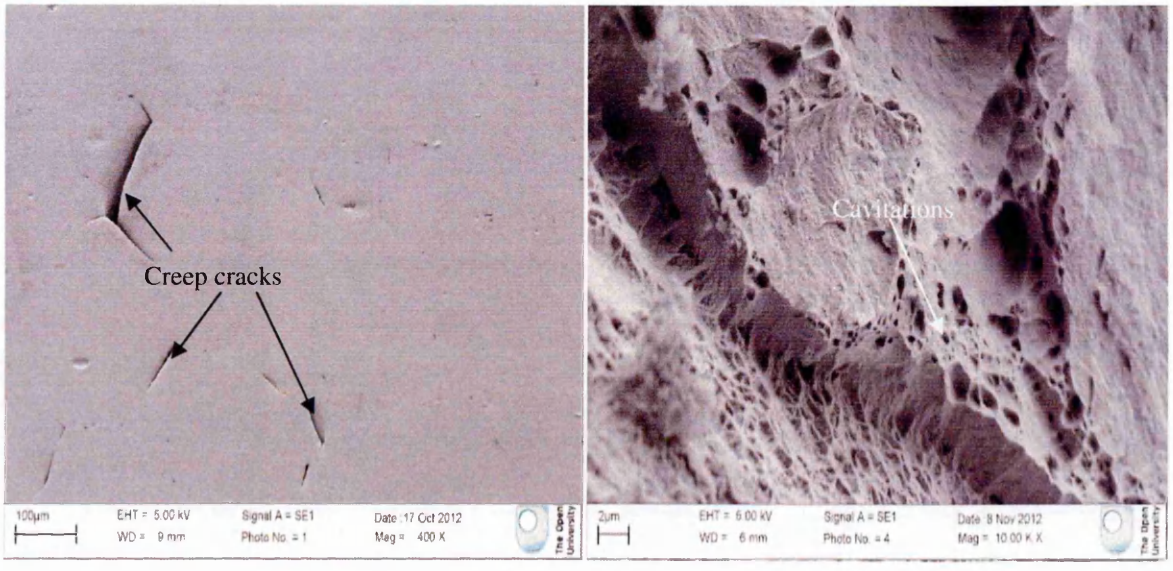

Fig. 7.8. SEM micrographs of service-aged Type 316H stainless steel showing: (a) creep cracks after 0.068 creep strain, and (b) intergranular cavitations on creep ruptured surface.

7.2.3.2. Creep tests results at 675°C

A summary of the interrupted creep tests results for specimens without prestrain obtained at 675°C is given in Table 7.2. The minimum creep strain rates and initial loading strains of the different specimens were similar, indicating good repeatability of the tests which is essential for comparative study of the misorientation development. The creep strain and rate curves for Sample A specimens obtained at 675°C and 150MPa are shown in Fig. 7.9 and Fig. 7.10, respectively. These conditions gave a tertiary dominated creep response [8] which made the assessment of the primary creep difficult. A large rupture strain was recorded, indicating enhanced flow behaviour under these conditions.

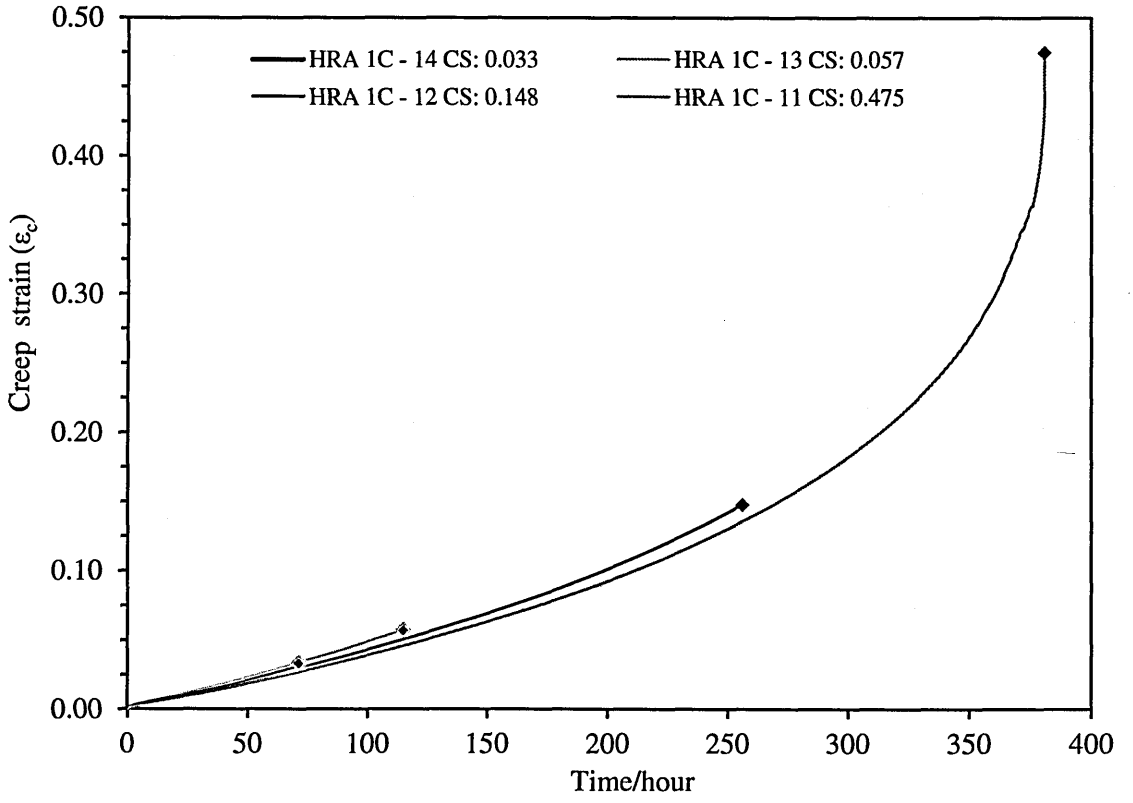

Fig. 7.9. Creep curves for service-aged Type 316H stainless steel crept at 675°C as in Table 7.2.

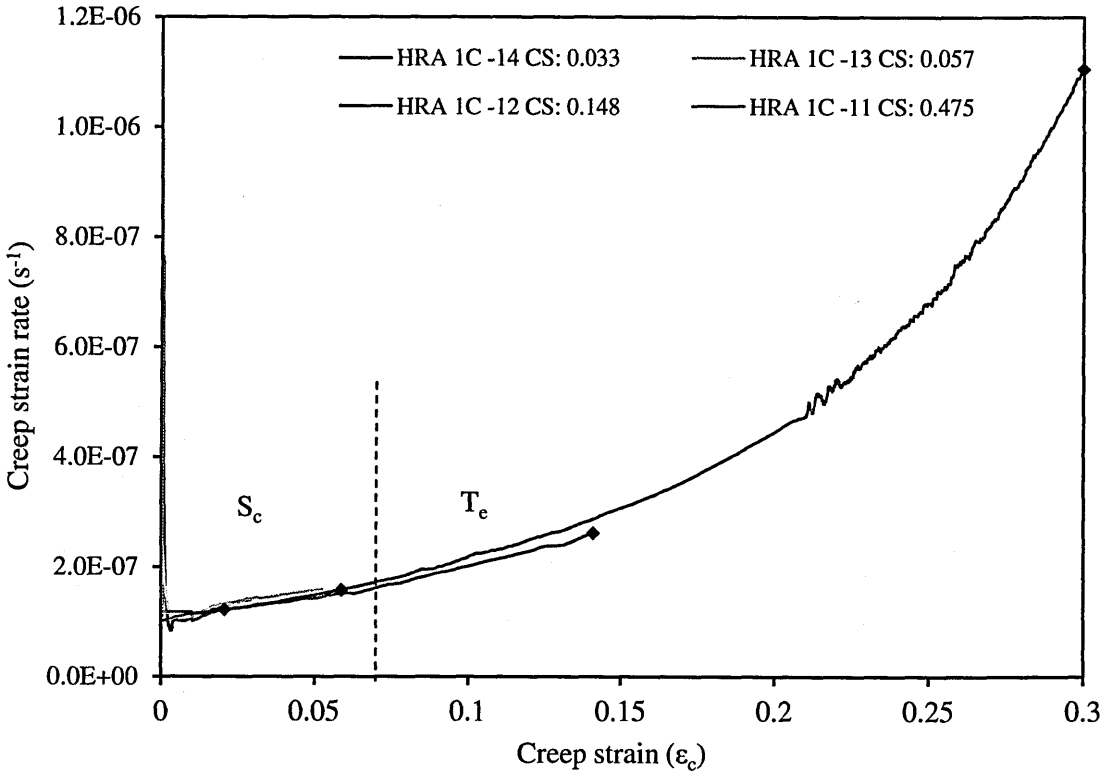

Fig. 7.10. Creep strain rate versus creep strain for service-aged Type 316H stainless steel crept at 675°C as in Table 7.2.

The creep response of RST steel (Sample B) at 675°C and 100MPa is shown in Fig. 7.11a, and results summarised in Table 7.2. The test which was interrupted after an accumulated creep strain of 0.05 indicated minimal primary creep. The service-aged steel (Sample A) exhibited similar strain hardening rates to RST steel at 675°C as shown in Fig. 7.11b, indicating a possible re-precipitation in Sample B at this temperature. Serrations were conspicuously absent from the flow curves indicating that dynamic strain aging does not occur under these conditions.

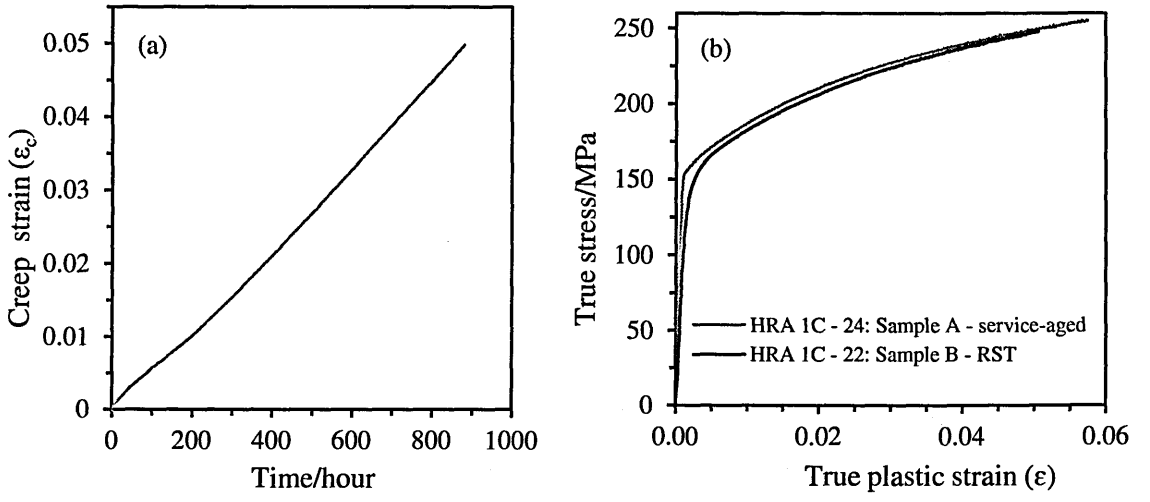

Fig. 7.11. (a) Creep response at 675°C and σ = 100MPa for re-solution heat treated Type 316H stainless steel. (b) Flow curves at 675°C for Type 316H stainless steels.

7.2.4. EBSD measurement results

7.2.4.1. Influence of creep strain on local misorientation distribution

The spread of the KAM frequency distribution increased with increasing creep strain. This was evident for both specimens with (see Fig. 7.12) and without (see Fig. 7.13) prior plastic deformation.

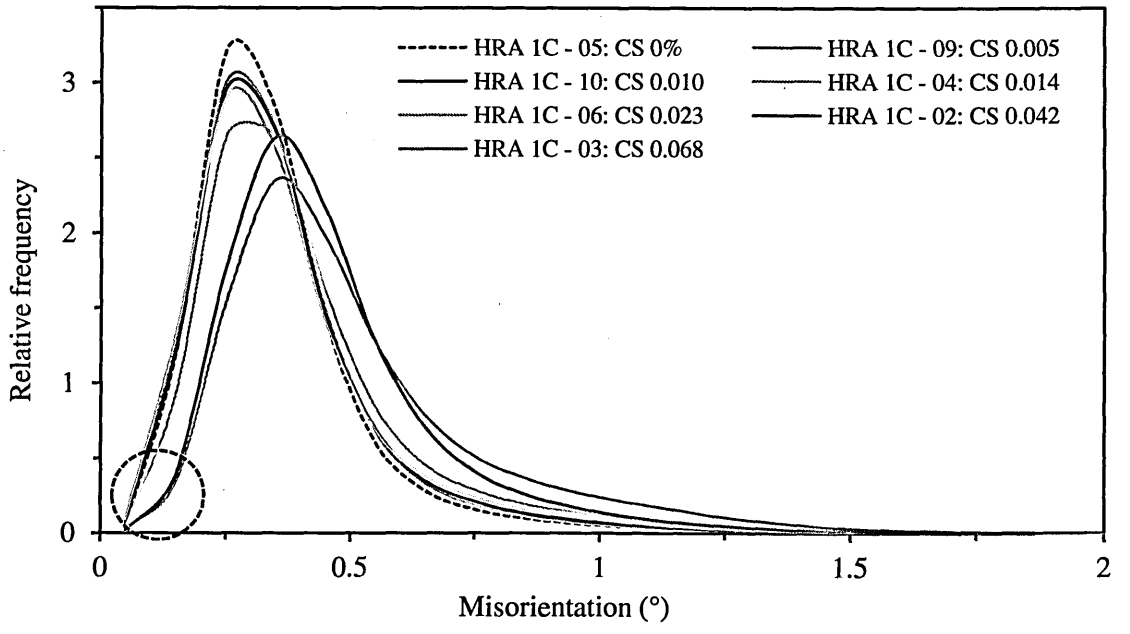

Fig. 7.12. Effects of creep strain on local misorientation distribution for service-aged Type 316H stainless steel deformed at 550°C as in Table 7.1.

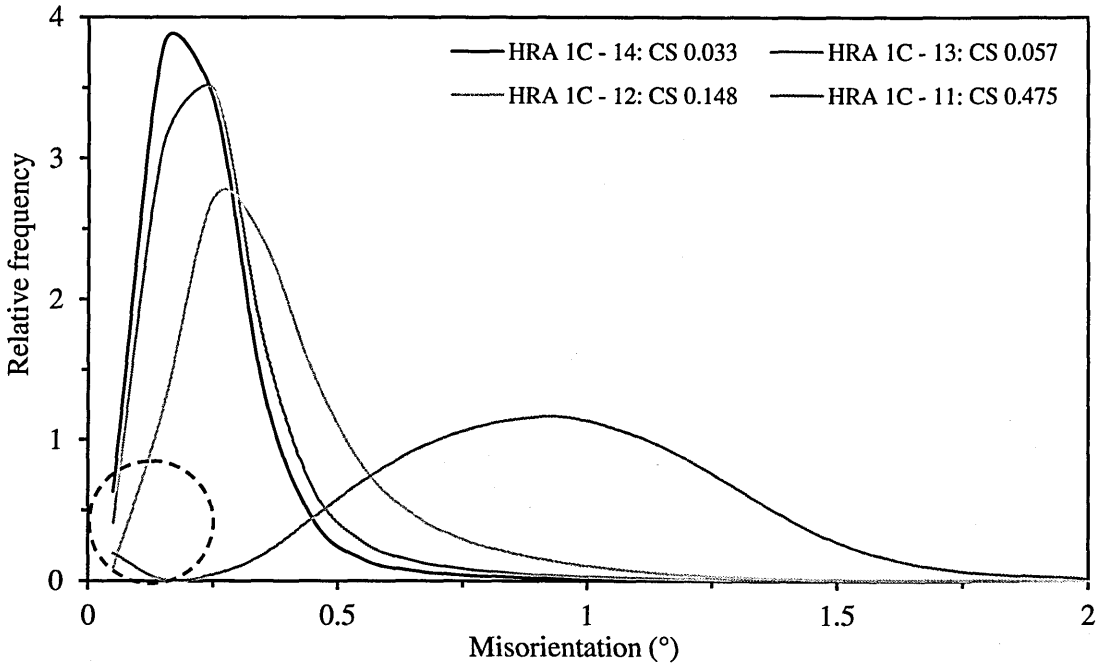

Fig. 7.13. Effects of creep strain on local misorientation distribution for service-aged Type 316H stainless steel deformed at 675°C as in Table 7.2.

In both service-aged and RST steels, plastic strain produced a marginally larger spread in the KAM distributions than deformation in creep, as seen in Fig. 7.14. It is apparent from Fig. 7.12 that the peak of the KAM distribution shifted after 0.023 strain, which corresponded to the initial stages of the tertiary creep as shown in Fig. 7.7. The orientation 'noise' in the data, represented by local misorientations <0.15°, increased with increasing creep strain in both specimens with and without prestrain as demonstrated by the changing curve profile in Fig. 7.12 and Fig. 7.13 (circled part). As seen in Fig. 7.13 the distribution approached a normal curve for the highly deformed specimen.

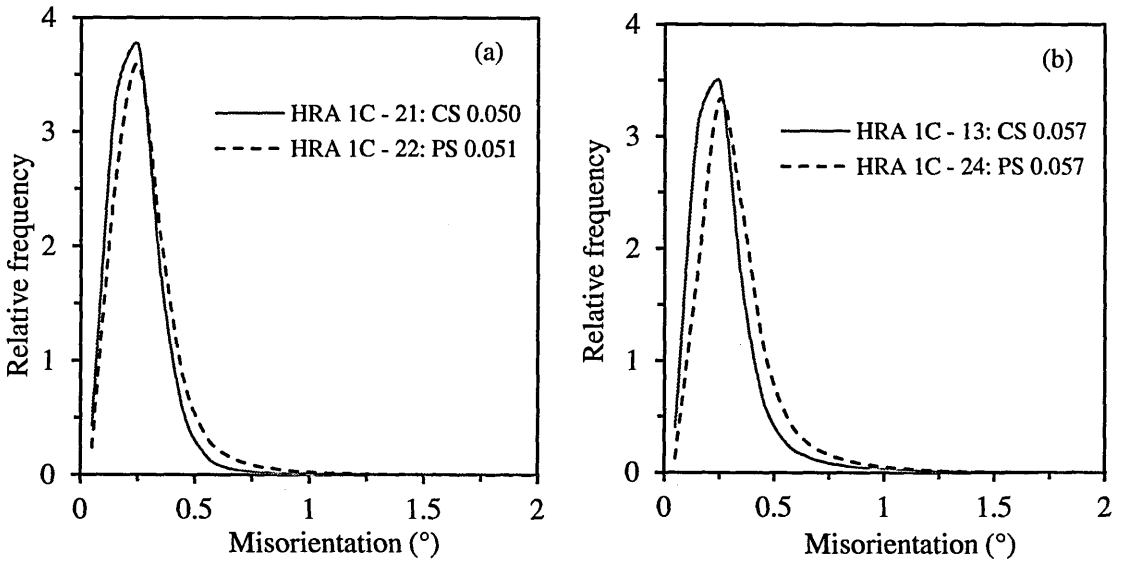

Fig. 7.14. Comparison between plastic strain (PS) and creep strain (CS) effects on local misorientation distribution at 675°C for (a) re-solution heated treated, and (b) service-aged Type 316H stainless steel. Marginal increase in spread under plastic deformation is evident.

7.2.4.2. Development of creep-induced local misorientations

The build-up of local misorientations (KAM_a) at 550°C in the prestrained specimens increased as a function of creep strain as seen in Fig. 7.15a. The sum of creep and prior plastic strain is referred to here as the total strain while the sum of their corresponding KAM_a, is referred to as the total KAM_a. This nomenclature applies to all the other metrics in this Chapter. Since the prior deformation was constant at 0.079 strain, the local misorientations due to creep built additively on the existing misorientations (those due to prior strain). It is evident that the creep strain had a significant effect on the development of misorientations <2°. This was more apparent for specimens crept at 675°C without prestrain, shown in Fig. 7.15b where, KAM_a increased with increasing creep strain.

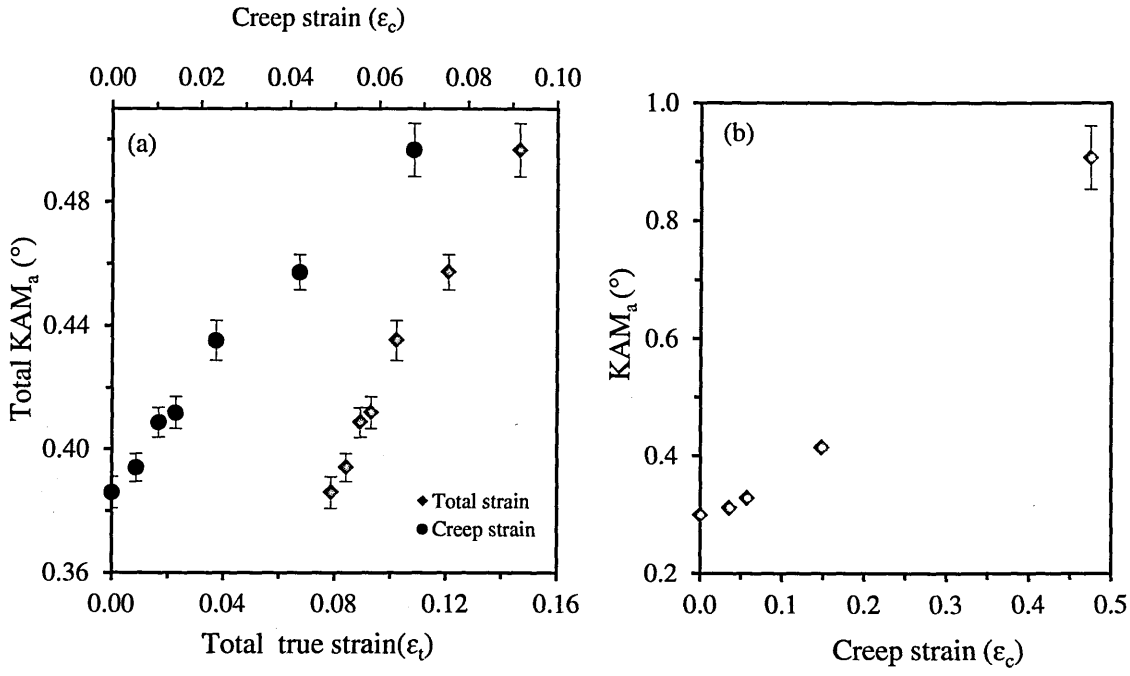

Fig. 7.15. Variation of (a) total KAM_a with total strain (primary axis) and with creep strain (secondary axis) for service-aged Type 316H stainless steel deformed at 550°C as in Table 7.1, and (b) KAM_a with creep strain for specimens deformed at 675°C as in Table 7.2.

Local misorientations based on LAMF also increased with increasing creep strain at 550°C, as seen in Fig. 7.16a for specimens with prior plastic deformation. Similarly, at 675°C the development of LAMF in specimens without prestrain increased with increasing creep strain as seen in Fig. 7.16b. Apparently the development of local misorientations in the range 2°-15° was not significant for creep strains <0.1. However, at higher creep strains, LAMF increased implying a correspondence between LAM (low angle misorientation) development and the creep deformation in the primary, secondary and tertiary stages as deduced from Fig. 7.6, Fig. 7.7, Fig. 7.9 and Fig. 7.10. The concentration of LAMs in the regions bordering grain boundaries increased with the creep strain as seen in Fig. 7.17.

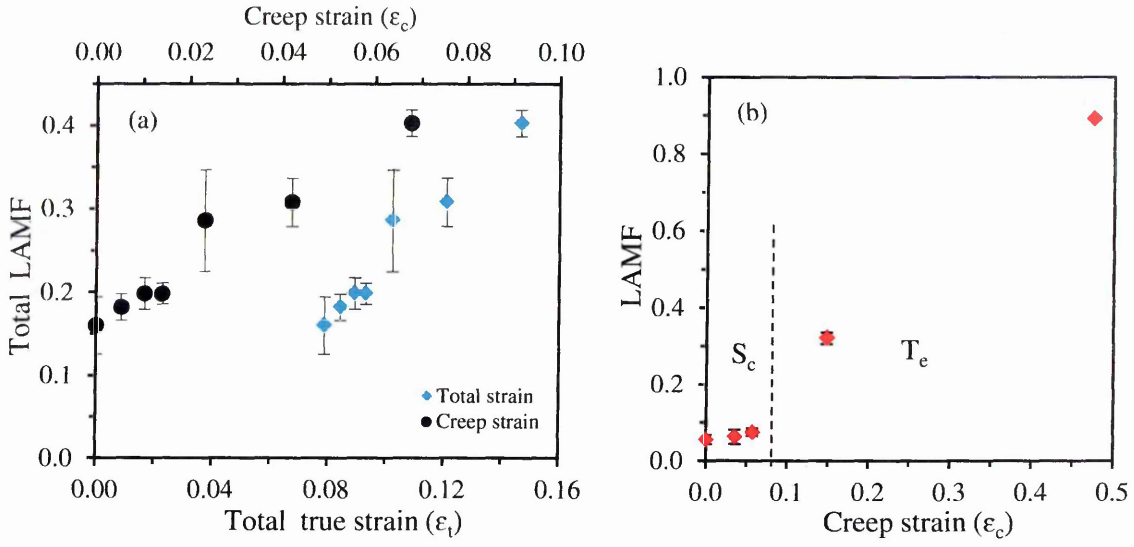

Fig. 7.16. Variation of (a) total LAMF with total strain (primary axis) and with creep strain (secondary axis) for service-aged Type 316H stainless steel deformed at 550°C as in Table 7.1, and (b) LAMF with creep strain for specimens deformed at 675°C as in Table 7.2.

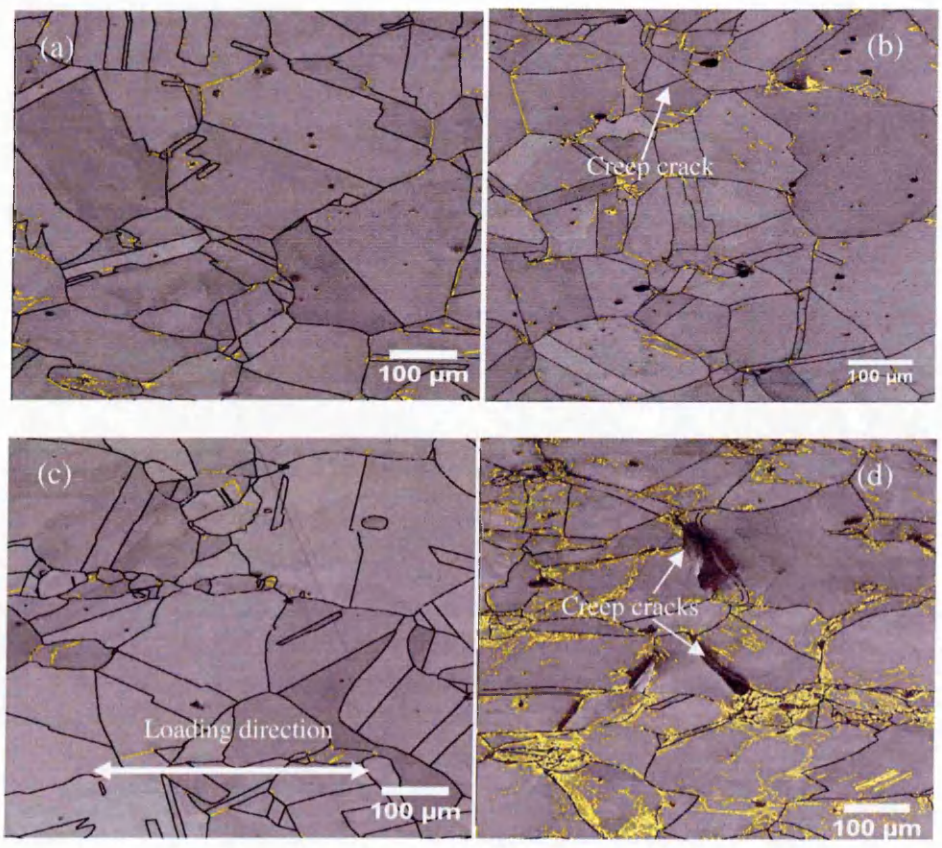

Fig. 7.17. Distribution of LAMs (yellow marks) in service-aged Type 316H stainless steel crept at 550°C by (a) 0.01, (b) 0.068 strains, and at 675°C by (c) 0.05, (d) 0.47 strains. Increased deformation along grain boundaries is evident at higher creep strains.

7.2.4.3. Development of creep-induced long-range misorientations

The accumulation of long-range misorientations as measured by $AMIS_a$ increased linearly with the applied creep strain as shown in Fig. 7.18a, for the prestrained specimens. This increase of uncorrelated misorientation with creep indicates a rearrangement of the dislocations structures within the individual grains (see section 4.3.5.2). $AMIS_a$ also increased similarly for specimens crept at 675°C without prestrain as seen in Fig. 7.18b, indicating an increase in grain deformation as the creep progresses from primary to tertiary stage. As shown in Fig. 7.19, grains with higher AMIS values frequently had higher overall Schmid factor values. A complete correspondence is however, not expected since the overall stress direction specified in the software is modified at the local level due to the anisotropy of the grains' deformations.

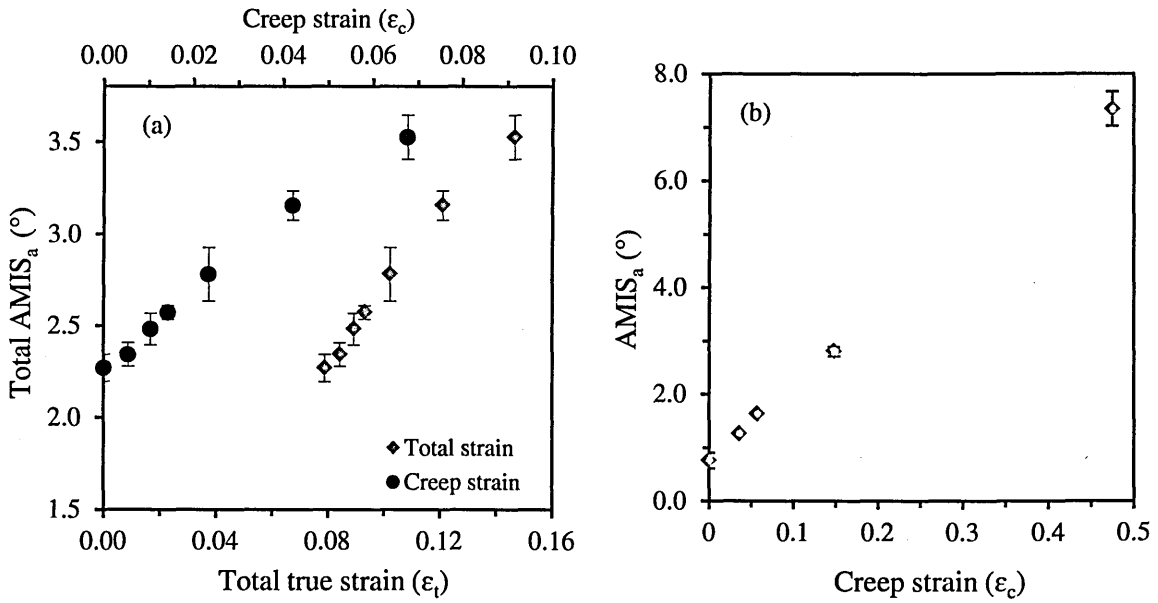

Fig. 7.18. Variation of (a) total $AMIS_a$ with total strain (primary axis) and with creep strain (secondary axis) for service-aged Type 316H stainless steel deformed at 550°C as in Table 7.1, and (b) $AMIS_a$ with creep strain for specimens deformed at 675°C as in Table 7.2.

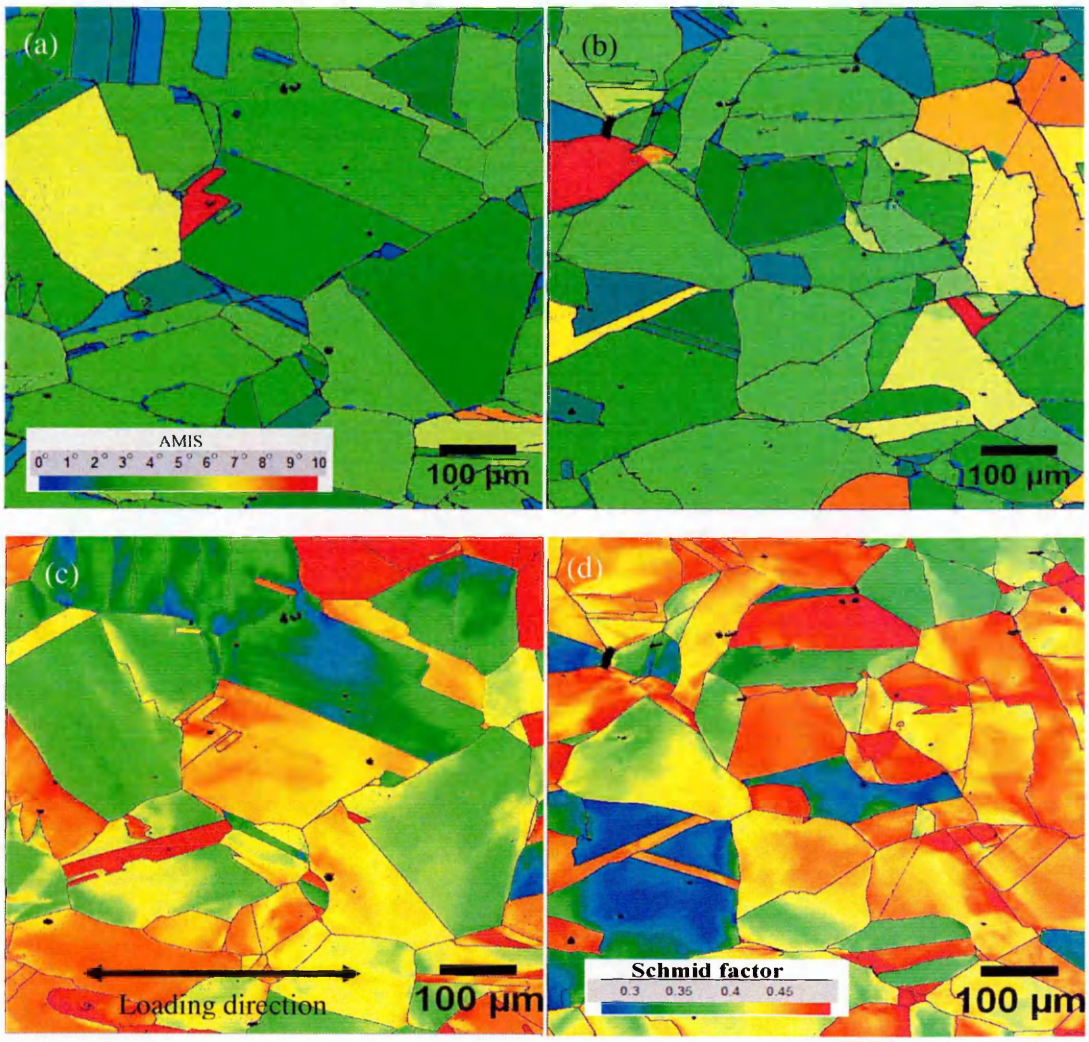

Fig. 7.19. AMIS maps (a-b) and corresponding Schmid factor maps (c-d) for service-aged Type 316H stainless steel deformed as in Table 7.1 to (a) 0.01, and (b) 0.068 creep strain showing frequently higher AMIS values in grain with higher overall Schmid factor values. Insert: maps legends.

The proportion of deformed grains increased with increasing creep deformation as shown in Fig. 7.20a, for specimens with prior plastic deformation. DGF increased rapidly in the primary and secondary stages after which it gradually decreased toward the tertiary stage. This suggests that the number of deformed grains increases at a reducing rate as the creep progresses from the primary to tertiary stage with DGF asymptotically approaching 1. This was more obvious for specimens crept without prestrain at 675°C, where DGF was close to 1 after 0.47 creep strain as seen in Fig. 7.20b. The rate at which individual grains

started to deform (see Fig. 7.20b) corresponded with the overall creep deformation rate as shown in Fig. 7.9 and Fig. 7.10 where it was highest in the primary and secondary stages and lowest in the tertiary stage.

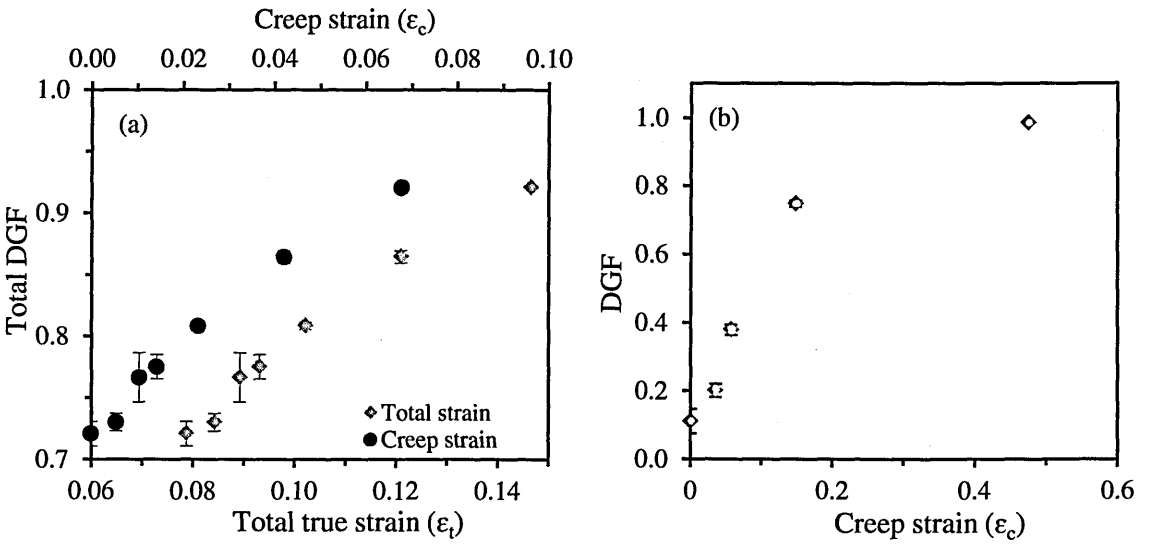

Fig. 7.20. Variations of: (a) total DGF with total strain (primary axis) and with creep strain (secondary axis) for service-aged Type 316H stainless steel deformed at 550°C as in Table 7.1, and (b) DGF with creep strain for specimens deformed at 675°C as in Table 7.2.

7.2.4.4. Comparisons of creep and plastic strain-induced misorientations

The accumulation of local misorientations (KAM_a) as a function of strain is shown in Fig. 7.21a for both specimens deformed in tension at 550°C and those prestrained and crept at 550°C using an initial stress of 320MPa. At equivalent strains, KAM_a values were only comparable for specimens originally from nearby positions (*HRA 1c* or *HRA 1a*) indicating the sensitivity of the metric to microstructural variations. Local misorientations based on LAMF gave similar results as shown in Fig. 7.21b. The large scatter in the data indicates the sensitivity of this metric to microstructural variations. These results underline the importance of considering only similar materials when conducting comparative local misorientation studies.

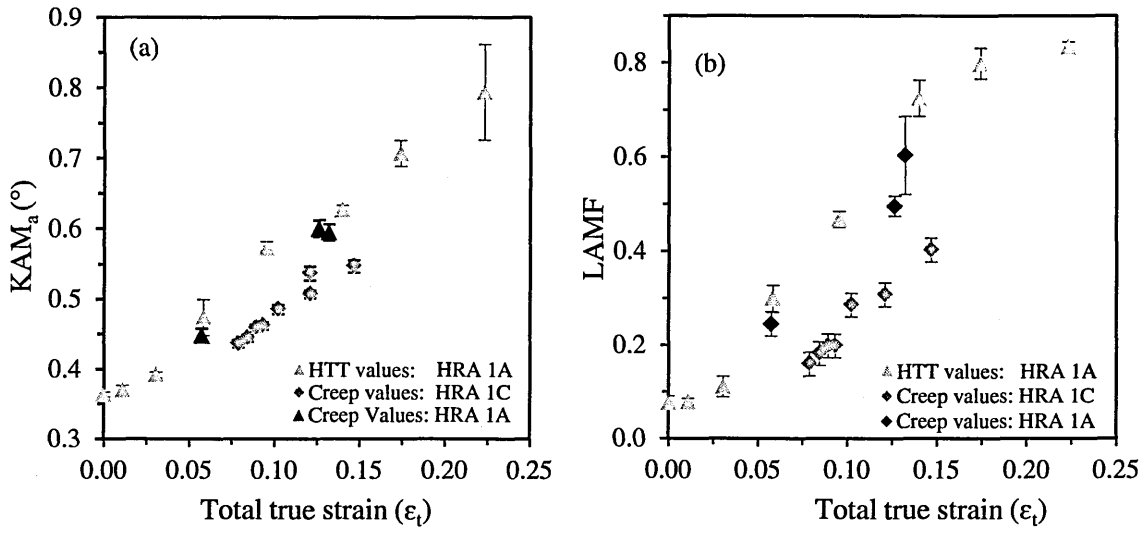

Fig. 7.21. Variations of (a) KAM_a and (b) LAMF with total true strain for service-aged Type 316H stainless steel deformed in tension (see Table 6.1) and in creep at 550°C (see Table 7.1).

The development of the long-range misorientations on which $AMIS_a$ is based was little influenced by the local variations in the material as shown in Fig. 7.22a. At equivalent total strains the values obtained from HTT tested specimens and from prestrained crept specimens were comparable, despite differences of their origins. Similarly, as seen in Fig. 7.22b the evaluation of misorientation based on DGF metric seemed completely insensitive to variations in material's microstructure as values obtained from different specimens followed a single curve. The correlation between DGF and total strain was also independent of the existing prestrain level prior to creep deformation. This implies that the DGF correlation based on HTT tests can be used to estimate the total strain in crept components regardless of their differences in microstructure.

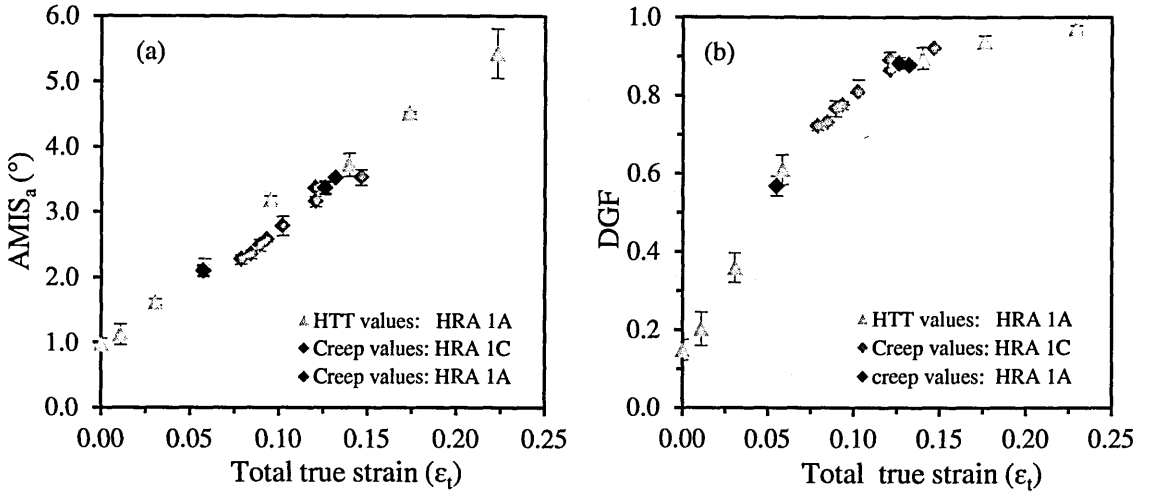

Fig. 7.22. Variations of (a) $AMIS_a$ and (b) DGF with total true strain for service-aged Type 316H stainless steel deformed in tension (see Table 6.1) and in creep at 550°C (see Table 7.1).

In Sample A specimens, both local and long-range misorientations developed faster in pure plastic than in pure creep deformation as shown in Fig. 7.23a. Similar results were obtained from Sample B specimens as seen in Fig. 7.23b.

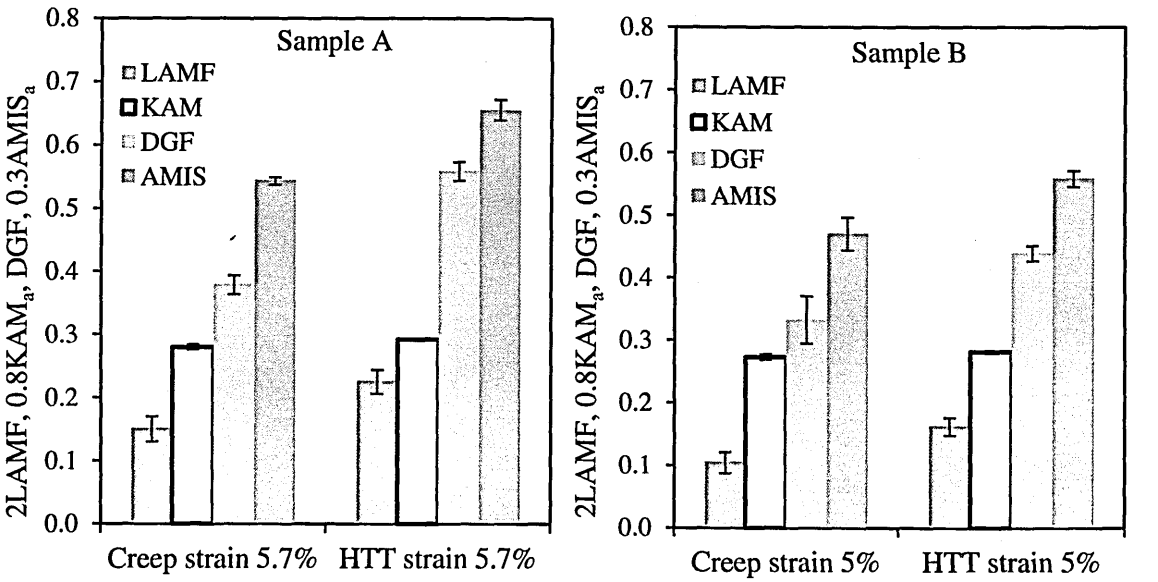

Fig. 7.23. Dependence of misorientation development on deformation mechanism and misorientation metric in Type 316H stainless steel deformed at 675°C.

Interestingly, at equivalent strains the KAM_a values obtained in plastic and in creep were comparable, unlike the other metrics which exhibited large differences. Therefore, by comparing the strain estimate derived from the KAM_a metric and those derived from the

other metrics, it is possible to estimate the accumulated creep strain from the differences since all the metrics are computed from the same data. This assessment is suitable for components with both prior deformation and accumulated creep strain. As seen in Fig. 7.24a, after prestrain the development of long-range misorientations due to creep strain added to the existing misorientation and followed the curve dictated by the prestrain level, while in the absence of prestrain, the misorientations obtained were significantly lower. This difference was not so apparent however, when a similar assessment was based on KAM_a particularly at total strain <0.2 as shown in Fig. 7.24b. In the current work, the metric's creep sensitivity factor (Ω) is defined as p_c/p_p, where p_p and p_c are the metric's values associated with plastic and creep strains, respectively. Ω for tests conducted at 675°C is listed in Table 7.3.

Table 7.3: Metric's creep sensitivity factor (Ω) at 675C°for service-aged Type 316H stainless steel.

Descriptors	Sample	Deformation	True strain	KAM_a	LAMF	DGF	$AMIS_a$
Ω	A	Creep @150MPa	0.057	1.0	0.7	0.7	0.8
Ω	B	Creep @100MPa	0.050	1.0	0.6	0.8	0.8

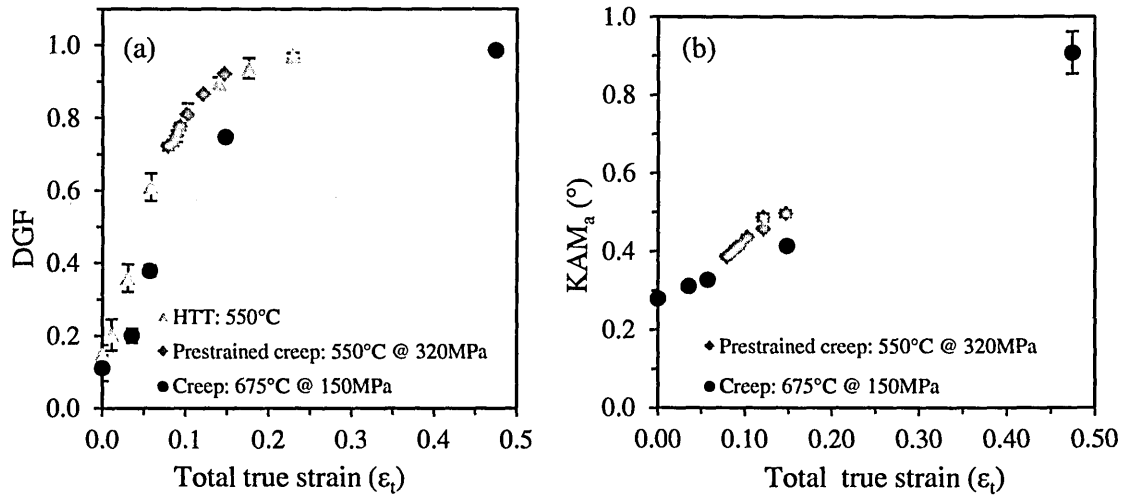

Fig. 7.24. Variations of: (a) DGF and (b) KAM_a with total strain for service-aged Type 316H stainless steel crept at 550°C (see Table 7.1) and at 675°C (see Table 7.2).

7.2.4.5. The influence of creep and plastic strain on twin boundary fractions

The twin boundary fractions (TBF) decreased with increasing plastic strain as shown in Fig. 7.25. This was apparent for all tests conducted in tension and in compression at 550°C.

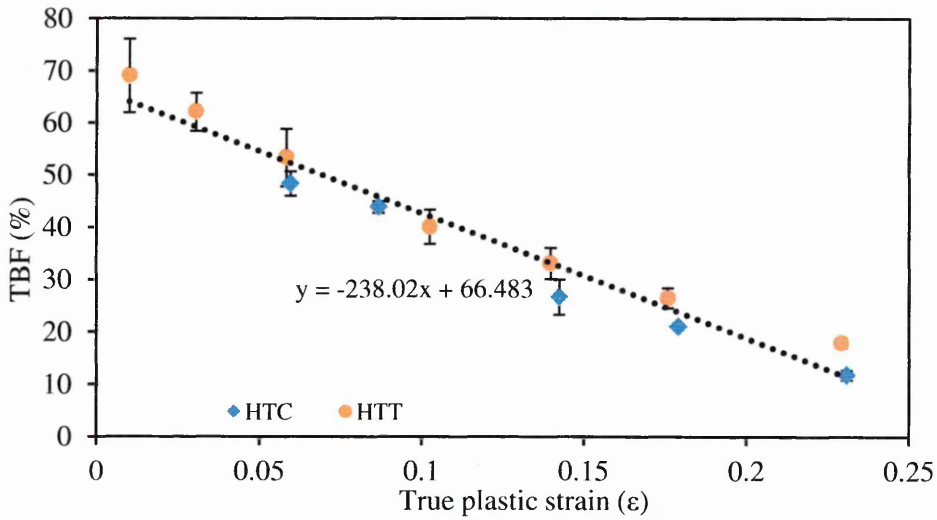

Fig. 7.25. Variation of twin boundary fractions with true plastic strain for service-aged Type 316H stainless steel deformed as in Table 6.1.

As seen in Fig. 7.26 for the room temperature *in-situ* EBSD measurement, grain boundaries with the near-twin orientation in the unstrained sample deviated from this orientation as the strain was increased to 0.247.

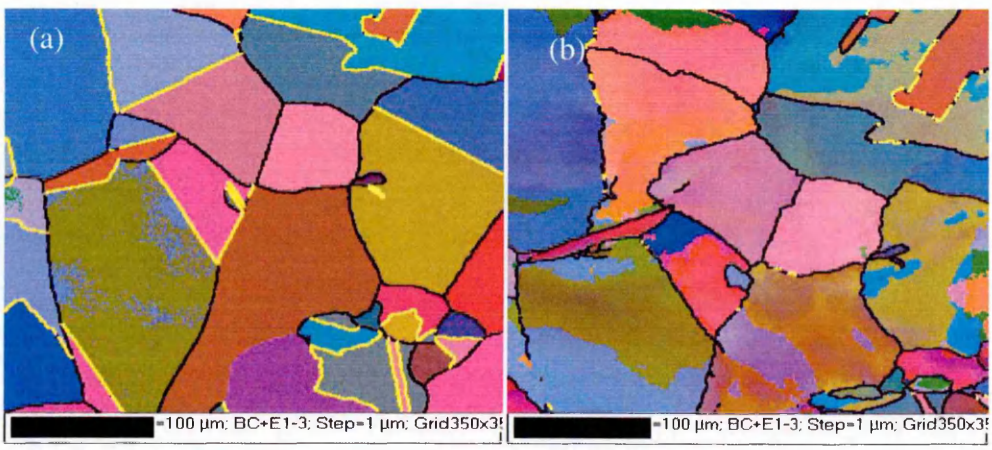

Fig. 7.26. Orientation map of service-aged Type 316H stainless steel deformed as in Table 6.5 showing the near-twin boundaries (yellow lines): (a) at 0 strain, and (b) after 0.247 strain.

At equivalent strain (0.057) and temperature (675°C), the reduction in TBF was higher in creep deformation than in plastic deformation as shown in Fig. 7.27a. However, for specimens with constant prestrain of about 0.079 (see Table 7.1), the accumulation of creep strain reduced the initial TBF monotonically as seen in Fig. 7.28. Similarly, in specimens without prior plastic deformation (see Table 7.2), the TBF reduced with increasing creep strain as seen in Fig. 7.29.

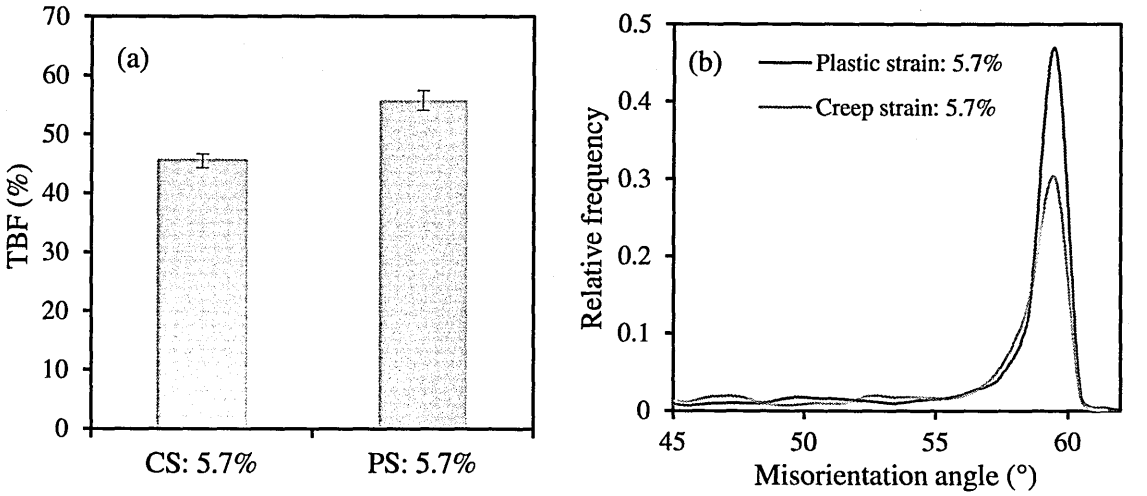

Fig. 7.27. Variations of twin boundary fractions (a), and misorientation angle distributions (b), as a function of creep strain (CS) and plastic strain (PS) for service-aged Type 316H stainless steel deformed at 675°C.

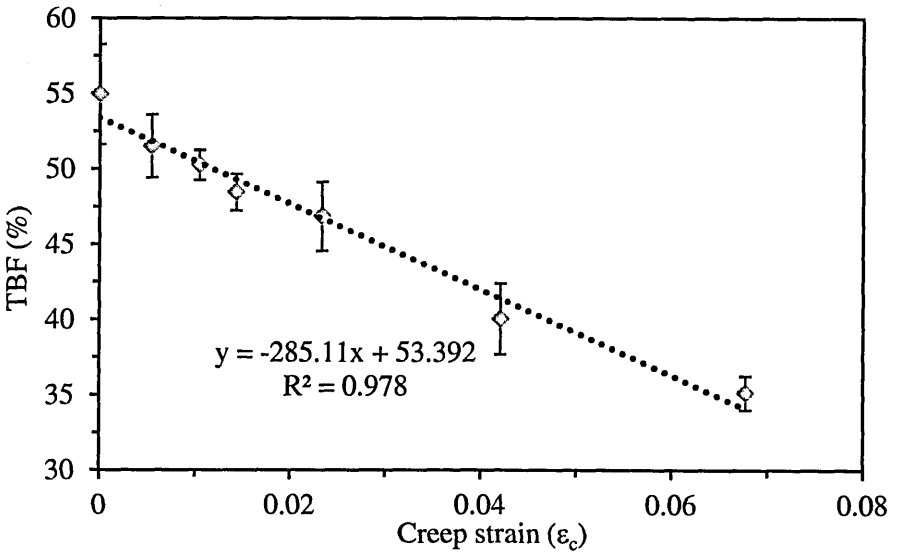

Fig. 7.28. Variation of TBF with creep strain for service-aged Type 316H stainless steel prestrained to 0.079 strain at 550°C.

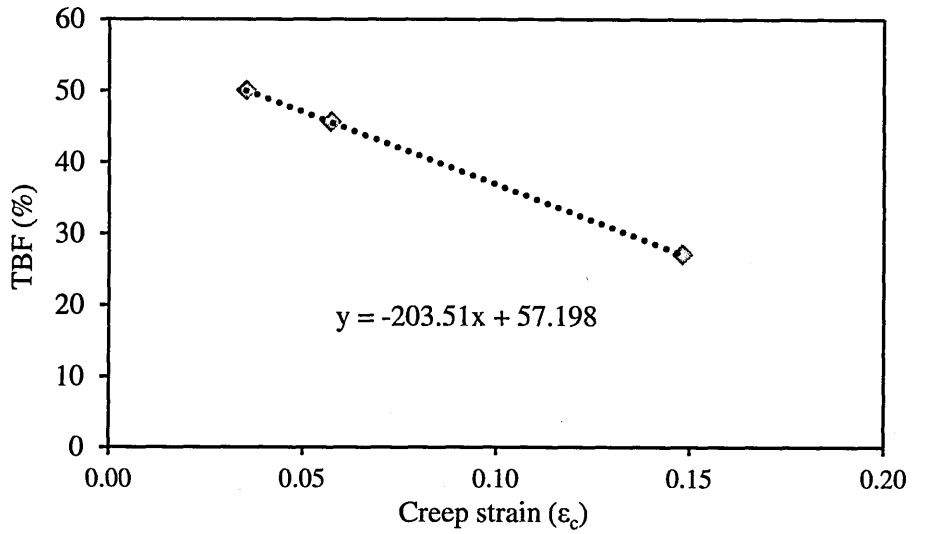

Fig. 7.29. Reduction of the TBF with increasing creep strains for service-aged Type 316H stainless steel deformed at 675°C as in Table 7.2.

As seen in Fig. 7.30 the peaks in the misorientation angle plots corresponding to the near-twin boundaries (i.e. rotation about 60°) progressively broaden and reduced in intensity with increasing strain for deformation conducted at 550°C in tension. As seen in Fig. 7.27b this change was more in creep than in plastic deformation.

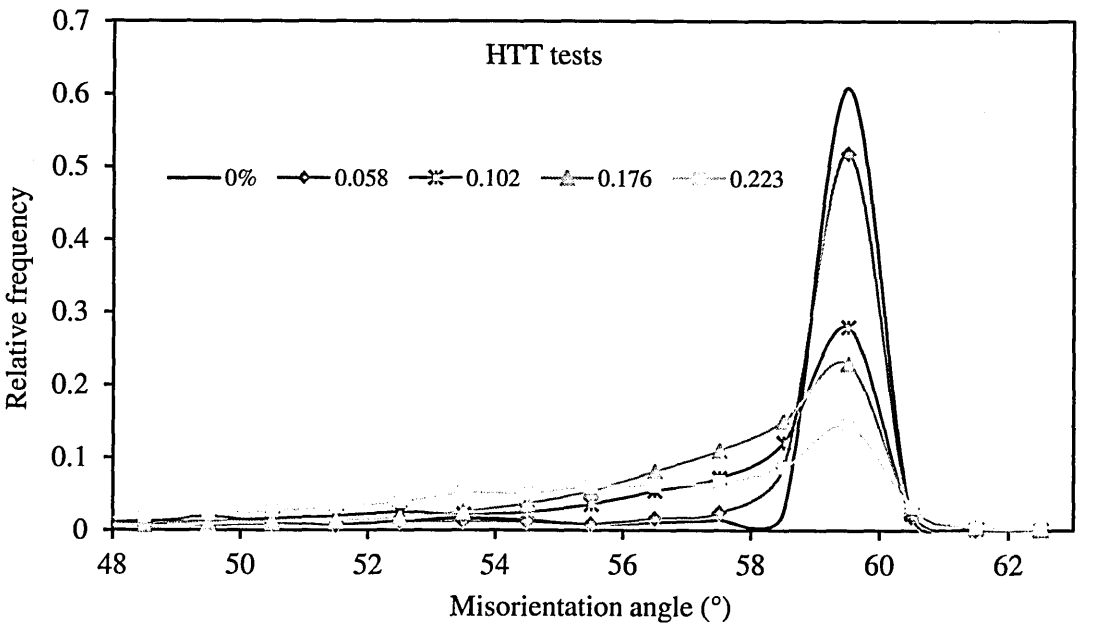

Fig. 7.30. Misorientation angle plots of service-aged Type 316H stainless steel showing reduction in intensity and increase in spread as the applied plastic strain increases.

7.2.5. *Discussion*

7.2.5.1. Creep responses for the service-aged and RST steels

The study of the effects of prior deformation on creep behaviour is important since most components used in power plants enter service in a prestrained condition e.g. welded components. As shown in Fig. 7.3 prior tensile deformation reduces the creep rupture strain and minimum creep strain rate ($\dot{\varepsilon}_m$) while increasing the creep rupture life (t_r). These effects increase with the level of prestrain applied and also depend on the condition under which the specimen is cooled during the prestraining stage. Specimens cooled under load had slightly lower creep resistance than those cooled without load as seen in Fig. 7.5. According to the Ashby deformation map for Type 316 stainless steel [16], dislocation creep is predicted to be the main deformation mechanism under the current creep conditions of stress and temperature in which $\sigma/G \sim 10^{-3}s^{-1}$ and $T/T_m = 0.5$.

The apparent improvement in creep resistance due to prestraining can therefore be explained in relation to the Orowan equation [15] $\dot{\varepsilon}_m = v_m b \rho_m$ where ρ_m represents the density of mobile dislocations and is a function of temperature and stress only, b the Burger vector magnitude and v_m the average velocity of the dislocations. Dislocation density increases with increasing plastic strain as seen in Fig. 4.15 and at high temperature some of the dislocation structures introduced are preserved [48] therefore serving to restrict the dislocation movement during subsequent creep (see section 4.3.5.2). Effectively this reduces the dislocation velocity in the Orowan equation, leading to a reduction in $\dot{\varepsilon}_m$ when the ρ_m remains unchanged. However, if the dislocations introduced during the prestraining stage remain mobile during the subsequent creep, creep resistance will reduce due to an increase in ρ_m.

It is therefore possible that during creep, differences in the mobility of the dislocations introduced during the prestraining stage may explain the discrepancies in the creep responses of prestrained specimens cooled with and without load even though their

tensile behaviours were similar as seen in Fig. 7.5a. Cooling under load may hinder rearrangement of dislocation structures and thus the relief of macro- and micro-stresses [30]. The resultant residual stresses may act on the dislocations in the subsequent loading making them more mobile since $v_m = M\sigma_s b$ where, M is a factor describing dislocation mobility in presence of obstacles and σ_s is the stress acting per unit length of dislocation line [16]. The dependence of the creep strain rate on ρ_m is also demonstrated in Fig. 7.3 where both as-received and prestrained specimens have comparable initial deformation (Table 7.1) but extremely different creep resistances. The as-received specimen is plastically deformed during creep meaning that the mobility of the dislocations introduced may remain high, unlike in the prestrained specimen where dislocation mobility may be reduced by rearrangement of the dislocation structures on unloading prior to creep deformation.

The observed reduction in creep ductility on prestrained specimens (see Fig. 7.3) can be linked to deformation inhomogeneity as seen in Fig. 5.5. This could favour cavity nucleation due to the high local stresses [184] generated at triple junctions and around intergranular particles as result of deformation incompatibilities. This would accelerate creep failure which is seen to occur through the nucleation and growth of intergranular cavities (see Fig. 7.8 and Fig. 7.17d).

Prestraining reduces the initial creep loading strain, as seen in Table 7.1. This is mostly due to strain hardening of the specimen owing to plastic deformation in the prestraining stage. The amount of instantaneous strain on creep loading depends mainly on the difference between the highest prestraining stress and the initial applied stress during creep. Creep loading strains are minimal, when the prestraining stress is higher than the initial stress applied in creep, as in the present case, and most are recoverable as seen in Fig. 7.1. In agreement with current findings [185] the creep loading strains in service-aged Type 316 stainless steel were found to decrease with increasing prestrain.

Microstructural variations have a significant effect on the creep response of the service-aged Type 316 stainless steel as seen in Fig. 7.4, where two specimens extracted from different sections of the same parent material (Sample A) exhibited different creep resistance. The specimens had comparable yield strengths, as seen in Fig. 7.2, indicating similar mechanical histories. However, the observed difference in their flow stresses with increasing strain clearly indicates differences in their microstructure and/or composition (see section 2.2.2). Possibly, there was more precipitation in block *HRA 1a* than in block *HRA 1c* which could have required higher stresses on *HRA 1a* to achieve similar deformation in the two sets of specimens. Surprisingly, when deformed similarly in creep, specimens exhibiting higher prestraining stresses (*HRA 1a*) had lower creep resistance compared to those from *HRA 1c*. As discussed in Chapter 5, the possible explanation for this surprising result could be the differences in microstructures particularly in the number density of intergranular precipitates. During the tensile deformation, the strain rates are relatively high and so the propensity for GBS is reduced but at low strain rates, as in creep, GBS is more pronounced. It is possible that an additional precipitation in the matrix may have led to higher stresses during tensile deformation [158] and that coarsening of the intergranular precipitation may have reduced creep resistance [47]. Since precipitation alters the concentration of key alloying elements such as C, Cr and Mo in solid-solution within the austenite phase, this may also account for the reduced creep resistance in microstructures postulated to have higher precipitation i.e. *HRA 1a*, owing to their reduced resistance to dislocations movement (see section 2.2.2.2).

The difference between the microstructures of blocks *HRA 1c* and *HRA 1a* could possibly be due to variations in the temperature distribution of the steam header (see Fig. 4.2) during service which could have resulted in differences in the number densities and coarseness of precipitates in regions close to and remote from the nozzle. However, this assertion needs to be validated may be through thermal modelling of this component.

To reduce scatter in the creep responses (see Fig. 7.6) it was therefore imperative to use material of comparable microstructures. Other sources of scatter in the creep responses include variations in temperature and applied stresses, which needs proper control during testing as explained in Chapter 3. Minimisation of scatter was vital to allow meaningful comparative misorientation studies of the different crept specimens.

The creep responses for Sample A specimens at 675°C and 150MPa are shown in Fig. 7.9. Overlaying of the creep curves implies little microstructural variability among the specimens tested and also proper control of test conditions. At these conditions where $\sigma/G \sim 10^{-3}s^{-1}$ and $T/T_m = 0.58$, the dominant creep deformation mechanism is predicted from the Ashby deformation map for Type 316 stainless steel to be dislocation creep. The tertiary-dominated creep response shows little primary creep (see Fig. 7.10) and is consistent with the relatively high homologous temperature and applied stress. The relatively high creep strain rates shown in Table 7.2 can be attributed to higher atomic diffusion rates at this higher temperature since these are rate controlling in dislocation creep. The fact that the loading strains were low (see Table 7.2) means that there were fewer dislocations already generated to obstruct the movement of others during creep. This could have led to a relatively high dislocation velocity and in accordance with Orowan law, a relatively high creep strain rate.

The similarity of the flow behaviour of specimens from Sample A and Sample B deformed similarly at 675°C (see Fig. 7.11b) indicates that re-precipitation may have occurred in Sample B specimen during the heating stage since their room temperature flow behaviour were significantly different as seen in Fig. 5.1. The specimen was heated at 675°C for 1 hour to allow temperature homogenisation and according to the temperature-time precipitation diagram for annealed Type 316 stainless steels (see Fig. 2.2) this time is adequate for the precipitation of $M_{23}C_6$ carbides. The absence of serrations from the curves

for both specimens indicates the higher diffusion rate of solute atoms at 675°C which makes DSA less likely.

7.2.5.2. Distribution of local misorientation under creep conditions

The mean and spread of the local misorientation distribution as measured by KAM, increases with increasing creep strain as seen in Fig. 7.12 and Fig. 7.13. This clearly indicates that there is a net increase in the GND densities as the creep strain increases which leads to the development of more and larger misorientations, causing the observed spread in the distributions. As seen from Fig. 7.12 there is small increase in the spread and thus of the dislocation densities during primary and secondary creep. This can be attributed to the competing processes of strain hardening and the rate of thermal recovery by rearrangement and annihilation of dislocations [31]. However, the transition to tertiary creep is accompanied by; a wider spread in the distribution, a shift in the distribution peaks and by a higher proportion of misorientation <0.15°, referred here as orientation 'noise'. This may indicate a larger increase in GND densities in tertiary creep, causing a larger spread in the misorientation distributions. On the other hand, the observed increase in the orientation 'noise' is an indication of the reduced precision of orientation measurement by the EBSD system at higher strains (see section 2.4.4.3). The distribution of local misorientation approaches the normal distribution as the creep strain increases to rupture as seen in Fig. 7.13, indicating an increasing tendency toward a random distribution of misorientation angles.

Plastic deformation generates more GNDs and thus a wider spread in the local misorientation distribution than creep deformation as seen in Fig. 7.14 (a and b). This arises from the different deformation mechanisms where the number of slip planes available for dislocation glide may be more limited in plastic than in creep deformation at this temperature. More dislocations must be generated to accommodate plastic strain, while

the processes of cross-slip and climb in creep allow similar strains to be accommodated by relatively low dislocation densities. Since both deformations were performed at 675°C it is the strain rate that determined the predominant deformation mechanism with the slower rate allowing more time for atomic diffusion and thus dislocation climb. These findings reveal the potential of the local misorientation distributions to distinguish creep strains from plastic strains but since such distribution depends on many other factors discussed previously, this assessment may not be very reliable.

7.2.5.3. Evolution of local misorientation with creep strain

It is apparent from Fig. 7.15 that local misorientations as measured by KAM_a increase with increasing creep strain. The creep strain was accommodated by the generation of GNDs and so the increase in KAM_a could have resulted from a general increase in the local lattice curvature arising from the increased GND densities. The results from the prestrained specimens (see Fig. 7.15a) indicate that the misorientations developed during creep, added to the pre-existing misorientations irrespective of the prestrain level. This assertion is based on a setting where dislocation creep is the main deformation mechanism and may therefore not apply generally to other creep deformation mechanisms.

The development of local misorientations in the range of 2°-15° is less influenced by primary and secondary creep as seen in Fig. 7.16b. It is evident that at these creep stages no significant increase in LAMF is observed and so the local misorientation build-up is mainly below 2°. This is supported by fact that KAM_a which assesses misorientations <2° exhibits a monotonic increase with creep strain (see Fig. 7.15b). However, an increase in LAMF is seen towards the tertiary stage of creep, indicating an increase in the misorientations between 2° and 15° and reflecting more significant distortion of the steel microstructure. As seen from Fig. 7.12 and Fig. 7.13 there is a general increment in the average local misorientation as the creep strain increases and this could have led to the

development of the LAMs (2°-15°) during the tertiary creep. It is also possible that an increase in recovery rates as the creep progresses from the primary to the tertiary stages led to an increase in LAMs.

7.2.5.4. Evolution of long-range misorientation with creep strain

The processes of climb and glide which characterise dislocation creep ensure that accumulation of dislocations occurs at much longer length scales. Accordingly, during creep deformation the development of long-range misorientations which contribute to AMIS is expected and, as seen Fig. 7.18, $AMIS_a$ increases almost linearly with increasing creep strain. This indicates that the evolution of long-range misorientations due to creep continues to build on the existing misorientations and that there is a constant increase in each grains' deformation as the creep progresses from the primary to the tertiary stage. This reaffirms the findings from Fig. 7.12 and Fig. 7.13 which showed a general increase in dislocation densities with increasing creep strain. An increase in $AMIS_a$ generally corresponds to an increase in dislocation densities as seen in Fig. 6.12.

The general increase of the grains' deformation with increasing creep strain means more and more grains will be considered deformed as their AMIS surpasses the threshold value defining an undeformed grain (see section 3.4.1.5d). The fraction of deformed grains in a given area (DGF) increases with increasing creep strain at a reducing rate as seen in Fig. 7.20. As shown in Fig. 7.19, AMIS is frequently higher for grains with higher overall Schmid factors and so deformation will occur first in these grains during the primary and secondary creep. This gives a high rate of DGF development with respect to the accumulated strain, but as the global deformation increases the rate of DGF increase reduces as the deformation progresses to grains with relatively low overall Schmid factors, leading to the observed saturation. At the grain level in polycrystalline materials, creep is therefore more prevalent in grains with relatively high overall Schmid factor values and so

in reference to the maximum principal stress direction they can be termed as "creep weak grains". These grains have their slip systems favourably oriented with the respect to the applied stresses. The ease of creep deformation of these grains during service could have resulted in intragranular precipitation variations amongst grains as discussed in section 4.3.3.1. It is therefore possible that the evolution of DGF with creep strain is a function of the existing texture in the material. In general, as the creep progresses the number of deformed grains also increases giving a DGF of ~1 at the rupture point. Accordingly, the DGF metric gives a good representation of the macroscopic strains obtained over many grains in a polycrystalline material.

7.2.5.5. Evolution of plastic and creep strain misorientation

The evolution of local misorientations with plastic and creep strain is highly dependent on the microstructure of the material. As seen in Fig. 7.21, the local misorientations produced by creep and plastic deformations to the same total strain can be different. However, a closer scrutiny of the data reveals that this difference is due to variations in the microstructure since specimens of similar origin showed comparable values at equivalent strains. As explained in Chapter 5, the development of misorientations during deformation is dependent on the microstructure. The microstructural sensitivity was shown to be higher on the LAMF metric than the KAM_a metric which agrees with the results shown in Fig. 7.21. The influence of microstructure on the long-range misorientations as measured by $AMIS_a$ and DGF was shown to be minor, which is consistent with the results shown in Fig. 7.22.

At comparable strains and microstructure, the development of both local and long-range misorientations occurred at a faster rate in plastic than in creep deformation, as seen in Fig. 7.23. This can be attributed to differences in the deformation mechanisms, as explained previously, where low rates of deformation in creep facilitates dislocation climb

over barriers thereby reducing their number density at such features. However, it is important to note that each metric increases at a different rate in plastic and in creep, with KAM_a showing comparable rates under the two conditions while LAMF shows the largest discrepancy. As discussed in section 7.2.5.3, creep strain has a significant influence on the misorientation <2° and therefore under creep deformation, the KAM_a development can be comparable with that under plastic deformation. However, due to variations in dislocation densities, values obtained under creep are likely to be lower. Conversely, LAMF is less sensitive to creep strain which therefore explains the large difference observed under the two deformation conditions. The dependence of AMIS on the overall grain deformation make it sensitive to the difference between plastic and creep strain, as higher dislocation densities are expected from the former than the latter. As shown in Fig. 7.20, Fig. 7.23 and Fig. 7.24a, the proportion of deformed grains also increases with creep strain, albeit at lower rate than with plastic strain due to differences in the deformation mechanism. The current results are consistent with the findings of Chapter 6 which showed misorientation development to be strain rate dependent and the KAM_a metric to be less sensitive to strain rate variations compared to the other metrics.

7.2.5.6. The influence of plastic and creep strain on twin boundary fractions

The length fractions of twin boundaries as measured through orientation imaging strongly depend on the strain level, as shown in Fig. 7.25. The TBF is highest in undeformed material which may be attributed to well known tendency of austenitic stainless steel to develop annealing twins [34]. However, during deformation the twin boundaries may be effective barriers to dislocation motion [186, 187] resulting in dislocation pile-ups and/or absorptions. These interactions may introduce lattice rotation at the twin boundaries such that their near-twin orientation is progressively lost (see section 2.2.2). From the misorientation angle distribution plots (see Fig. 7.30) it is obvious that an

increase in strain leads to broadening and loss of intensity of peaks corresponding to near-twin boundaries. By examining the orientation maps from the *in-situ* tensile test (see

Fig. 7.26) it is evident that twin boundary fractions reduce with increasing strain. The deviation from the perfect twin boundary orientation may explain the observed reduction in TBF with increasing strain. A reduction in twin length fractions following room temperature straining of copper has also been reported [188] where it was postulated that twins act as non-regenerative sources of dislocations. In Type 304 stainless steel deformed at 1000°C, a progressive decrease in twin densities with increasing strain has also been reported [189]. This was attributed to deviations from the perfect twin orientation during hot working as a result of lattice rotation arising from slip dislocation interactions with the twin boundaries.

The existing TBF in the prestrained specimens reduced with increasing creep strain as shown in Fig. 7.28. Similar reductions were also observed in specimens deformed in creep at 675°C without prestrain as seen in Fig. 7.29. However, as seen in Fig. 7.27 the TBF reduction was more under creep than in plastic deformation. As described in [190] the extrinsic dislocations near the twin boundaries in austenitic steel can recover during creep into configurations of least energies which may alter the axis-angle pair describing their boundaries. It was shown in that work that the density of these recovered dislocations increases with increasing secondary creep strain and that the recovery was strain rate dependent being least during the primary creep. It is therefore possible that during plastic deformation, the GNDs interacting with the twin boundaries result in lattice curvature which alters their near-twin orientation thus reducing the measured TBF. It is plausible that this alteration in twin boundary orientation increases during subsequent creep deformation as more GNDs accumulate at the twin boundaries through dislocation climb and glide processes. In this context, higher TBF is expected in plastic than in creep deformation which is consistent with the current findings.

At comparable plastic strains the decay of twin boundaries was more in service-aged than in RST steels (see Fig. 7.31). As discussed in Chapter 5, the presence of precipitates in the matrix may initiate slip in multiple systems during deformation and the looping of dislocations on precipitates influences both their density and distribution. The generally complex deformation in the service-aged steel may therefore account for the rapid decay of its twin boundaries with increasing strain. Grain boundary precipitates would seem to promote accumulation of dislocations at twin boundaries thus altering their near-twin orientation.

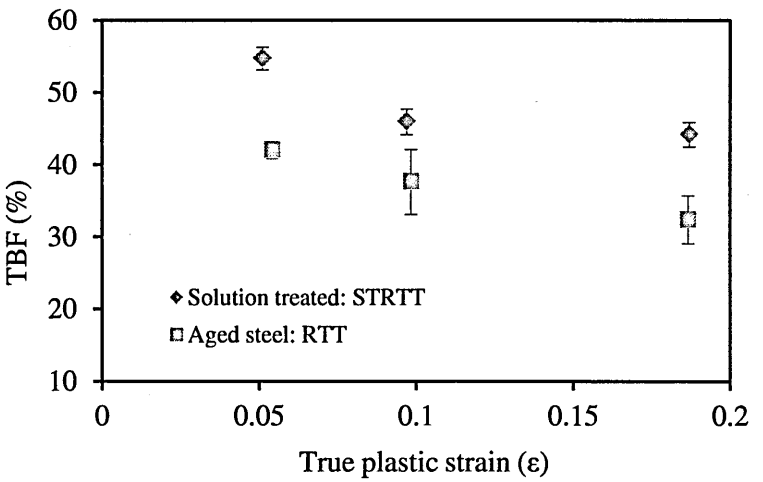

Fig. 7.31. Variations of the TBF with true plastic strain at 24°C for service-aged and re-solution heat treated Type 316H stainless steel.

7.2.5.7. Methodology for estimating accumulated creep strain

Estimation of the accumulated creep strain in power plant components can be fairly simple if their prior deformation before service is known. It was shown previously that misorientations due to creep strain builds on the pre-existing misorientations in the microstructure and so the total strain can be estimated from the total measured misorientation. Any metric can be used for the total strain estimation but preference should be given to DGF due to its insensitivity to microstructural changes which may occur during service. The accumulated creep strain is then given by the difference between the estimated

total strain and the prior strain before service. However, when the prior deformation before service is unknown e.g. in case of in-service and ex-service weldments, estimation of accumulated creep strain becomes complicated owing to the fact that both creep and plastic strain lead to misorientation development, albeit at different rates. In the current work two methods have been proposed for discriminating creep from plastic strain in such components;

(a) Differential Misorientation Development (DMD) Method

The importance of the findings in section 7.2.5.5 is that by exploiting the differences in misorientation development rates among the different metrics, it is possible to estimate the accumulated creep strain in a prestrained component. This is based on the fact that all the metrics are computed using the same data and so variations in the estimated strain levels from different metrics could result from their respective sensitivities to creep strain. As seen in Fig. 7.23 and Table 7.3, KAM_a develops at a similar rate under both plastic and creep deformation unlike the other metrics. Accordingly, the calibration curve based on KAM_a developed from the tensile tests can be used to give an accurate estimation of the total strain. Similar estimation based on the other metrics will slightly underestimate the total strain as they do not increase at the same rate under the two different deformation conditions.

The comparison between the strains estimated by different metrics is complicated by their microstructural sensitivity. As previously explained this sensitivity is higher for metrics assessing local misorientation development such as LAMF and KAM_a and lower for $AMIS_a$ and DGF which measure the development of the long-range misorientations. For instance, metrics derived from the aged steel will underestimate strain when applied on solution annealed steel. So, before applying them it is important to ensure they give

comparable estimate of strain where it is known to be constant e.g. in the far field of a welded component.

For materials of comparable microstructure with the metric's calibration material, correlations based on plastic deformation can be used for the assessment of creep strain since the misorientation development due to creep, adds to the existing misorientations. In cases where prior plastic deformation (ε_p) is known or equals to zero, the accumulated creep strain (ε_c) will be given by:

$$\varepsilon_c = \varepsilon_t - \varepsilon_p, \quad or \quad \varepsilon_c = \varepsilon_t \qquad \text{Eq. 7.1}$$

where ε_t is the total strain as estimated from the KAM_a metric (see Eq. 6.2). However, if the prior plastic deformation is unknown the accumulated creep strain can only be inferred from the difference between the strains estimated from the different metrics. To estimate the accumulated creep strain at 550°C in service-aged steel with unknown prior plastic deformation, the following procedure is adopted;

1. Calculate the total strain ($\varepsilon_{t_{KAM}}$) using the KAM_a metric (i.e. Eq. 6.2):

   $$\varepsilon_{t_{KAM}} = \varepsilon_{pKAM} + \varepsilon_{cKAM} \qquad \text{Eq. 7.2}$$

   where ε_{pKAM} and ε_{cKAM} are plastic and creep strain components of the total strain as estimated by the KAM_a.

2. Calculate the total strain (ε_{t_M}) using any of the other metrics (i.e. Eq. 6.3 - Eq. 6.5):

   $$\varepsilon_{t_m} = \varepsilon_{pm} + \varepsilon_{cm} \qquad \text{Eq. 7.3}$$

   where ε_{pm} and ε_{cm} are plastic and creep strain components of the total strain as estimated by any of the other metrics.

3. From steps (1) and (2), calculate the partial value of the accumulated creep strain (ε_{c_p}) as:

   $$\varepsilon_{c_p} = \varepsilon_{t_{KAM}} - \varepsilon_{t_M} \qquad \text{Eq. 7.4}$$

4. From Table 7.3, select the creep sensitivity factor (Ω) for the metric used in step (2). Ω is defined as p_c/p_p, where p_p and p_c are the metric's values associated with plastic and creep strains, respectively (see section 7.2.4.4). For KAM_a, Ω = 1, while for the other metrics Ω is <1 (see notes below).
5. Determine the fraction (p_m) of the partial creep strain in step (3) from step (4) as:

$$p_m = 1 - \Omega \qquad \text{Eq. 7.5}$$

6. Calculate the total accumulated creep strain (ε_c) from step (3) and (5) as:

$$\varepsilon_c = \frac{\varepsilon_{c_p}}{p_m} \qquad \text{Eq. 7.6}$$

Notes on DMD method

The DMD method works on the premise that the misorientation development as measured by KAM_a occurs similarly in plastic and in creep deformation while for the other metrics it occurs more slowly in creep. This assertion is supported by the findings of section 7.2.4.4. Since the metrics are calibrated using plastic deformation data, the estimate of the plastic component of the total strain should be similar for all the metrics. However, the estimate of the creep component of the total strain is a variable which is metric dependent.

The main assumption in the DMD method is that at comparable plastic and creep strains, the metric's creep sensitivity factor (Ω) is independent of the creep deformation conditions. This is a reasonable assumption only when the changes in the deformation conditions do not change the creep deformation mechanism which in the case studied was dislocation creep. Misorientations may develop at different rates during creep by different mechanisms. It is also assumed that Ω is independent of the plastic and creep strain values used. This assumption can be justified by the findings of Chapter 6 and 7 which showed that the accumulation of both plastic and creep strain results in misorientation development, albeit at different rate.

The DMD method is suitable for low deformation rates (characteristic of creep) where differences in misorientation development rates at the local and long-range scales are more apparent. As the deformation rate increases these differences decrease, reducing the efficacy of the method. Due to the sensitivity of KAM_a to microstructural variations, the method is only applicable to materials of comparable microstructure to the metric's calibration material.

(b) Twin Boundary Fraction (TBF) method

In section 7.2.5.6, the fractions of twin boundaries were shown to decrease with increasing creep and plastic strain. The TBF method is based on these findings and assumes the following;

I. The TBF in solution annealed Type 316 stainless steel with an average grain size of 93±12μm is constant and equals to 0.7±0.03 (see Table 7.4). This assumption is based on experimental observation of unstrained re-solution heat treated steel studied in the current work.

II. The decrease of TBF with increasing plastic strain is linear. This assumption is supported by the experimental data from the high temperature tensile and compression tests as shown in Fig. 7.25.

III. The decrease of existing TBF with increasing creep strain is linear at any given prestrain level. This assumption is derived from the experimental data as shown in Fig. 7.28 and Fig. 7.32.

To estimate the accumulated creep strain at 550°C in the service-aged steel the following procedure is adopted;

1. Obtain the gradient of TBF versus plastic strain (ε_p) graph. This is referred to here as TBF plastic strain sensitivity ($TBF\varepsilon_p$) and is given by:

$$TBF\varepsilon_p = \frac{\Delta TBF\varepsilon_p}{\Delta\varepsilon_p} \quad \text{Eq. 7.7}$$

2. Obtain the gradient of TBF versus creep strain (ε_c) graph. This is referred to here as TBF creep strain sensitivity (TBFε_c) and is given by:

$$TBF\varepsilon_c = \frac{\Delta TBF\varepsilon_c}{\Delta\varepsilon_c} \quad \text{Eq. 7.8}$$

3. Calculate the total strain (ε_t) using misorientation metrics: KAM_a, $AMIS_a$, LAMF, and DGF. See notes below for guidance on metric selection. Total strain ε_t has both plastic and creep strain components.

$$\varepsilon_t = \varepsilon_p + \varepsilon_c \quad \text{Eq. 7.9}$$

4. From the assumption (I) and step (1) estimate the prestrain TBF (TBFε_{pe}) by assuming at this point $\varepsilon_c = 0$. Therefore from step (3) the calculated prestrain (ε_{pe}) is given by $\varepsilon_t = \varepsilon_{pe}$ and

$$TBF\varepsilon_{pe} = 0.7 - \left(TBF\varepsilon_p * \varepsilon_{pe}\right) \quad \text{Eq. 7.10}$$

5. Measure TBF in a deformed component (TBF_m)
6. Calculate the change in TBF due to creep from step (4) and step (5) as:

$$\Delta TBF\varepsilon_c = TBF\varepsilon_{pe} - TBF_m \quad \text{Eq. 7.11}$$

7. Calculate the accumulated creep strain (ε_{ce}) from step (2) and step (6) as:

$$\varepsilon_{ce} = \frac{\Delta TBF\varepsilon_c}{TBF\varepsilon_c} \quad \text{Eq. 7.12}$$

8. Calculate total strain (ε_{te}) from step (4) and step (7) as:

$$\varepsilon_{te} = \varepsilon_{ce} + \varepsilon_{pe} \quad \text{Eq. 7.13}$$

9. If $\varepsilon_{te} = \varepsilon_t$ then the component has no accumulated creep strain i.e. $\varepsilon_c = 0$.

   If $\varepsilon_{te} \neq \varepsilon_t$ then a lower value of ε_{pe} is selected and steps 4-8 repeated. This process is repeated until $\varepsilon_{te} = \varepsilon_t$ at which point the accumulated creep strain and the prior plastic deformation are given by ε_{ce} and ε_{pe}, respectively.

Notes on TBF method

The estimation of total strain from the misorientation metrics can be performed using any of the equations Eq. 6.2 - Eq. 6.5. This is based on the premise that the misorientation due to creep deformation adds to the existing misorientations in a component as mentioned previously. Total strain estimation based on KAM_a is preferred here since the metric develops similarly in plastic and in creep deformation (see section 7.2.4.4) but its strong dependence on the microstructure limits its general applicability in the favour of the DGF metric. It is advisable to check the discrepancies in total strain estimates from all the four metrics. A large difference between the total strain estimates will indicate either the influence of microstructure and/or strain sensitivity limitation of the metrics.

The TBF method works on the premise that an undeformed material has the highest TBF which decays as a function of plastic and/or creep strain. This assumption is based on the experimental findings and also from the fact that high densities of annealing twins are expected in undeformed *f.c.c* material [15, 34] since in this state there are few accumulated dislocations at the boundaries to alter the twin orientation (i.e. 60° rotation about the <111> axis). The effect of prestrain level on the rate of TBF reduction during creep deformation was postulated in the present study to be minimal. This is based on the experimental finding that the change of TBF per unit strain was similar under different prestrain levels (see Fig. 7.32a). From the same data, TBF was shown to reduce with increasing total strain independently of the prestrain levels (see Fig. 7.32b). As mentioned before, total strain is a sum of prior strain and subsequent creep strain.

Table 7.4: Average TBF in re-solution heat treated steel (Sample B).

No. maps	Average TBF	S.D	limit at 95% C.L
26	0.702	0.074	0.028

Map size: 700μm x 700μm, S.D: standard deviation, C.L: confidence level

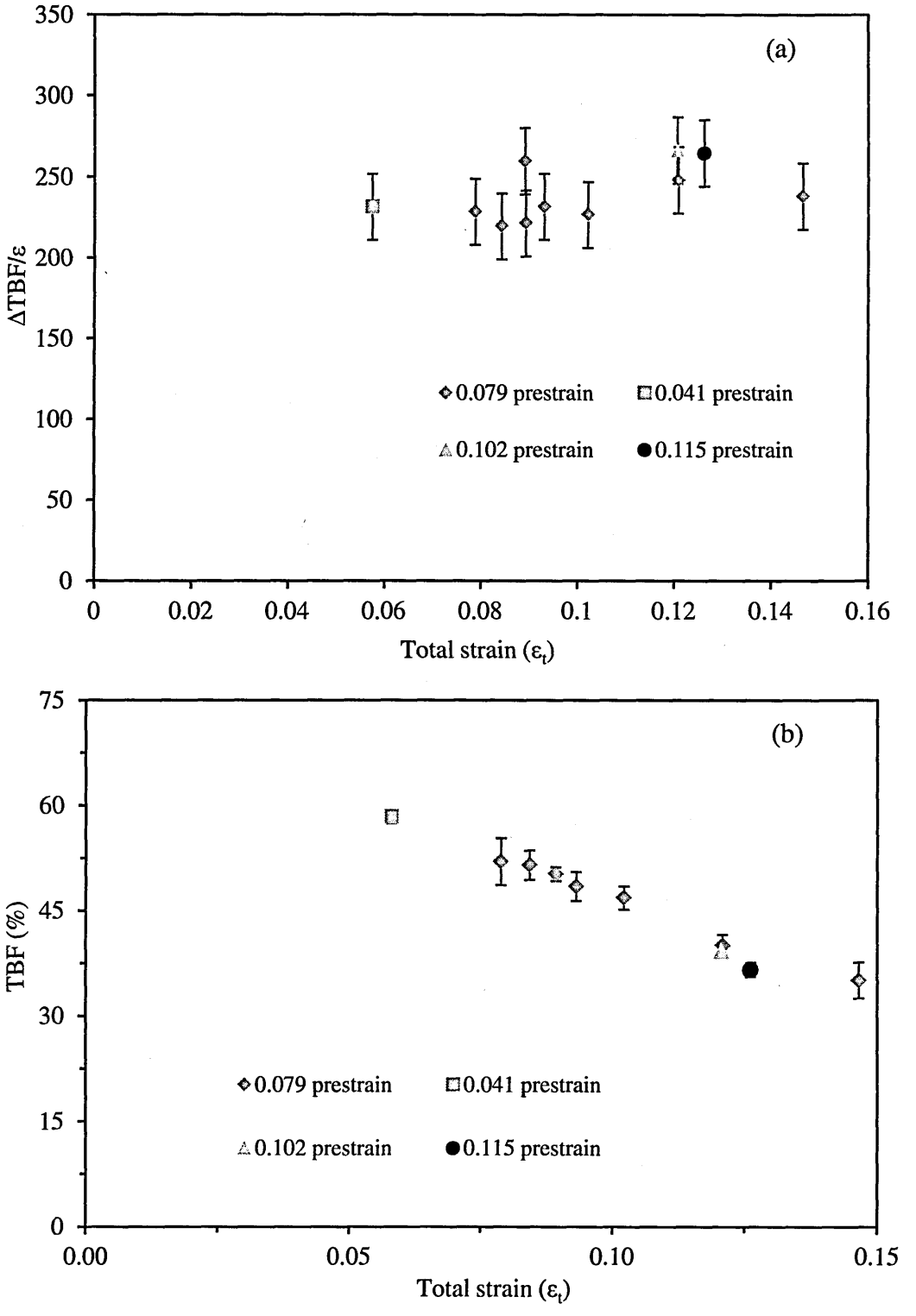

Fig. 7.32. Variation of (a) ΔTBF/ε, and (b) TBF with total strain for service-aged Type 316H stainless steel deformed as in Table 7.1 showing marginal TBF dependence on prestrain level.

Since the change in TBF depends on dislocations in the material interacting with the twin boundaries, the TBF method may not be generally applicable where deformation mechanism does not involve the generation and accumulations of dislocations e.g. in diffusion creep. The influence of grain size on the TBF has been neglected during the formulation of the TBF method. It has been shown by [191] that the twinning frequency in Type 316 stainless steel is virtually independent of the grain size in the range of 1.5μm to 100μm. This is the same grain size range for the steels studied in the current work. Compared to the DMD method, TBF method is more generic as it is applicable across a greater microstructural size range.

7.3. Summary

The key findings in this chapter can be summarised as follows;

- The deformation mechanism was found to influence the rate of misorientation development with increasing strain. The development rate was metric dependent and was higher in plastic than in creep deformation. The creep-induced misorientation was found to add to the existing misorientations in the material.
- The accumulation of strains during primary and secondary creep was shown to have a significant influence on misorientation <2° and resulted in rapid deformation of grains with relatively high overall Schmid factor values.
- The long-range misorientation as measured by $AMIS_a$ was found to increase linearly with increasing creep strain indicating a continuous increase in grains' deformation as the creep deformation progresses.
- The development of DGF with increasing creep strain was shown to be little influenced by the microstructural variations and occurred at a reducing rate indicating a declining number of additional deforming grains per unit strain.

- The development of misorientation as measured through KAM_a was found to occur at comparable rates in plastic and in creep deformation while the development as assessed through LAMF, $AMIS_a$ and DGF was shown to occur more slowly in creep than in plastic deformation. A new DMD method is proposed for creep strain estimation in service-aged steel which exploits the difference in the metrics' sensitivities to plastic and creep strains.
- The twin boundary fraction (TBF) in service-aged steel was shown to decrease monotonically with increasing total strain. The decrease was established to be more in creep than in plastic deformation. The prior TBF in service-aged steel was shown to reduce with increasing creep strain independently of the prestrain level. A new TBF method is proposed for creep strain estimation in service-aged steel which exploits the differences in twin boundary decay as a function of both plastic and creep strain.

CHAPTER 8

VALIDATION AND APPLICATION OF THE STRAIN ASSESSMENT METHODS

8.1. Introduction

This chapter has five main sections. In section 8.2, the assessment of deformation through hardness measurement is reported and the relationship between hardness and the misorientation metrics is also explored. Validation of the proposed strain assessment methods is provided in section 8.3. A detailed description of the specimens used in the validation process is given together with the EBSD measurement procedures and the data analysis performed. The evaluation of relative errors in the proposed strain assessment methods is also covered in this section. In section 8.4, the precision of the proposed strain assessment methods and their optimal strain sensitivity range is reported. Section 8.5 covers the application of the proposed methods to real power plant components. The section provides the details of plastic and creep strain distributions in weldments after different periods in service, based on the proposed methods. The results of creep deformation assessment through Digital Image Correlation (DIC) and the subsequent assessment through EBSD methods are also reported in this section. Finally a summary of the key findings in this chapter are provided in section 8.6.

8.2. Assessment of deformation through hardness measurements

As explained in Chapter 2, EBSD strain assessment depends on the changes in lattice orientation arising from GNDs accumulation. Similarly, materials' hardness corresponds to near-surface dislocation density [60] and can therefore be used to complement the EBSD strain measurements. However, direct correspondence between the two techniques is limited by their different spatial resolutions and the extent of strain fields analysed. The lateral resolutions used in the current study were 1μm and 18μm for the

EBSD and nanohardness measurements, respectively, while the depth sampled by the nanohardness measurement was about 1μm and by the EBSD technique 10-100nm [73, 84].

The hardness measurements were carried out in accordance with the procedures outlined in Chapter 3 on specimens deformed under the conditions given in Table 6.1, Table 7.1 and Table 7.2. The mean hardness of 39 measurements on each specimen increased with increasing creep strain as seen in Fig. 8.1 which can be attributed to an increase in strain hardening at these creep conditions i.e. the strain hardening was dominant over the recovery process during the creep deformation. Similar findings attributed to strain hardening have been reported previously [41] which showed that hardness increased with creep strain for Type 304 stainless steel deformed at T = 650°C and σ = 177MPa. In the current case, the increase in hardness due to precipitation hardening can be neglected since an over-aged material was creep tested.

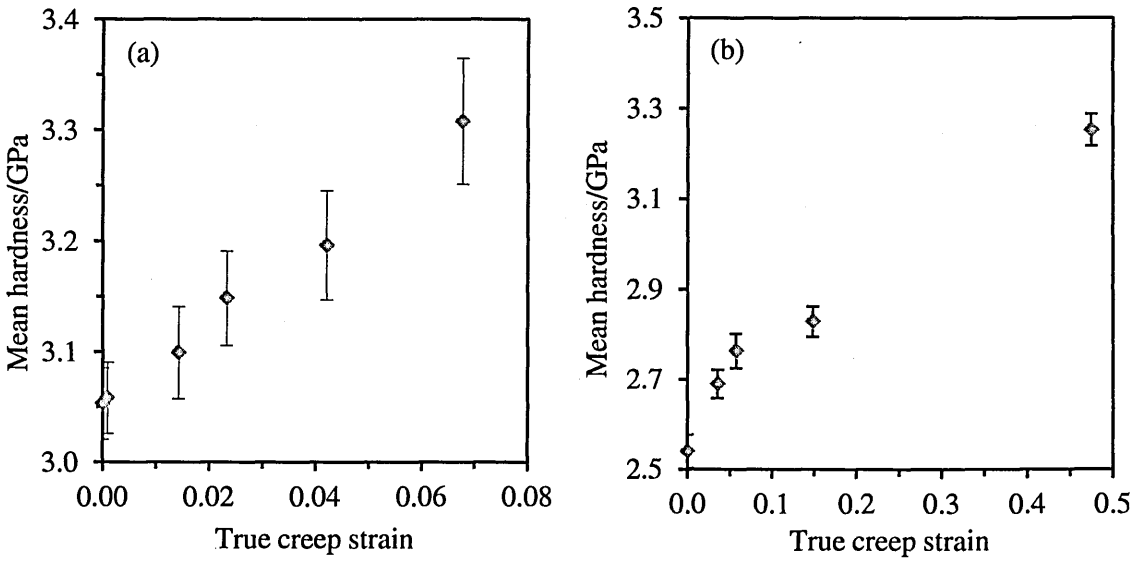

Fig. 8.1. Mean hardness versus creep strain for service-aged Type 316H stainless steel deformed at (a) 550°C and 320MPa (see Table 7.1), and (b) 675°C and 150MPa (see Table 7.2).

As seen Fig. 8.2, both nano- and macro-hardness increased with increasing plastic strain and for strain rates down to ~$10^{-5}s^{-1}$, they appeared insensitive to the deformation temperature and deformation mode. Accordingly, the differences in the straining hardening between flow curves at 24°C and 550°C (see Fig. 6.1) are not detected by the hardness measurements.

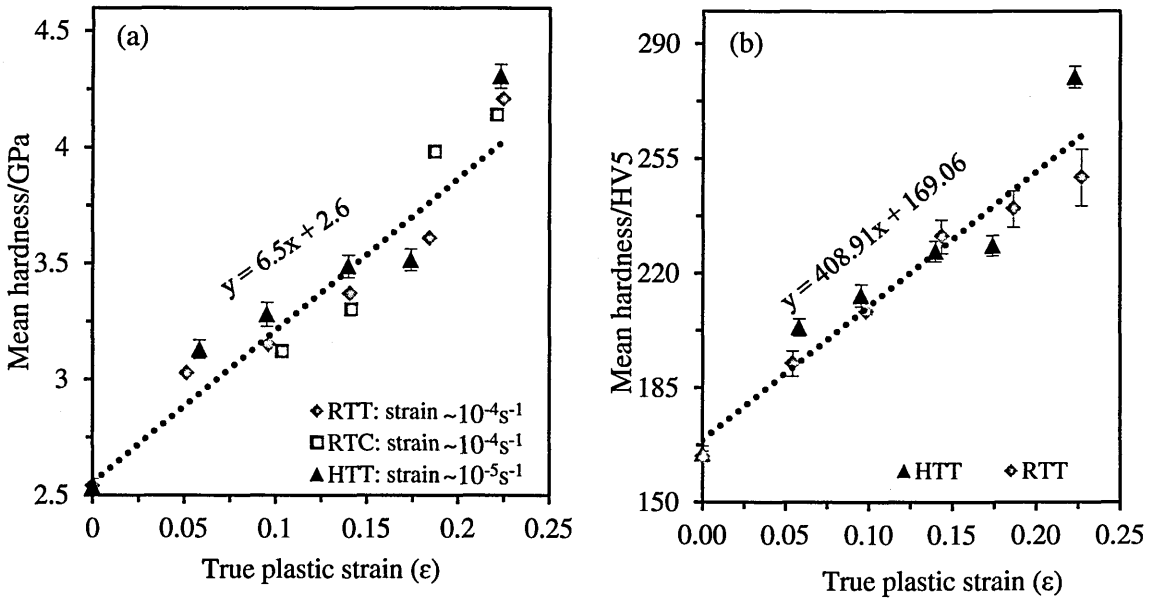

Fig. 8.2. Mean hardness at (a) nano-, and (b) macro-scale, as a function of true plastic strain for service-aged Type 316H stainless steel deformed as in Table 6.1.

For compression specimens deformed at 550°C to strains >0.1, the hardness varied along the gauge length as shown Fig. 8.3. This can be attributed to non-uniform deformation along the gauge length possibly due to the slight barrelling effects indicated in Table 6.2. As seen in Fig. 8.4a, at a constant strain the mean hardness decreased with decreasing strain rate for specimens deformed at 550°C. This can be attributed to a decrease in dislocation density in agreement with the results presented in section 4.3.4.

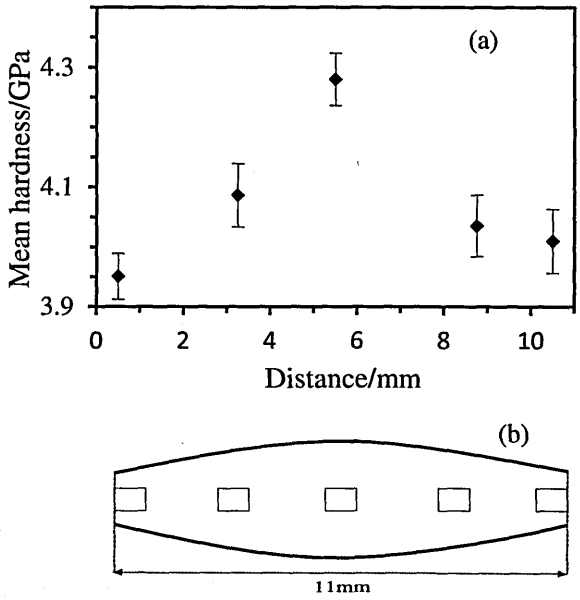

Fig. 8.3. (a) Hardness variation along a compression specimen deformed to 0.23 strain at 550°C, and (b) schematic of hardness measurements locations (square areas) along the mid-plane of (a).

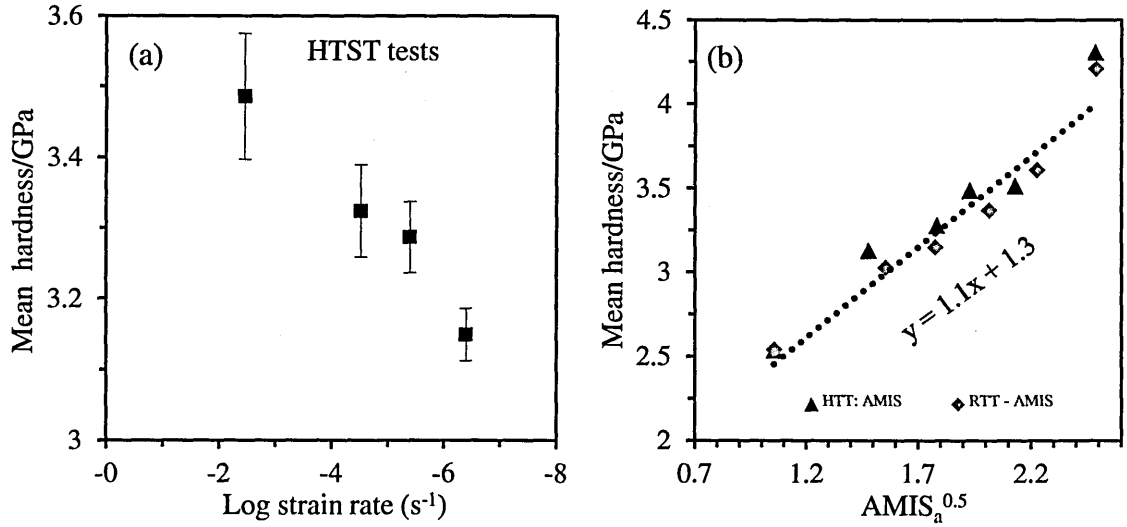

Fig. 8.4. Variations of the mean nano-hardness of service-aged Type 316H stainless steel with: (a) strain rate (see Table 6.1), and (b) square root of $AMIS_a$.

A comparison between Fig. 8.1 and Fig. 7.18, Fig. 8.2 and Fig. 6.15, and Fig. 8.4(a) and Fig. 6.14 shows that the hardness and EBSD measurements yield analogous responses under similar deformation conditions, even though the hardness values exhibit larger scatter, as evident from the error bars. This scatter is attributable to local microstructural

variations (e.g. in precipitate density or in grain sizes) and to the inhomogeneity of deformation as seen in Fig. 5.5. The presence of precipitates in the service-aged steel and their non-uniform distribution in the microstructure (see section 4.3.3.1) could have affected the local hardness values with higher hardness expected in regions with dense than sparse precipitation. Since the hardness measurements were averaged over many grains, this would explain the observed large scatter in their values. As seen in Fig. 8.4b, the mean hardness increased linearly with the $AMIS_a^{0.5}$, and since hardness is taken as a linear function of $\rho^{0.5}$ [60], the current results confirm the findings of Chapter 6 which showed $AMIS_a$ relating linearly to the dislocation density. For service-aged material (e.g. Sample A) the increase in hardness with increasing creep and plastic strain can therefore be attributed to strain hardening effects while a decrease in hardness may indicate a possible reduction in dislocation density.

8.3. Validation of strain assessment methods

The strain assessment methods developed in the current work were applied on Sample E specimens (creep ruptured specimens) to assess their efficacy in strain estimation. The specimens' deformation and service histories are summarised in Table 4.3.

8.3.1. EBSD measurements

The specimens were prepared for the EBSD measurements as described in Chapter 3. The measurements were carried out on the mid-plane parallel to the loading direction, starting from the ruptured point toward the specimen's threading section as shown in Fig. 8.5a. Each measurement covered an area of 700μm x 700μm and the measurements were conducted in series for a distance of 6mm from the ruptured point (see Fig. 8.5b). Measurements were also performed on the threaded region of the specimen where minimal deformation was expected. The presence of creep cracks near the ruptured surface (see Fig. 8.6) reduced the indexing rates during the measurement. To avoid losing details associated

with plastic and creep deformation, no data cleaning was performed, but repeat measurements were conducted in the adjacent areas. A sample of orientation maps is given in Appendix 3E.

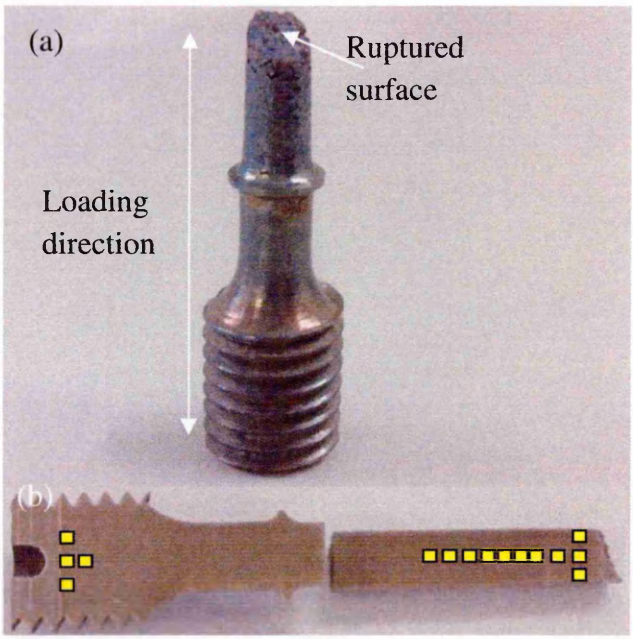

Fig. 8.5. Photograph of (a) creep ruptured Type 316H stainless steel specimen, and (b) the EBSD measurement areas (shaded zones) along the longitudinal mid-plane of (a).

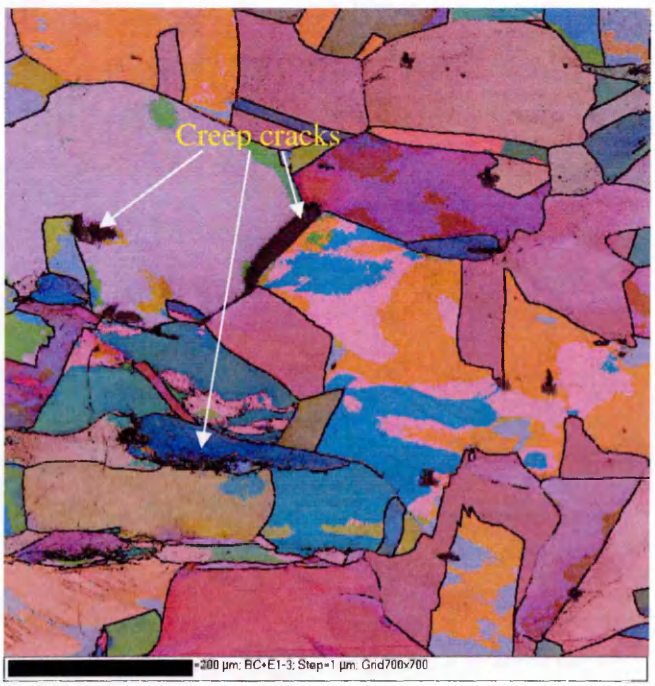

Fig. 8.6. EBSD orientation map of Type 316H stainless steel showing creep cracks in creep ruptured specimen.

8.3.2. *EBSD measurement results*

The build-up of the local (KAM_a and LAMF) and long-range ($AMIS_a$ and DGF) misorientations along the gauge length of the creep ruptured specimens is shown in Fig. 8.7. Apart from the KAM_a metric, all the other metrics exhibited little variations in the measured misorientations over the length studied.

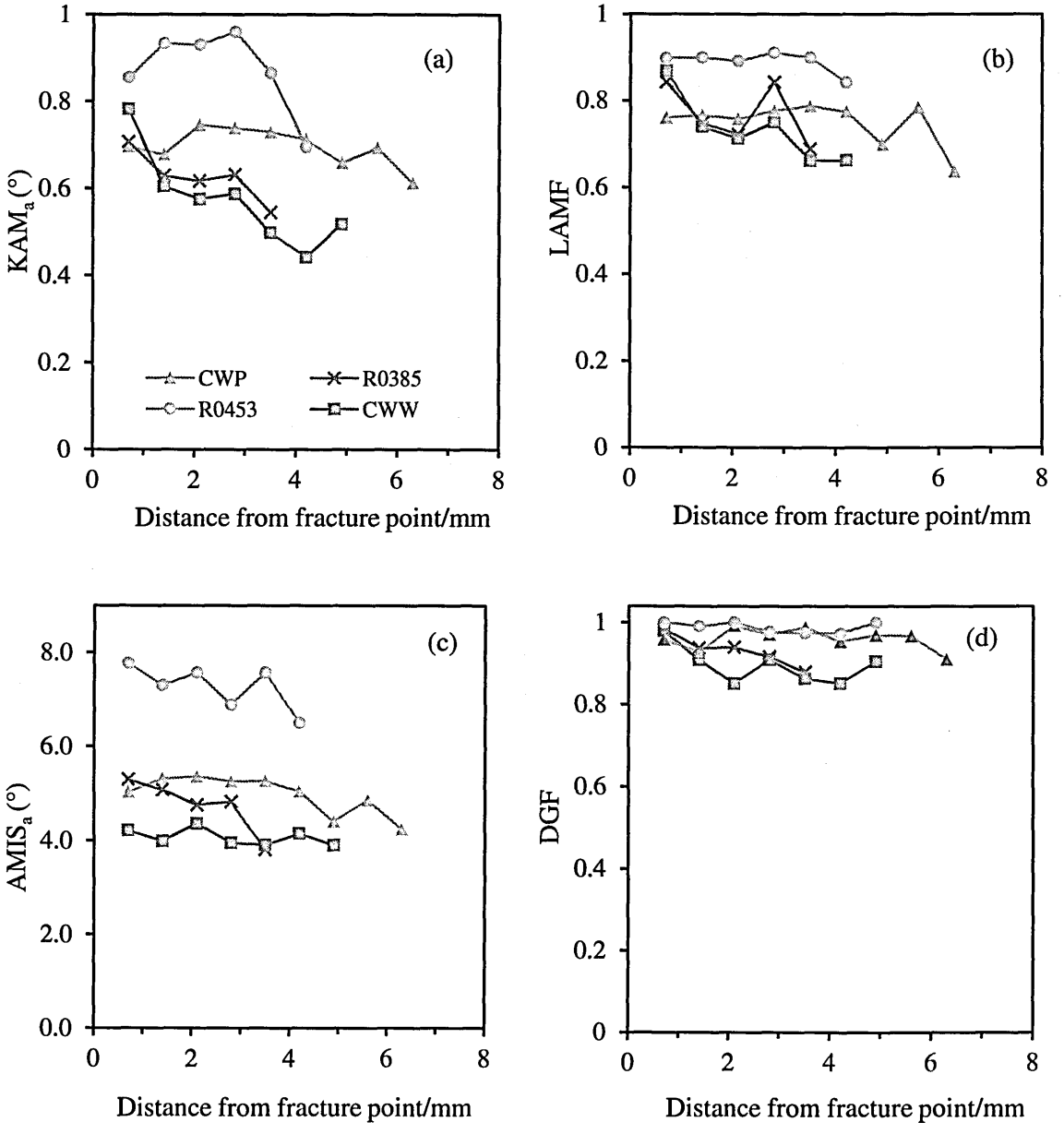

Fig. 8.7. Variation of local (a-b) and long-range (c-d) misorentation along the gauge length of creep ruptured specimens deformed as in Table 4.3.

8.3.3. Accuracy of strain estimation

To estimate total strain in the creep ruptured specimens, an average misorientation value from measurements made over the first 3mm from the point of rupture was used. In this region the measured misorientations remained relatively uniform. The comparison between the globally measured total strain during creep test and the estimated total strain after the test, based on the equations Eq. 6.2 - Eq. 6.5 is given in Table 8.1. The calculated relative error in strain estimation for each metric is given in brackets. The negative errors indicate overestimation of the total strain from the true total strain (represented in this case by the globally measured values). All metrics were insensitive to global strain of ~0.003 except KAM_a which gave a comparable total strain estimate. For the other strain levels, all metrics were sensitive and gave strain estimates comparable to the globally measured total strains except for the R0385 specimen, where they gave significantly lower values apart from the DGF metric.

Table 8.1: Measured and estimated total strains for Type 316H stainless steel crept as in Table 4.3.

		Measured strain	Estimated total strain (Relative error)			
Test Number	**σ**	**ε_t**	**DGF**	**KAM_a**	**LAMF**	**$AMIS_a$**
R0453 thread	0	0.000	0.000	0.000	0.000	0.000
R0452	160	0.003	0.000	0.002	0.000	0.000
IRD CWW	260	0.127	0.127 (0%)	0.132 (-4%)	0.146 (-14%)	0.157 (-24%)
IRD CWP	240	0.174	0.179 (-3%)	0.159 (8%)	0.143 (18%)	0.172 (1%)
R0385	360	0.213	0.185 (13%)	0.137 (36%)	0.154 (28%)	0.167 (22%)
R0453	200	0.226	0.288 (-27%)	0.224 (1%)	0.243 (-7%)	0.268 (-19%)

σ: applied stress/MPa, ε_t: true total strain

The current results underline the importance of using several different metrics for strain estimation since the values obtained may be influenced by the microstructural variations, the metric's strain sensitivity and/or the deformation histories. Since the metrics were calibrated using the service-aged steel with extensive precipitation (see Fig. 8.8f),

their strain estimates will be dependent on the microstructure, particularly for the metrics that are based on local misorientation (e.g. KAM_a and LAMF) as explained in Chapter 5. The strain estimate can also be influenced by the metric's strain sensitivity as explained in Chapter 6. This is mainly in the DGF metric whose strain sensitivity reduces beyond 0.1 strains and the LAMF metric which only exhibit good sensitivity between 0.03 - 0.15 strain range. Since misorientation develops at different rates in plastic and in creep deformation as shown in Chapter 7, the deformation history of a material could also influence the metrics' strain estimates since their calibration are based on plastic deformation. This is mainly problematic when using the LAMF, $AMIS_a$, and DGF metrics since their measured misorientation develops slower in creep strain than that of KAM_a (see section 7.2.4.4).

It is possible that the differences in the total strain estimated by the different metrics (see Table 8.1) resulted from the microstructural variations between the specimens examined (see Fig. 8.8), since all metrics are sensitive to these variations except the DGF. The reduced precipitation in R0385 specimen (see Fig. 8.8a) could therefore explain why its total strain estimate was significantly lower than the globally measured value. The observed relative error variations between different metrics can therefore be attributed to the three factors mentioned above.

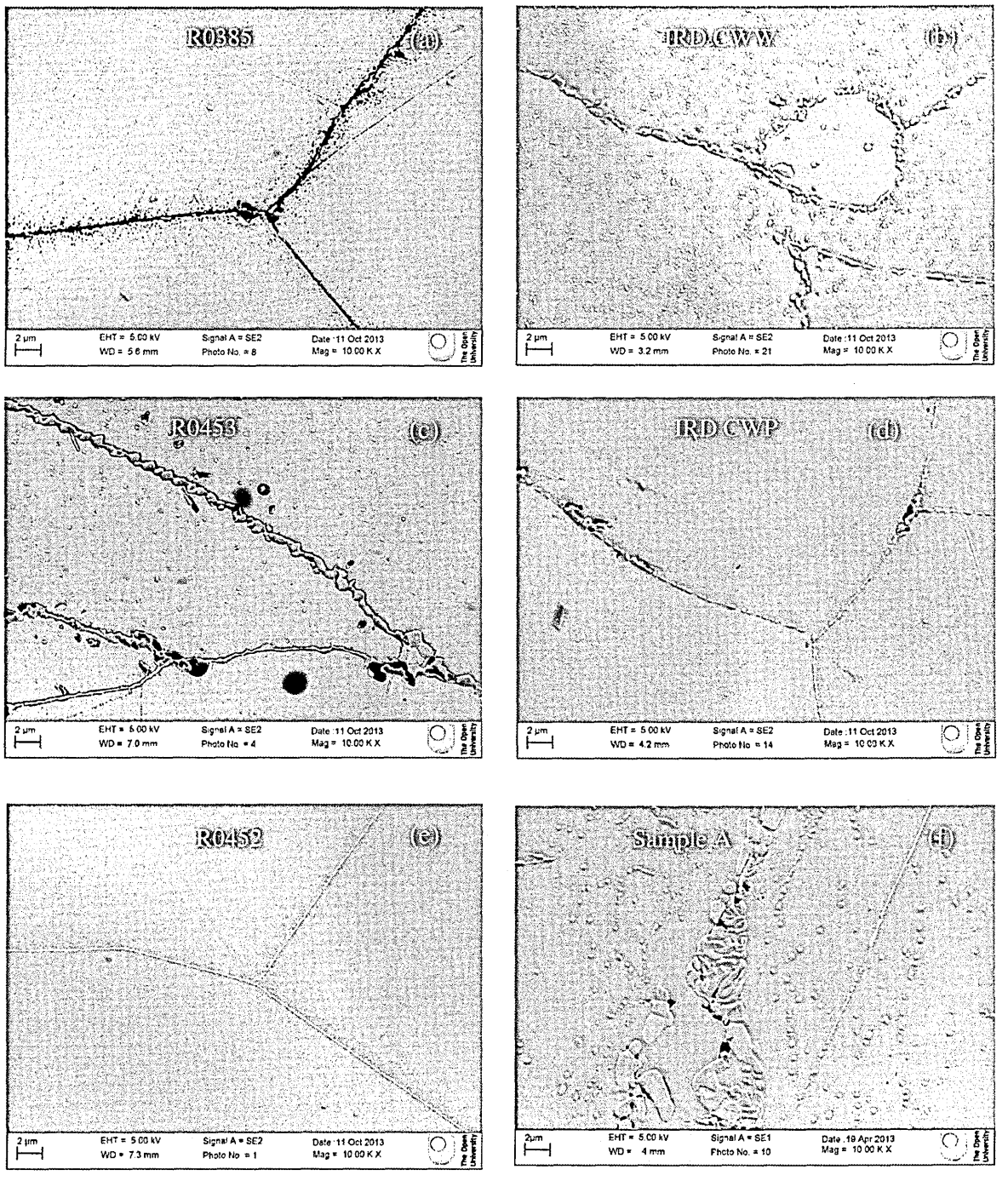

Fig. 8.8. SEM micrographs showing inter- and intra-granular precipitation variations in Type 316H stainless steel crept as in Table 4.3. Micrograph of service-aged Type 316H stainless steel is included for comparison (f).

For comparison, the measured misorientation as a function of the globally measured total strain in the creep ruptured specimens have been included in the correlations developed in Chapter 6 between plastic strain and misorientation build-up. As

seen in Fig. 8.9 and Fig. 8.10, the evolutions of local misorientation in the creep ruptured specimens (Sample E) and plastically deformed specimens (Sample A), were comparable at equivalent strains. The development of the long-range misorientation exhibited similar results as seen in Fig. 8.11 and Fig. 8.12. These results thus suggest that the correlations described by equations Eq. 6.2 - Eq. 6.5 can be used to quantify the total strain in the crept specimens as demonstrated above. However, apart from the DGF all the other metrics showed anomalous misorientation development in the R0385 specimen (0.213 strain). This can be attributed to differences in the microstructure, since as seen in Fig. 8.8 the specimen had less precipitation than the other specimens. The misorientation build-up in the threaded section of the creep ruptured specimen R0453 (0 strain assumed) was significantly lower than that of un-strained service-aged material (see Fig. 8.9 - Fig. 8.12) indicating a possible recovery of the dislocation structures after a long term exposure at 550°C.

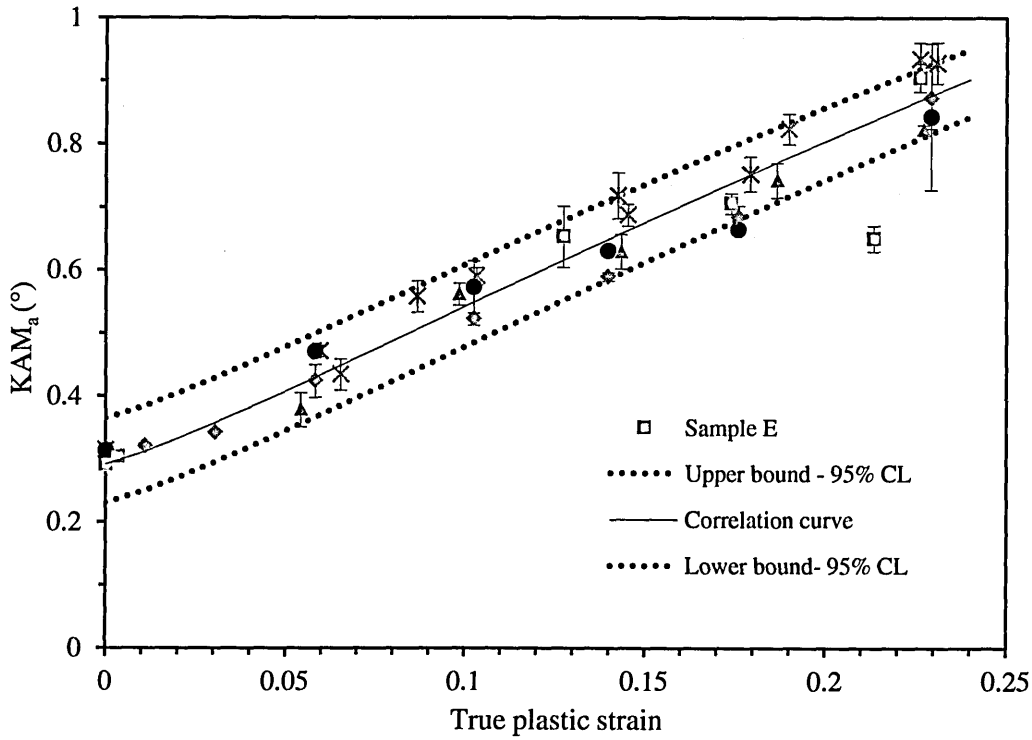

Fig. 8.9. KAM_a versus true plastic strain for service-aged Type 316H stainless steel deformed as in Table 6.1. Scatter band for KAM_a data is plotted at 95% confidence level. KAM_a data for creep ruptured specimens (see Table 4.3) are included for comparison.

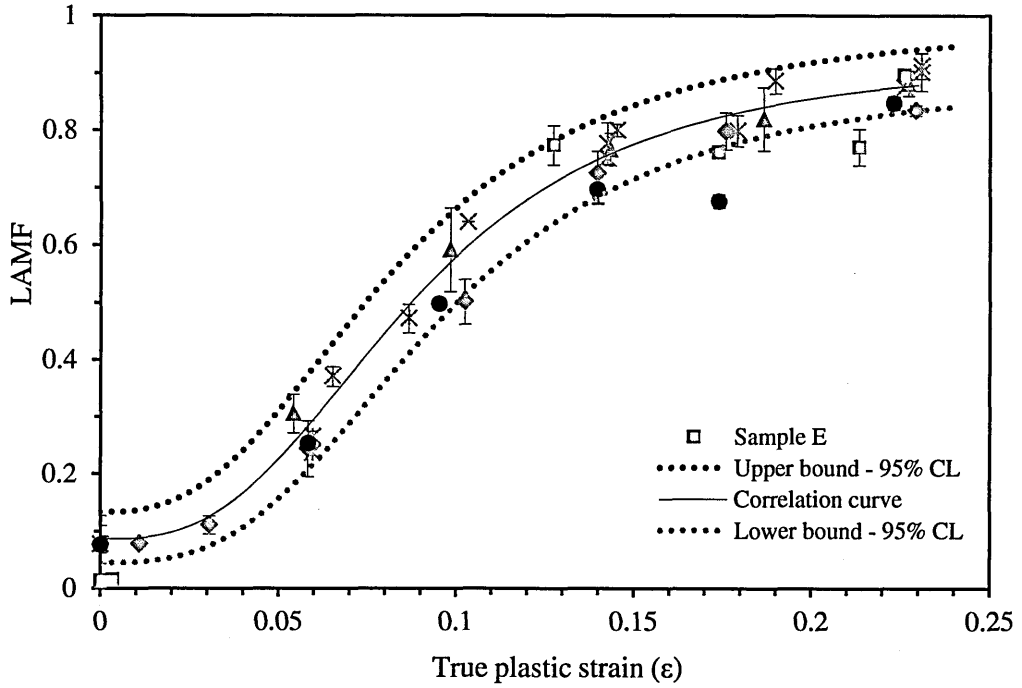

Fig. 8.10. LAMF versus true plastic strain for service-aged Type 316H stainless steel deformed as in Table 6.1. Scatter band for LAMF data is plotted at 95% confidence level. LAMF data for creep ruptured specimens (see Table 4.3) are included for comparison.

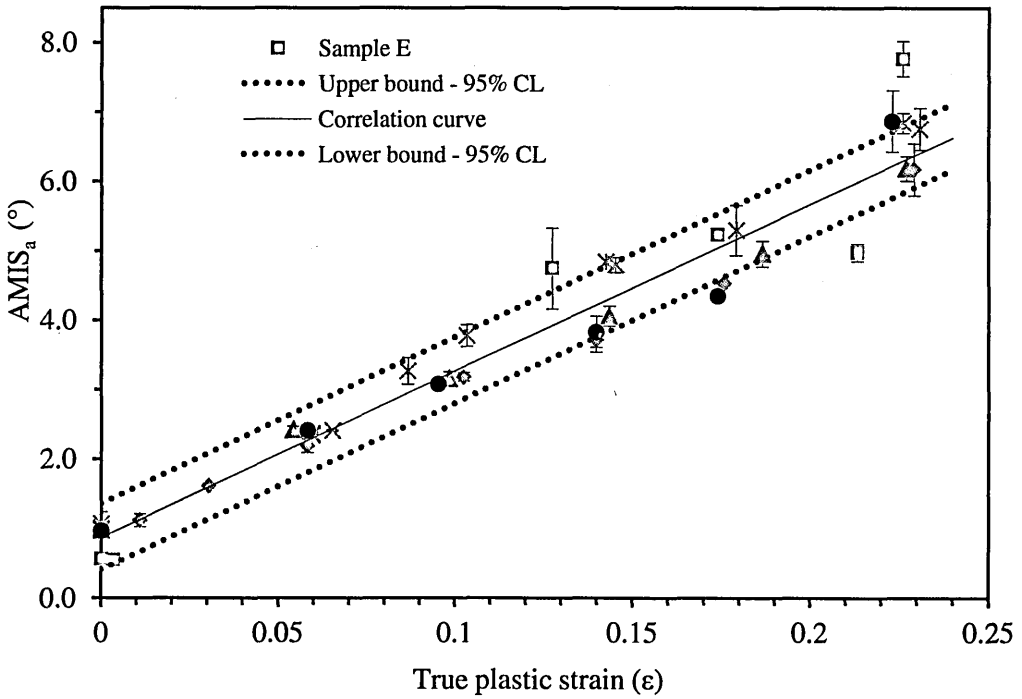

Fig. 8.11. $AMIS_a$ versus true plastic strain for service-aged Type 316H stainless steel deformed as in Table 6.1. Scatter band for $AMIS_a$ data is plotted at 95% confidence level. $AMIS_a$ data for creep ruptured specimens (see Table 4.3) are included for comparison.

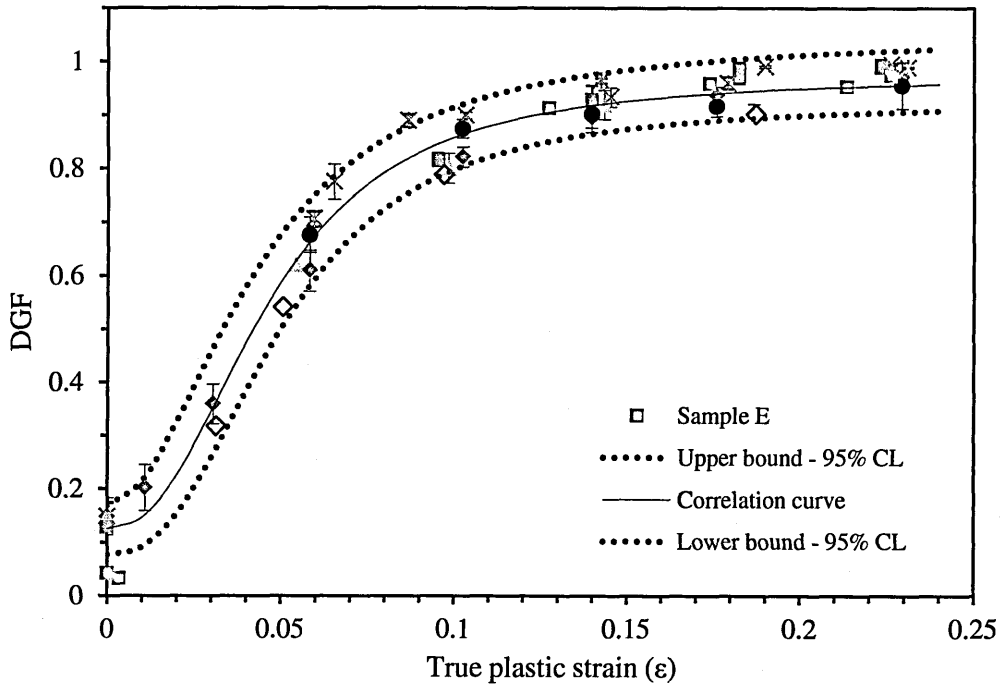

Fig. 8.12. DGF versus true plastic strain for service-aged Type 316H stainless steel deformed as in Table 6.1. Scatter band for DGF data is plotted at 95% confidence level. DGF data for creep ruptured specimens (see Table 4.3) are included for comparison.

The estimation of the accumulated creep strain was based only on the TBF method (see section 7.2.5.7b) since the application of DMD method (see section 7.2.5.7a) was limited by the apparent microstructural differences (see Fig. 8.8) between the specimens and the service-aged steel (Sample A) from which equations Eq. 6.2 to Eq. 6.5 were derived. As seen in Table 8.2, most of the creep strain estimates from the DMD method were negative implying that the total strain estimates from the KAM_a metric were underestimated (see Eq. 7.4). This can be attributed to microstructural differences between the metric's calibration material and the specimen material as explained previously. However, the estimated creep strains based on the TBF method were comparable with the globally measured values. In this assessment, the total strain estimates used in the TBF method were based on the DGF metric apart from the R0453 specimen, where KAM_a was used. The DGF metric was selected on the basis of its insensitivity to microstructural

variations. Its strain sensitivity was judged to be good for strains <0.2 since it gave a comparable strain estimate to $AMIS_a$ whose strain sensitivity remains relatively constant over a wide range of applied strains (see section 6.2.5.4). However, the use of DGF means that the total strain is slightly underestimated since it develops more slowly in creep than in plastic deformation. This means that the estimated prestrain in the TBF method (see Eq. 7.9 - Eq. 7.13) is underestimated which leads to overestimation of the creep strain. This may explain why the creep strains reported here are slightly higher than the globally measured values apart from the one in which KAM_a was used (R0453 specimen). KAM_a develop similarly in plastic and in creep deformation and therefore gives a better estimate of creep strain compared to the other metrics when applied in the TBF method.

Table 8.2: Measured and estimated creep strains for Type 316H stainless steel crept as in Table 4.3.

		Measured strains		Estimated creep strains	
Test Number	**σ**	**ε_p**	**ε_c**	**TBF (S.D)**	**DMD**
R0453 thread	0	0	0	0	0
R0452	160	0.001	0.002	0	0
IRD CWW	260	0.024	0.103	**0.111** (0.033)	0.018
IRD CWP	240	0.025	0.149	**0.152** (0.018)	-0.065
R0385	360	0.133	0.08	**0.108** (0.003)	-0.160
R0453	200	0.015	0.211	**0.199** (0.033)	-0.212

ε_c: true creep strain, ε_p: true loading plastic strain, **σ**: applied stress/MPa **S.D**: standard deviation

The microstructure of R0453 specimen (see Fig. 8.8c) compared relatively well with that of the calibration material (see Fig. 8.8f) and so the influence of microstructure on the local misorientation development was judged to minimal and KAM_a was therefore used in the TBF method to estimate the total strain in this specimen. From Table 8.1, it is evident that the KAM_a and LAMF metrics gave comparable total strain estimates for all the specimens examined, indicating their similar sensitivity to microstructure which is consistent with the findings of Chapter 5.

From the current results it can be concluded that the TBF method is little influenced by the prior plastic deformation histories (see Table 8.2) of the material and that it is insensitive to very small creep strains e.g. ~0.002.

8.4. Precision of strain measurement

The development of both local and long-range misorientations can be correlated directly to the applied strain. For strain rates down to ~$10^{-5}s^{-1}$ these correlations have been shown to be relatively insensitive to deformation temperature and mode and can therefore be used for strain assessment in similar materials. However, the precision of strain estimation needs to be determined due to scatter in the measured misorientation data. At comparable strains, the main sources of scatter based on the findings of Chapters 5 and 6 include; microstructural variations, deformation in-homogeneities, grain size variations and variations in the quality of orientation data. The scatter could also result from inaccuracies in strain measurement during deformation but this can be controlled through proper experimentation as described in Chapter 3.

In the current study, the strain data were assumed to be measured with little or no error, while the misorientation data were assumed to be affected by the aforementioned experimental errors. The upper and lower bounds of the scatter bands shown in Fig. 8.9 - Fig. 8.12 were determined at 95% confidence level [192, 193] from the spread of misorientation data about their mean value as defined by the correlation equation for each metric. Table 8.3 lists the strain estimation precision of the metrics at the strain range where they are most sensitive. The precision values were calculated from the scatter bands. The values given here represent the worst-case scenario since they are derived from data obtained under different deformation conditions. Better strain estimation precisions can be obtained by considering data obtained under similar conditions e.g. HTT data.

Table 8.3: Precision and sensitivity range of the strain assessment methods.

Metric	Precision (±)	Strain range
DGF	0.02	<0.1
$AMIS_a$	0.02	0.00 - 0.23
LAMF	0.01 - 0.03	0.05 - 0.15
KAM_a	0.02	0 .00 - 0.23

8.5. Application of strain assessment methods to real power plant components

8.5.1. Plastic strain estimation in welded joints

The applicability of the proposed plastic strain estimation methods were assessed using Weld-3 and Weld-2 components which were in as-welded and as-welded repaired condition, respectively as detailed in Chapter 4.

From each component a 3mm thick slice was sectioned by wire EDM in the through thickness direction as shown in Fig. 4.4. The surface preparation for EBSD measurements was in accordance with the procedures outlined in Chapter 3 but owing to the large size of the samples the grinding and polishing processes were carried out manually. The polished slices were then masked using chemical resistant tapes to limit electropolishing to specific zones as shown schematically in Fig. 8.13. EBSD measurements were then conducted on the electropolished regions as described in Chapter 3. Each measurement covered an area of 700μm x 700μm and proceeded in series from the fusion boundary (FB) toward the base metal until no further changes in misorientation build-up was detected. At each zone, three series of measurements were conducted adjacent to each other. Macro-hardness measurements were also performed at each zone starting from the FB toward the base metal using the procedures outlined in Chapter 3.

8.5.1.1. Quantification of plastic strain in Weld-3

The weld geometry of Weld-3 component is shown schematically in Fig. 8.13. Its heat affected zone (HAZ) near the FB was free of precipitation as seen in Fig. 8.14a

despite the fact that the base metal was an ex-service material. This can be attributed to the solution treatment effects arising from the welding process in the regions bordering the FB [52, 53]. Similarly, as seen in Fig. 8.14b there was no evidence of precipitation in the far-field even though preferential etching was apparent along the grain boundaries which could have resulted from the erosion of intergranular precipitates.

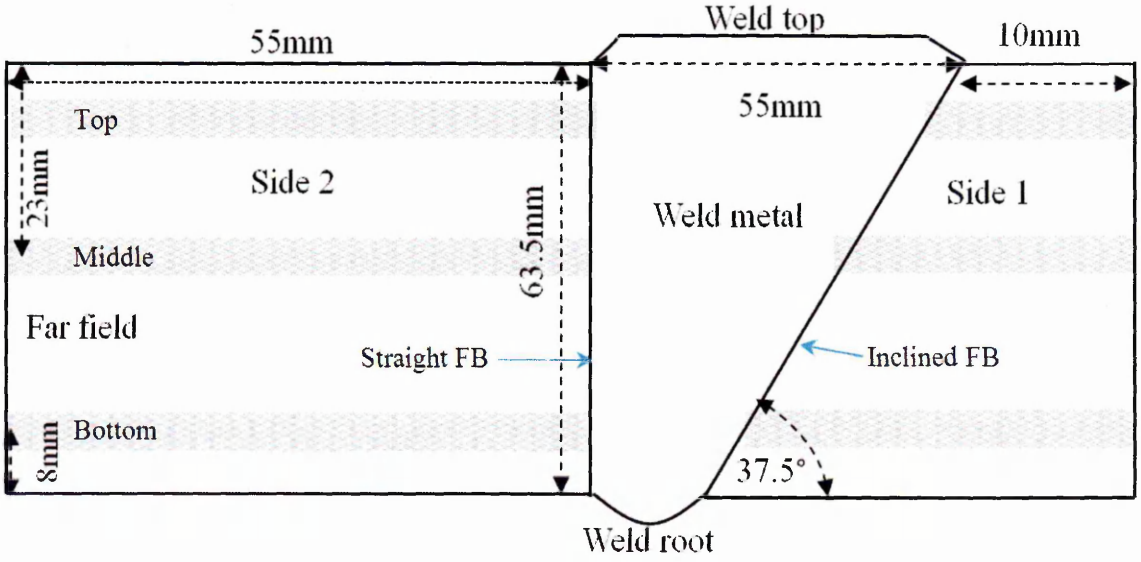

Fig. 8.13. Schematic drawing showing the through thickness weld profile and the EBSD measurement areas (shaded zones) of Type 316H stainless steel weldment (Weld-3).

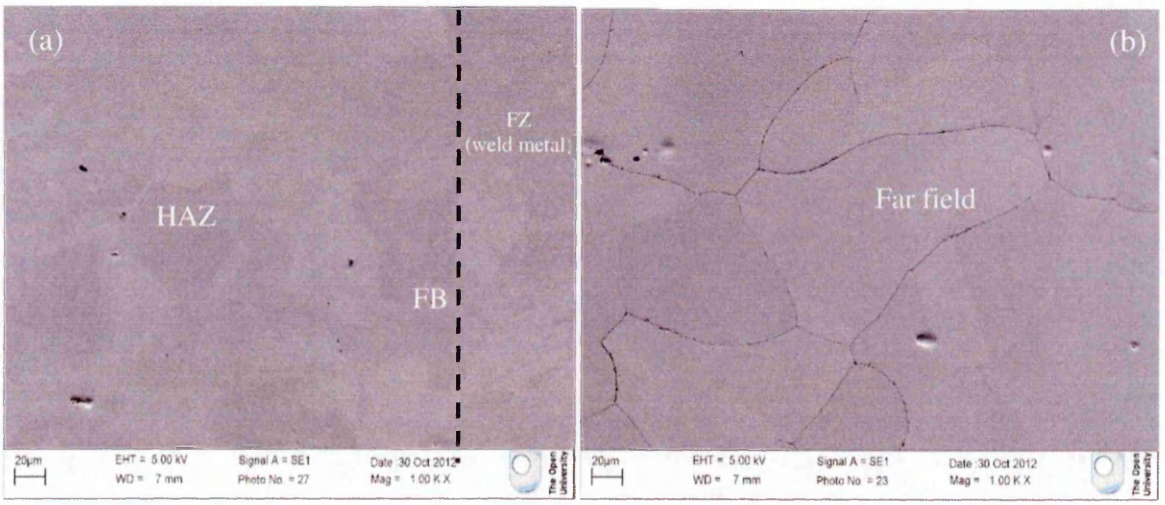

Fig. 8.14. SEM micrographs of Type 316H stainless steel weldment (Weld-3): (a) near the FB, and (b) in the far field from the FB (b). No precipitation in the microstructure.

Fig. 8.15 and Fig. 8.16 show the estimated true strain distributions at three positions through the thickness as a function of distance from the FB for Side 2 and Side 1 of the component, respectively. The strain estimation was based on equations Eq. 6.2, Eq. 6.4, and Eq. 6.5 and each point in the plot represented an average strain value from three adjacent orientation maps.

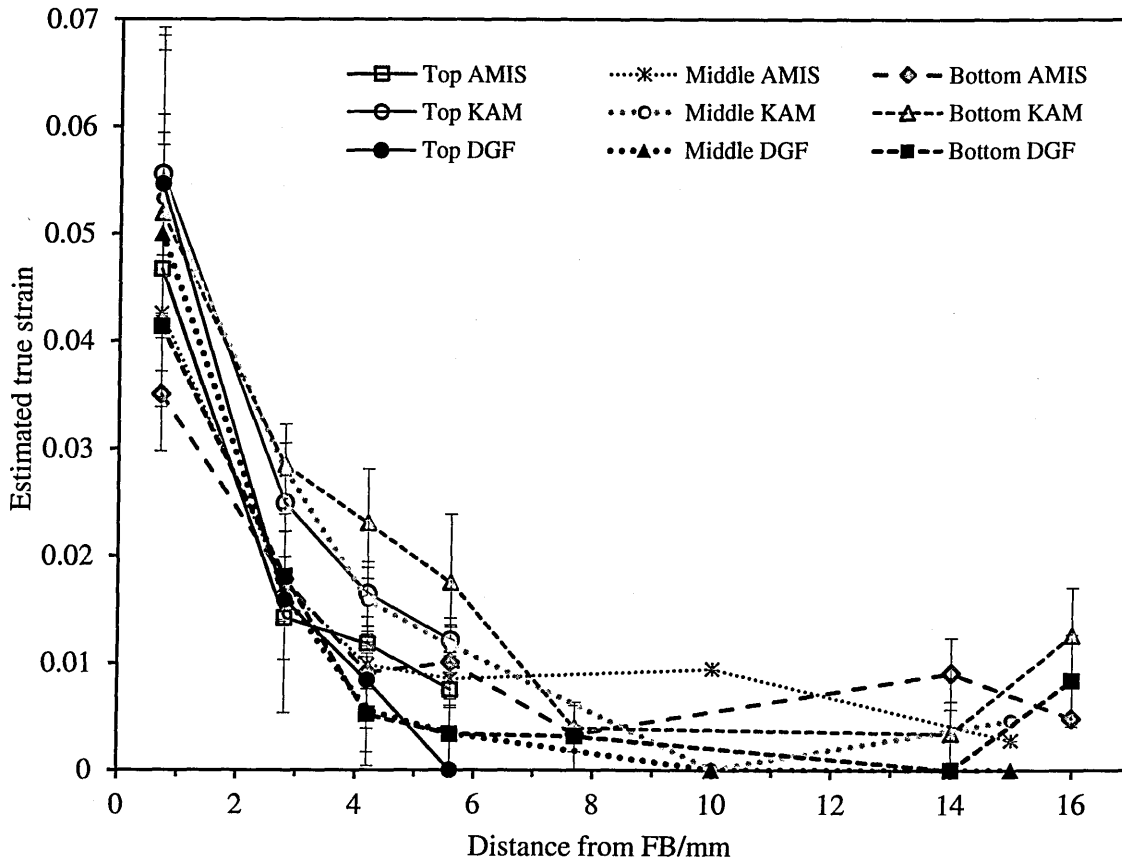

Fig. 8.15. Estimated true plastic strain in Type 316H stainless steel weldment (Weld-3, Side 2) based on Eq. 6.2, Eq. 6.4 and Eq. 6.5, as a function of distance from the FB at the three positions shown in Fig. 8.13.

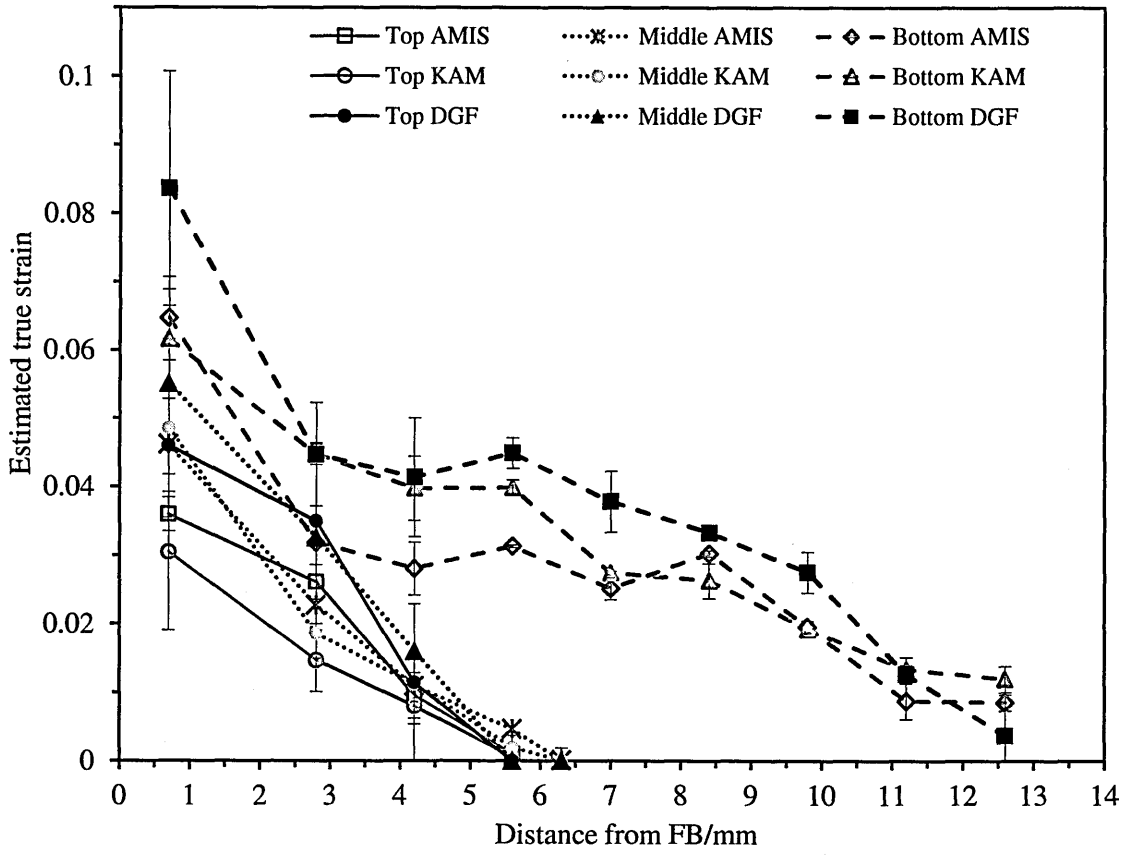

Fig. 8.16. Estimated true plastic strains in Type 316H stainless steel weldment (Weld-3, Side 1) based on Eq. 6.2, Eq. 6.4 and Eq. 6.5, as a function of distance from the FB at the three positions shown in Fig. 8.13.

Discrepancies in the estimated strain values from different metrics can be ascribed to the microstructural differences between Weld-3 and the service-aged steel from which the equations were derived. As shown in Chapter 5, misorientations evolve at a faster rate in aged than in un-aged steel, which could lead to an underestimation of the strain when equations derived from an aged material are applied on un-aged material. The estimated values based on the DGF metric are more reliable in this case, owing to its insensitivity to microstructural variations.

In general, the results indicate a reduction of plastic strain from a maximum value of ~8% near the inclined FB (Side 1) and ~5.5% near the straight FB (Side 2) to ~0% in the far field. The strain affected zone (SAZ) spreads about 7mm from the straight FB and

about 12.5mm from the inclined FB near the weld root. Possibly, as the welding progressed from the root to the top, the inclination of the FB allowed the strain hardening effects from the welding thermal cycles to spread further from the FB near the weld root than in the case of the straight FB. The strain variation in the through thickness direction was not very significant on the straight FB side but on the inclined FB side, the weld geometry seemed to have a larger influence on the strain distribution, particularly near the root, where the weld experiences more thermal cycles and thus maximum deformation. As seen in Fig. 8.17 the strain increased from the weld top to weld root, which can be attributed to the increase in the strain hardening as the number of welding passes increases [194].

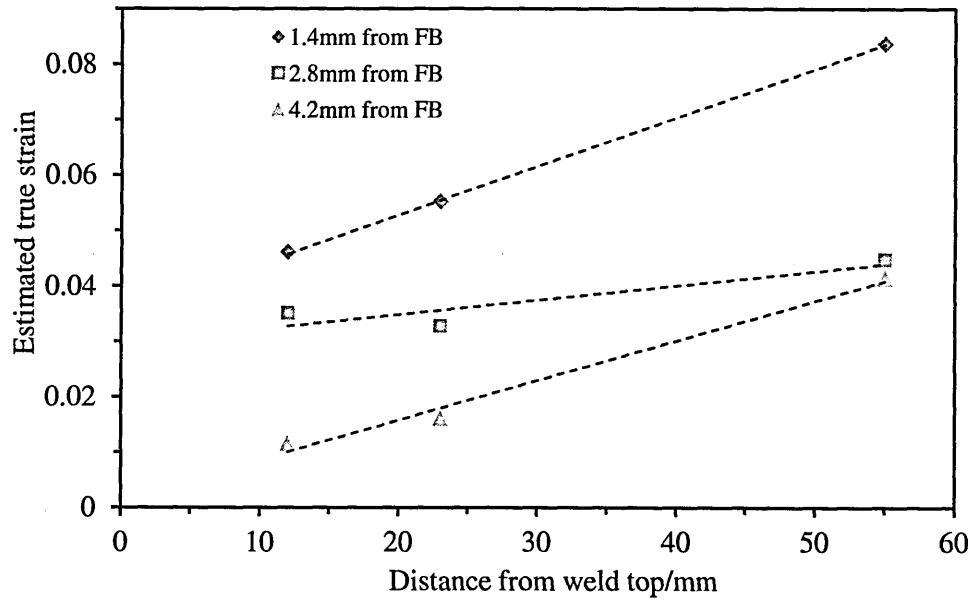

Fig. 8.17. Estimated true plastic strains in Type 316H stainless steel weldment (Weld-3, Side 1) based on Eq. 6.5, as a function of distance from the weld top to weld root. Measurements taken at 1.4mm, 2.8mm and 4.2mm from the FB.

Strain estimations along the bottom section (Side 2) of the weld based on hardness and EBSD measurements are shown in Fig. 8.18a. The hardness strain estimates were based on calibration given in Fig. 8.2b. The estimated strains from the two techniques were

comparable even though large scatter existed in the values estimated by the hardness method. As seen in Fig. 8.18b, the hardness values were characterised by large scatter which makes this method less suitable for localised strain assessment. Generally, a decrease in strain is seen as the distance from the FB increases, which indicates a continued reduction in dislocation densities and thus the abundance of misorientations. The two techniques also estimated similar spread of the SAZ of about 7mm from the FB (see Fig. 8.18a).

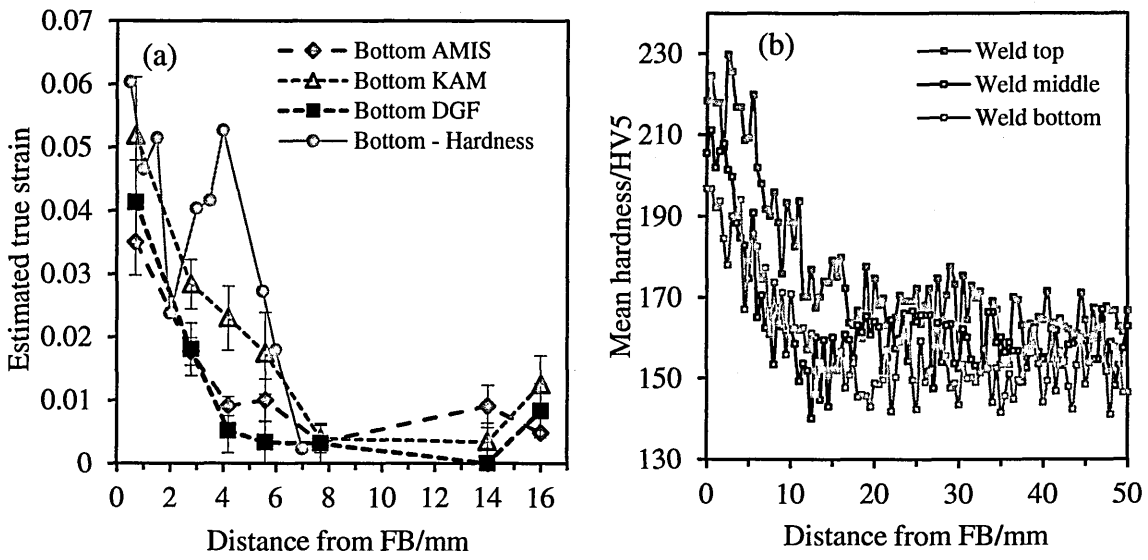

Fig. 8.18. (a) Estimated true plastic strains in Type 316H stainless steel weldment (Weld-3, Side 2) bottom section based on EBSD and hardness measurements. (b) Hardness measurements in Weld-3 (Side 2) at the top, middle and bottom sections.

8.5.1.2. Quantification of plastic strain in Weld-2

In Weld-2 (ex-service Type 316H stainless steel weldment), the quantification of plastic strain was limited to the repaired section of the weld marked as "T" in Fig. 8.19. The microstructure near the FB was free of precipitation unlike that in the far field which exhibited extensive intragranular and intergranular precipitation as seen in Fig. 8.20. This can be ascribed to the same reasons given in the case of Weld-3.

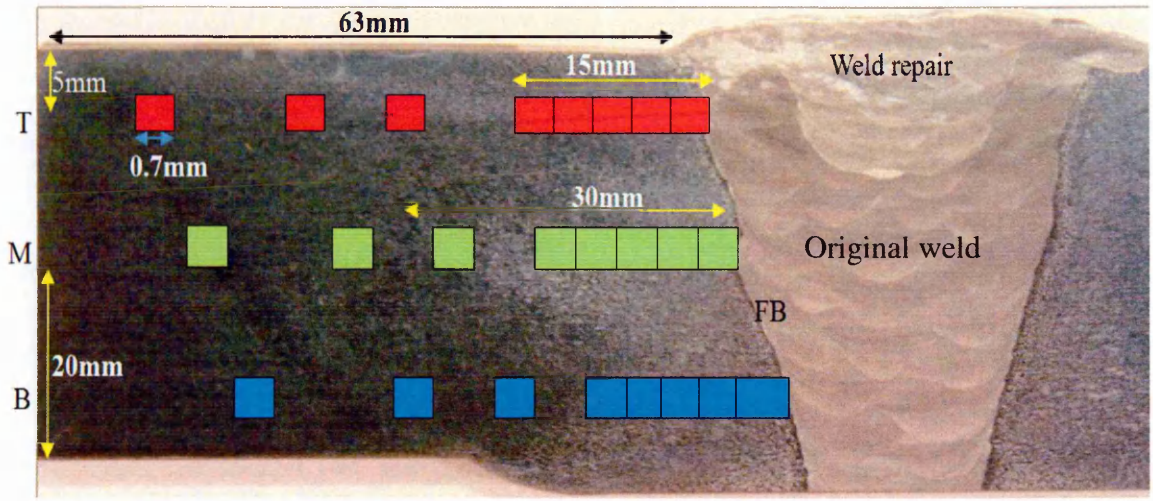

Fig. 8.19. Macrograph of an ex-service Type 316H stainless steel weldment (Weld-2) showing the through thickness cross-section, EBSD measurement areas (shaded zones) and weld repair at the top section.

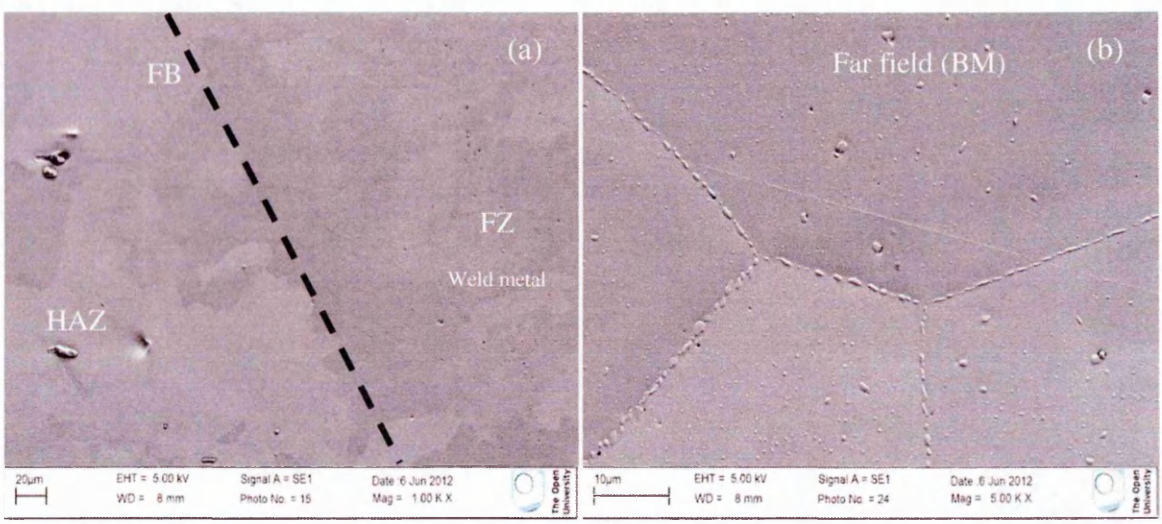

Fig. 8.20. SEM micrographs of Weld-2 obtained at section marked "T" in Fig. 8.19 showing (a) precipitation free HAZ and (b) extensive precipitation in the far field from the FB.

Fig. 8.21 shows the estimated strain distributions at three positions through the thickness as a function of distance from the FB, based on the KAM_a, $AMIS_a$ and DGF metrics. The discrepancies in the estimated strain values from the different metrics can be attributed to the same reasons given for the Weld-3 component. In the repaired section of the weld, it is expected that the solution treatment effects near the FB could have cleared

its deformation history and so the strain estimated in this region is mostly plastic from the welding process. However, the accumulated creep strain during service is expected to contribute to the total strain in regions far from the weld repair such as one marked with "M" and "B" in Fig. 8.19.

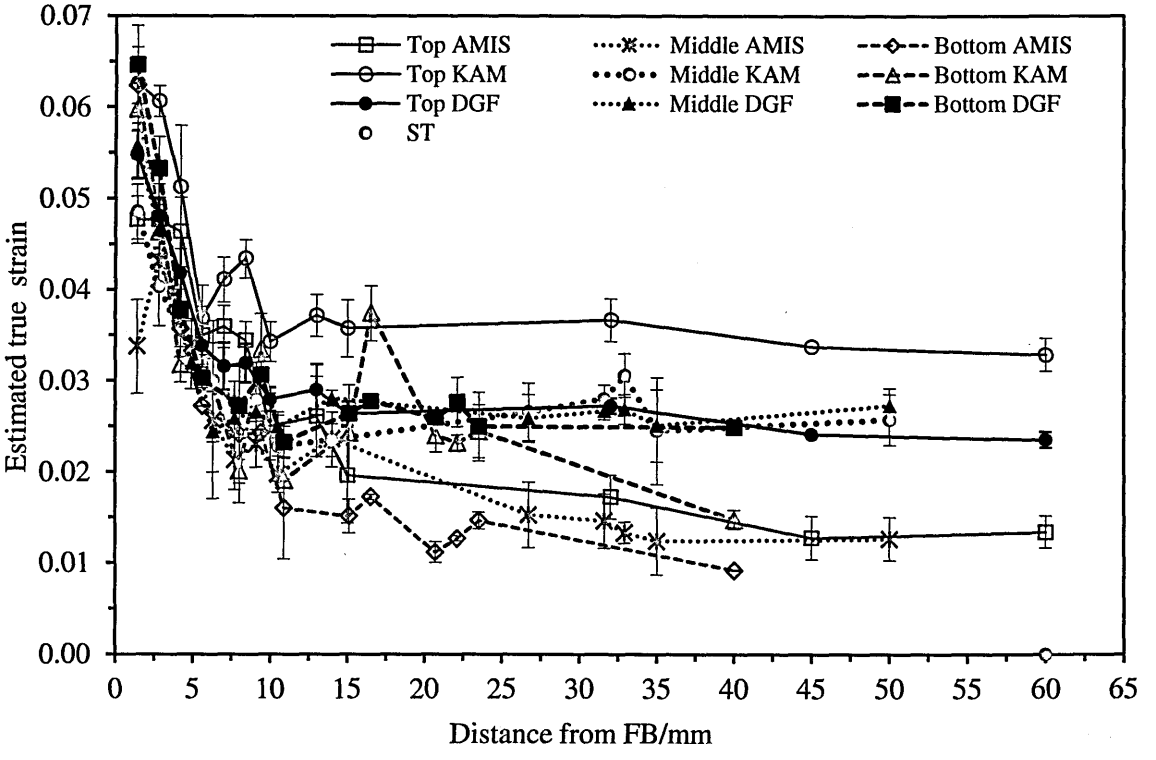

Fig. 8.21. Estimated total strains in Weld-2 based on Eq. 6.2, Eq. 6.4 and Eq. 6.5, as a function of distance from the FB at the three positions (T, M and B) shown in Fig. 8.19.

In general, at the top section of the weld (see Fig. 8.22) the total strain reduced from a maximum value of about 5.5% near the FB to a minimum value of about 2% in the far field, based on the DGF strain estimation. Along the bottom section of the weld (see Fig. 8.21) the total strain reduced from a maximum value of about 6.5% near the FB to about 2% in the far field, based on the DGF strain estimation. The residual strain observed in the far field was later determined to be real as it reduced to zero on solution treatment (ST). The uniformity of residual strain in the through thickness direction in the far field, shows that the deformation in the base metal was uniform and could have been introduced

when the component was in service and/or during the weld repair. The SAZ extended ~12mm from the FB in the top, middle and bottom sections of the weld.

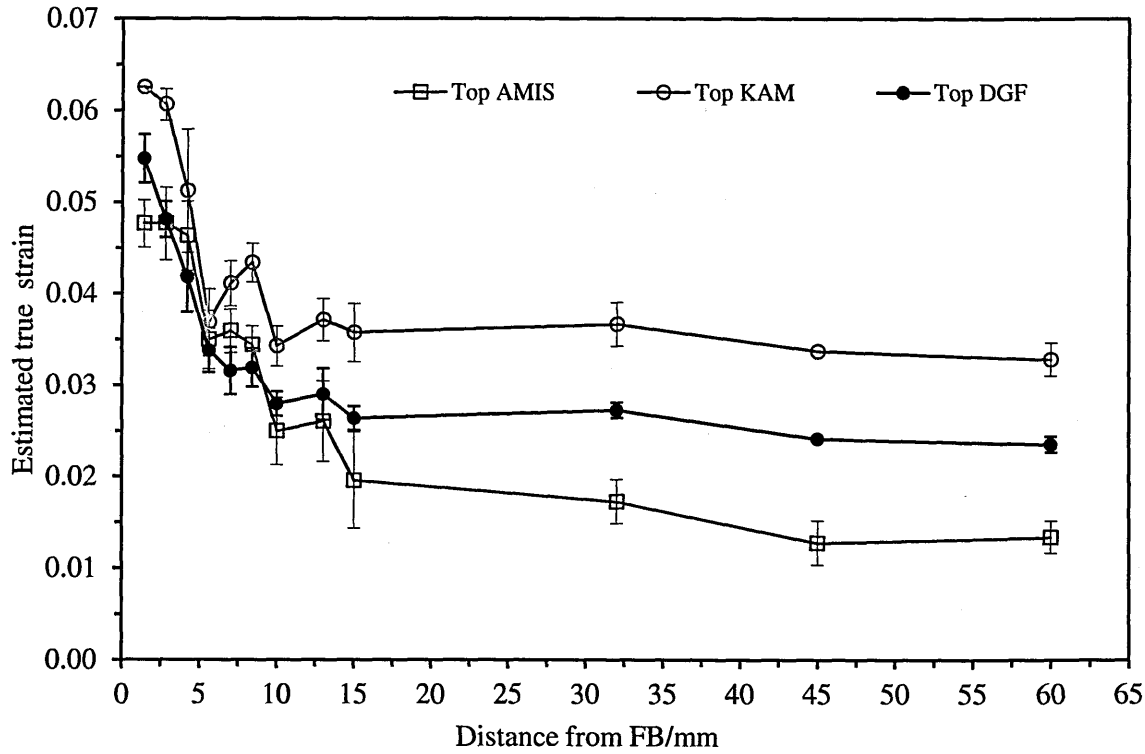

Fig. 8.22. Estimated true plastic strains in Weld-2 top section based on Eq. 6.2, Eq. 6.4 and Eq. 6.5, as a function of distance from the FB.

The estimation of the strain distribution based on the hardness measurements was consistent with the EBSD strain estimations even though the hardness strain estimates varied widely as seen in Fig. 8.23a, owing to scatter in the hardness measurements as seen in Fig. 8.23b. The strain estimation from hardness measurement seemed insensitive to the residual strain in the far field as it dropped rapidly to zero beyond 10mm from the FB.

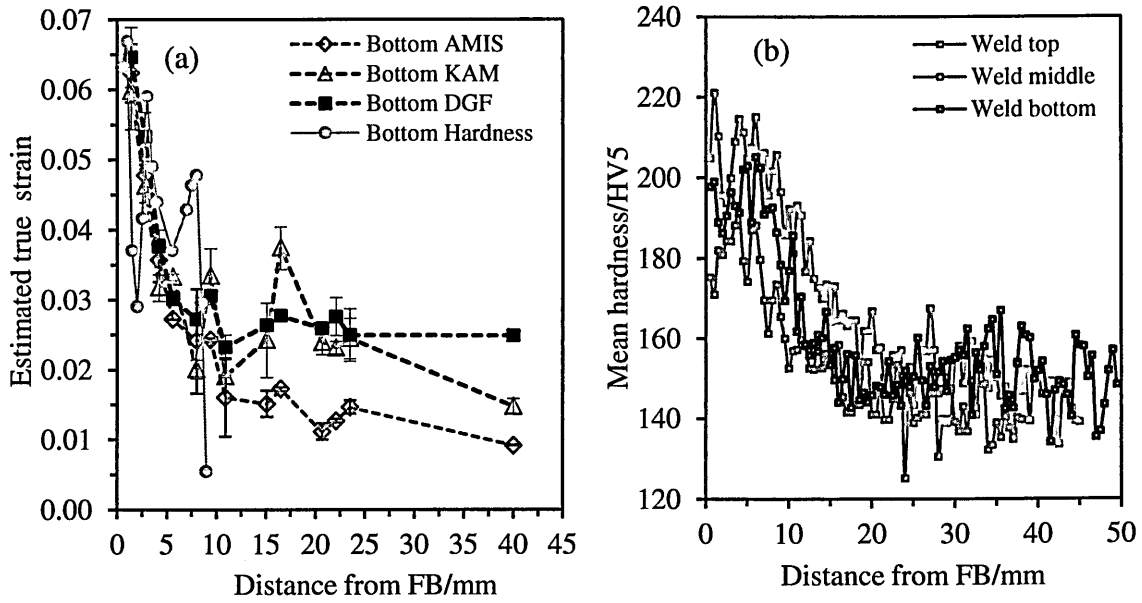

Fig. 8.23. (a) Estimated true strains in Weld-2 bottom section based on hardness and EBSD measurements. (b) Hardness measurements at the top, middle and bottom sections of Weld-2.

8.5.2. Creep strain estimation in an ex-service weldment

The applicability of the proposed creep strain assessment methods was assessed using the Weld-1 component which had been removed from service after 90,930 hours, as detailed in Chapter 4. The weld geometry is shown in Fig. 8.24 in which the areas used for EBSD measurements have been indicated. Similar procedures to those applied on Weld-2 and Weld-3 were followed during Weld-1 sectioning, surface preparation and EBSD measurements.

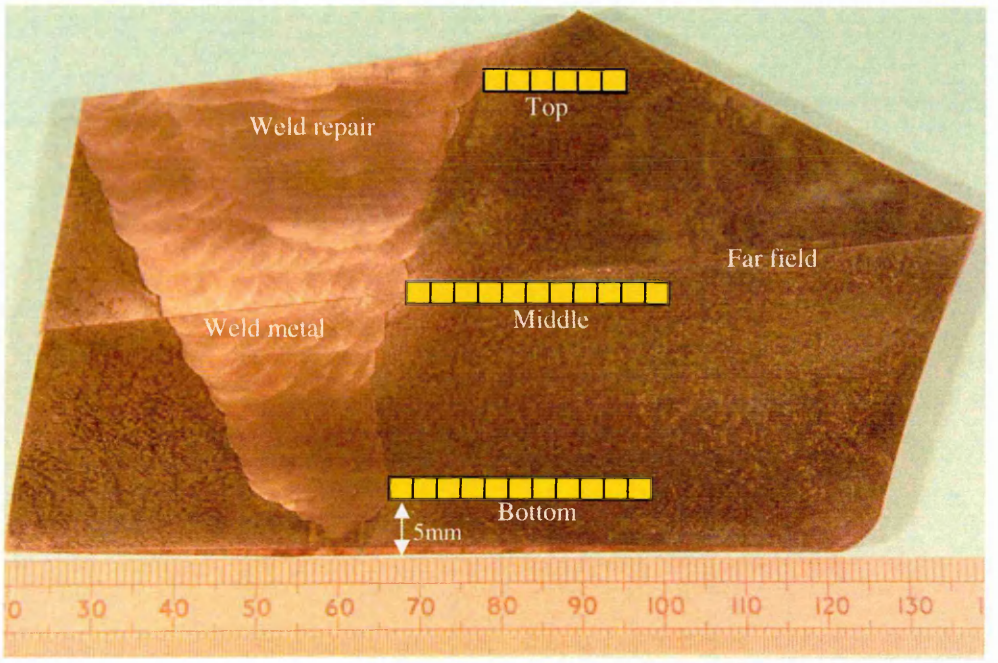

Fig. 8.24. Macrograph of Weld-1 through thickness cross-section showing EBSD measurement areas (shaded zones) and evidence of a weld repair at the top position.

The microstructure of Weld-1 near the FB exhibited no visible precipitation as seen in Fig. 8.25a while in the far field there was evidence of both intragranular and intergranular precipitation, though not extensive, as seen in Fig. 8.25b.

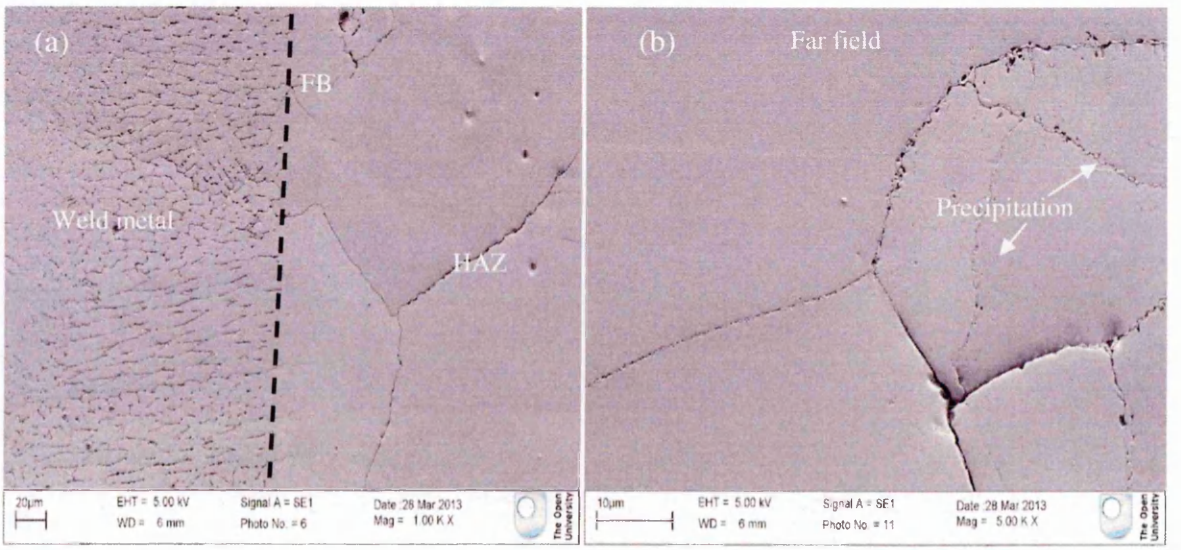

Fig. 8.25. SEM micrographs of Weld-1 showing (a) precipitation free HAZ, and (b) inter- and intra-granular precipitation in the far field from the FB.

Fig. 8.26 shows the estimated total strain distributions at three positions through the thickness as a function of distance from the FB, based on Eq. 6.2 and Eq. 6.5. In general, the results indicate a reduction of the total strain from a maximum value of ~6.5% at the top section and ~5% at the bottom section to ~0% after 6mm from FB, based on the DGF strain estimation. Total strain estimation based on KAM_a indicates a reduction from a maximum value of ~4% at the top section and ~6% at the bottom section to ~0% after 6mm from FB. The discrepancies in the estimated total strains from the two metrics can be ascribed to the microstructural variations, as explained previously, and to the accumulated creep strain.

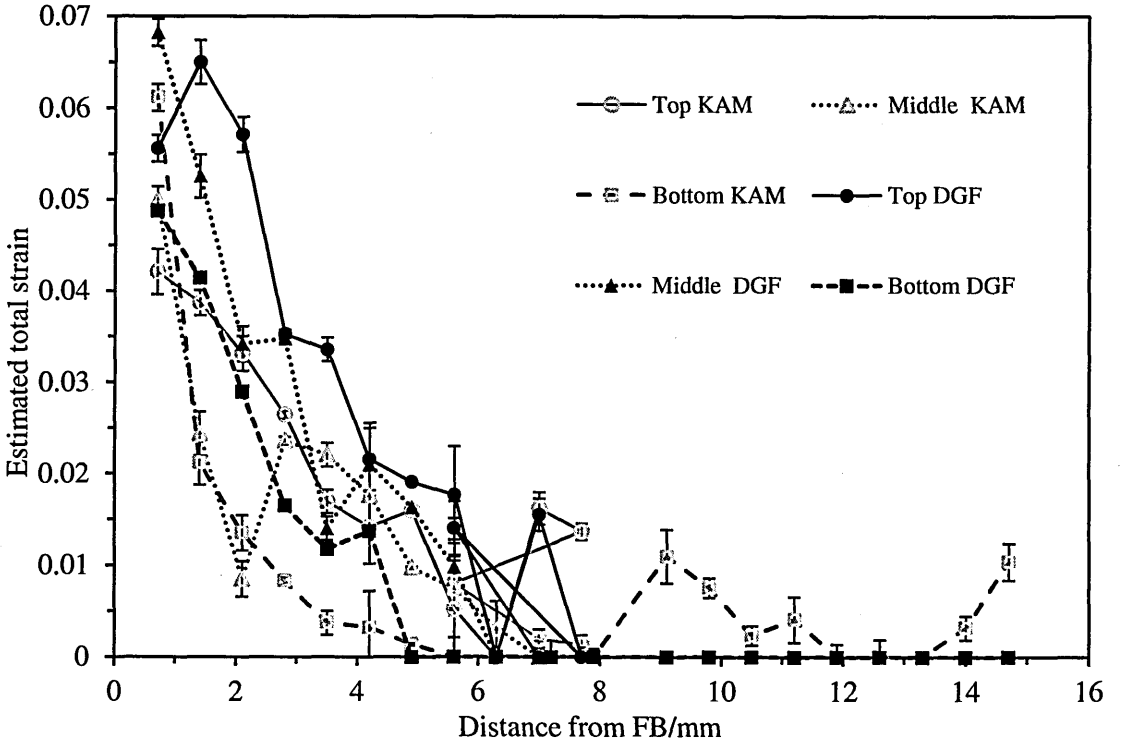

Fig. 8.26. Estimated total true strains in Weld-1 based on Eq. 6.2 and Eq. 6.5, as a function of distance from the FB at the three positions shown in Fig. 8.24.

8.5.2.1. Creep strain estimation in Weld-1

The estimation of creep strain was based on TBF method due to the apparent microstructural variations in Weld-1(see Fig. 8.25) which limits the applicability of the DMD method as explained previously.

The TBF method mainly depends on the correct estimation of the total strain using the proposed misorientation metrics (i.e. KAM_a, LAMF, $AMIS_a$ and DGF). To avoid the problems associated with the microstructural variations, DGF metric was used in this case and the procedures stated in section 7.2.5.7b were followed. Fig. 8.27 shows the distribution of the estimated creep strains as a function of distance from the FB along the bottom, middle and top sections of Weld-1. The result indicates a maximum local creep strain of ~3.2%, ~1.6% and ~3.5% in the bottom, middle and top sections, respectively. In the bottom and middle sections the maximum creep accumulation occurred 0.7mm from the FB and decayed to ~0% after about 2.8mm. In the top section, creep strain increased from ~0% near the FB to a maximum value of ~3.5% before dropping to ~0% after 4mm from the FB. As seen in Fig. 8.24, there was evidence of a weld repair at the top section which could have cleared the accumulated creep strain history near the FB. This may explain why no creep strain was detected in this region even though it had a total strain of ~5.5% (see Fig. 8.26).

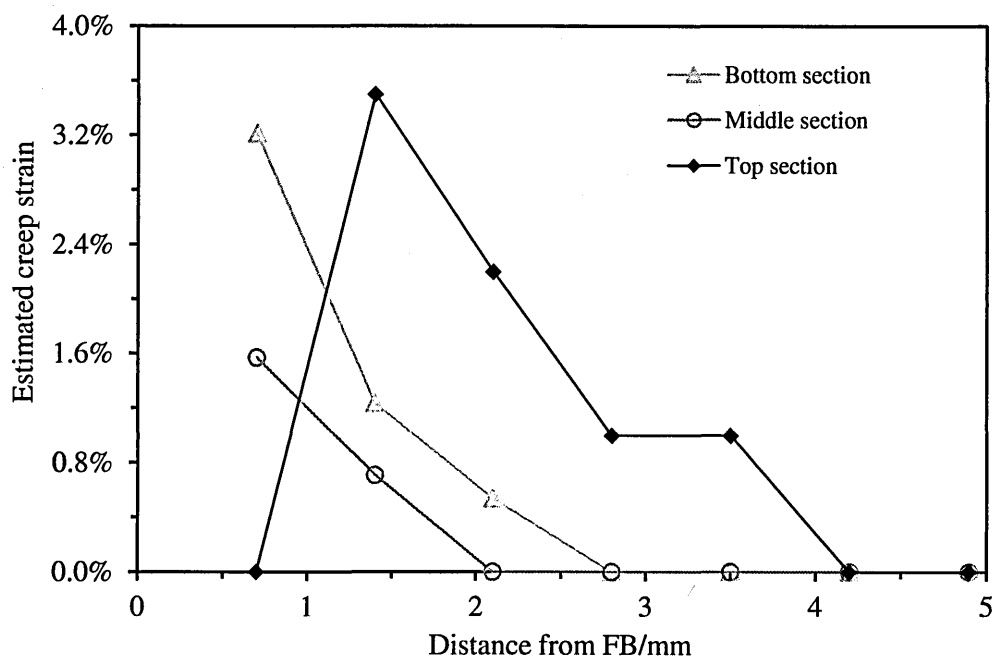

Fig. 8.27. Estimated creep strains in Weld-1 based on TBF method, as a function of distance from the FB at the three positions shown in Fig. 8.24.

The base metal (BM) had no detectable creep strain. It is clear from the results that a through-thickness creep strain variation existed in Weld-1 with more creep accumulation occurring along the bottom than in the middle section of the weld. Since the DGF metric was used in the TBF method, it is possible that the creep strain values reported here are slightly overestimated (see section 8.3.3).

Since the TBF method is little influenced by the prior deformation in a crept material (see section 8.3.3), it is suitable for creep strain estimation in weldments where such variations exist (see section 8.5.1). It is evident from the current results that the accumulation of creep strain during service is limited to the SAZs of the weldment. It is possible that when the component is subjected to relatively uniform stresses during service, the additional welding stresses (see section 2.2.4) near the FB may increase the proportion of mobile dislocations resulting in an increased creep strain in the SAZs than in the BM. For a uniaxial creep test on a cross-weld specimen, the BM may experience more creep deformation owing to strain hardening effects in the SAZs, as explained later in section 8.5.3. Application of the TBF method to Weld-3 (in the as-welded condition) detected no creep strain which provides evidence underpinning the reliability of the method for creep strain assessment.

8.5.3. Assessment of deformation through DIC and EBSD

Digital image correlation (DIC) is a surface-based technique that evaluates deformation by measuring displacements between surface features from a series of captured images (see section 2.3.2). The DIC creep results presented in this section are derived from the work of Sakanashi [58] who conducted cross-weld creep measurements on a specimen extracted from Weld-3 along the middle section in a plane perpendicular to the through-thickness direction as shown schematically in Fig. 8.28. A flat specimen 70mm long, 6mm wide and 3mm thick was deformed under constant load creep conditions

at 545°C using an initial applied stress of 315MPa. The measurement was conducted in a similar creep frame to the one described in Chapter 3, except that the furnace had a side widow which allowed digital images to be taken (at a predetermined frequency) as the creep test progressed. The specimen was painted to give a high contrast speckle pattern. The specimen ruptured after 2300 hours during which a total of 480 images were captured and used for evaluating local strain evolution as a function of time. The assessment was carried out using DaVis DIC software and entailed calculating the displacements of the speckles from their original positions using images taken over the test period, allowing full field strain measurement. Further details concerning the procedures followed during the DIC measurements and the data analysis can be found in [58].

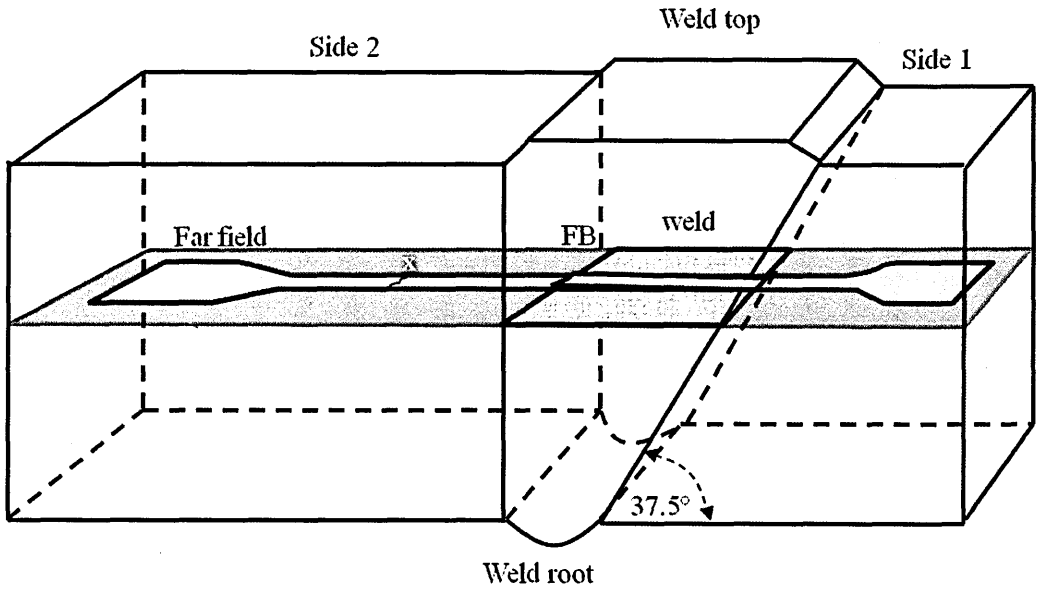

Fig. 8.28. 3D schematic drawing of Weld-3 illustrating the plane and position of cross-weld creep specimen used for DIC measurements. The specimen rupture position is indicated by "x".

The creep ruptured specimen was prepared for the EBSD measurement as described in Chapter 3. The preparation was only on the surface on which DIC measurements were performed and owing to the large size of the specimen, the grinding and polishing processes were conducted manually. After polishing, the whole surface was

electropolished as described in Chapter 3. A series of EBSD measurements each covering an area of 700μm x 700μm were performed, starting from the FB toward the ruptured end of the specimen (see Fig. 8.28). The EBSD indexing rates reduced near the point of rupture mostly due to the existence of creep cracks as seen in Fig. 8.29a. Repeat measurements were conducted in this region in adjacent areas with fewer creep cracks and only orientation maps with indexing >96% were considered for the strain analysis.

Examination of the microstructure revealed little precipitation in the HAZ as seen in Fig. 8.29b, but in the far field where the specimen ruptured there was evidence of intergranular and intragranular precipitation as seen Fig. 8.29a.

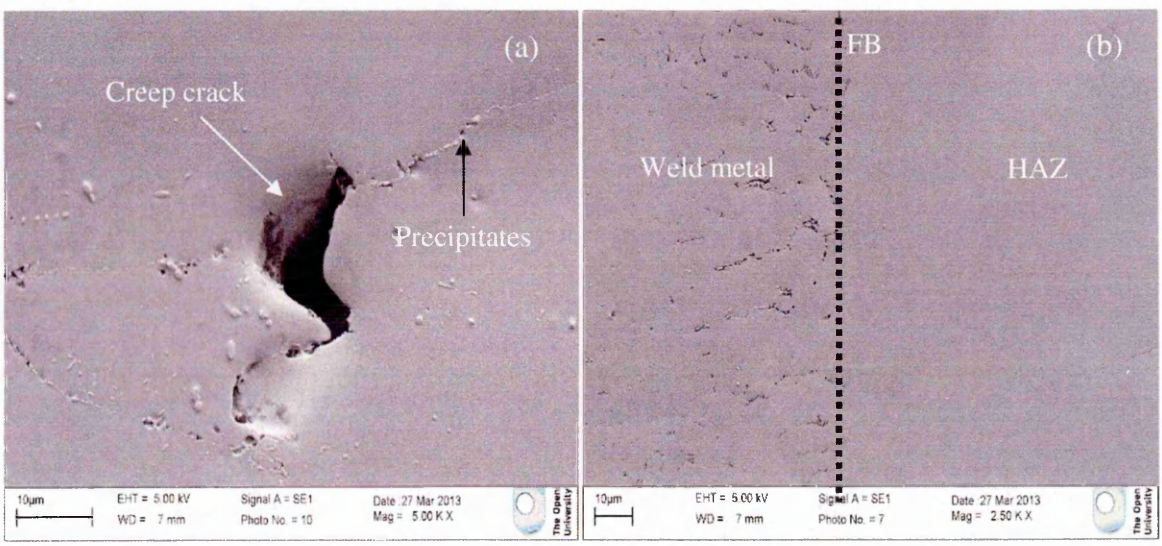

Fig. 8.29. SEM micrographs of DIC creep ruptured specimen showing (a) creep cracks and precipitation near the ruptured surface, and (b) precipitation free HAZ.

The EBSD strain assessment along the ruptured specimen was based on the DGF metric owing to the apparent microstructural variations seen in Fig. 8.29. The estimated total strain was about 0.06 near the FB which decreased to about 0.02 after 4mm before rising to about 0.17 near the point of rupture as shown in Fig. 8.30. A corresponding decrease in the estimated total strain occurred as the distance from the ruptured point toward the other end of the specimen increased. For comparison, the total strain for the uncrept component as estimated along the middle section of Weld-3 in Fig. 8.13 has been

included even though the measurements in this case were made on a plane parallel to the through thickness direction. In the uncrept condition, the total strain decayed gradually from about 0.05 near the FB to <0.01 after 4mm. Interestingly it is at about this point that an increase in total strain was seen in the creep-ruptured specimen.

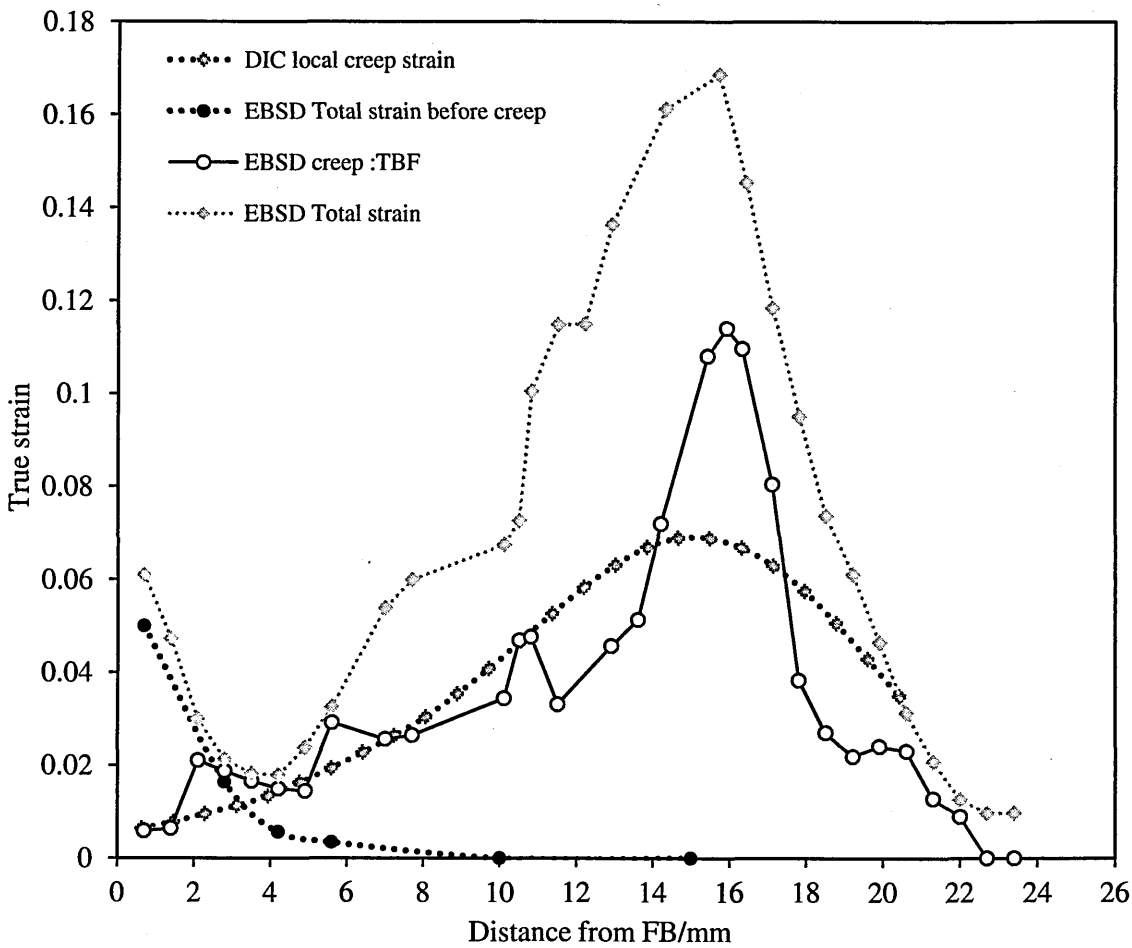

Fig. 8.30. Creep strain distribution on cross-weld specimen based on DIC measurement during the test and EBSD estimations after the test. (Including the total strains before and after creep test, based on the EBSD estimations).

The estimated local creep strain as measured by the TBF method shows good correspondence with the local creep strain as measured by the DIC method. Since creep rupture occurs rapidly, it is possible that some images were not captured at this time during the DIC measurement. This may explain the observed difference in the estimated and measured creep strains near the point of rupture. Since the DGF metric was used in the

TBF method, it is possible that the estimated creep strains are slightly overestimated as explained previously. The estimation of creep strain based on the DMD method was not possible owing to microstructural variations in the specimen (see Fig. 8.29) which limits the applicability of the method.

The difference between the estimated total strain and the creep strain indicates that most of the instantaneous strain during creep loading occurred in the far field. This is possibly due to strain hardening effects from the welding process [194] which had spread by about 4mm from FB. Referring to Fig. 6.1, the strain for the service-aged steel at 315MPa is ~0.05 at 550°C which is close to the difference between the estimated total strain and creep strain obtained in the current case at the point of rupture (i.e. about 0.06 strain). However, this is an approximate assessment owing to the differences in the test temperatures and the aged steels involved.

From the Ashby deformation mechanism map for Type 316 steel [16], dislocation creep is predicted to be the main deformation mechanism under the current creep conditions (i.e. 345°C and 315MPa). The creep deformation along the cross-weld specimen can therefore be explained in relation to the Orowan equation (see section 7.2.5.1). It is possible that most of creep loading strains occurred in the far field as the regions close to the FB may have been strain hardened during the welding process. So, the ρ_m in the far field could have been higher than that near the FB resulting in its reduced creep resistance. From Fig. 8.30, it is clear that most of the creep deformation occurred in the far field. However, there was about 0.01 creep strain accumulation near the FB which could explain the differences in the total strains before and after the creep test at this point. According to the TBF method, the minimum creep accumulation occurred near the FB. This is in contrast to results obtained on the ex-service weldment where the maximum creep strain was observed near the FB (see section 8.5.2.1). This is possibly due to differences in the densities of mobile dislocations in the SAZs of the two components as discussed in section

8.5.2.1. Loading a cross-weld specimen may result in higher ρ_m in the far-field than near the FB owing to welding strain hardening effects. In the case of the ex-service weldment experiencing relatively uniform stresses during service, the additional welding stresses near the FB may increase the proportion of ρ_m. Following the Orowan equation (see Eq. 2.6) an increase in ρ_m would results in a reduced creep resistance.

8.6.Summary

The key findings in this chapter can be summarised as follows;

- The hardness and the EBSD measurements showed similar responses under comparable deformation conditions indicating their dependence on dislocation densities. Hardness measurements exhibited large scatter which limited its application in localised strain assessment.
- The precisions of the proposed strain assessment methods were found to depend on the metric used for misorientation quantification and the strain range considered. The accuracies of the methods are postulated to depend on the microstructure and the strain sensitivity of each metric.
- The estimation of the accumulated creep strains on components with varying deformation histories was shown to be possible through the TBF method. However, microstructural variation was found to limit the applicability of the DMD method in creep strain estimation.
- Good agreement was established between the creep strains as measured by the DIC method during the test and those estimated by the TBF method after the test.
- The applicability of the proposed strain assessment methods to real power plant components was demonstrated by the successful mapping of plastic and creep strain distributions in weldments after different periods in service.

CHAPTER 9

OVERALL CONCLUSIONS AND SUGGESTIONS FOR FUTURE WORK

9.1. Introduction

The work presented in this thesis is concerned with the characterisation of plastic and creep strains derived from lattice orientation measurements. The main objective of the research was to explore the potential of electron backscatter diffraction (EBSD) for characterising localised inelastic strain at high spatial resolution.

EBSD is a technique for measuring the local crystallographic orientation of areas within individual crystallites in a polycrystalline material. Its use for assessment of plasticity work on the principle that imperfections in crystal lattice caused by microstructural features such as dislocation introduces lattice rotations which leads to local changes in crystal orientation. Therefore, by assessing these changes through EBSD the degree of deformation accumulated in a given material can be estimated. Although EBSD has been used in several studies [63, 116, 195-198] for inelastic strain characterisation, there was little previous information available on how such assessments maybe influenced by a material's microstructure and/or deformation conditions.

In the current research an experimental approach was adopted to investigate the development of strain-induced misorientations under different deformation conditions and in materials of varying microstructures.

9.1.1. Materials

AISI Type 316H austenitic stainless steel was investigated in this thesis. It came in two main forms: service-aged steel (ex-service) and un-aged steel (as-manufactured). The service-aged steel had extensive inter- and intra-granular precipitation unlike the un-aged steel. Its average grain size was about 3 times that of the un-aged steel.

9.1.2. Experimental programme

The experimental programme consisted of the following:

9.1.2.1. Mechanical testing

The aim of mechanical testing was to introduce controlled amount of deformation in the steels studied. A series of monotonic tests were performed in tension, compression and in constant load creep. These tests were conducted at different temperatures (24°C, 550°C and 675°C) and strain rates ($3.5x10^{-3}s^{-1}$–$4.0x10^{-7}s^{-1}$) on steels of varying microstructures and average grain sizes (service-aged, re-solution heat treated, thermally-aged and un-aged steels). The tests were interrupted at specific strains. From these tests the influence of microstructure, grain size, deformation temperature, deformation mode, and deformation strain rate on the development of strain-induced misorientations was investigated.

9.1.2.2. Material characterisation

Characterisation of grain size was based on optical microscopy and orientation imaging microscopy methods. The microstructures of the steels studied were examined using SEM while the dislocation structures and densities were characterised using TEM. This combination was used to establish the relationship between the microstructure and the observed effects of deformation on intragranular misorientations.

9.1.2.3. Standardization of sample preparation for EBSD measurements

Since EBSD is a surface sensitive technique, for a proper comparative study of different specimens, it was essential to prepare them identically and with a minimum of preparation-induced deformation. A standard procedure was established consisting of grinding, polishing and electropolishing.

9.1.2.4. Optimisation of EBSD measurements parameters

The aim of optimisation process was to ensure the settings used for EBSD measurement gave good angular resolution within a reasonable measurement time. The main settings affecting angular resolution which were optimised included: the number of bands detected, the Hough resolution, the number of frames averaged, and the CCD camera binning. Measurements were conducted on the same region with different settings and the combination which gave the lowest KAM_a was adopted.

9.1.2.5. Orientation measurements

To develop a misorientation-based strain assessment method, EBSD measurements were performed on all the deformed specimens. Each measurement, conducted on a square grid of points 1μm apart, covered an area of 700μm x 700μm, ensuring that at least 100 grains were analysed. No data cleaning was performed and only orientation maps with >96% indexing rate were considered for strain analysis. The development of strain-induced misorientation was assessed at the local scale (spatially correlated) using the KAM_a and LAMF metrics and at the long-range scale (spatially uncorrelated) using the $AMIS_a$ and DGF metrics. The application of the local and long-range metrics on the same orientation data, enabled plastic and creep strain characterisation owing to their different sensitivities to the two deformation mechanism.

From the analysis of the orientation data obtained under different conditions, misorientation-based strain assessment methods were developed, validated and applied to real power plant components. Detailed discussion of each aspect described here is given in previous chapters.

9.2. Overall conclusions

The main conclusions which can be drawn from the work presented in this thesis include:

9.2.1. *Material characterisation*

- The characterisation of grain size of Type 316H stainless steel based on the optical microscopy and orientation imaging microscopy methods gives comparable results.
- Long-term service exposure to temperatures in the region of 516°C leads to extensive inter- and intra-granular precipitation in Type 316H stainless steel. The precipitation varies between the grains and this is judged to arise from the differences in their overall Schmid factor values with "creep weak grains" accumulating more creep strain which serves as the nucleation sites for carbide precipitation.
- The dislocation density in the service-aged steel studied increased with increasing strain and strain rate at 550°C. The development of dislocation structures varied from relatively uniform distribution at low strains to cell-like structures, consisting of diffuse dislocation walls, at high strains. The distinctness of the cell-like structures increased with decreasing rate of deformation. From discussion in section 4.3.5.1, the presence of a high number density of intragranular precipitate was postulated to aid the formation of diffuse cell-wall structures

9.2.2. *The influence of microstructure, thermal aging, and grain size on strain-induced misorientation*

- The assessment of the local and the long-range misorientations in the deformed steels of comparable microstructures and average grain sizes shows that thermal aging at 550°C for 1000 hours has minimal effects on the misorientations already developed in the material. This implies that static recovery is minimal at this aging temperature and time.
- The evolution of long-range misorientation following room temperature plastic deformation on steels of comparable microstructures is relatively insensitive to grain size but at the local scale, the misorientation build-up as measured by KAM_a is faster

in the fine-grained steel than in the coarse-grained steel. This demonstrates the effects of intragrain deformation inhomogeneity.

- Comparative study of the room temperature plastic deformation of the service-aged and re-solution treated steel of similar average grain sizes shows that the evolution of long-range misorientation is little influenced by the precipitate-dislocation interactions but at the local scale, the misorientation build-up is faster in the service-aged steel than in re-solution treated steel. This demonstrates the localised effects of dislocation accumulations on precipitates.
- The assessment of strain-induced misorientations using the new DGF metric shows least sensitivity to either grain size variations or precipitation effects. This demonstrates the potential of the metric in general characterisation of strain in Type 316 stainless steel regardless of its thermal history.

9.2.3. The influence of plastic strain and strain rate on misorientation development

- The measured distribution of local misorientations (KAM) developing in Type 316H stainless steel under uniaxial isothermal loading is shown to be a function of the applied strain, strain rate, grain size, microstructure and the measurement step-size. An empirical model predicting the local misorientation distribution as a function of deformation conditions is proposed.
- The measured evolution of local and long-range misorientations in the service-aged steel is relatively independent of the deformation temperature (between 24°C and 550°C) and deformation mode (tension vs. compression) for strain rates down to ~$10^{-5}s^{-1}$. Empirical correlations between accumulated plastic strain and misorientation metrics (KAM_a, LAMF, $AMIS_a$ and DGF) have been developed for true strains up to 0.23. Systematic strain rate studies at 550°C shows that the correlations can be applied for strain rates down to ~$10^{-6}s^{-1}$. The strain sensitivities of the correlations

based on DGF and LAMF varies with the applied strain, while those based on KAM_a and $AMIS_a$ their strain sensitivities remains relatively constant between 0 and 0.23 strains.

- The development of strain-induced local and long-range misorientations at 550°C in the service-aged steel is relatively independent of the EBSD measurement plane orientation with respect to the loading axis. This suggests a uniform spatial distribution of misorientations for true strains up to 0.23.
- The development of strain-induced local (KAM_a) and long-range ($AMIS_a$) misorientations at 550°C correlate with measured dislocation densities in the service-aged steel. This demonstrates the appropriateness of using misorientation measurement for strain assessment.
- The development of both local and long-range misorientations in the service-aged steel deformed to ~0.098 strain at 550°C vary significantly with applied strain rates below $4.0x10^{-6}s^{-1}$. This suggests a change in the deformation mechanism which gives rise to reduced dislocation densities as the strain rate is reduced.

9.2.4. The influence of creep strain on misorientation development

- The deformation mechanism influences the rate of misorientation development in Type 316H stainless steel. A systematic study of plastic and creep deformations in steels of similar microstructures and grain sizes shows that misorientations develop in both cases but at a higher rate in plastic than in creep deformation. The development rate is shown to be metric dependent and that the creep-induced misorientation adds to the existing misorientation in the material.
- In the service-aged steel, the primary and secondary creep strains accumulated at 675°C and 150MPa (i.e. under dislocation creep) significantly influence

misorientations <2° and results in rapid deformation of grains with relatively high overall Schmid factor values.

- The long-range misorientations as measured by $AMIS_a$ in the service-aged steel increase almost linearly with increasing creep strain under dislocation creep. This indicates a continuous increase in the grains' deformation as the creep deformation progresses.
- In Type 316H stainless steels studied, the development DGF with increasing creep strain under dislocation creep is little influenced by microstructural variations and occurs at a reducing rate. This indicates a declining number of additional deforming grains per unit strain as the creep deformation progresses.
- In Type 316H stainless steels studied the development of misorientation as measured by KAM_a occurs at comparable rates both in plastic and in creep deformation at 675°C while the development of misorientation based on the LAMF, $AMIS_a$ and DGF metrics occurs more slowly in creep than in plastic deformation. A new DMD method is proposed for creep strain estimation in service-aged steel which exploits the difference in the metrics' sensitivities to plastic and creep strains.
- The twin boundary fraction in the service-aged steel decreased monotonically with increasing total strain at 24°C, 550°C and 675°C. This is postulated to arise from the interactions between dislocations and twin boundaries which alter their near-twin orientation. The decrease is established to be greater in creep than in plastic deformation. At 550°C the prior TBF in service-aged steel reduced with increasing creep strain independently of the prestrain level. A new TBF method is proposed for creep strain estimation in service-aged steel which exploits the differences in twin boundary decay as a function of both plastic and creep strain.

9.2.5. Validation and application of the strain assessment methods

- The hardness and the EBSD measurements show similar responses under comparable deformation conditions indicating their dependence on dislocation densities. The strain estimates from the two techniques shows good correspondence. However, hardness measurements exhibit large scatter which limit their application in localised strain assessment.
- The estimation of accumulated creep strain in service-aged steels of varying deformation histories is shown to be possible through the TBF method. However, microstructural variation limits the applicability of the DMD method in creep strain estimation.
- There is good agreement between the creep strains as measured by the DIC method during the test and those subsequently estimated by the TBF method after the test. This increases confidence in the reliability of the proposed TBF method.
- The applicability of the proposed strain assessment methods to real power plant components is demonstrated by the successful mapping of plastic and creep strain distributions in weldments after different periods in service.

9.3. Suggested Future work

This thesis has laid a foundation on the assessment of both plastic and creep strain in service-aged Type 316H stainless steel using EBSD. As with all pioneering work some grey areas still exist which need further investigation before the technique can be used routinely for strain assessment. The following tasks are suggested for future work;

i. The applicability of the proposed creep assessment methods under different creep deformation mechanisms should be verified. The current methods are based on the dislocation creep and may not be generally applicable where the predominant deformation mechanism does not involve movement of dislocations e.g. in diffusion

creep. It was shown in this thesis that creep-induced misorientations builds on the existing misorientations which makes the assessment of the accumulated creep strain easy when prior deformation history is known. However, difficulties arise when estimating creep strain without knowledge of such histories. The proposed methods have addressed the problem but not exhaustively since the effects of creep deformation mechanisms were not considered during their formulation. It is not yet clear how local and long-range misorientations evolve under different creep deformation mechanisms.

ii. The progressive reduction of twin boundary fraction with creep strain needs further TEM investigation to increase understanding of the contributing mechanisms and thus strengthen the proposed TBF method. In the current study the effect of prior plastic deformation on the subsequent TBF reduction during creep was not exhaustively investigated. The results from the limited tests showed TBF reduction was independent of the prior plastic deformation but there is need for further systematic investigation to confirm this. This is important as it will improve the accuracy of creep strain estimation in components with varied prior plastic deformation histories.

iii. The metric's creep strain sensitivity factor (Ω) established in the current work was assumed to be constant for the whole range of dislocation creep. It was also assumed to be independent of the plastic and creep strain values used in its computation. These assumptions were based on limited experimental evidence and it is necessary to interrogate them further in future in order to ascertain their authenticity. This will improve the accuracy of the DMD method since Ω is an important parameter in this method for complete estimation of creep strain.

iv. The proposed strain assessment methods could be applied to other types of stainless steels commonly used in power generating plants. This will increase the understanding of how strain-induced lattice orientation changes evolve in different structures thus

allowing determination of the material dependence of various parameters of the proposed empirical equations.

v. Since deformation in real industrial components rarely occurs monotonically, the evolution of lattice orientation changes under different deformation modes (e.g. cyclic) should be investigated and their effects, if any, incorporated into the proposed strain assessment methods.

vi. The service-aged steel used in the development of strain assessment methods exhibited little texture. However, to ensure the methods are generally applicable their dependence on the existing texture in material should be investigated.

vii. The application of the developed creep assessment methods in remnant life assessment proved to exceed the scope of this work and therefore needs to be considered in future. This will allow the proposed strain assessment methods to play a role in the life-extension programs of the UK's aging power stations.

9.4. Future potential of the novel strain assessment methods

In this thesis several methods have been proposed for characterising inelastic deformation in Type 316 stainless steel from lattice orientation changes measured using a commercial EBSD system. The novel methods were developed taking into consideration factors affecting the evolution of strain-induced misorientation, such as the deformation conditions and the microstructure. As there has been little published work on how these factors influence misorientation development, these new methods, particularly those insensitive to microstructural variations e.g. the DGF metric, are likely to be widely used for strain assessment in 316 steels in future.

The innovation in the current methods is the ability to assess the inelastic strain history of a given component after service. Currently there is no existing technique with this capability and so the work presented in this thesis will be invaluable in 'post mortem'

studies of failed power plant components operated under creep regimes. Such studies will help to characterise both the prior plastic and the accumulated creep strains thus enabling establishment of the critical inelastic strains for such components. These can then be used as reference values when assessing the remaining life of a similar component in service.

The applicability of these new methods for assessing small inelastic strains is limited by the current angular resolution of commercial EBSD systems using Hough transforms in orientation measurement. This limitation makes it impossible to detect very small changes in lattice orientation which may arise from elastic strain and/or lattice distortion. However, this is possible through emerging new techniques such as cross-correlation EBSD [199-201], which measure strain through comparison of EBSD patterns' zone axes' shifts between strained and unstrained region of the crystal. This method is most suitable for assessing localised intragranular strain and may be used to strength the work reported in this thesis by evaluating the local effects of precipitates and solute atoms on lattice rotation. Since the method relies on high resolution DP images its application for strain assessment on as large areas as those associated with the Hough-based method, is limited by the massive size of the data collected.

REFERENCES

[1] Department of Energy and Climate Change, *UK Energy in Brief 2013*, National Statistics, London, 2013. https://www.gov.uk/government/collections/uk-energy-in-brief, Access date: October 2013.

[2] Lillington JN. *The Future of Nuclear Power.* Amsterdam: Elsevier, 2004.

[3] Viswanathan R. *Damage Mechanisms and Life Assessment of High Temperature Components.* Ohio: ASM International, 1989.

[4] Maslin M. *Global Warming: Causes, Effects, and the Future.* Minnesota: Voyageur Press, 2007.

[5] Department of Energy and Climate Change, 2011 UK Greenhouse Gas Emissions, National Statistics, London, 2013. https://www.gov.uk/government/uploads/system/uploads/attachment_data/file/180823/ghg_national_statistics_release_2011_final_results.pdf, Access date: October 2013.

[6] Beer JM. *Progress in Energy and Combustion Science* 2007;33:107.

[7] Abe F, Kern TU, Viswanathan R. *Creep-Resistant Steels.* Cambridge: Woodhead Publishing Ltd, 2008.

[8] Evans RW, Wilshire B. *Introduction to Creep.* London: The Institute of Materials, 1993.

[9] O'Donnell MP, Bradford RAW, Dean DW, Hamm CD, Chevalier M. *Structural Integrity of Nuclear Power Plant: High Temperature issues in Advanced Gas Cooled Reactors (AGR). TAGSI/FESI.* Abington: EMAS Publishing, 2013. p.1.

[10] BS 806: 1993 Specification for design and construction of ferrous piping installations for and in connection with land boilers

[11] Sposito G, Ward C, Cawley P, Nagy PB, Scruby C. *NDT & E International* 2010;43:555.

[12] Marder AR. *Replication Microscopy Techniques for NDE.* In: ASM, editor. *ASM Handbook: Nondestructive Evaluation and Quality Control*, Vol. 17. Ohio: ASM International, 1989. p.95.

[13] Cane BJ, Aplin PF. *The Journal of Strain Analysis for Engineering Design* 1994;29:225.

[14] Penny RK, Marriott DL. *Design for Creep.* London: Chapman & Hall, 1995.

[15] Hull D, Bacon DJ. *Introduction to Dislocations.* Oxford: Elsevier Ltd, 2011.

[16] Frost HJ, Ashby MF. *Deformation-Mechanism Maps: The Plasticity and Creep of Metals and Ceramics.* Oxford: Pergamon Press, 1982.

[17] Marshall P. *Austenitic Stainless Steels: Microstructure and Mechanical Properties.* Essex: Elsevier Applied Science, 1984.

[18] Davis JR. *ASM Speciality Handbook: Stainless Steel.* Ohio: ASM International, 1994.

[19] Davis JR. *ASM Speciality Handbook: Heat-Resistant Materials.* Ohio: ASM International, 1997.

[20] Douthett J. *Heat Treating of Stainless Steels.* In: ASM, editor. *ASM handbook: Heat Treating*, Vol. 4. Ohio: ASM International, 1991. p.1684.

[21] Maziasz PJ. *Precipitation Response of Austenitic Stainless Steel to Simulated Fusion Irradiation.* Tennessee: Oak Ridge National Laboratory, 1978.

[22] Weiss B, Stickler R. *Metallurgical and Materials Transactions* 1972;3:851.

[23] Gavriljuk VG, Berns H. *High Nitrogen Steels: Structure, Properties, Manufacture, Applications.* Berlin: Springer, 1999.

[24] Bhadeshia HKDH, Honeycombe RWK. *Steels: Microstructure and Properties.* Oxford: Elsevier Ltd, 2006.

[25] McGuire MF. *Stainless Steels for Design Engineers.* Ohio: ASM International, 2008.

[26] Rios PR, Padilha AF. *Precipitation from Austenite*. In: Buschow KHJ, editor. *Encyclopedia of Materials: Science and Technology*. Oxford: Elsevier, 2005. p.1.

[27] Horak JA, Sikka VK, Raske DT. *Review of Mechanical Properties and Microstructures of Types 304 and 316 Stainless Steel after Long-Term Aging. IAEA Specialists on Mechanical Properties of Structural Materials*. Chester, UK 1983. p.35.

[28] Sourmail T. *Material Science and Technology* 2001;17:1.

[29] Brick RM, Gordon RB, Phillips A. *Structure and Properties of Alloys: The Application of Phase Diagrams to The Interpretation and Control of Industrial Alloy Structures*. London: McGraw-Hill, 1965.

[30] Murthy VSR, Jena AK, Gupta KP, Murty GS. *Structure and Properties of Engineering Materials*. New Delhi: Tata McGraw-Hill, 2003.

[31] Dieter GE. *Mechanical Metallurgy*. London: McGraw-Hill, 1988.

[32] Francois D, Pineau A, Zaoui A. *Mechanical Behaviour of Materials: Volume 1: Micro- and Macroscopic Constitutive Behaviour*: Springer, 2012.

[33] Randle V. *Acta Materialia* 2004;52:4067.

[34] Gertsman VY, Tangri K. *Philosophical Magazine A* 1991;64:1319.

[35] Washko SD, Aggen G. *Wrought Stainless Steels*. In: ASM, editor. *ASM Handbook: Properties and Selection of Irons, Steels and High Performance Alloys*, Vol. 1. Ohio: ASM International, 1992. p.2049.

[36] Raghavan V. *Physical Metallurgy: Principles and Practice*: PHI Learning, 2006.

[37] Li JCM. *Transactions of the Metallurgical Society of AIME* 1963;227:239.

[38] Morris Jr JW. *Dislocation-controlled Plasticity of Crystalline Materials: Overview*. In: Buschow KH, editor. *Encyclopedia of Materials: Science and Technology (Second Edition)*. Oxford: Elsevier, 2001. p.2245.

[39] Arsenlis A, Parks DM. *Acta Materialia* 1999;47:1597.

[40] Ashby MF. *Philosophical Magazine* 1970;21:399.

[41] Tanaka H, Murata M, Abe F, Irie H. *Materials Science and Engineering: A* 2001;319-321:788.

[42] Challenger K, Moteff J. *Metallurgical and Materials Transactions B* 1973;4:749.

[43] Bampton CC, Jones IP, Loretto MH. *Acta Metallurgica* 1978;26:39.

[44] Bressers J. *Creep and Fatigue in High Temperature Alloys*. London: Applied Science Publishers Ltd, 1981.

[45] Kassner ME, Perez-Prado MT. *Fundamentals of Creep in Metals and Alloys*. London: Elsevier Science, 2004.

[46] Mannan SL, Rodriguez P. *Metal Science* 1983;17:63.

[47] Tanaka H, Murata M, Abe F, Yagi K. *Materials Science and Engineering: A* 1997;234-236:1049.

[48] Wilshire B, Willis M. *Metallurgical and Materials Transactions A* 2004;35:563.

[49] Ohashi Y, Kawai M, Momose T. *Journal of Engineering Materials and Technology* 1986;108:68.

[50] Li DF, O'Dowd NP, Davies CM, Nikbin KM. *International Journal of Pressure Vessels and Piping* 2010;87:531.

[51] Zhang YH, Knowles DM. *Materials Science and Technology* 2002;18:917.

[52] Weisman C. *Welding Handbook: Fundamental of Welding*. London: Macmillan Press, 1976.

[53] Kobe-Steel. *Arc Welding of Specific Steels and Cast Irons*. Tokyo: Kobe Steel Ltd, 2011.

[54] Chon LT, Chin. M.T. *Heat Flow in Fusion Welding*. In: ASM, editor. *ASM Handbook: Welding, Brazing and Soldering*, Vol. 6. Ohio: ASM International, 2006. p.22.

[55] Yin Y, Faulkner RG. *Physical and Elastic Behaviour of Creep-Resistant Steels*. In: Abe F, Kern TU, Viswanathan R, editors. *Creep-Resistant Steels*. Cambridge: Woodhead Publishing Ltd, 2008. p.217.

[56] Viswanathan R, Stringer J. *Journal of Engineering Materials and Technology, Transactions of the ASME* 2000;122:246.

[57] Maharaj C, Dear JP, Morris A. *Strain* 2009;45:316.

[58] Sakanashi Y. *Measurement of Creep Deformation in Weldments*, PhD Thesis, Open University, Milton Keynes, 2013.

[59] Sutton MA, Wolters WJ, Peters WH, Ranson WF, McNeill SR. *Image and Vision Computing* 1983;1:133.

[60] Predeleanu M, Gilormini P. *Advanced Methods in Materials Processing Defects.* Amsterdam: Elsevier science B.V, 1997.

[61] BS EN ISO 14577-1:2002 Metallic materials - Instrumented indentation test for hardness and materials parameters - Part 1: Test method.

[62] Auzoux Q, Allais L, Caës C, Monnet I, Gourgues AF, Pineau A. *Journal of Nuclear Materials* 2010;400:127.

[63] Yoda R, Yokomaku T, Tsuji N. *Materials Characterization* 2010;61:913.

[64] Hou J, Shoji T, Lu ZP, Peng QJ, Wang JQ, Han EH, Ke W. *Journal of Nuclear Materials* 2010;397:109.

[65] Shiwa M, Kishi T. *NDT-based Assessment of Damage: An Overview.* In: Buschow KHJ, editor. *Encyclopedia of Materials: Science and Technology (Second Edition).* Oxford: Elsevier, 2005. p.1.

[66] Stegemann D, Raj B. *NDT for Analysis of Microstructures and Mechanical Properties of Metallic Materials.* In: Buschow KHJ, editor. *Encyclopedia of Materials: Science and Technology (Second Edition).* Oxford: Elsevier, 2002. p.1.

[67] Venables JA, Harland CJ. *Philosophical Magazine* 1973;27:1193.

[68] Lassen NCK. *Automated Determination of Crystal Orientations from Electron Backscattering Patterns*, PhD Thesis, Technical University of Denmark, Lyngby, 1994.

[69] Kunze K, Wright SI, Adams BL, Dingley DJ. *Textures and Microstructures* 1993;20:41.

[70] Adams B, Wright S, Kunze K. *Metallurgical Transactions A* 1993;24:819.

[71] Wright SI, Adams BL. *Textures and Microstructures* 1991;14:273.

[72] Randle V. *Journal of Materials Science* 2009;44:4211.

[73] Baba-Kishi KZ. *Journal of Materials Science* 2002;37:1715.

[74] Humphreys FJ. *Journal of Materials Science* 2001;36:3833.

[75] Dingley D. *Journal of Microscopy* 2004;213:214.

[76] Randle V. *Materials Characterization* 2009;60:913.

[77] Maitland T, Sitzman S. *Electron Backscatter Diffraction (EBSD) Technique and Materials Characterization Examples*. In: Zhou W, Wang ZL, editors. *Scanning Microscopy for Nanotechnology: Techniques and Applications*. New York: Springer Science, 2007. p.41.

[78] Schwartz AJ, Kumar M, Adams BL. *Electron Backscatter Diffraction in Materials Science*. London: Kluwer Academic/Plenum Publishers, 2000.

[79] Randle V, Engler O. *Introduction to Texture Analysis: Macrotexture, Microtexture and Orientation Mapping*. Amsterdam: Gordon and Breach science, 2000.

[80] Eades A, Deal A, Bhattacharyya A, Hooghan T. *Energy Filtering in EBSD*. In: Schwartz AJ, Kumar M, Adams BL, Field DP, editors. *Electron Backscatter Diffraction in Materials Science*. New York: Springer US, 2009. p.53.

[81] Dingley DJ. *The Development of Automated Diffraction in Scanning and Transmission Electron Microscopy*. In: Schwartz AJ, Kumar M, Adams BL, editors. *Electron Backscatter Diffraction in Materials Science*. New York: Kluwer academic, 2000. p.1.

[82] Goodhew PJ, Humphreys J, Beanland R. *Electron Microscopy and Analysis*. New York: Taylor and Francis, 2001.

[83] Exner HE, Weinbruch, S. . *Scanning Electron Microscopy* In: Vander Voort GFV, editor. *ASM Handbook: Metallography and Microstructures* Vol. 9. Ohio: ASM International, 2004. p.833.

[84] Schwarzer RA, Field DP, Adams BL, Kumar M, Schwartz AJ. *Present State of Electron Backscatter Diffraction and Prospective Developments*. In: Schwartz AJ, Kumar M, Adams BL, editors. *Electron Backscatter Diffraction in Materials Science* London: Kluwer Academic/Plenum Publishers, 2009. p.1.

[85] Mingard K, Day A, Maurice C, Quested P. *Ultramicroscopy* 2011;111:320.

[86] Field DP. *Microscopy and Microanalysis* 2005;11:52.

[87] Wright S, Adams B. *Metallurgical Transactions A* 1992;23:759.

[88] Wright SI, Nowell MM, Field DP. *Microscopy and Microanalysis* 2011;17:316.

[89] Baba-Kishi KZ. *Scanning* 1998;20:117.

[90] Kumar M, Field D. *Electron Backscatter Diffraction of Aluminum Alloys*. In: Mackenzie DS, Totten GE, editors. *Analytical Characterization of Aluminum, Steel, and Superalloys*. Florida: CRC Press, 2005. p.519.

[91] Xu W, Ferry M, Mateescu N, Cairney JM, Humphreys FJ. *Materials Characterization* 2007;58:961.

[92] Ralph KI. *The Chemistry of Silica: Solubility, Polymerization, Colloid and Surface Properties, and Biochemistry*. New York: John Wiley and Sons, 1979.

[93] Goodhew PJ. *Practical Methods in Electron Microscopy*. In: Glavert AM, editor. *Specimen Preparation in Materials Science*, Vol. 1. Amsterdam: North-Holland Publishing Company, 1972.

[94] ASM. *Chemical and Electrolytic Polishing*. In: Vander Voort GF, editor. *ASM Handbook: Metallography and Microstructures*, Vol. 9. Ohio: ASM International, 2004. p.693.

[95] Schwarzer RA, Zaefferer S, Kunze K. *The Characterisation of Microtexture by Orientation Mapping. Denver X-ray Conference on Applications of X-ray Analysis*, Vol. 38. Steamboat Spring: Advances in X-Ray Analysis, 1995. p.547.

[96] Adams B, Wright S, Kunze K. *Metallurgical Transactions A* 1993;24:819.

[97] Humphreys FJ. *Journal of Microscopy* 1999;195:170.

[98] Schwarzer RA. *Ultramicroscopy* 1997;67:19.

[99] Schwarzer RA. *Micron* 1997;28:249.

[100] Humphreys FJ, Huang Y, Brough I, Harris C. *Journal of Microscopy* 1999;195:212.

[101] Goldstein J, Newbury D, Joy D, Lyman C, Echlin P, Lifshin E, Sawyer L, Michael J. *Scanning Electron Microscopy and X-ray Microanalysis*. New York: Springer, 2003.

[102] Ennos AE. *British Journal of Applied Physics* 1953;4:101.

[103] NordlysF and Fast Acquisition Software, HKL-Oxford Instruments 2010.

[104] Maitland TM. *Microscopy and Microanalysis* 2004;10:936.

[105] Bunge HJ. *Texture Analysis in Materials Science: Mathematical Methods*. London: Butterworths, 1982.

[106] Cho J-H, Rollett A, Oh K. *Metallurgical and Materials Transactions A* 2005;36:3438.

[107] Jeremy MK, Christopher SA. *Representations of Texture*. In: Schwartz AJ, Kumar M, Adams BL, Field DP, editors. *Electron Backscatter Diffraction in Materials Science*. New York: Springer Science, 2009. p.35.

[108] Humphreys FJ, Bate PS, Hurley PJ. *Journal of Microscopy* 2001;201:50.

[109] Lee H, Han HN, Kang SH, Sun J, Kim DH, Oh KH. *IEEE* 2006:116.

[110] Yardley VA, Matsuzaki T, Sugiura R, Yokobori AT, Tsurekawa S, Hasegawa Y. *Journal of Physics* 2010;240:1.

[111] Brewer LN, Othon MA, Young LM, Angeliu TM. *Microscopy and Microanalysis* 2006;12:85.

[112] Kocks UF, Norberto C, Wenk TH. *Texture and Anisotropy: Preferred Orientations in Polycrystals and their Effects on Material Properties*. Cambridge: Cambridge University Press, 1998.

[113] Banovic SW, Vaudin MD, Gnaeupel-Herold TH, Saylor DM, Rodbell KP. *Materials Science and Engineering A* 2004;380:155.

[114] Mishin OV, Godfrey A, Jensen DJ. *Analysis of Deformation Structures in FCC Materials using EBSD and TEM Techniques*. In: Schwartz AJ, Kumar M, Adams BL, editors. *Electron Backscatter Diffraction in Materials Science*. New York: Springer Science, 2009. p.263.

[115] Fujiyama K, Mori K, Matsunaga T, Kimachi H, Saito T, Hino T, Ishii R. *Materials Science and Engineering A* 2009;510-511:195.

[116] Fujiyama K, Mori K, Kaneko D, Kimachi H, Saito T, Ishii R, Hino T. *International Journal of Pressure Vessels and Piping* 2009;86:570.

[117] Yamazaki S, Lu Z, Ito Y, Takeda Y, Shoji T. *Corrosion Science* 2008;50:835.

[118] Wright SI. *Quantification of Recrystallization Fraction from Orientation Imaging Scans*. In: Szpunar JA, editor. *Proceedings of the Twelfth International Conference on Texture of Materials (ICOTOM 12)*, Vol. 12. Montreal: NRC Research Press, 1999.

[119] Lehockey EM, Lin Y, Lepik OE. *Mapping Residual Plastic Strain in Materials using Electron Backscatter Diffraction*. In: Schwartz AJ, Kumar M, Adams BL, editors. *Electron Backscatter Diffraction in Materials Science*. New York: Kluwer Academic, 2000. p.247.

[120] Godfrey A, Krieger Lassen NC. *Journal of Microscopy* 2000;197:249.

[121] Mirzadeh H, Cabrera JM, Najafizadeh A, Calvillo PR. *Materials Science and Engineering: A* 2012;538:236.

[122] Boehlert CJ, Dickmann DS, Eisinger NC. *Metallurgical and Materials Transactions A* 2006;37:27.

[123] Githinji D, Northover S, Bouchard PJ, Rist M. *Metallurgical and Materials Transactions A* 2013;44:4150.

[124] Kamaya M, Wilkinson AJ, Titchmarsh JM. *Nuclear Engineering and Design* 2005;235:713.

[125] Kamaya M, Wilkinson AJ, Titchmarsh JM. *Acta Materialia* 2006;54:539.

[126] BS EN ISO 6892-1:2009 Metallic materials - Tensile testing - Part 1: Method of test at ambient temperature.

[127] BS EN 10002-5:1992 Tensile testing of metallic materials - Part 5: Method of test at elevated temperatures.

[128] Acar MÖ. *Effects of Plastic Strain History on the Properties of Stainless Steel Boiler Tube Welds*, PhD Thesis, Open University, Milton Keynes, 2011.

[129] ASTM E9-89a: Standard test methods of compression testing of metallic materials at room temperature.

[130] Roebuck B, Lord JD, Brooks M, Loveday MS, Sellars CM, Evans RW. *Measuring Flow Stress in Hot Axisymmetric Compression Tests.* Teddington: National Physical Laboratory, 2002.

[131] Kalidindi SR, Abusafieh A, El-Danaf E. *Experimental Mechanics* 1997;37:210.

[132] BS EN ISO 204:2009 Metallic materials - Uniaxial creep testing in tension - Method of test

[133] Channel 5 Software, HKL Technology, 2004.

[134] BS EN ISO 6507-1:2005 Metallic materials - Vickers hardness test - Part 1: Test method.

[135] TestWorks® 4 Software for Nanoindentation, MTS Systems Corporation, Eden Prairie, MN, USA.

[136] ASM. *Mechanical Grinding and Polishing.* In: Vander Voort GF, editor. *ASM Handbook: Metallography and Microstructures* Vol. 9. ASM International, 2004. p.651.

[137] Brundle CR, Charles A. Evans J, Wilson S. *Encyclopedia of Materials Characterization*. Boston: Butterworth-Heinemann, 1992.

[138] Aztec 2.1 Software, Oxford Instruments NanoAnalysis, 2010-2013.

[139] Hayter AJ. *Probability and Statistics for Engineers and Scientists*. Boston: Brooks/Cole Centage Learning, 2012.

[140] Mood AM, Graybill FA, Boes DC. *Introduction to the Theory of Statistics*. New York: McGraw-Hill, 1974.

[141] Brandon DG. *Acta Metallurgica* 1966;14:1479.

[142] ASTM E112-12: Standard test methods for determining average grain size

[143] Abramoff MD, Magalhaes PJ, Ram SJ. *Biophotonics International* 2004;11:36.

[144] ASTM E2627-10: Standard practice for determining average grain size using Electron Backscatter Diffraction (EBSD) in fully recrystallized polycrystalline materials

[145] Hong HU, Rho BS, Nam SW. *Materials Science and Engineering A* 2001;318:285.

[146] Ham RK. *Philosophical Magazine* 1961;6:1183.

[147] Fultz B, Howe J. *Transmission Electron Microscopy and Diffractometry of Materials*: Springer, 2012.

[148] Williams D.B., Carter C.B. *Transmission Electron Microscopy: A Textbook for Materials Science*. London: Plenum Press, 1996.

[149] Sun QP, Tong P. *IUTAM Symposium on Size Effects on Material and Structural Behavior at Micron- and Nano-scales*. Dordrecht: Springer, 2006.

[150] Ashby MF. *Philosophical Magazine* 1970;21:399.

[151] Kashyap BP, McTaggart K, Tangri K. *Philosophical Magazine* 1988;57:97.

[152] Auzoux Q, Allais L, Caes C, Girard B, Tournie I, Gourgues AF, Pineau A. *Nuclear Engineering and Design* 2005;235:2227.

[153] Michel DJ, Moteff J, Lovell AJ. *Acta Metallurgica* 1973;21:1269.

[154] Kestenbach H, Luiz Da Silvelra T, Monteiro S. *Metallurgical Transactions A* 1976;7:155.

[155] Yunsung Kim YK, Daewhan Kim,Sungsoo Kim, Wonjong Nam and Heeman Choe. *Materials Transactions* 2011;52:507.

[156] Peng B, Zhang H, Hong J, Gao J, Zhang H, Wang Q, Li J. *Materials Science and Engineering: A*;528:3625.

[157] Barnby JT, Smith E. *Acta Metallurgica* 1964;12:1353.

[158] Fahr D. *Analysis of Stress-Strain Behavior of Type 316 Stainless Steel.* Tennessee: OAK Ridge National Laboratory, 1973.

[159] Stoter LP. *Journal of Materials Science* 1981;16:1039.

[160] Schweitzer E, Durst K, Amberger D, Gaken M. *MRS Online Proceedings Library* 2004;821.

[161] Simmons JW. *Materials Science and Engineering: A* 1996;207:159.

[162] Stoltz RE, Sande JB. *Metallurgical Transactions A* 1980;11:1033.

[163] Cullen AC, Frey HC. *Probabilistic Techniques in Exposure Assessment: A Handbook for Dealing with Variability and Uncertainty in Models and Inputs* New York: Plenum Press, 1999. p.130.

[164] Loucks DP, Van Beek E. *Concepts in Probability, Statistics and Stochastic Modelling*. Paris: Unesco, 2005. p.170.

[165] Govindarajulu Z. *Statistical Techniques in Bioassay*. Basel: S. Karger AG, 2001.

[166] Byun TS, Hashimoto N, Farrell K. *Acta Materialia* 2004;52:3889.

[167] Venugopal S, Mannan SL, Prasad YVRK. *Journal of Nuclear Materials* 1995;227:1.

[168] Samuel KG, Mannan SL, Rodriguez P. *Acta Metallurgica* 1988;36:2323.

[169] Samuel EI, Choudhary BK, Rao KBS. *Scripta Materialia* 2002;46:507.

[170] Shastry CG, Mathew MD, Rao KBS, Pathak SD. *Materials Science and Technology* 2007;23:1215.

[171] Nogueira MT, Fortes MA. *Scripta Materialia* 1984;18:505.

[172] Kashyap BP, Tangri K. *Acta Metallurgica et Materialia* 1995;43:3971.

[173] Hughes DA, Liu Q, Chrzan DC, Hansen N. *Acta Materialia* 1997;45:105.

[174] Pantleon W, Hansen N. *Acta Materialia* 2001;49:1479.

[175] Pantleon W. *Journal of Materials Research* 2002;17:2433.

[176] Hughes DA, Chrzan DC, Liu Q, Hansen N. *Physical Review Letters* 1998;81:4664.

[177] Bay B, Hansen N, Hughes DA, Kuhlmann-Wilsdorf D. *Acta Metallurgica et Materialia* 1992;40:205.

[178] Janecek M, Tangri K. *Journal of Materials Science* 1995;30:3820.

[179] Gottschalk PG, Dunn JR. *Analytical Biochemistry* 2005;343:54.

[180] Kurzydlowski KJ, McTaggart KJ, Tangri K. *Philosophical Magazine* 1990;61:61.

[181] Fukuoka C, Morishima K, Yoshizawa H, Mino K. *Scripta Materialia* 2002;46:61.

[182] Wang; X, Abe; T, ; NT, Shimizu; I. *Memoirs of the Faculty of Engineering* 2005;39:7.

[183] Stoudt MR, Hubbard JB. *Acta Materialia* 2005;53:4293.

[184] Kassner ME, Hayes TA. *International Journal of Plasticity* 2003;19:1715.

[185] Willis M, McDonaugh-Smith A, Hales R. *International Journal of Pressure Vessels and Piping* 1999;76:355.

[186] Konopka K, Wyrzykowski JW. *Journal of Materials Processing Technology* 1997;64:223.

[187] Karaman I, Sehitoglu H, Maier HJ, Chumlyakov YI. *Acta Materialia* 2001;49:3919.

[188] Field DP, True BW, Lillo TM, Flinn JE. *Materials Science and Engineering: A* 2004;372:173.

[189] Jorge-Badiola D, Iza-Mendia A, Gutierrez I. *Materials Science and Engineering: A* 2005;394:445.

[190] Howell PR, Nilsson JO, Dunlop GL. *Philosophical Magazine A* 1978;38:39.

[191] Varin RA, Kruszynska J. *Acta Metallurgica* 1987;35:1767.

[192] LeBlanc DC. *Statistics: Concepts and Applications for Science*: Jones and Bartlett, 2004.

[193] Bell S. *Measurement Good Practice Guide No. 11: A Beginner's Guide to Uncertainty of Measurement.* Teddington: National Physical Laboratory, 1999.

[194] Gowrisankar; I, Bhaduri; AK, Seetharaman; V, Verma; DDN, Achar; DRG. *Welding Research* 1987;Supplement:147.

[195] Kamaya M. *Materials Characterization* 2009;60:125.

[196] Buchanan PJ, Randle V, Flewitt PEJ. *Scripta Materialia* 1997;37:1511.

[197] Masayuki K. *Ultramicroscopy* 2011;111:1189.

[198] Kobayashi D, Miyabe M, Kagiya Y, Sugiura R, Yokobori AT. *Metallurgical and Materials Transactions A* 2013;44:3123.

[199] Wilkinson AJ, Meaden G, Dingley DJ. *Ultramicroscopy* 2006;106:307.

[200] Wilkinson AJ, Clarke EE, Britton TB, Littlewood P, Karamched PS. *Journal of Strain Analysis for Engineering Design* 2010;45:365.

[201] Britton TB, Wilkinson AJ. *Ultramicroscopy* 2012;114:82.

[202] Humbert M, Gey N, Muller J, Esling C. *Journal of Applied Crystallography* 1996;29:662.

APPENDIX 1: ORIENTATION SPREAD

At strain >0.1 crystal symmetry-related spread was noted within some grains where there were large deviations in the measured orientations all of which represented valid solutions for the diffraction patterns. In such cases the following procedure was adopted in the calculation of mean misorientation (Θ);

1. Conversion of each orientation expressed in Euler angles (φ_1, φ, φ_2) into a quaternion (q) whose components satisfy a normalisation constraint $q \equiv {q_0}^2 + {q_1}^2 + {q_2}^2 + {q_3}^2 = 1$, using equations [202]:

$$q_0 = \cos\frac{\varphi}{2}\cos\frac{(\varphi_1 + \varphi_2 - 2\pi)}{2} \quad \text{Eq. 11.1}$$

$$q_1 = -sin\frac{\varphi}{2}\,sin\,\frac{(\varphi_1 - \varphi_2 + 2\pi)}{2} \quad \text{Eq. 11.2}$$

$$q_2 = sin\frac{\varphi}{2}cos\frac{(\varphi_1 - \varphi_2 + 2\pi)}{2} \quad \text{Eq. 11.3}$$

$$q_3 = cos\frac{\varphi}{2}sin\frac{(\varphi_1 + \varphi_2 - 2\pi)}{2} \quad \text{Eq. 11.4}$$

2. Computing the dot product of $q.s_c$, where s_c is the 24 crystal symmetry-related operators given in quaternion (Table 11.1).
3. For each orientation, selecting the q with the highest q_0 out of the 24 equivalent solutions.
4. Computing the mean quaternion q_m from k quaternion with the highest q_0 in each grain using:

$$q_m = \frac{(q^1 + q^2 + q^3 + q^k)}{\|q^1 + q^2 + q^3 + q^k\|} \quad \text{Eq. 11.5}$$

5. Finally computing mean grain misorientation (Θ) based on mean quaternion as follows [202]:

$$\Theta = 4\sin^{-1}\sqrt{\left[\frac{1-(q_0 * q_0^k + V * V^k)}{2}\right]} \qquad \text{Eq. 11.6}$$

where q_0 is the first component of the mean quaternion, q_0^k is the first component of the k^{th} quaternion in a grain while V represents the other quaternion components $V \equiv q_1, q_2, q_3$. The arithmetic mean of the Euler angles does not give the same Θ result due to the orientation spread and should be avoided when calculating the mean orientation within a grain.

Quaternion algebra expresses 3-dimensional vector in a four dimensional space which allows easy computation of products, divisions and means of orientation data expressed in Euler angles.

Table 11.1: Cubic crystal symmetry operations expressed as quaternion [106].

Possible solution	s_c				**Possible solution**	s_c			
1	1	0	0	0	**13**	0.7071	0.7071	0	0
2	0	1	0	0	**14**	0.7071	0	0.7071	0
3	0	0	1	0	**15**	0.7071	0	0	0.7071
4	0	0	0	1	**16**	0.7071	-0.7071	0	0
5	0.5	0.5	0.5	0.5	**17**	0.7071	0	-0.7071	0
6	0.5	-0.5	-0.5	-0.5	**18**	0.7071	0	0	-0.7071
7	0.5	0.5	-0.5	0.5	**19**	0	0.7071	0.7071	0
8	0.5	-0.5	0.5	-0.5	**20**	1	-0.7071	0.7071	1
9	0.5	-0.5	0.5	0.5	**21**	0	0	0.7071	0.7071
10	0.5	0.5	-0.5	-0.5	**22**	0	0	-0.7071	0.7071
11	0.5	-0.5	-0.5	0.5	**23**	0	0.7071	0	0.7071
12	0.5	0.5	0.5	-0.5	**24**	0	-0.7071	0	0.7071

APPENDIX 2: MATERIAL TEST CERTIFICATE

SANDVIK

CERTIFICATE No. A/07-013609 Rev 00
Date 2007-03-14 Page 1/2

INSPECTION CERTIFICATE acc to
EN 10 204 3.1

INSPECTION STAMP
QA-TUBE

MITSUI BABCOCK ENERGY SVCS LIMIT
BAY NO. 3
BALTIC BUSINESS CENTRE
TYNE & WEAR

Customer References

	Customer order
MI. 74839	2006-09-27

180-00991 BAB007

Sandvik References

Order No.	Subs No.	ABSMT Dispatch note
627957	30129	44466/54

ABSMT No. 300-34187 C.Code 03

Material description
SEAMLESS STAINLESS COLD FINISHED SUPERHEATER TUBES.

Steel making process
Electric furnace

Steel/material Designations
Sandvik 6LR62
AISI TP316H/TP316
BS 316S51

DOOSAN BABCOCK
2 1 MAR 2007
NUCLEAR SERVICES

Technical requirements
BS 3059:Part 2:1990, TC1 MW

EXTENT OF DELIVERY

It	Product designation	Heat	Lot	Pieces	Kg	M
02	XTHR-6LR62-38-4T+ 38.00 X 4.00	509885	55099	40	1072.1	294.05
			Total	40	1072.1	294.05

TEST RESULTS
Chemical composition (weight%)

Heat	C	Si	Mn	P	S	Cr	Ni	Mo
509885	0.050	0.53	1.55	0.029	0.0054	16.89	11.25	2.04
	Co							
509885	0.089							

Tensile test at room temperature

	Yield strength	Tensile strength	Elongation
	MPa	MPa	%
Lot	Rpl.0	Rm	A
55099	179	649	50

Tensile test at 550 degrees C

	Yield strength		Tensile strength	Elongation	
	MPa	MPa	MPa	%	%
Lot	Rp0.2	Rpl.0	Rm	A	2"
55099	158	191	489	39	36

Quality assurance - Per Eriksson / QA-manager Tube & Pipe
MTC Service / Certificates

AB SANDVIK MATERIALS TECHNOLOGY Reg No. 556234-5892 VAT No. SE663000-060901
SE-81181 SANDVIKEN SWEDEN www.smt.sandvik.com mtc_service.smt@sandvik.com

APPENDIX 3: EBSD ORIENTATION MAPS

A: EBSD MAPS FOR TENSILE SPECIMENS DEFORMED AT 550°C

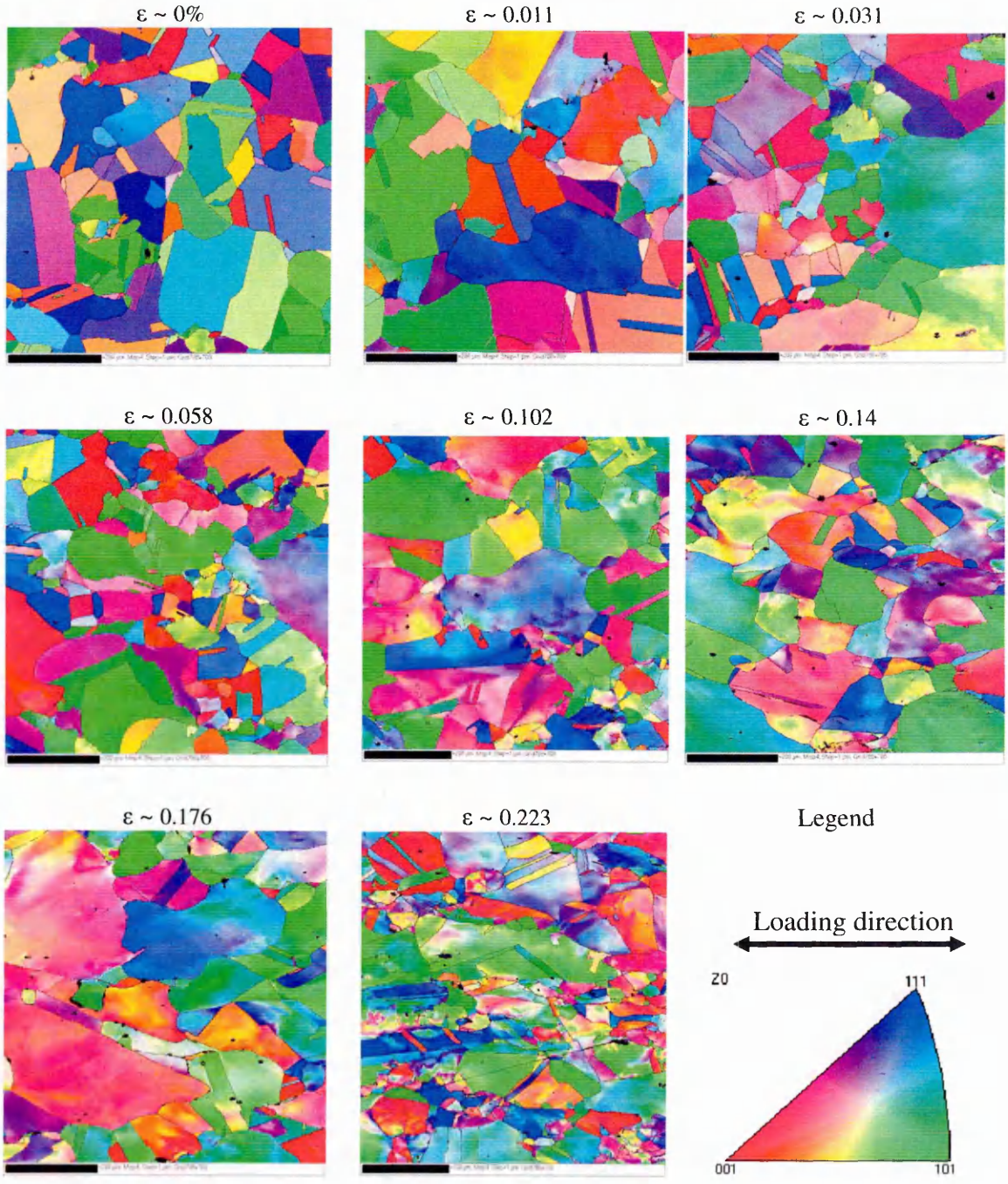

Fig. 13.1. Orientation maps of service-aged Type 316H stainless steel deformed in tension as in Table 6.1. Colour coding is based on crystal directions parallel to specimen's normal direction and no data cleaning is performed. Intragranular colour gradation is evident in many grains.

B: EBSD MAPS FOR COMPRESSION SPECIMENS DEFORMED AT 550°C

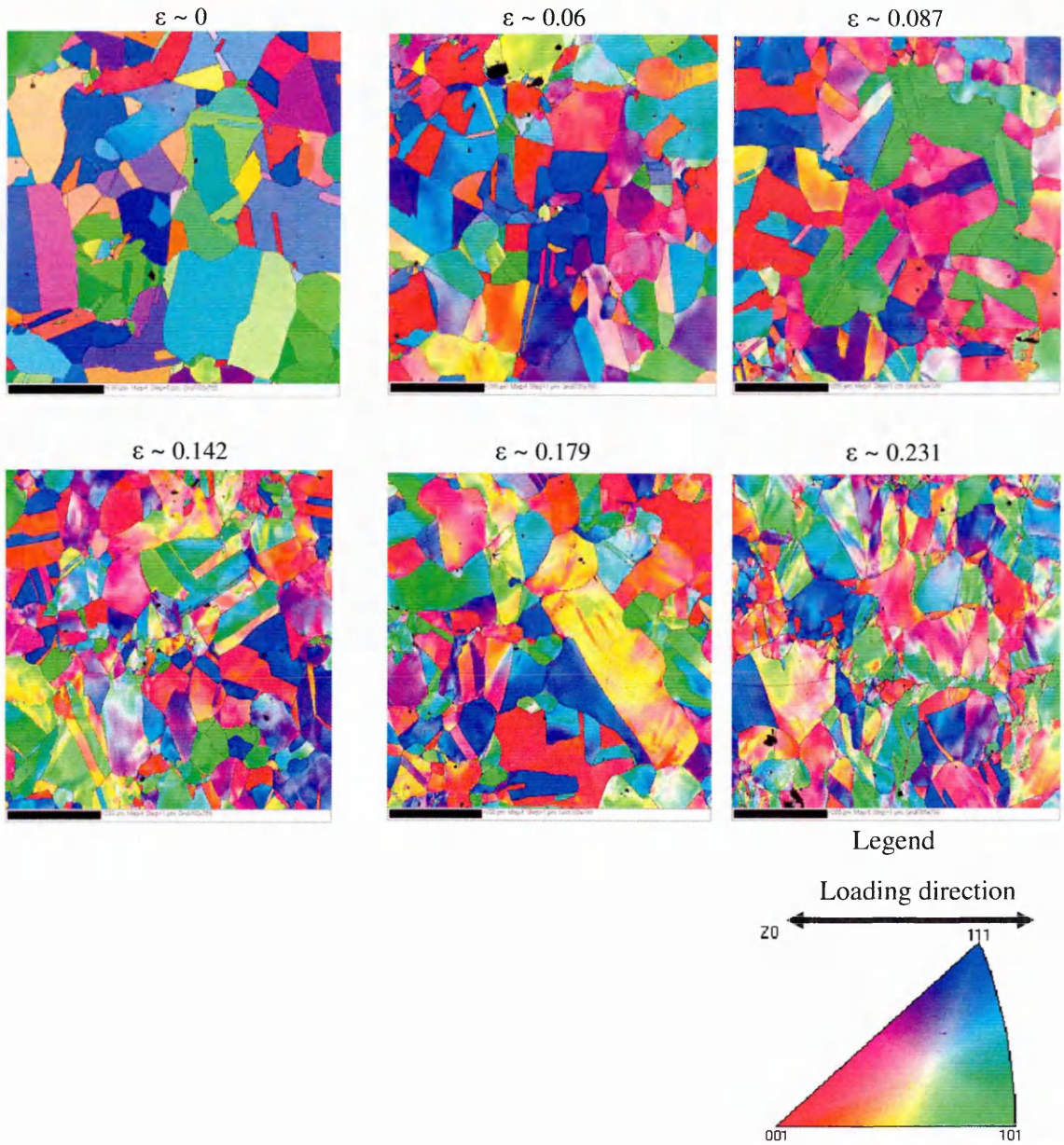

Fig. 13.2. Orientation maps of service-aged Type 316H stainless steel deformed in compression as in Table 6.1. Colour coding is based on crystal directions parallel to specimen's normal direction and no data cleaning is performed. Intragranular colour gradation is evident in many grains.

C: EBSD MAPS FOR CREEP SPECIMENS DEFORMED AT 550°C

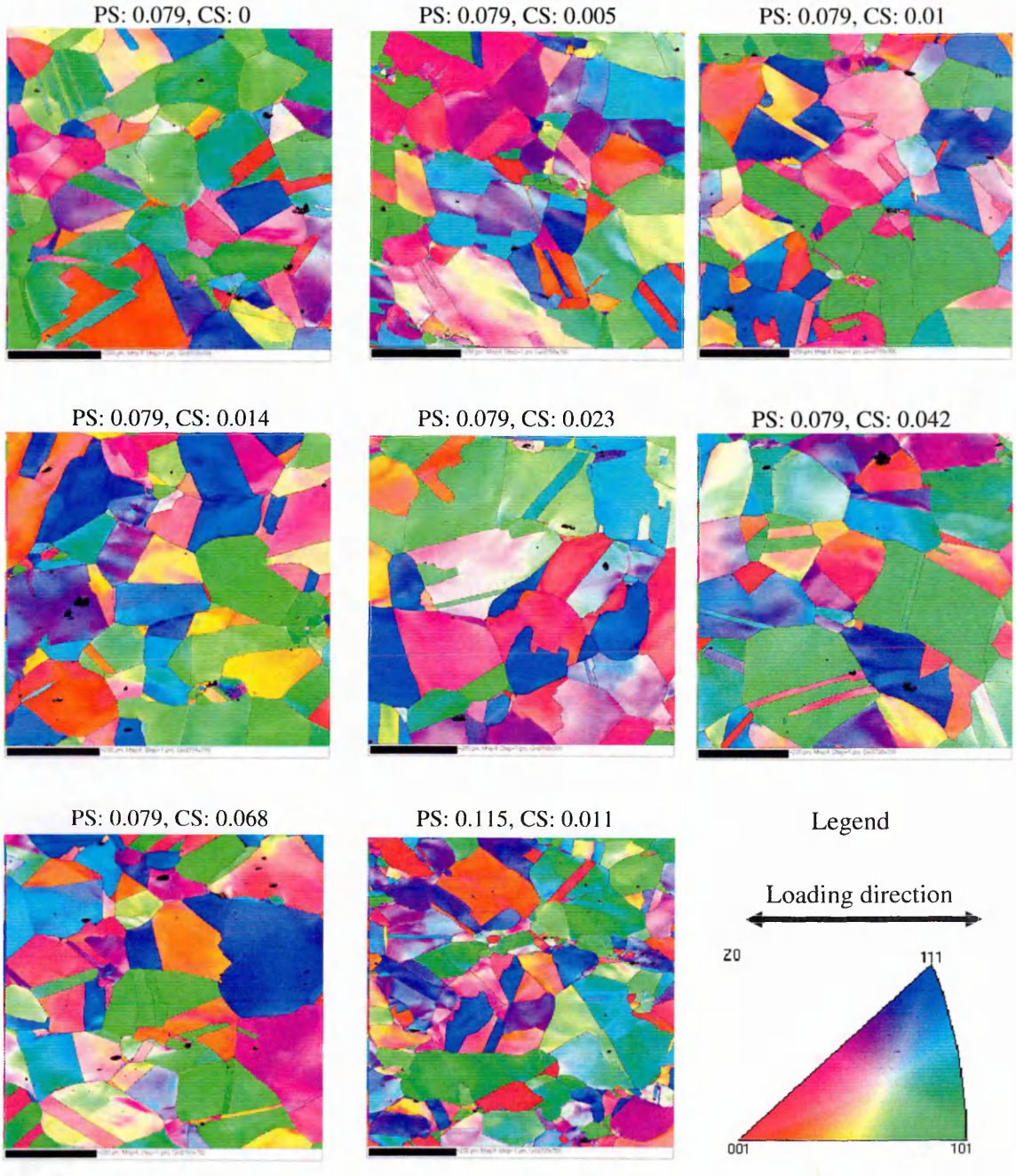

Fig. 13.3. Orientation maps of service-aged Type 316H stainless steel prestrained (PS) and crept (CS) as in Table 7.1. Colour coding is based on crystal directions parallel to specimen's normal direction and no data cleaning is performed. Intragranular colour gradation is evident in many grains.

D: EBSD MAPS FOR CREEP SPECIMENS DEFORMED AT 675°C

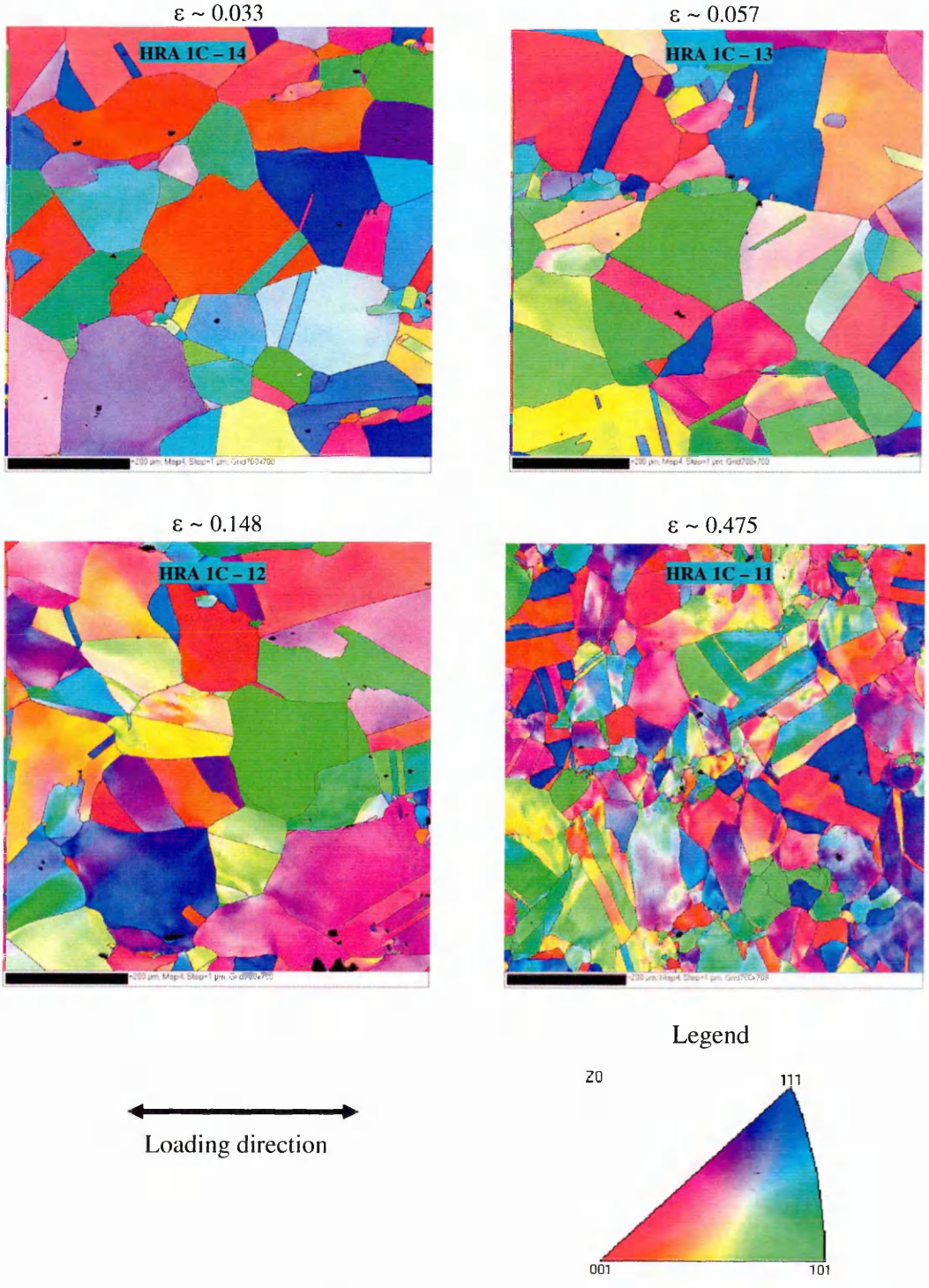

Fig. 13.4. Orientation maps of service-aged Type 316H stainless steel crept at 675°C as in Table 7.2. Colour coding is based on crystal directions parallel to specimen's normal direction and no data cleaning is performed. Intragranular colour gradation is evident in many grains.

E: EBSD MAPS FOR CREEP RUPTURED SPECIMENS AT 550°C

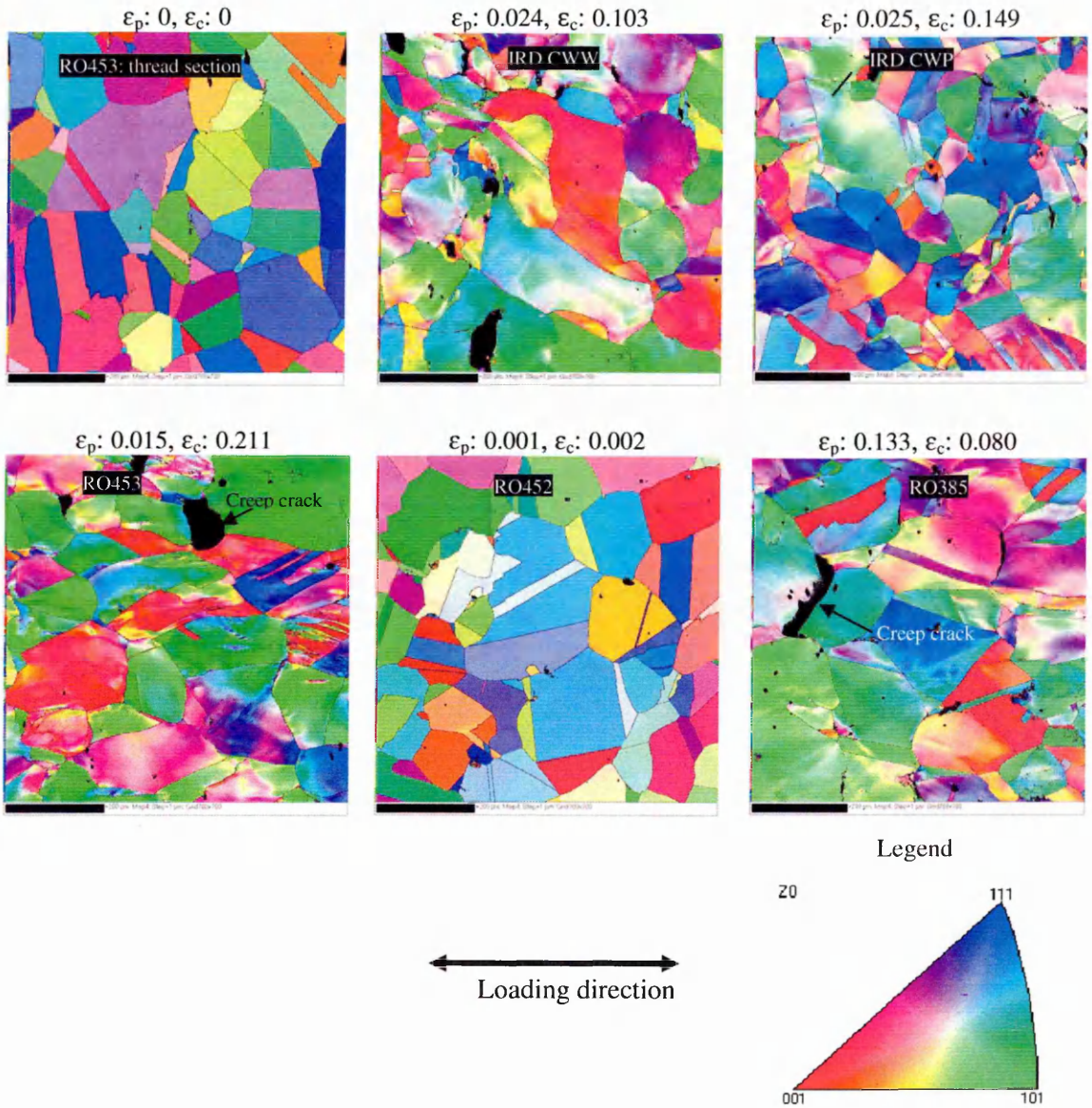

Fig. 13.5. Orientation maps of service-aged Type 316H stainless steel crept at 550°C as in Table 4.3. Colour coding is based on crystal directions parallel to specimen's normal direction and no data cleaning is performed. Intragranular colour gradation and creep cracks are evident in many grains.